# PHYSICAL PROPERTY ANALYSIS, NUMERICAL AND SCALE MODELING FOR PLANNING OF SURFACE SEISMIC SURVEYS: VOISEY'S BAY, LABRADOR

DEANNE DUFF

# Physical Property Analysis, Numerical and Scale Modeling for Planning of Surface Seismic Surveys: Voisey's Bay, Labrador

By

© Deanne Duff, B.Sc. (Hons.)

A thesis submitted to the

School of Graduate Studies

in partial fulfillment of the

requirements for the degree of

Master of Science

Department of Earth Sciences

Memorial University of Newfoundland

St. John's, Newfoundland

March 2007

## Abstract

The Voisey's Bay area is located on the northeast coast of Labrador and hosts one of the most important recent mineral discoveries in Canada – the Voisey's Bay Ni-Cu-Co deposit. The Inco Innovation Centre at Memorial University and Voisey's Bay Nickel Company are using the Voisey's Bay property as a test site for the development of seismic methods for minerals exploration. Extensive drilling, logging and core analysis of unmined ore bodies provides an excellent database designing seismic acquisition, processing and interpretation strategies. An important element of preparation of the seismic experiments is an analysis of an extensive physical properties database and a program of 2-D and 3-D forward modeling designed to help foresee acquisition and processing issues.

The Voisey's Bay ore bodies consist of massive sulphides and breccias of variable sulphide content associated with a geometrically complex troctolitic intrusion hosted in gneiss of variable composition. The physical properties data indicate typical compressional velocities of 6500 m/s for the troctolite, 6100 m/s for the gneiss, and 4400 m/s for the massive sulphide. Also, the mean velocity contrast between the gneiss and troctolite is +8%, and -25-35% between the gneiss/troctolite and the massive sulphide. Mean reflection coefficients between gneiss and troctolite are +0.06, but a modest -0.03 between the troctolite and massive sulphide.

Due to significant variance in the physical properties of all of the rock types, mean values only represent a part of the story. Extensive potential reflectivity modeling has been carried out using Monte Carlo simulation that uses the actual probability distribution of physical properties coupled with transition probabilities that characterize the likelihood of occurrence of a particular lithologic transition, to predict more representative probability distributions for reflection coefficients. Synthetic seismograms were produced to further aid in the assessment of reflective potential of the contrasting lithologies and the necessary source frequencies for adequate resolution in the Voisey's Bay area. In general, the physical properties data indicate that velocity-sensitive techniques are more likely to be effective for direct detection of ore bodies at Voisey's Bay and impedance-sensitive techniques more effective for imaging the magmatic system and structural mapping. However, the data support significant potential for impedance driven ore body detection depending upon the specific setting of the ore body.

The Voisey's Bay area offers a wide range of viable seismic targets of differing complexity that can be used to develop suitable acquisition and processing techniques for minerals exploration. A 2-D forward model was designed that incorporated both the geometry and geometric complexity of the Eastern Deeps zone in the Voisey's Bay area according to the working model for the Voisey's Bay deposit suggested by Cruden et al. (2000). By starting off with the simplest form of this model (i.e. constant velocities) and then progressing to greater and greater complexities (i.e. heterogeneity and velocity gradients) it was possible to fine-tune the processing parameters for a 2-D seismic survey at Voisey's Bay and to provide a basic template for interpretation of the reflection data.

Evaluation of the modeled data determined that there were many processing and interpretation challenges such as the absence of stratified reflectivity, complex scattering, inconsistent stacking velocities, important near-critical events and incoherent arrivals. In order to image the events in the model it was necessary to deal with both reflected and scattered events. Limited offsets of 0-2000 m were used for stacks and migrations because the long offsets did not contribute constructive information. A pre-stack Kirchhoff migration algorithm was preferred for imaging, as opposed to the more commonly used post-stack Kirchhoff migration algorithm, because it allowed more control over which velocities and events were stacked. This was necessary because of the conflicting velocities for diffractions and specular reflections that were present in this typical mineral exploration data-set.

Although 3-D seismic techniques have been demonstrated to be effective for imaging ore bodies, the cost of such surveys is often prohibitive. We are developing new approaches based on dense receiver arrays and sparse source arrays that should decrease the cost of 3-D seismic and make the technology more cost-effective for mineral exploration. Forward modeling, aimed at a first evaluation of the technique, demonstrates the potential of using sparsely illuminated seismic volumes and animated time-slicing to detect the distinctive scattering pattern associated with ore body sized targets. Time-slices of the individual sources reveal that sparse illumination effectively displays the characteristic 'bulls-eye' pattern of an individual scattering body. Stacking of the individual sources provides illumination from all sides of the scatterer and demonstrates that scattering occurs from multiple source points on the scattering body. 3-D migration of the stacked sections illustrates that the diffractions are essentially collapsed to small area located at the apex of the diffraction hyperbola as expected. However, comparison between unmigrated and migrated time-slices reveals that the unmigrated data are more effective for diffraction detection while the migrated data provide better localization of the scatterer. This approach of using few sources but many receivers for 3-D land seismic acquisition has the potential to be a cost-effective exploration and development tool.

Analysis of the extensive data-set of physical property measurements from the Voisey's Bay area suggests that, despite the complexity of the region and the variability of the geological settings of the various mineralized zones, detection of the ore bodies and mapping of the host magmatic system should be possible with both surface reflection surveys and travel-time tomography. Also, scale modeling has demonstrated the potential of cost-effective 3-D land acquisition geometries involving limited numbers of sources and dense receiver arrays.

## Table of Contents

## List of Tables

## List of Figures

## List of Abbreviations

| | |
|---|---|
| 2-D | two dimensional |
| 3-D | three dimensional |
| CDP | common depth point |
| DHZ | Discovery Hill zone |
| EDZ | Eastern Deeps zone |

| | |
|---|---|
| Ni-Cu-Co | nickel-copper-cobalt |
| NMO | normal moveout |
| RBZ | Reid Brook zone |
| RMS | root-mean-squared |
| S/N | signal-to-noise |
| VBNC | Voisey's Bay Nickel Company Limited |
| VSP | vertical seismic profiling |

# CHAPTER 1: INTRODUCTION

Currently, mineral exploration is focused on discovering and developing deeper deposits as the known shallow deposits become quickly depleted. As a result, the geophysical methods conventionally used in mineral exploration (such as electromagnetic, electrical, and potential field techniques) must be modified or adapted and unconventional or new techniques must be introduced for locating deeper deposits (Laletsang, 2001). Seismic techniques that are commonly applied in hydrocarbon exploration show promise for mineral exploration but conventional acquisition, processing and interpretation techniques require significant modification for the technique to be effective for the complex targets encountered in hardrock environments.

Surface seismic reflection methods have rarely been used in hardrock environments because they are more expensive than conventional geophysical methods. Acoustic impedance contrasts and signal-to-noise ratios are normally low and reflections are often laterally discontinuous due to complex geometries associated with intrusive processes and polyphase deformation (Eaton et al., 2003a). However, although surface seismic reflection methods are more costly than conventional geophysical methods such as electromagnetic, electrical, and potential field techniques they retain better resolution with increasing depth and have the potential to detect and image mineral deposits. It is possible to mine minerals from depths greater than 2000 m yet conventional geophysical methods are only capable of penetrating up to depths of 100-300 m in hardrock environments (Milkereit et al., 1996) while seismic reflection methods have the potential to penetrate to depths greater than 500 m. Thus, a better understanding of mineral

potential and geologic complexity could be acquired through the use of seismic reflection methods in hardrock environments.

Seismic reflection methods have been the principal exploration tool for over 70 years in hydrocarbon exploration. The method owes its success to the sub-horizontal, continuous and homogeneous nature of sedimentary boundaries. Thus, sedimentary basins have been explored for hydrocarbon reservoirs by mapping stratigraphic and structural discontinuities in the subsurface (Eaton et al., 2003a). Ore bodies however, are characterized by complex shapes and rarely occur in simple stratigraphic settings or sheet-like forms (Eaton et al., 2003b). Therefore, they lack the distinct lateral continuity of prominent seismic reflectors (Milkereit et al., 1996) and are better observed through seismic scattering. As a consequence, seismic techniques commonly applied in sedimentary environments are not directly applicable to hardrock environments. Both the acquisition and processing strategies need to be adapted to deal with the heterogeneous and complex nature characteristic of these hardrock environments.

Acquisition, processing and interpretation techniques need to be tuned to the predicted response of ore deposits (Bohlen et al., 2003). Some specific aspects that should be considered when evaluating the utility of seismic techniques include:

Pre-Acquisition:

- Physical rock properties studies are an essential prerequisite in understanding the anomalous elastic properties characteristic of orebodies (Eaton et al., 2003b).

- Forward modeling studies in conjunction with a physical properties database allow for a better understanding of the scattering response of an orebody while also providing a valuable foundation for survey design (Eaton et al., 2003b).

Acquisition:

- Higher-than-usual source frequencies (> 100 Hz) are necessary in order to resolve targets in high-velocity hardrock environments (Eaton et al., 2003b).
- High-fold datasets are necessary to offset low reflection coefficients (Adam et al., 2003).
- VSP techniques or significant shot-receiver offsets may be necessary in order to deal with steeply dipping targets (Salisbury et al., 2000).
- The cost associated with collecting and processing 3-D seismic data is not cost-effective for exploration mining. Techniques able to reduce these costs are potentially valuable.

Processing:

- Robust processing sequences need to be developed to deal with the lack of pronounced stratified reflectivity (Eaton et al., 2003a).

Interpretation:

- Interpretation techniques that focus on scattered waves rather than specular reflections are required.

Both time and resources need to be taken into account when considering each of the previous points for planning an exploration project in any hardrock environment.

This thesis investigates a range of issues related to the application of 2-D and 3-D seismology to exploration for massive sulphides. The work is carried out in preparation for a series of field experiments that will be carried out at the Voisey's Bay nickel-copper-colbalt deposit in Labrador. The specific objectives of this thesis are to:

1. study the seismic properties of the ores and host rocks at Voisey's Bay,
2. fine-tune acquisition parameters for a 2-D survey planned to delineate the structural setting of the deposit,
3. investigate an alternative approach to 3-D acquisition and processing.

Composition, metamorphic grade, and fractures affect the seismic response of both the ores and the host rocks. Therefore, seismic properties studies are an important prerequisite for any seismic surveys in crystalline rock. I have studied the seismic properties of the ores and host rocks by compiling and evaluating a comprehensive density and velocity database for each of a weakly- and a highly-fractured area. These databases provided the foundation for evaluation of both the acoustic impedance and the potential reflectivity for both the ores and the host rocks in these two different types of areas. Overall analysis of the data identified whether or not the ores are strong reflectors against the host rocks thereby validating the use of seismology for delineating the structural setting of the deposit.

The Voisey's Bay site offers a wide range of viable seismic targets of differing complexity that can be used to develop suitable acquisition and processing techniques for

mineral exploration. A 2-D forward model-based study was designed and data acquired to study and fine-tune the acquisition and processing sequence that is best suited for hardrock environments such as Voisey's Bay.

In general there is a processing strategy that many seismologists apply to collected seismic data; however, this processing strategy has been mainly designed for data collected in sedimentary environments not in hardrock environments. Evaluation of the data determined that there were many processing and interpretational challenges such as the absence of stratified reflectivity, complex scattering, inconsistent stacking velocities, important near-critical events, incoherent arrivals, etc... Application of various processing techniques to synthetic seismic data helped develop a processing strategy designed for data collected in hardrock environments. This model-based study helped to foresee many acquisition and processing issues before implementation of a field-based 2-D seismic reflection experiment thereby allowing for the design of high quality experiments.

Several 3-D seismic datasets have been acquired to detect and image signals associated with ore bodies; however, the cost associated with collecting and processing 3-D seismic data is not practical for mineral exploration. If we concern ourselves with simply detecting the presence of ore bodies rather than imaging them, it may be possible to develop more cost-effective methods. Research is presently concentrated on developing methods that combine dense receiver arrays and sparse source arrays to locate strong scatterers in the subsurface. This method may be applicable for locating strong scatterers (i.e., ore bodies). A distinctive indicator of a strong scattering body in 3-D

seismic volumes is a "bulls-eye" pattern formed by diffractions in the horizontal time-slices. I have designed, acquired, and processed a sparse source and dense receiver synthetic seismic survey to determine whether this seismic technique may be a feasible alternative to 3-D seismic surveys for mineral exploration. If the time-slicing of the "pseudo 3-D" synthetic seismic data also image this "bulls-eye" pattern, it may provide a more cost-effective approach to locating possible drill targets.

# CHAPTER 2: PHYSICAL PROPERTIES

## 2.1 Introduction

The subsurface is illuminated by seismic methods through the use of elastic (P and S) waves (Eaton et al., 2003a). Abrupt changes in elastic rock properties, such as at lithological and structural boundaries, cause reflection, refraction, and scattering of these elastic waves to occur (Eaton et al., 2003a). Interpretation of the seismic wave field requires a thorough understanding of the physical properties of the rocks in the study area. Specifically, it requires knowledge of P- and S-wave velocities and density from which acoustic impedance (Z) is determined. To the first order, the magnitude of detectable acoustic impedance contrast (the reflection coefficient) predicts whether or not two different lithologies will produce detectable reflections. The reflection coefficient (R) is the ratio of reflected to incident energy (Salisbury et al., 2003). The following equation describes the reflection coefficient for a downward traveling normal-incidence P-wave in the case of two lithologies in contact along a planar surface:

$$R = \frac{Z_2 - Z_1}{Z_2 + Z_1} = \frac{V_{P2}\rho_2 - V_{P1}\rho_1}{V_{P2}\rho_2 + V_{P1}\rho_1},$$

where $Z_1$, $V_{P1}$, and $\rho_1$ are the acoustic impedance, P-wave velocity, and density, respectively, of the upper medium and $Z_2$, $V_{P2}$, and $\rho_2$ are the equivalent parameters for the lower medium (Salisbury et al., 2003). As a rule of thumb, an impedance difference of roughly $2.5 \times 10^6$ kg·m$^{-2}$·s$^{-1}$ is required to give a reflection coefficient of 0.06 which is the minimum coefficient necessary to provide an acceptable reflection in most basement settings (Salisbury et al., 1996). Comparison of the acoustic impedances of the various

lithologies present in a given setting provides first order prediction of which lithologic boundaries can be detected by seismic reflection methods (Figure 2.1.1).

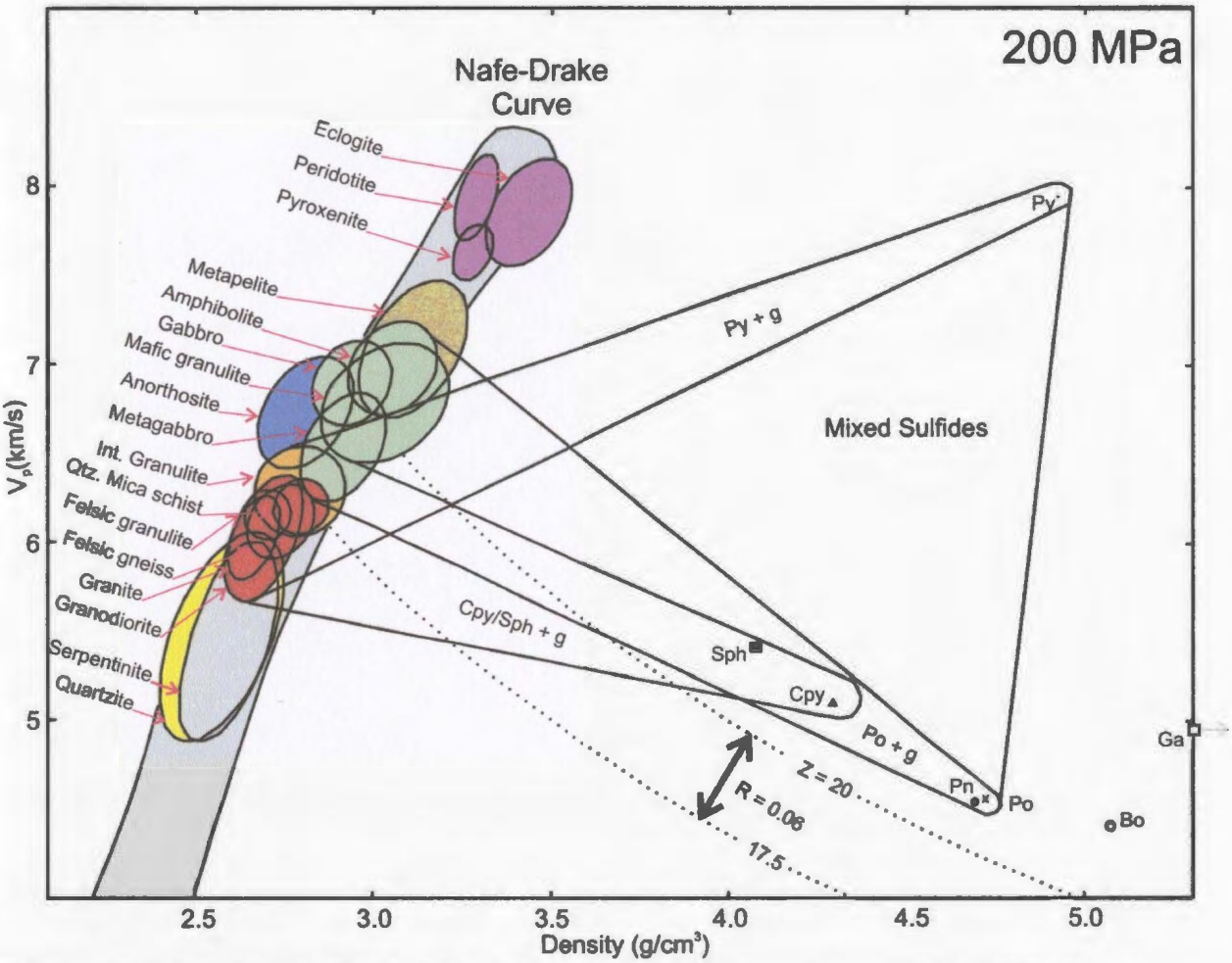


Figure 2.1.1: $V_p$-density fields for common sulphides superimposed on a $V_p$ versus density plot for common silicate rocks at 200 MPa. Also lines of constant acoustic impedance are shown for both felsic ($Z=17.5 \times 10^6$ kg·m$^{-2}$·s$^{-1}$) and mafic rocks ($Z=20 \times 10^6$ kg·m$^{-2}$·s$^{-1}$) and the minimum reflection coefficient required for strong reflections ($R=0.06$).The following is a list of abbreviations used: Py (pyrite), Sph (sphalerite), Cpy (chalcopyrite), Po (pyrrhotite), Pn (pentlandite), Ga (galena), and g (gangue). Modified from Salisbury et al., 2003.

Figure 2.1.1 clearly demonstrates that the velocity-density field for ore minerals is noticeably different from that for common silicate rocks. The velocities of the host rocks increase with density along the Nafe-Drake curve for silicate rocks (Ludwig et al., 1971)

while the sulphides lie to the far right of the Nafe-Drake curve in a large velocity-density field controlled by the end-member properties of pyrite, pyrrhotite, chalcopyrite, and sphalerite (Salisbury et a1., 2000). Pyrite is very dense and fast (5.0 $g \cdot cm^{-3}$, 8.0 km/s), therefore ores dominated by this mineral increase in velocity with increasing density (Salisbury et al., 1996). In contrast, pyrrhotite is very dense and slow (4.6 $g \cdot cm^{-3}$, 4.7 km/s), and chalcopyrite and sphalerite are both similarly intermediate in density and velocity (4.1 $g \cdot cm^{-3}$, ~5.5 km/s), which cause ores dominated by any of these minerals to generally decrease in velocity with increasing density (Salisbury et al., 1996).

Furthermore, most mafic rocks ($Z=20 \times 10^6$ $kg \cdot m^{-2} \cdot s^{-1}$) will provide strong reflections when in contact with felsic rocks ($Z=17.5 \times 10^6$ $kg \cdot m^{-2} \cdot s^{-1}$) since the acoustic impedance difference between the two meets the minimum requirement to produce adequate reflections (Salisbury et al., 1996). Also due to the high densities associated with ore minerals they normally will have higher acoustic impedances than most felsic and mafic hosts and thus could also make strong reflectors against many of the common silicate host rocks (Salisbury et al., 2003). For example, depending upon the pyrite content, any mixture of chalcopyrite, sphalerite, and pyrite should be a strong reflector in most felsic and mafic hosts while massive pyrrhotite should be easily detectable in felsic hosts (Salisbury et al., 2000). Therefore, in principle impedance-based techniques such as reflection seismology may be considered more appropriate for characterization of magmatic/ore systems than other geophysical systems.

Effective design of a quality seismic survey requires accurate analysis of the physical properties of the study area rocks. Physical properties analysis of the Voisey's

Bay site was made possible by the Voisey's Bay Nickel Company (VBNC) who provided a specific gravity database for each borehole in the Voisey's Bay area. These databases were calculated by VBNC by performing regression analysis on geochemical data. Full waveform sonic data was also provided for specific wells located in both the Reid Brook (VB-03588, -03589, -03591, -03593, -03594, -03596, -03597, -03599, -03606, -03610, -96282, -96334A, -96339, -96342, and -97416) and the Eastern Deeps zones (VB-00542, -00543, -00544, -00545, -00546, -00547, -96214, and -96230). The abundant data available for the Voisey's Bay area provide the basis for a detailed analysis of the physical properties of both the ores and host rocks.

## 2.2 Rock Lithologies

This section gives a brief description of the various rock lithologies found in both the Reid Brook and Eastern Deeps zones, which can help in understanding the physical properties. Figure 2.2.1 shows the geology of the Voisey's Bay area and Figure 2.2.2 gives a brief illustration of the expected contrasting lithologies in cross-section.

- Gneiss

The Reid Book zone host rock is a "Proterozoic sulphidic garnetiferous paragneiss" (Evans-Lamswood et al., 2000) which has been termed the Tasiuyak gneiss. Gneissosity defined by a compositional layering constitutes the development of the fabric (Evans-Lamswood, 1999).

The Eastern Deeps zone host rock is an Archean "moderately to strongly lineated hypersthene-bearing granodioritic (opdalite) to tonalitic (enderbite) rock" (Evans-

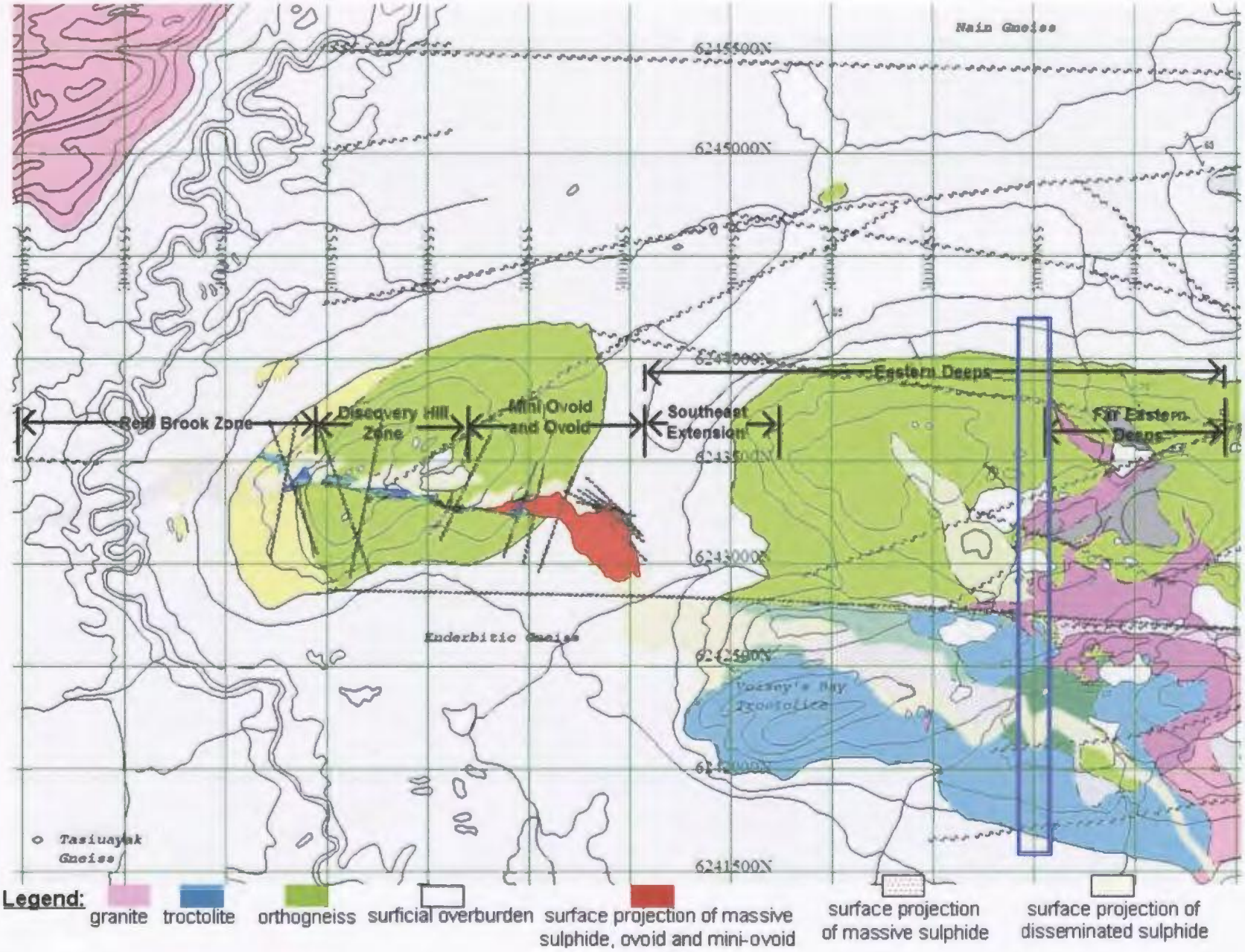


Figure 2.2.1: Geology map of the Voisey's Bay area. Blue box illustrates location of cross-section shown in Figure 2.2.2 (Modified from VBNC).

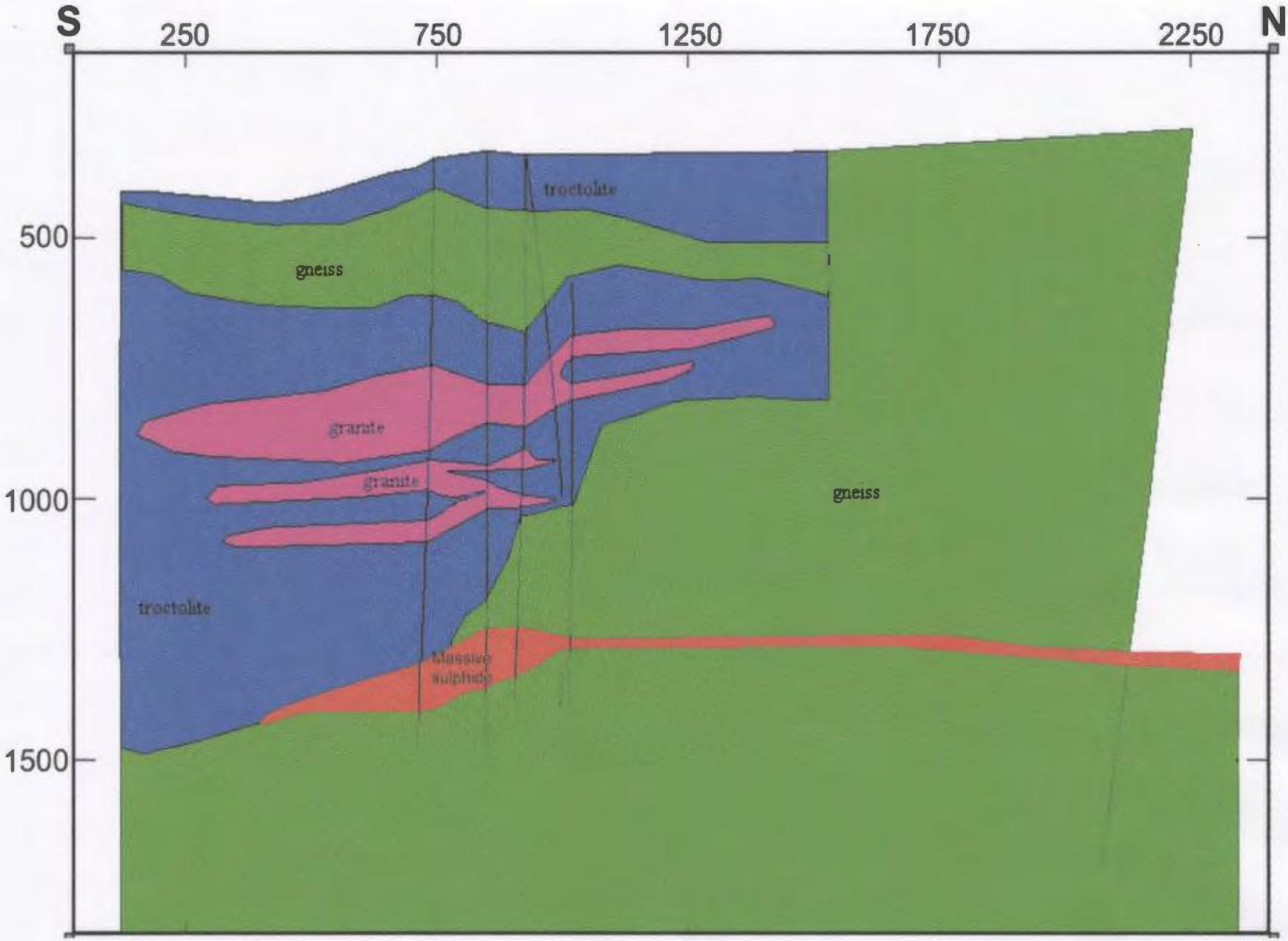


Figure 2.2.2: Illustrates expected contrasting lithologies where the scale is in metres.

Lamswood et al., 2000; Ryan, 2000) which, collectively has been termed enderbitic gneiss. The fabric is developed as a gneissosity defined by strong compositional banding (Evans-Lamswood, 1999).

- Granite

The majority of the granite present in both the Reid Brook and Eastern Deeps zones is believed to occur as thin sheets and is not considered to be a volumetrically major component of the Voisey's Bay magmatic and structural system.

- Breccia

The Breccia which is associated with both the Reid Brook and the Eastern Deeps zones is typically referred to as basal breccia and normally contains inclusions of either gneiss or gabbro-troctolite (Evans-Lamswood, 1999). In general, the fragments maintain random orientations as opposed to preferred orientations (Evans-Lamswood, 1999).

- Troctolite

Troctolite is essentially a variety of a gabbro. It is a "coarse-grained igneous rock composed of olivine and calcic plagioclase with little or no pyroxene" (MacDonald et al., 2003). The troctolite which hosts the Voisey's Bay deposit in both the Reid Brook and Eastern Deeps zones can be sub-divided into chamber and conduit troctolites. The chamber rocks consist of both variable- and normal-textured troctolites and gabbros (Li and Naldrett, 1999). The variable-textured troctolite is characterized by a locally bleached appearance with minor pegmatitic zones (Ryan, 2000). Traces of sulphides (up to 15 % of the bulk composition) are present within local zones (Ryan, 2000; Evans-Lamswood, 1999). The normal-textured troctolite is a homogeneous sequence of barren,

fragment-free troctolite (Ryan, 2000). The conduit rocks consist of fragment-laden, sulphide-rich, gabbros-troctolites (Evans-Lamswood, 1999) and troctolite breccias (Ryan, 2000). Mineralization occurs as fine- to coarse-grained, disseminated to semi-massive sulphides crosscut by massive sulphides (Evans-Lamswood, 1999; Ryan, 2000).

- Massive Sulphide

Massive Sulphide is generally considered to be a body of rock made up mainly or wholly of sulphide minerals, such as pyrite, pyrrhotite, or chalcopyrite. The main sulphide and oxide minerals contained in the massive sulphides at Voisey's Bay are: pyrrhotite, pentlandite, chalcopyrite, cubanite, mackinawite, sphalerite, magnetite, and ilmenite (Naldrett et al., 2000).

## 2.3 Physical Properties of the Reid Brook and the Eastern Deeps Zones

- **2.3.1 Velocity versus Density Plots**

Preliminary analysis of the supplied density and velocity datasets for both the Reid Brook and the Eastern Deeps zones illustrates that in general the host rocks behave as expected with their average velocities increasing with increasing density (Figures 2.3.1.1 and 2.3.1.2, respectively). The ores however, behave in the reverse manner with their average velocities decreasing with increasing density (Figures 2.3.1.1 and 2.3.1.2). This indicates that the physical properties of the massive sulphides in both the Reid Brook and the Eastern Deeps zones are largely controlled by the minerals pyrrhotite and pentlandite which are both dense and slow (Figure 2.1.1). This general characteristic of the massive sulphides is also illustrated when trace to large amounts of sulphide are

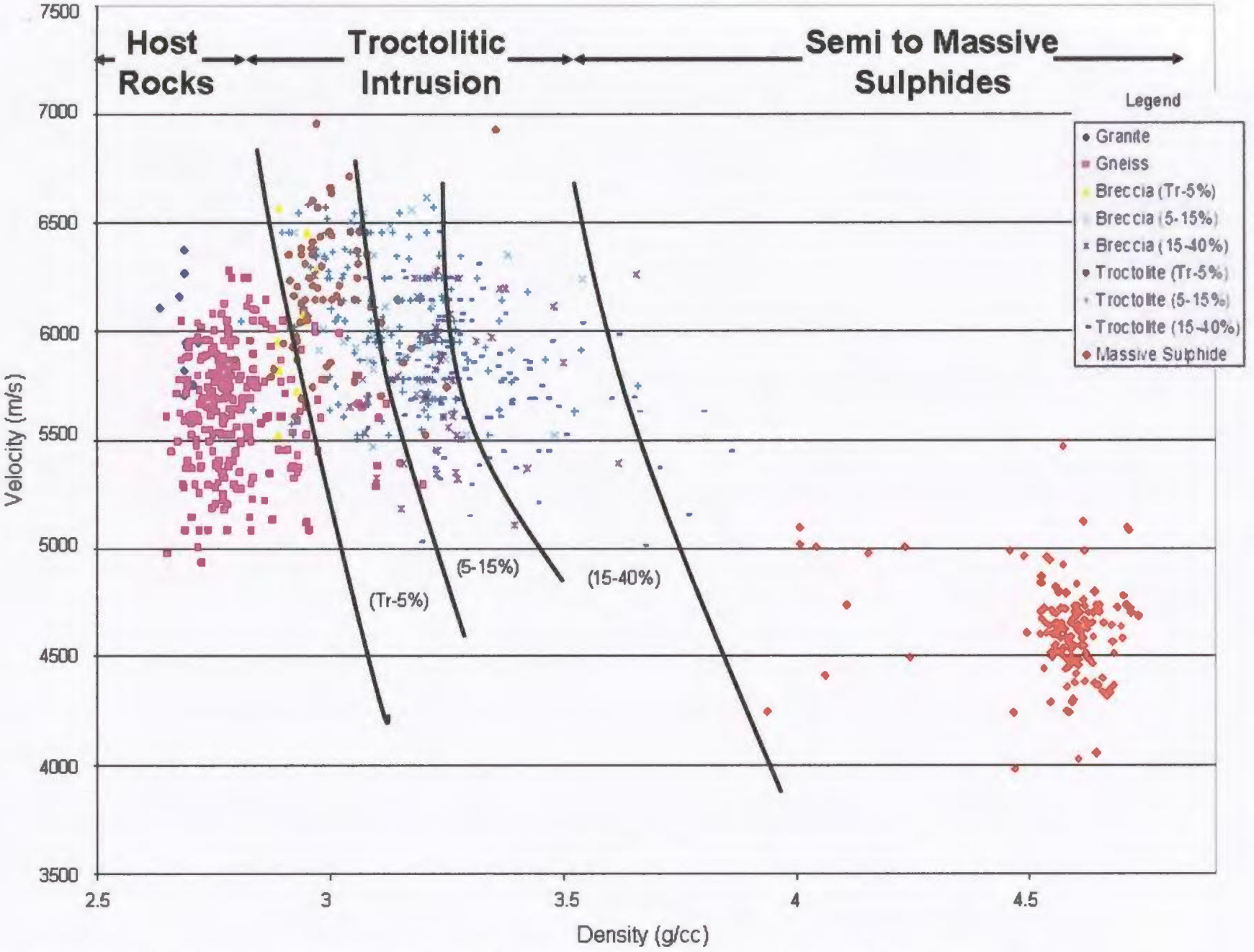


Figure 2.3.1.1: Velocity versus density plot for both the ores and host rocks of the Reid Brook zone illustrating their various trends. Tr-5%, 5-15%, and 15-40% refer to the amount of sulphide present.

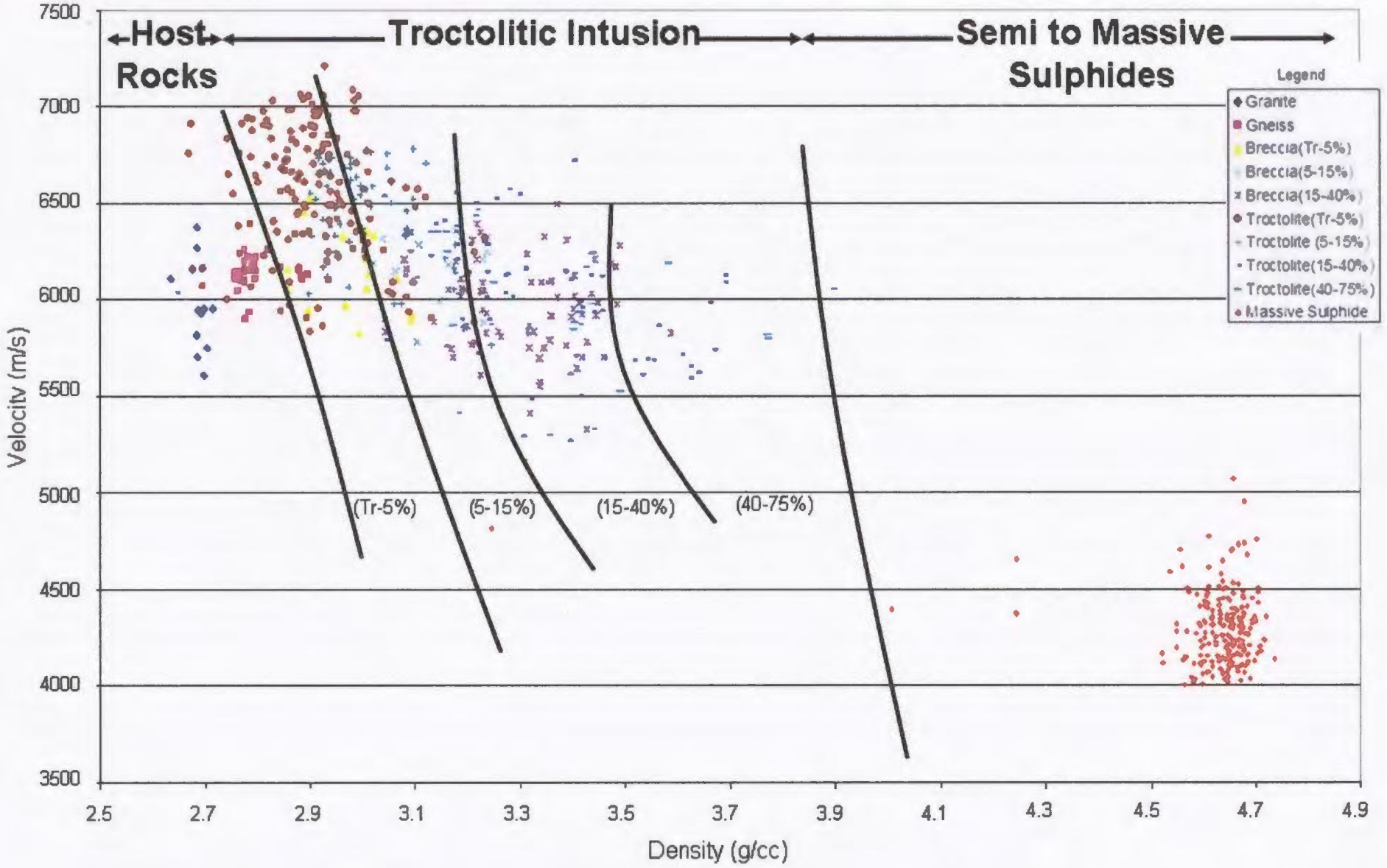


Figure 2.3.1.2: Velocity versus density plot for both the ores and host rocks for the Eastern Deeps zone illustrating their various trends. Tr-5%, 5-15%, 15-40%, and 40-75% refer to the amount of sulphide present.

present in the troctolitc intrusion. Figures 2.3.1.1 and 2.3.1.2 illustrate that as the amount of mineralization increases in the troctolite, velocities decrease while densities increase.

- **2.3.2 Statistical Distribution of Physical Properties**

Average physical properties for both the host rocks and the ores in the Reid Brook and Eastern Deeps zones were analyzed using histograms calculated from the supplied datasets. In general, both the host rocks and the ores demonstrate a Gaussian distribution for each physical property. The density and velocity values provided for granite in the Reid Brook zone were abnormal when compared to expected values for granite (Figure 2.3.1.1). As a result, all the velocity and density values for granite in the Reid Brook zone were discarded. It is most likely that an error in rock lithology identification was made during core logging. Since the compositions of the granites are the same for both zones, the average granite physical properties for the Eastern Deeps zone will also be used for the Reid Brook zone since they are more reliable. Density, velocity, and acoustic impedance histograms for both the host rocks and the ores for both areas can be found in Appendix A. Tables 2.3.2.1 and 2.3.2.2 display the average values for density, velocity, and acoustic impedance for the Reid Brook and the Eastern Deeps zones respectively.

Table 2.3.2.1: Average values of density, velocity, and acoustic impedance with first order standard deviations for the Reid Brook Zone.

| Rock Type | Number of Samples | Density (g/cc) | Velocity (m/s) | Acoustic Impedance E+05 ($kg*m^{-2}*s^{-1}$) |
|---|---|---|---|---|
| Gneiss | 267 | 2.80 ± 0.0968 | 5642 ± 279 | 158 ± 9.64 |
| Breccia (Tr-5%) | 9 | 2.92 ± 0.0319 | 6050 ± 342 | 177 ± 10.8 |

| | | | | |
|---|---|---|---|---|
| Breccia (5-15%) | 39 | 3.13 ± 0.136 | 6039 ± 294 | 189 ± 11.4 |
| Breccia (15-40%) | 47 | 3.26 ± 0.131 | 5781 ± 329 | 188 ± 13.7 |
| Troctolite (Tr-5%) | 69 | 2.99 ± 0.0954 | 6158 ± 301 | 185 ± 11.2 |
| Troctolite (5-15%) | 155 | 3.14 ± 0.138 | 6031 ± 287 | 189 ± 10.4 |
| Troctolite (15-40%) | 121 | 3.31 ± 0.153 | 5803 ± 290 | 192 ± 10.2 |
| Massive Sulphide | 167 | 4.55 ± 0.167 | 4700 ± 328 | 213 ± 13.8 |

Table 2.3.2.2: Average values of density, velocity, and acoustic impedance with first order standard deviations for the Eastern Deeps zone.

| Rock Type | Number of Samples | Density (g/cc) | Velocity (m/s) | Acoustic Impedance E+05 ($kg*m^{-2}*s^{-1}$) |
|---|---|---|---|---|
| Granite | 12 | 2.69 ± 0.0194 | 5964 ± 230 | 162 ± 5.35 |
| Gneiss | 26 | 2.79 ± 0.0395 | 6133 ± 82 | 171 ± 3.47 |
| Breccia (Tr-5%) | 16 | 2.98 ± 0.0773 | 6142 ± 210 | 183 ± 6.39 |
| Breccia (5-15%) | 15 | 3.14 ± 0.0725 | 6163 ± 188 | 193 ± 7.23 |
| Breccia (15-40%) | 74 | 3.30 ± 0.122 | 5975 ± 240 | 197 ± 9.95 |
| Breccia (40-75%) | 6 | 3.25 ± 0.112 | 5746 ± 265 | 187 ± 11.5 |
| Troctolite (Tr-5%) | 162 | 2.91 ± 0.0994 | 6564 ± 330 | 191 ± 10.4 |
| Troctolite (5-15%) | 57 | 3.02 ± 0.103 | 6430 ± 275 | 194 ± 7.38 |
| Troctolite (15-40%) | 85 | 3.31 ± 0.196 | 6043 ± 355 | 200 ± 12.7 |
| Troctolite (40-75%) | 12 | 3.44 ± 0.198 | 5950 ± 211 | 205 ± 11.5 |
| Massive Sulphide | 217 | 4.62 ± 0.122 | 4372 ± 370 | 202 ± 17.0 |

Comparison of the two datasets reveals that the densities are generally consistent while the velocities in the Reid Brook zone are consistently lower than in the Eastern Deeps zone. This however is to be expected due to the large amount of fracturing present in the Reid Brook zone which would lower the sonic log velocities.

Further analysis of the physical properties dataset through velocity and acoustic impedance contrasts between different rock lithologies provides insight into which seismic techniques may be more effective for direct detection of the ore bodies and for imaging the magmatic system and structural mapping at Voisey's Bay. Tables 2.3.2.3 and 2.3.2.4 show velocity and acoustic impedance contrasts between various rock lithologies in both the Reid Brook and Eastern Deeps zones respectively.

Table 2.3.2.3: Velocity and acoustic impedance contrasts between various rock lithologies for the Reid Brook zone.

| Rock Types | Velocity Contrast (%) | Acoustic Impedance Contrast (%) |
|---|---|---|
| Gneiss/Troctolite (Tr-5%) | + 8 | + 15-17 |
| Gneiss/Massive Sulphide | - 17-20 | + 26-35 |
| Troctolite (Tr-5%)/Massive Sulphide | - 24-32 | + 13-15 |

Table 2.3.2.4: Velocity and acoustic impedance contrasts between various rock lithologies for the Eastern Deeps zone.

| Rock Types | Velocity Contrast (%) | Acoustic Impedance Contrast (%) |
|---|---|---|
| Gneiss/Troctolite (Tr-5%) | + 8 | + 10-12 |
| Gneiss/Massive Sulphide | - 29-40 | + 15-18 |
| Troctolite (Tr-5%)/Massive Sulphide | - 33-50 | + 5 |

In general, the Eastern Deeps zone has larger velocity contrasts but smaller acoustic impedance contrasts when compared to the Reid Brook zone. One reason for this difference may be attributed to the fact that the Eastern Deeps is documented to have a higher percentage of nickel, copper, and cobalt than the Reid Brook zone (Naldrett et al., 2000; Evans-Lamswood et al., 2000). These higher percentages indicate that pyrrhotite most likely plays a larger role in the Eastern Deeps zone which would account for a lower velocity for the massive sulphides in that area. As a result, this would cause both the larger velocity contrasts and smaller acoustic impedance contrasts exhibited in Table 2.3.2.4.

For both datasets there is a modest velocity contrast between the gneiss that is the predominant country rock and the troctolitic intrusion that hosts the sulphide mineralization. However, there is a significant velocity contrast between the gneiss and massive sulphide and the troctolite and massive sulphide. For the Reid Brook zone there is a moderate to large acoustic impedance contrast between the gneiss and troctolite, the gneiss and massive sulphide and the troctolite and massive sulphide. The Eastern Deeps zone also exhibits a moderate to large acoustic impedance contrast between the gneiss and troctolite and the gneiss and massive sulphide; however, the contrast between the troctolite and massive sulphide is less significant but still noteworthy. These results demonstrate that impedance-sensitive techniques such as reflection seismology would be appropriate for both direct characterization of the ore bodies and imaging the magmatic system and structural mapping for the Reid Brook zone. By contrast, velocity-sensitive techniques such as borehole-borehole tomography may be most appropriate for direct

characterization of the ore bodies and impedance-sensitive techniques may be most appropriate for imaging the magmatic system and structural mapping for the Eastern Deeps zone.

- **2.3.3 Potential Reflectivity Distributions**

If one defines reflectivity as "a measure of the abundance, amplitude, and continuity of reflections" then it can be deduced that "reflectivity is a product of both the strength and geometric configuration of the acoustic impedance contrasts" (Hurich et al., 2001). As a result, analysis of the probability distribution of potential acoustic impedance contrasts and thus the probability distribution of reflection coefficients leads to an estimate of potential reflectivity (Hurich et al., 2001), which can then aid in the prediction of observing reflections from potential lithologic contrasts.

Using the average acoustic impedances and standard deviations from Tables 2.3.2.1 and 2.3.2.2 it was possible to predict a probability distribution of reflection amplitudes for the various lithologies. Potential reflectivity distributions were produced using a MATLAB program that uses Monte Carlo simulation to determine the probability distribution function for potential reflection coefficients. The program assumes a Gaussian distribution of acoustic impedances for each rock type (which is justified by the histograms for acoustic impedance in Appendix A) and only allows juxtaposition of different rock types. For these simulations the transition probability for all rock types was set to 1, thus transitions from rock type 1-2 and 2-1 are equally likely. The number of interfaces simulated for each distribution (lithology pair) was 20,000 and the diagrams (Figures 2.3.3.1-2.3.3.5) represent the absolute values of the reflection coefficients. A

reflection coefficient threshold of 0.06 was used for each simulation as a standard of comparison. From this it was possible to assess the cumulative percentage of reflection coefficients above this threshold, thereby allowing for a reasonable prediction of which lithologic contrasts would result in detectable reflections in the Voisey's Bay area.

The average potential reflection coefficients and percent above the 0.06 threshold for various contrasting lithologies are shown in Tables 2.3.3.1 and 2.3.3.2 with corresponding figures listed for both the Reid Brook and Eastern Deeps zones respectively.

Table 2.3.3.1: Displays the average potential reflection coefficients and percent above the 0.06 threshold for the Reid Brook zone.

| Lithology Contrast | Average Potential Reflection Coefficient | Percent greater than 0.06 | Corresponding Figure |
|---|---|---|---|
| Troctolite/Gneiss | 0.07 | 67 | 2.3.3.1a |
| Troctolite/Granite | 0.07 | 57 | 2.3.3.2a |
| Troctolite/Massive Sulphide | 0.08 | 60 | 2.3.3.3a |
| Gneiss/Granite | < 0.01 | 11 | 2.3.3.4a |
| Gneiss/Massive Sulphide | 0.15 | 98 | 2.3.3.5a |

Table 2.3.3.2: Displays the average potential reflection coefficients and percent above the 0.06 threshold for the Eastern Deeps zone.

| Lithology Contrast | Average Potential Reflection Coefficient | Percent greater than 0.06 | Corresponding Figure |
|---|---|---|---|
| Troctolite/Gneiss | 0.06 | 43 | 2.3.3.1b |
| Troctolite/Granite | 0.09 | 75 | 2.3.3.2b |
| Troctolite/Massive Sulphide | < 0.04 | 30 | 2.3.3.3b |
| Gneiss/Granite | 0.03 | 6 | 2.3.3.4b |
| Gneiss/Massive Sulphide | 0.09 | 71 | 2.3.3.5b |

In general, the average potential reflection coefficients for the lithology contrasts of troctolite/gneiss, troctolite/granite, troctolite/massive sulphide, and gneiss/massive sulphide are significant while they are inconsequential for gneiss/granite. For the most

part troctolite hosts the large granite inclusions and therefore we do not expect there to be a gneiss/granite boundary, thus it is immaterial that this boundary has low potential reflectivity. However, the average potential reflection coefficient for troctolite/massive sulphide in the Eastern Deeps zone is less than 0.04 with only 30 % of the hypothetical contacts having discernible reflectivity. Evans-Lamswood et al. (2000) have documented that the percent of indicated nickel, copper, and cobalt is larger in the Eastern Deeps zone than in the Reid Brook zone. Therefore, this anomalously low reflection coefficient may be a result of this increase in the proportion of pyrrhotite in the Eastern Deeps Zone as opposed to the Reid Brook zone. An increase in pyrrhotite content causes a lower velocity for the massive sulphides and thus a lower acoustic impedance contrast. As a result, a smaller reflection coefficient would be expected at the boundary between massive sulphides and any other contrasting lithology in the Eastern Deeps zone than in the Reid Brook zone. This observation is further supported by the fact that, while still significant, the average potential reflection coefficient for gneiss/massive sulphide is a great deal less in the Eastern Deeps zone than in the Reid Brook zone.

For both the Reid Brook and the Eastern Deeps zones the proportion of possible reflection coefficients with absolute values greater than 0.06 is close to or above 50 % for most of the various lithologic contrasts. Exceptions include the gneiss/granite boundary in both areas and more importantly the troctolite/massive sulphide boundary in the Eastern Deeps zone. This indicates that the potential for discerible reflection coefficients for the majority of the various lithologic contrasts in both the Reid Brook and Eastern

a)

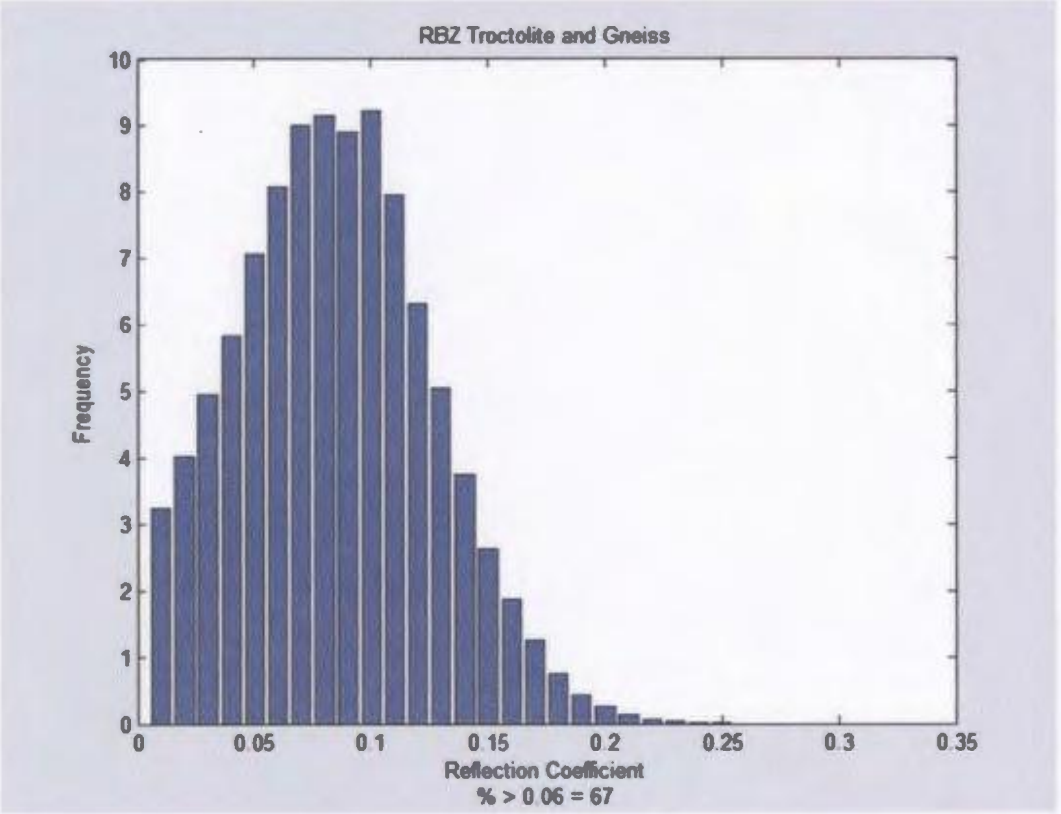


b)

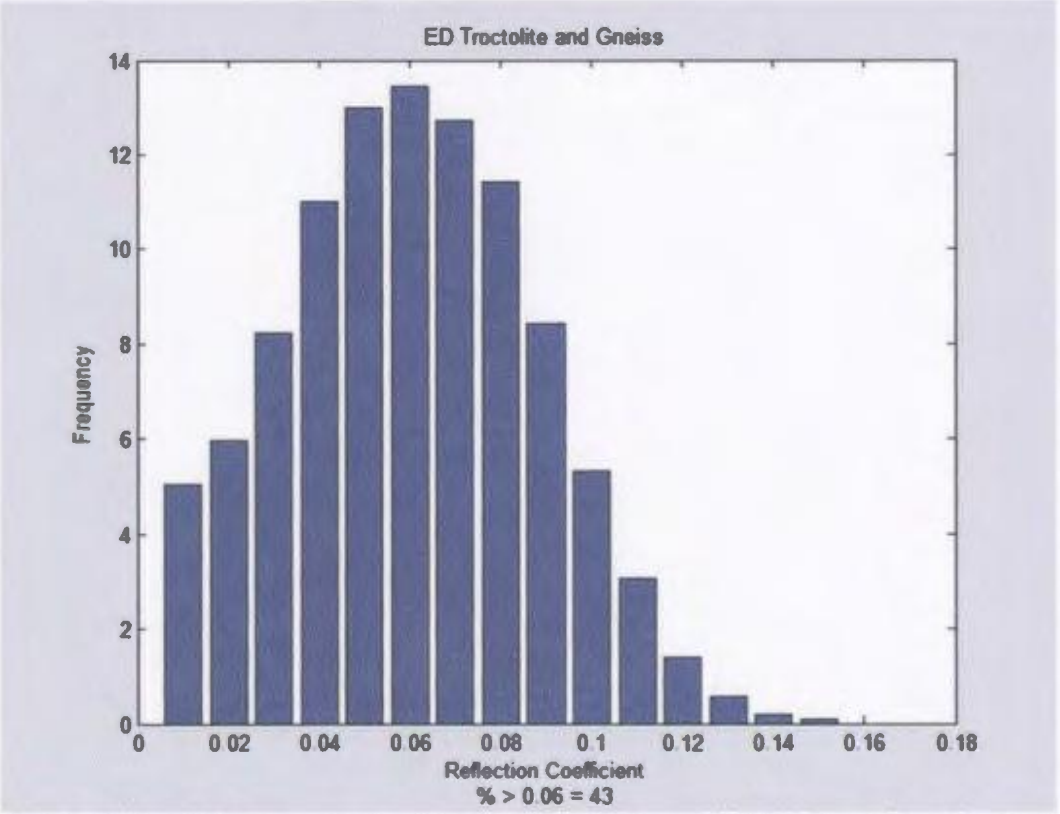


Figure 2.3.3.1: Potential reflectivity distribution for troctolite and gneiss for a) Reid Brook zone and b) Eastern Deeps zone. The vertical axis, frequency, indicates the percentage of synthetic interfaces having a reflection coefficient in a particular bin.

a)

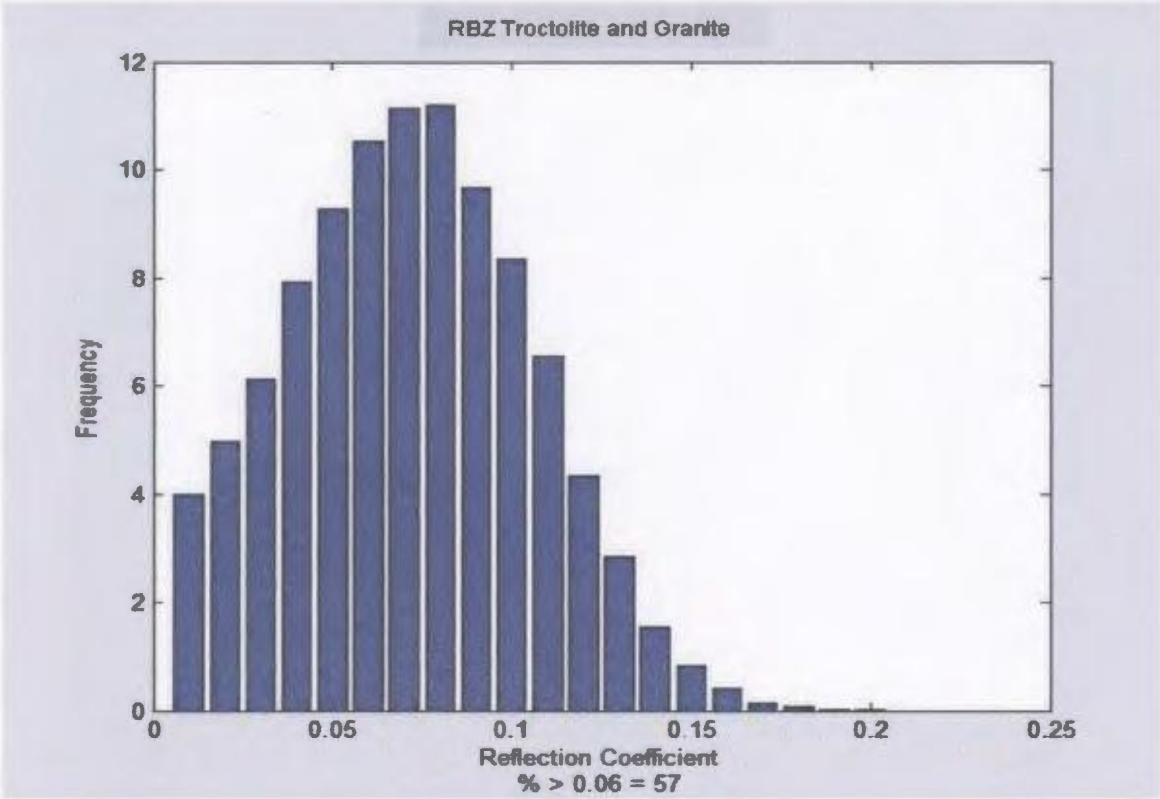


b)

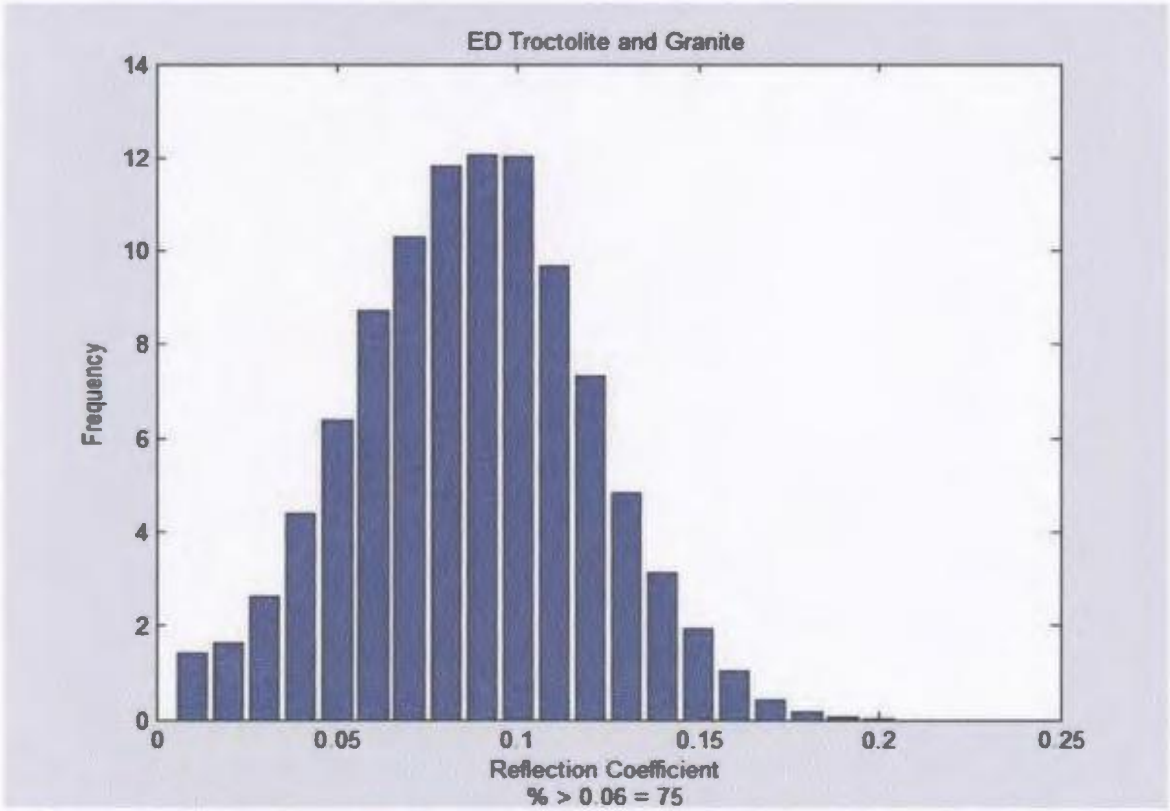


Figure 2.3.3.2: Potential reflectivity distribution for troctolite and granite for a) Reid Brook zone and b) Eastern Deeps zone. The vertical axis, frequency, indicates the percentage of synthetic interfaces having a reflection coefficient in a particular bin.

a)

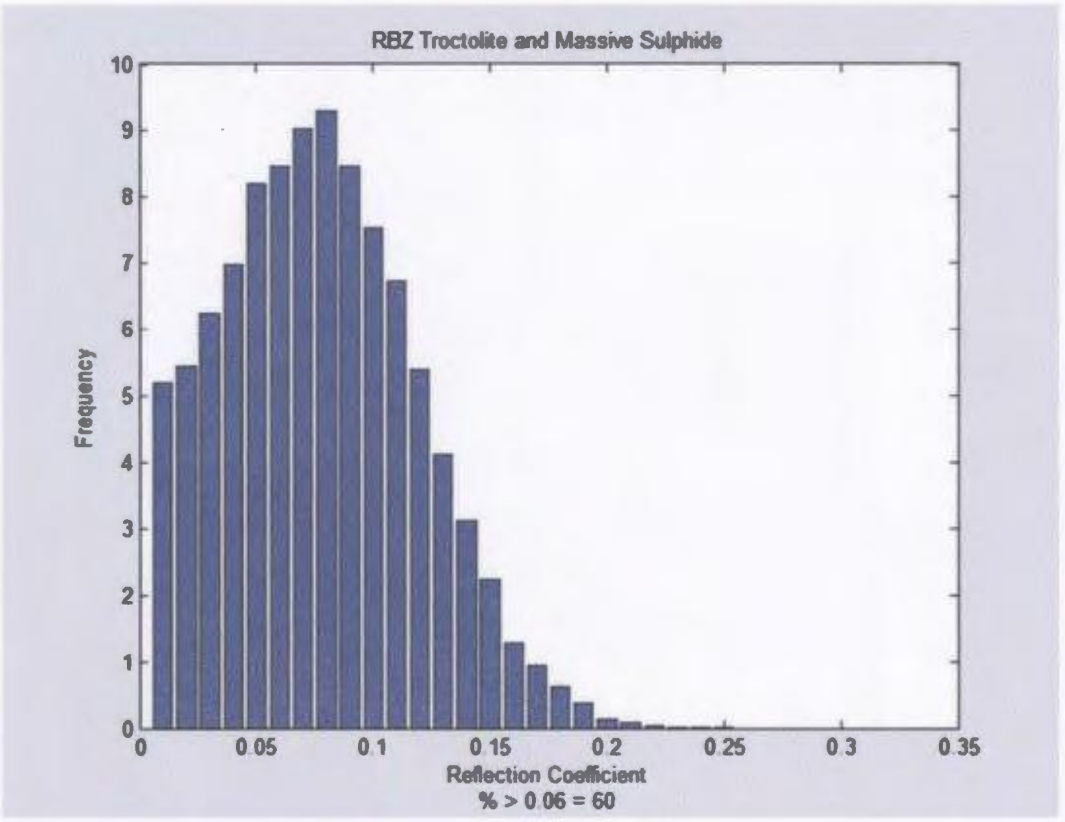


b)

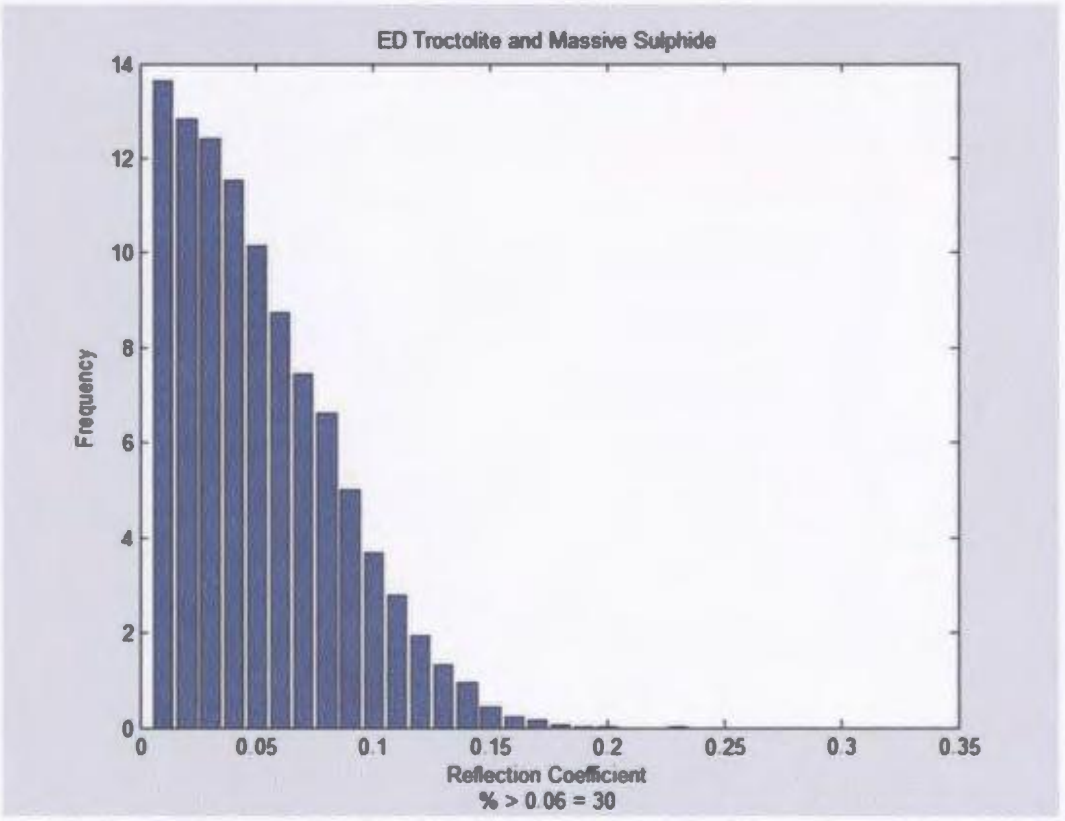


Figure 2.3.3.3: Potential reflectivity distribution for troctolite and massive sulphide for a) Reid Brook zone and b) Eastern Deeps zone. The vertical axis, frequency, indicates the percentage of synthetic interfaces having a reflection coefficient in a particular bin.

a)

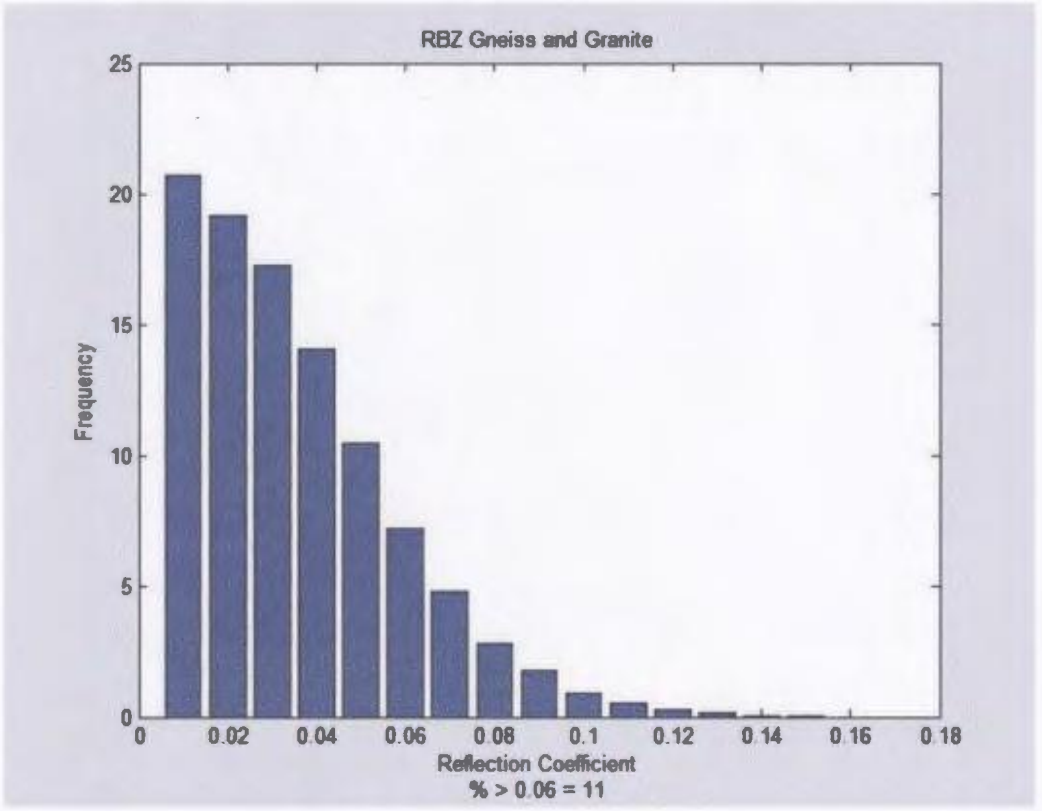


b)

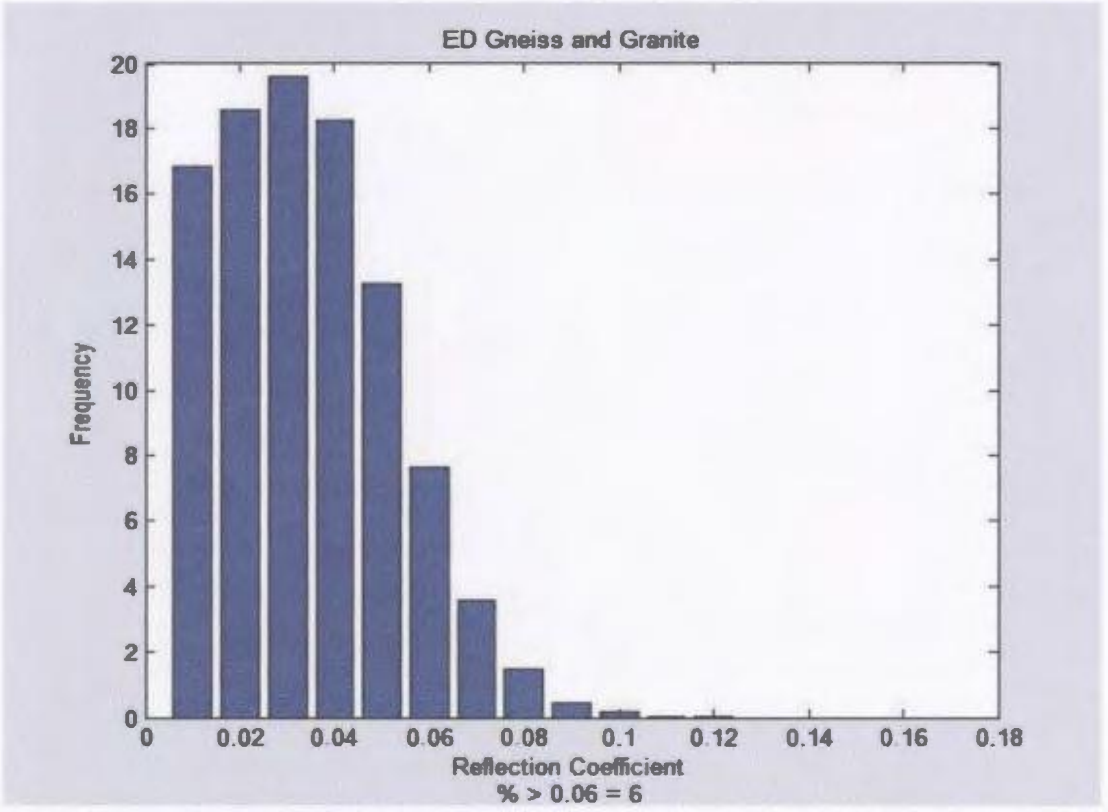


Figure 2.3.3.4: Potential reflectivity distribution for gneiss and granite for a) Reid Brook zone and b) Eastern Deeps zone. The vertical axis, frequency, indicates the percentage of synthetic interfaces having a reflection coefficient in a particular bin.

a)

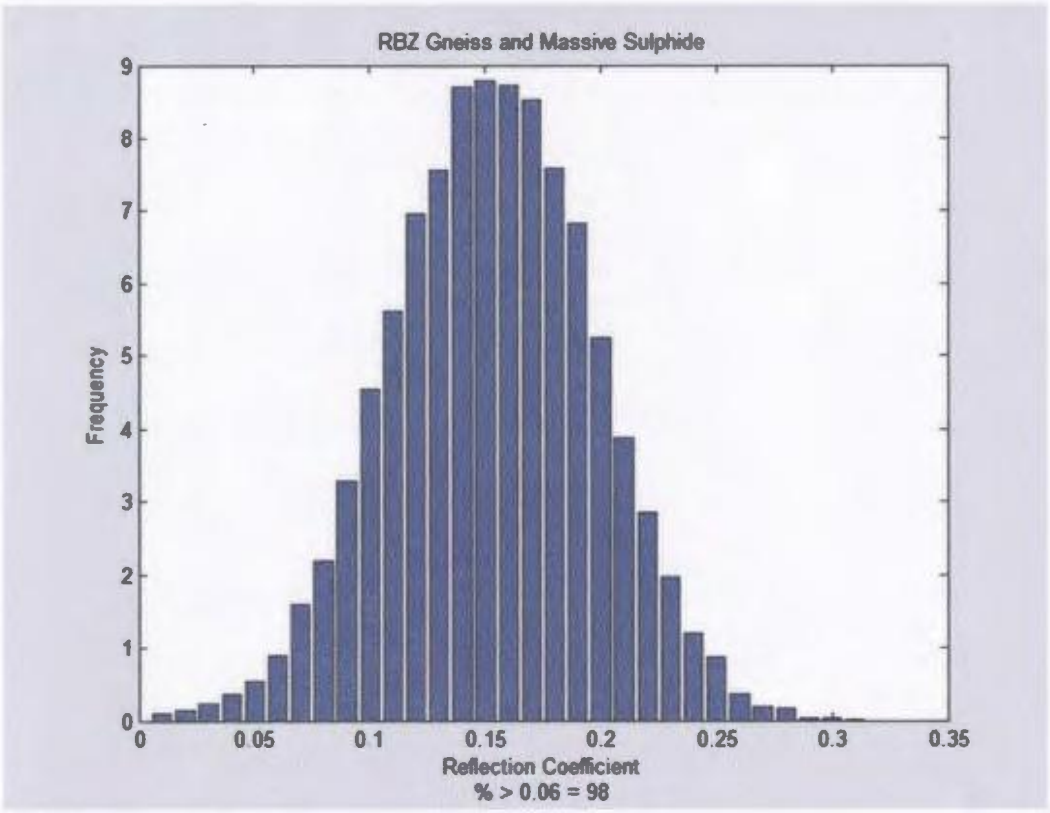


b)

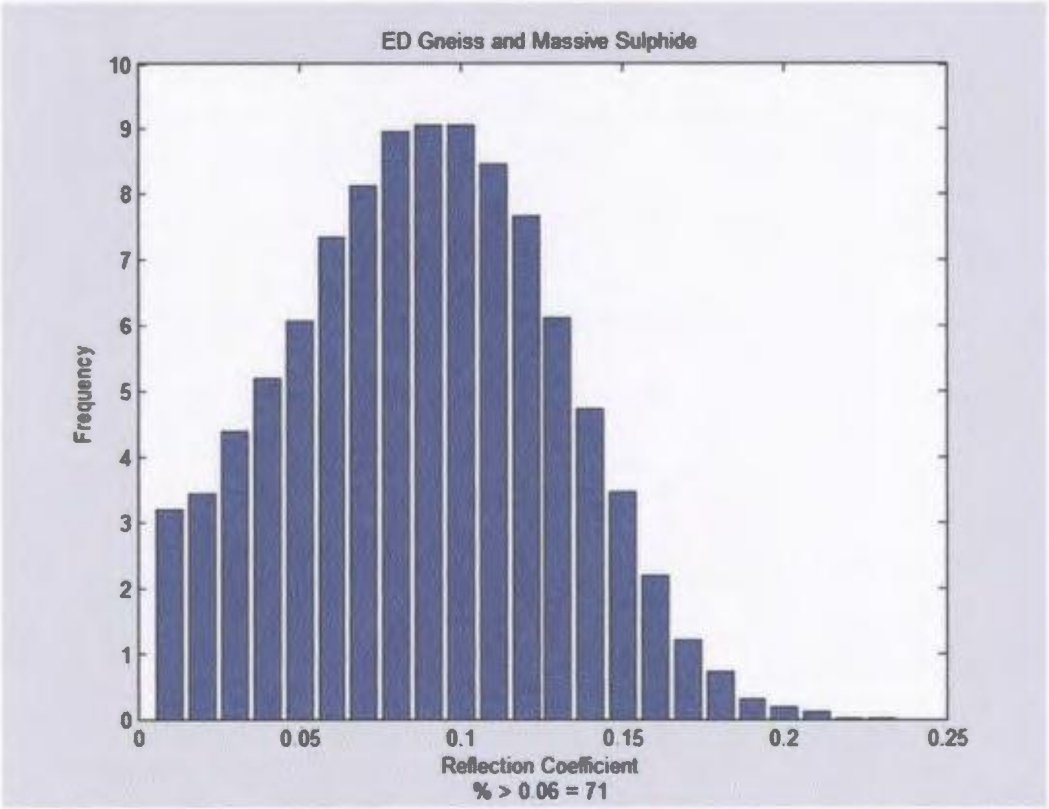


Figure 2.3.3.5: Potential reflectivity distribution for gneiss and massive sulphide for a) Reid Brook zone and b) Eastern Deeps zone. The vertical axis, frequency, indicates the percentage of synthetic interfaces having a reflection coefficient in a particular bin.

Deeps zones is substantial. Therefore, seismic reflection techniques hold promise for detecting and imaging major lithologic contrasts in the Voisey's Bay area.

### 2.4 Borehole Sonic and Density Logs, and Synthetic Seismograms

Borehole sonic and density logs provide the information from which acoustic impedances can be derived. From the assessment of the acoustic impedance log, important interfaces across which there is a clear contrast in impedance can be readily identified (Reynolds, 1997). The acoustic impedance log can then be used to derive a vertical reflectivity series, which is the determination of the series of reflection coefficients across the interfaces (Reynolds, 1997). A synthetic seismogram can then be generated by convolving the vertical reflectivity series with an assumed artificial wavelet, often a Ricker wavelet (Sheriff and Geldart, 1995). "One of the major uses of synthetic seismograms is to compare them with actual seismic data in order to identify reflections with particular interfaces" (Sheriff and Geldart, 1995). Synthetic seismograms were produced for both the Reid Brook and Eastern Deeps zones to aid in the evaluation of reflective potential of the contrasting lithologies, the effect of velocity gradients (e.g. caused by a mineralized troctolitic halo), the frequency content in the seismic data, and the necessary source frequencies for adequate resolution in the Voisey's Bay area.

Synthetic seismograms were produced using a MATLAB program that uses supplied borehole sonic and density data to determine both acoustic impedance and the vertical reflectivity series, which is then convolved with a Ricker wavelet which has a predetermined dominant frequency. The synthetic seismograms are one-dimensional and

thus it is assumed that raypaths are vertical and interfaces are horizontal. Figure 2.4.1 illustrates the general concept of producing synthetic seismograms.

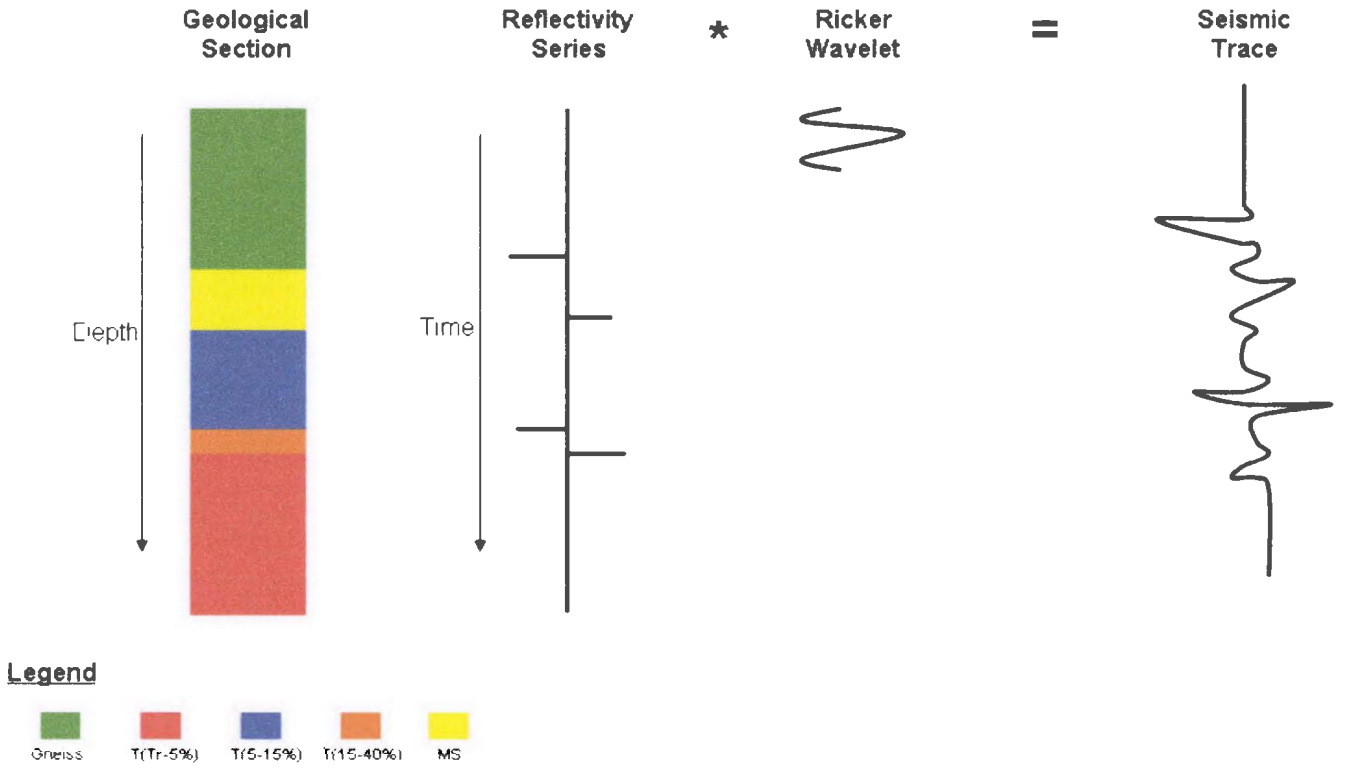


Figure 2.4.1: Diagram illustrating the concept for generating synthetic seismograms. T represents troctolite with its corresponding percentage of sulphides and MS represents massive sulphides.

Synthetic seismograms were produced for boreholes VB-96282, VB-96334, and VB-03596 for the Reid Brook zone and boreholes VB-95214, VB-00544, and VB-00545 for the Eastern Deeps zone. Examination of the density and velocity logs for both the Reid Brook and Eastern Deeps zones further confirms that the host rocks have low densities and high velocities while the massive sulphides have high densities and low velocities as previously explained in Section 2.3.1 (Figures 2.4.2A, and E-2.4.7A, and E). Analysis of the acoustic impedance logs for both the Reid Brook and Eastern Deeps zones verifies that there is only a modest acoustic impedance contrast between the

troctolite and massive sulphides as a consequence of the common mineralized troctolitic halo surrounding the massive sulphides; however, there is a significant contrast between the gneiss and massive sulphides as documented in Section 2.3.2 (Figures 2.4.2F-2.4.7F). As a consequence of this small acoustic impedance contrast between the troctolite and massive sulphides only modest reflection coefficients are produced at that boundary: < 0.08 and < 0.04 for the Reid Brook and Eastern Deeps zones respectively (Figures 2.4.2D-2.4.7D). As anticipated from the large acoustic impedance contrast, significant reflection coefficients (~ 0.15) are produced at the boundary of gneiss/massive sulphide for the Reid Brook zone (Figures 2.4.2G-2.4.4G). The three boreholes investigated for the Eastern Deeps zone did not contain any gneiss juxtaposed against massive sulphide. Nevertheless, considerable reflection coefficients would still be expected at that boundary. These calculated reflection coefficients are consistent with the potential reflection coefficients predicted for these contrasting lithologies in Section 2.3.3.

In general, the massive sulphide zones logged in the boreholes in the Reid Brook zone are on the order of 5-15 m thick and thus, are thinner than those in the Eastern Deeps zone which are on the order of 20-60 m thick (Figures 2.4.2A-2.4.7A). Dominant frequencies of 50, 120, and 400 Hz were used for the Ricker wavelet to illustrate the different tuning responses to the layers in the two different zones. As a rule of thumb for a low-velocity layer contained within a high-velocity layer (or vice versa) the tuning thickness is one-quarter of the wavelength. Tables 2.4.1 and 2.4.2 display tuning thicknesses for the various lithologies in the boreholes for both the Reid Brook and Eastern Deeps zones respectively.

Table 2.4.1: Tuning thicknesses for various lithologies contained in the boreholes for the Reid Brook zone.

| Lithology | Tuning Thickness (if $F_{dom}$ = 50 Hz) | Tuning Thickness (if $F_{dom}$ = 120 Hz) | Tuning Thickness (if $F_{dom}$ = 400 Hz) |
|---|---|---|---|
| Gneiss | 28 m | 12 m | 3.5 m |
| Troctolite(Tr-5%) | 31 m | 13 m | 4 m |
| Troctolite(5-15%) | 30 m | 12.5 m | 4 m |
| Troctolite(15-40%) | 29 m | 12 m | 3.5 m |
| Massive Sulphide | 23.5 m | 10 m | 3 m |

Table 2.4.2: Tuning thicknesses for various lithologies contained in the boreholes for the Eastern Deeps zone.

| Lithology | Tuning Thickness (if $F_{dom}$ = 50 Hz) | Tuning Thickness (if $F_{dom}$ = 120 Hz) | Tuning Thickness (if $F_{dom}$ = 400 Hz) |
|---|---|---|---|
| Gneiss | 30 m | 13 m | 4 m |
| Troctolite(Tr-5%) | 33 m | 14 m | 4 m |
| Troctolite(5-15%) | 32 m | 13 m | 4 m |
| Troctolite(15-40%) | 30 m | 12.5 m | 4 m |
| Massive Sulphide | 22 m | 9 m | 3 m |

The Ricker wavelets have a relatively narrow bandwidth that centers on the dominant frequency (Figures 2.4.8A, B, and C-2.4.13A, B, and C). Figures 2.4.8D, E, and F-2.4.13D, E, and F illustrate that the frequency spectra of the synthetic seismograms also have a narrow bandwidth but different frequency peaks than just the dominant frequency. This indicates that there is a tuning response to the layers in the boreholes for each of the different dominant frequencies that corresponds to one-quarter of the source wavelength.

Figures 2.4.2C-2.4.4C illustrate that a Ricker wavelet with a dominant frequency of 120 Hz seems to allow for the best tuning response to the massive sulphides in the Reid Brook zone. This is because the shape of the wavelet detects the boundaries of the thin massive sulphides. This is reasonable since the tuning thickness is approximately 10

m which is the thickness of the majority of the massive sulphides logged in the boreholes in this area. However, a Ricker wavelet with a dominant frequency of 50 Hz seems to allow for the most optimum tuning response to the massive sulphides in the Eastern Deeps zone (Figures 2.4.5B-2.4.7B). Given that the tuning thickness is approximately 22 m for the massive sulphides in the Eastern Deeps zone a dominant frequency of 50 Hz or less may be most appropriate for tuning to the 20-60 m thick massive sulphide zones. At a very high dominant frequency of 400 Hz the synthetic seismogram appears to tune to both the large acoustic impedance contrasts and the internal variations present within the layers for both the Reid Brook and Eastern Deeps zones (Figures 2.4.2D-2.4.7D). Since the tuning thickness is on the order of 3-4 m regardless of the different lithologies for both the Reid Brook and Eastern Deeps zones it is expected that much greater detail and resolution within the layers would be detected.

Unfortunately, high vertical resolution requires broad bandwidth signals and therefore sources that must be capable of generating a wide band of both low and high frequencies. Although the massive sulphide zones may be detected at low to moderate frequencies only low resolution data would be attained using a source that generated only low frequencies. High frequencies (short wavelengths) provide better resolution and detail of structures than are obtainable from low frequencies (long wavelengths); however, high frequency vibrations do not travel as well through rock as low frequency vibrations (Fowler et al., 2005). Therefore for the Voisey's Bay area, it would be desirable to use a source that can generate a broad bandwidth of frequencies that includes both low (< 50 Hz) and high (> 120 Hz) frequencies. This way a wide variety of detail is

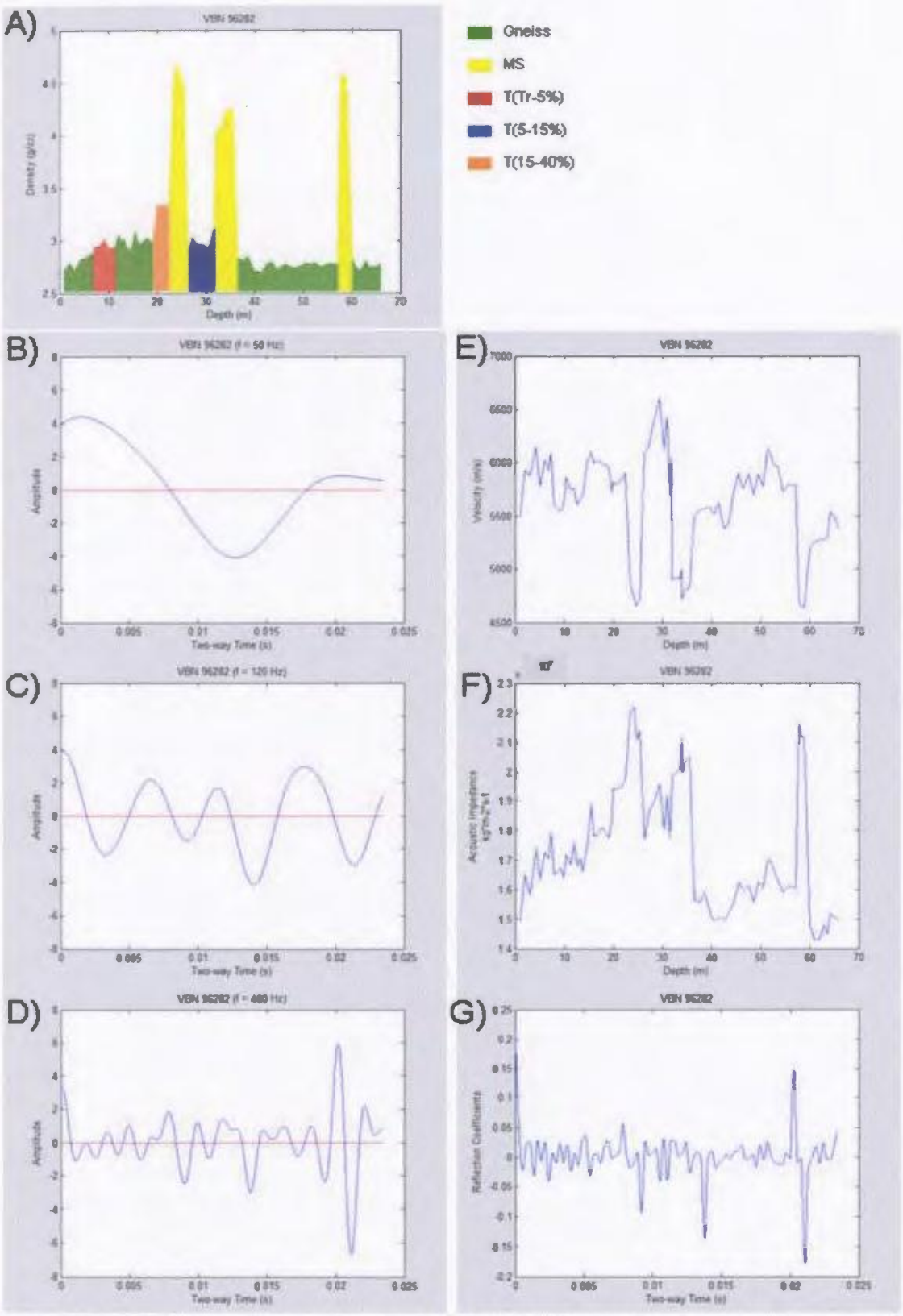


Figure 2.4.2: Reid Brook zone borehole VB-96282. A) density log, B) synthetic seismogram ($F_{dom}$ = 50 Hz), C) synthetic seismogram ($F_{dom}$ = 120 Hz), D) synthetic seismogram ($F_{dom}$ = 400 Hz), E) velocity log, F) acoustic impedance log, G) reflection coefficient log. T represents troctolite and its percentage of sulphides, MS represents massive sulphides.

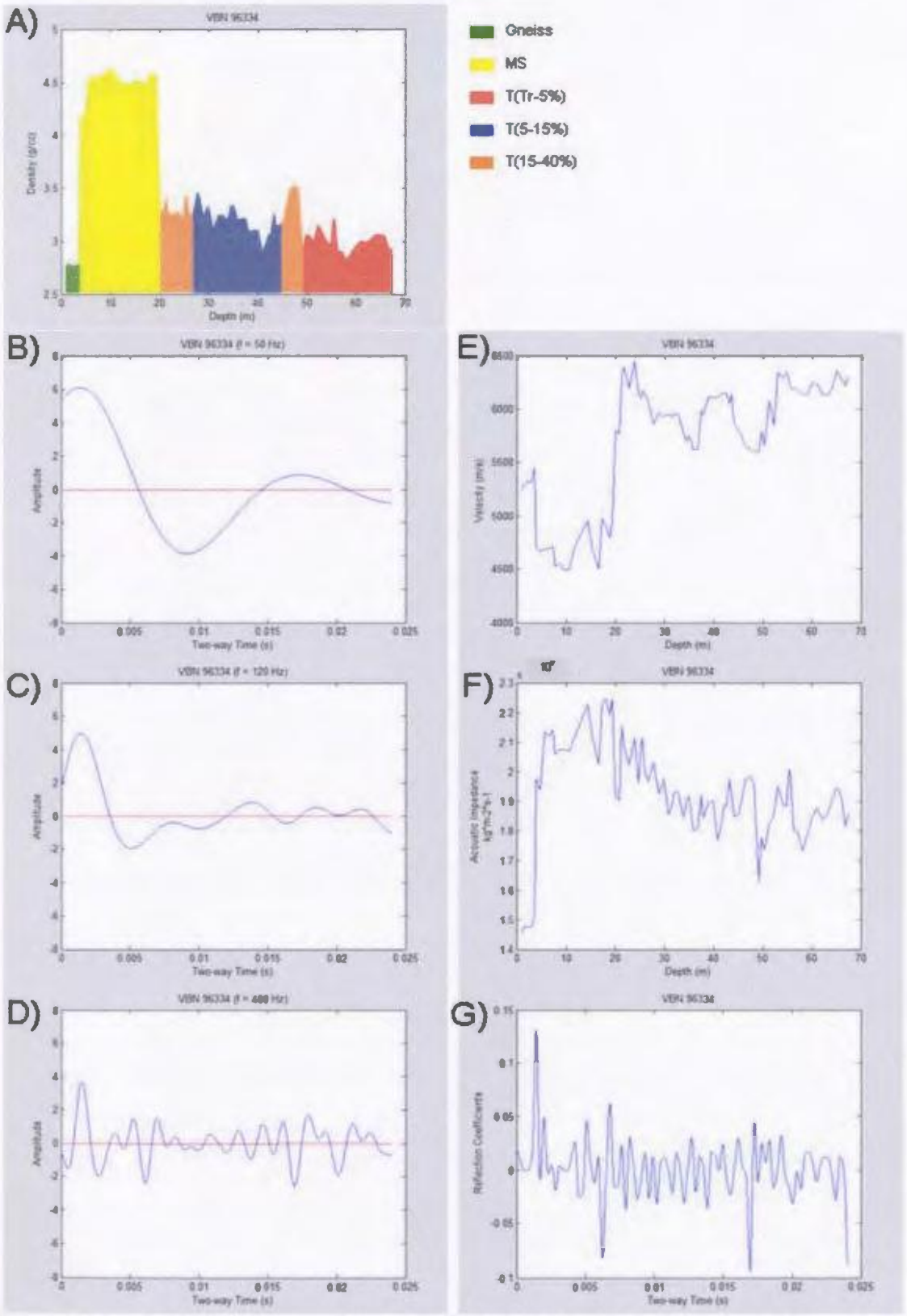


Figure 2.4.3: Reid Brook zone borehole VB-96334. A) density log, B) synthetic seismogram ($F_{dom}$ = 50 Hz), C) synthetic seismogram ($F_{dom}$ = 120 Hz), D) synthetic seismogram ($F_{dom}$ = 400 Hz), E) velocity log, F) acoustic impedance log, G) reflection coefficient log. T represents troctolite and its percentage of sulphides, MS represents massive sulphides.

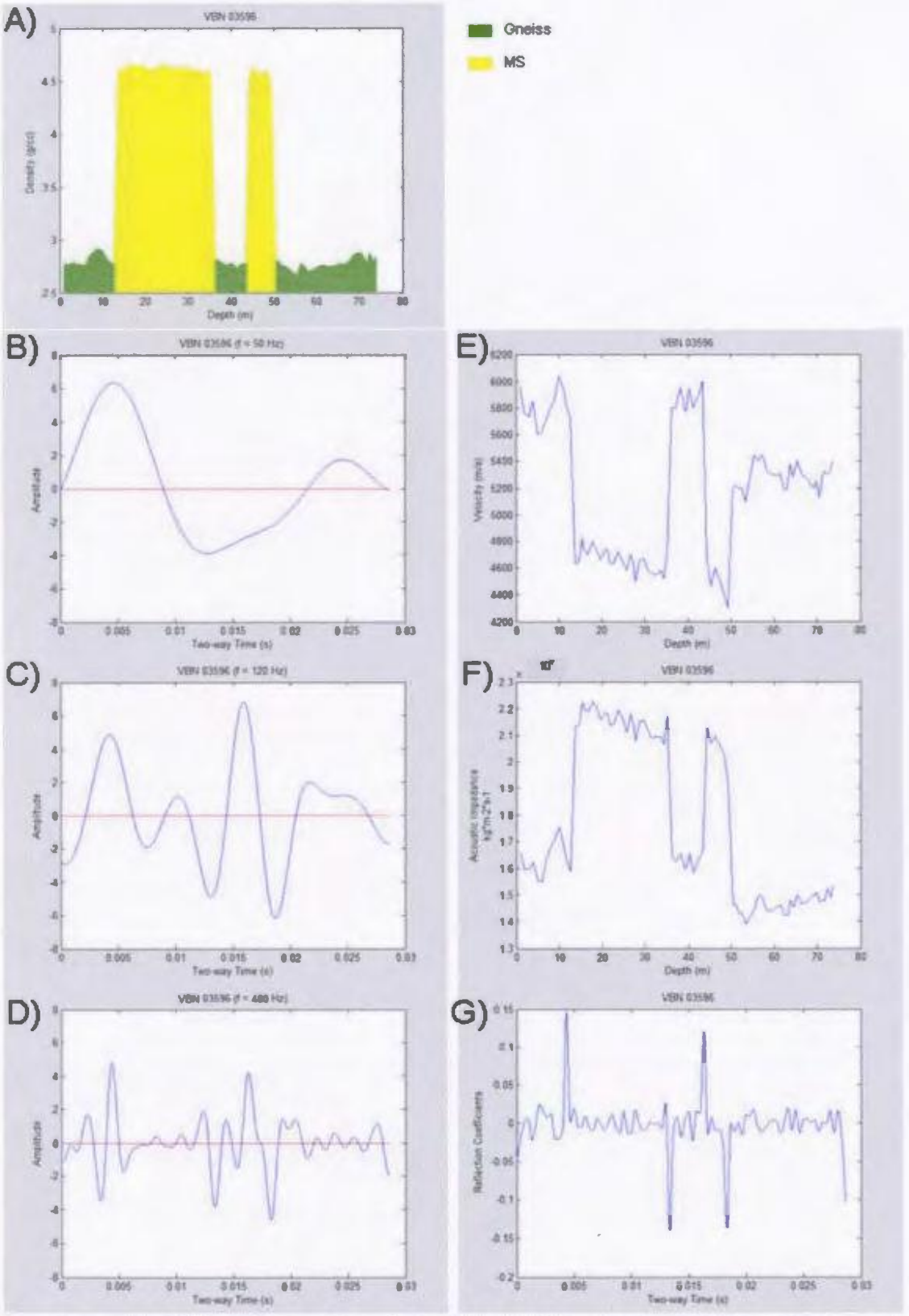


Figure 2.4.4: Reid Brook zone borehole VB-03596. A) density log, B) synthetic seismogram ($F_{dom}$ = 50 Hz), C) synthetic seismogram ($F_{dom}$ = 120 Hz), D) synthetic seismogram ($F_{dom}$ = 400 Hz), E) velocity log, F) acoustic impedance log, G) reflection coefficient log. MS represents massive sulphides.

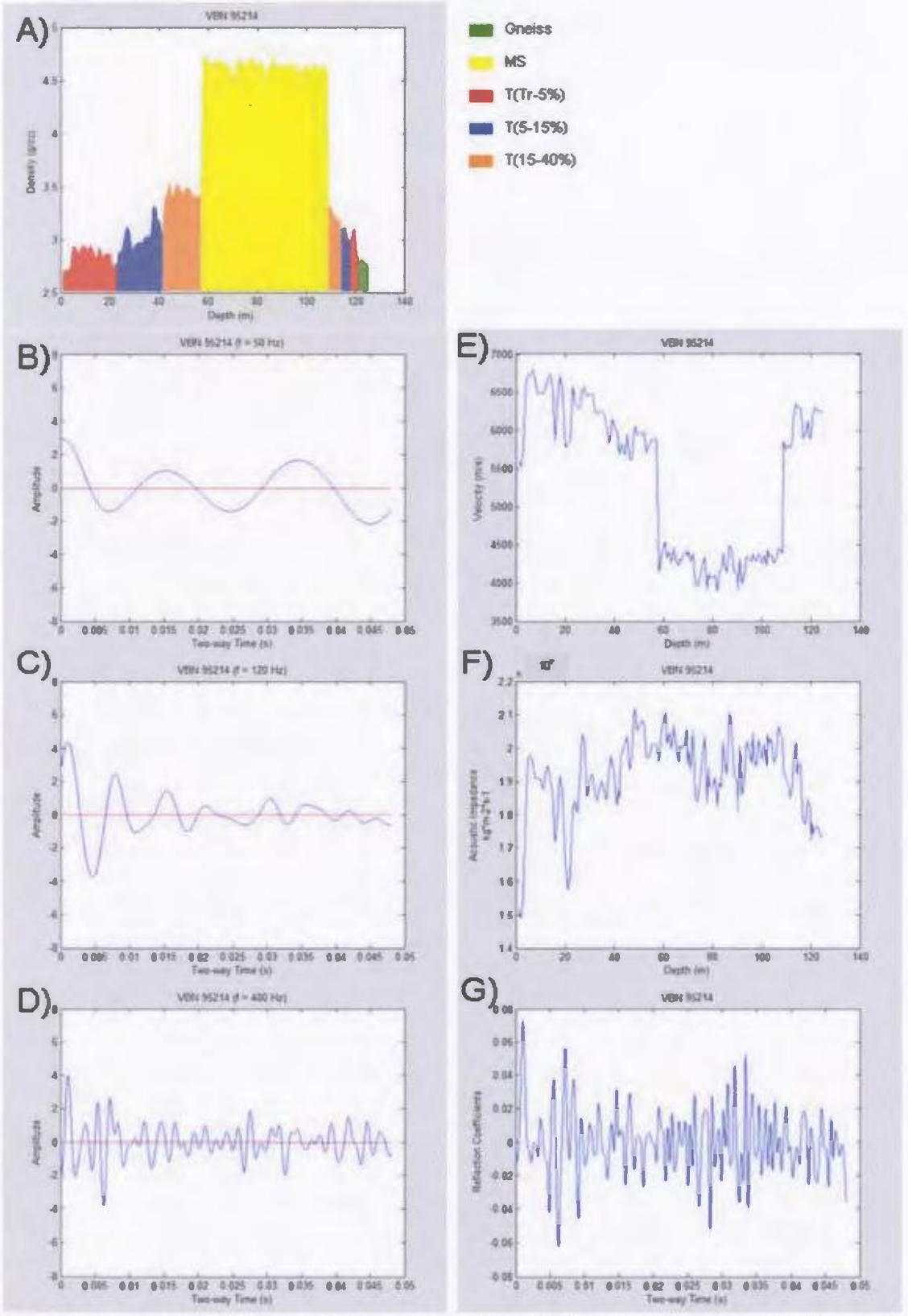


Figure 2.4.5: Eastern Deeps zone borehole VB-95214. A) density log, B) synthetic seismogram ($F_{dom}$ = 50 Hz), C) synthetic seismogram ($F_{dom}$ = 120 Hz), D) synthetic seismogram ($F_{dom}$ = 400 Hz), E) velocity log, F) acoustic impedance log, G) reflection coefficient log. T represents troctolite and its percentage of sulphides, MS represents massive sulphides.

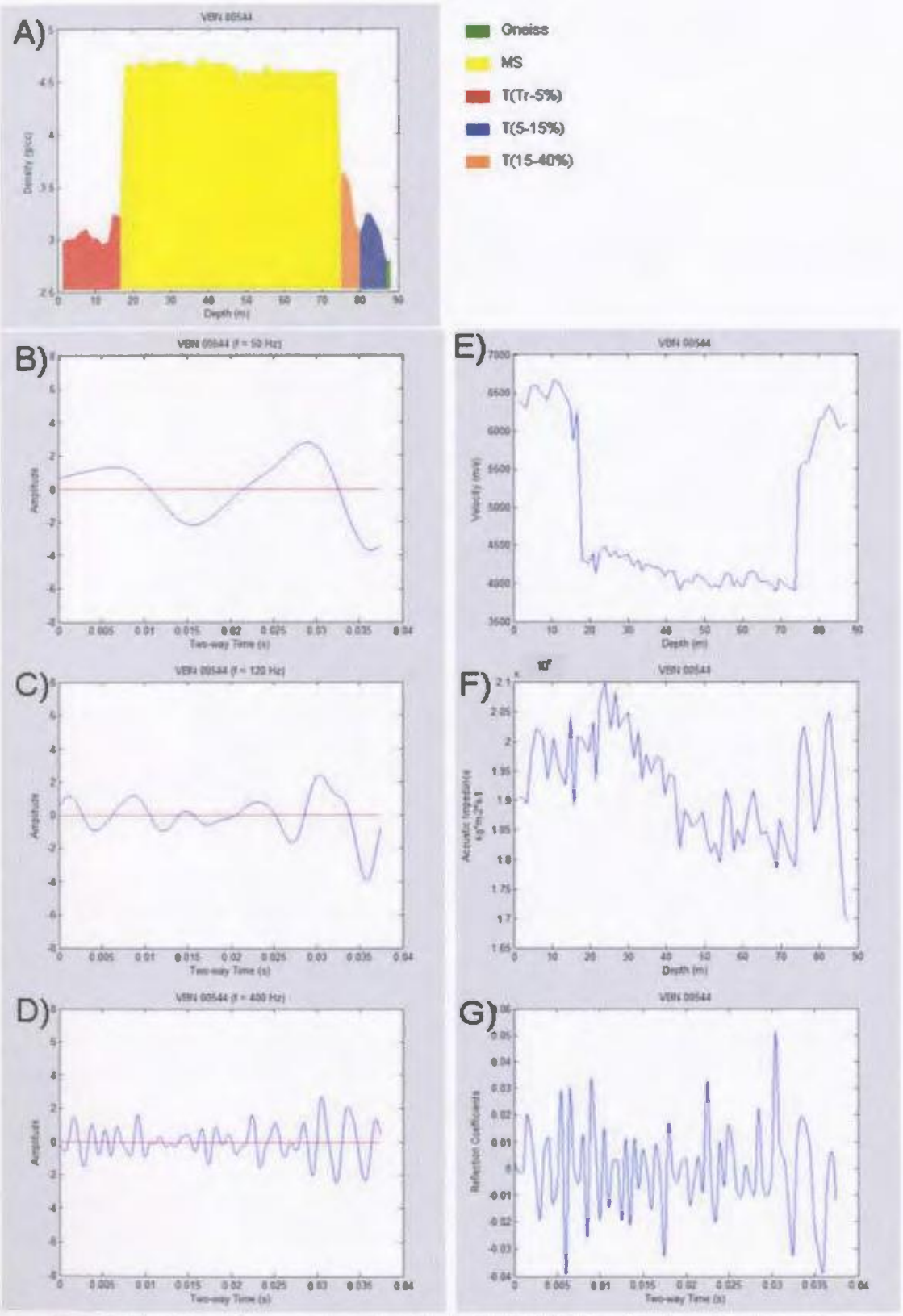


Figure 2.4.6: Eastern Deeps zone borehole VB-00544. A) density log, B) synthetic seismogram ($F_{dom}$ = 50 Hz), C) synthetic seismogram ($F_{dom}$ = 120 Hz), D) synthetic seismogram ($F_{dom}$ = 400 Hz), E) velocity log, F) acoustic impedance log, G) reflection coefficient log. T represents troctolite and its percentage of sulphides, MS represents massive sulphides.

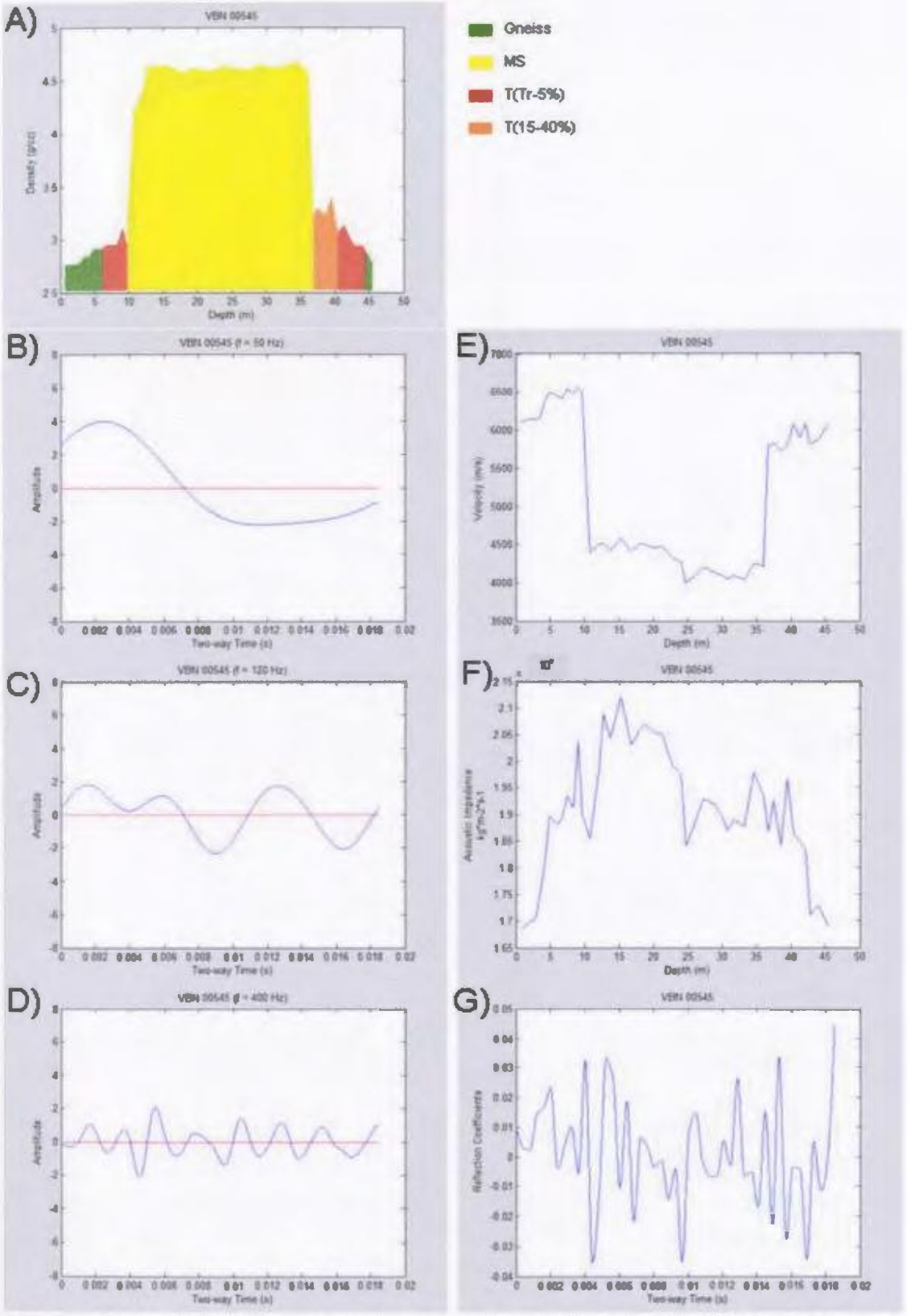


Figure 2.4.7: Eastern Deeps zone borehole VB-00545. A) density log, B) synthetic seismogram ($F_{dom}$ = 50 Hz), C) synthetic seismogram ($F_{dom}$ = 120 Hz), D) synthetic seismogram ($F_{dom}$ = 400 Hz), E) velocity log, F) acoustic impedance log, G) reflection coefficient log. T represents troctolite and its percentage of sulphides, MS represents massive sulphides.

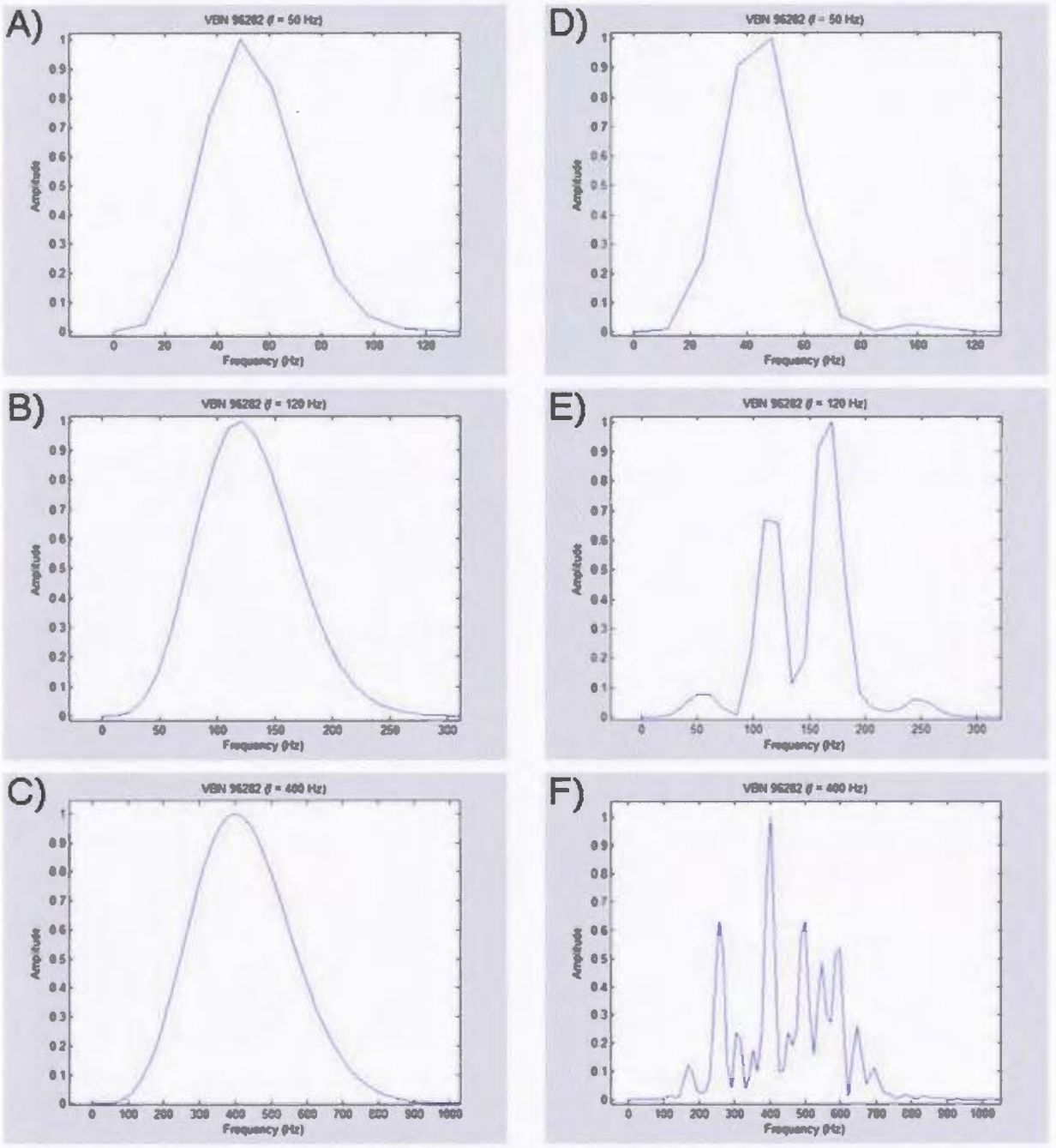


Figure 2.4.8: Reid Brook zone borehole VB-96282. A) frequency spectrum of wavelet ($F_{dom}$ = 50 Hz), B) frequency spectrum of wavelet ($F_{dom}$ = 120 Hz), C) frequency spectrum of wavelet ($F_{dom}$ = 400 Hz), D) frequency spectrum of synthetic seismogram ($F_{dom}$ = 50 Hz), E) frequency spectrum of synthetic seismogram ($F_{dom}$ = 120 Hz), F) frequency spectrum of synthetic seismogram ($F_{dom}$ = 400 Hz).

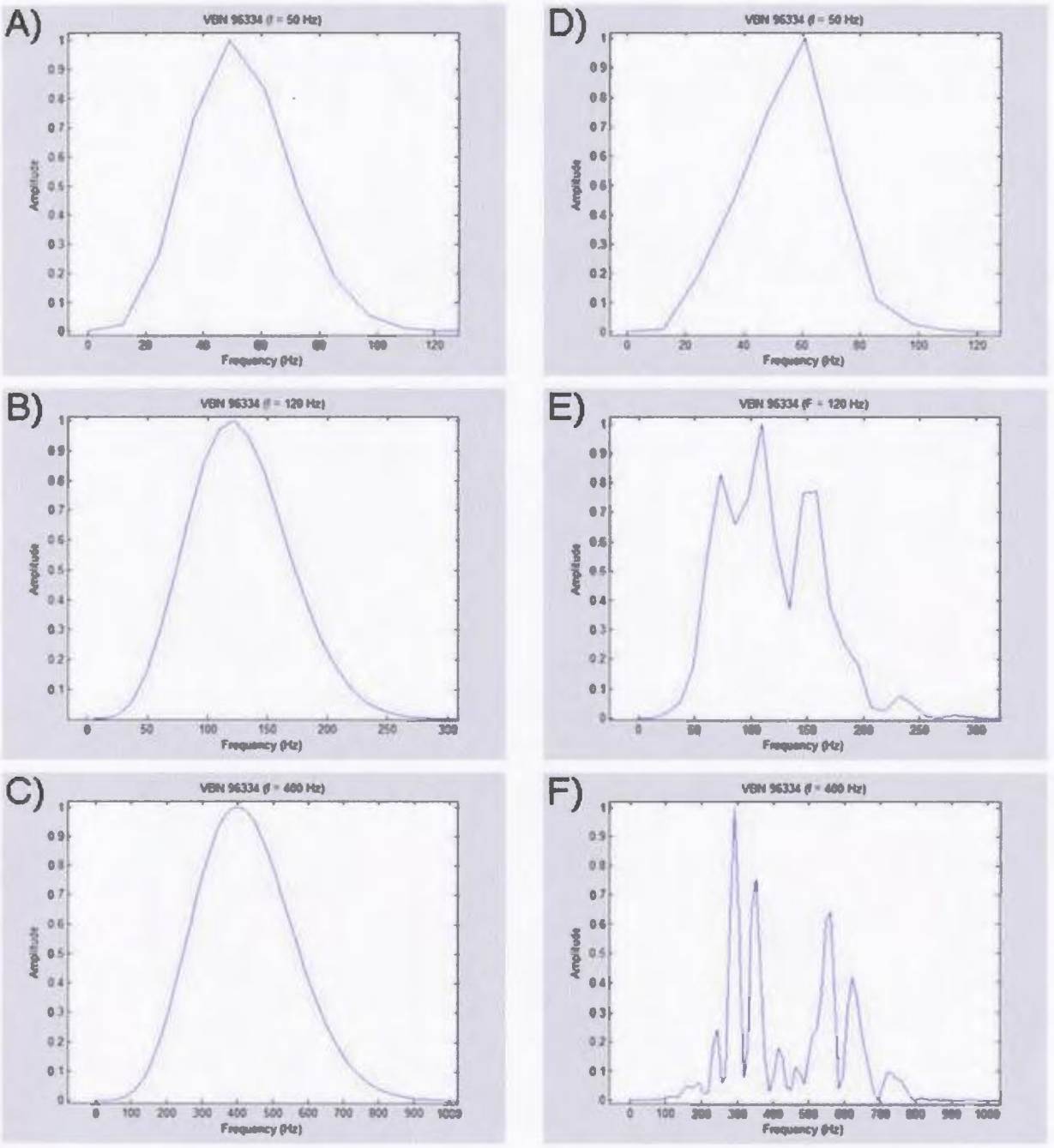


Figure 2.4.9: Reid Brook zone borehole VB-96334. A) frequency spectrum of wavelet ($F_{dom}$ = 50 Hz), B) frequency spectrum of wavelet ($F_{dom}$ = 120 Hz), C) frequency spectrum of wavelet ($F_{dom}$ = 400 Hz), D) frequency spectrum of synthetic seismogram ($F_{dom}$ = 50 Hz), E) frequency spectrum of synthetic seismogram ($F_{dom}$ = 120 Hz), F) frequency spectrum of synthetic seismogram ($F_{dom}$ = 400 Hz).

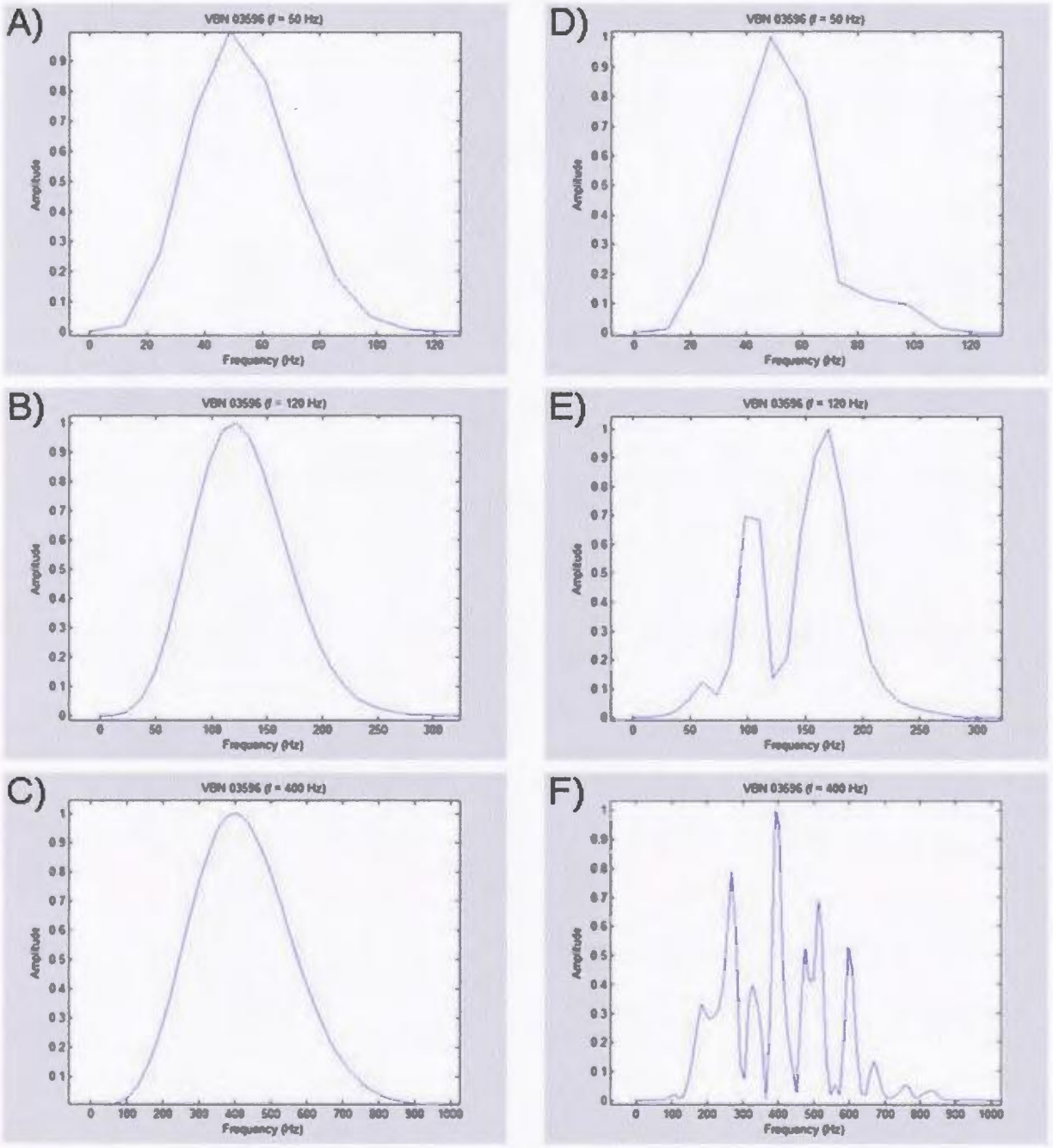


Figure 2.4.10: Reid Brook zone borehole VB-03596. A) frequency spectrum of wavelet ($F_{dom}$ = 50 Hz), B) frequency spectrum of wavelet ($F_{dom}$ = 120 Hz), C) frequency spectrum of wavelet ($F_{dom}$ = 400 Hz), D) frequency spectrum of synthetic seismogram ($F_{dom}$ = 50 Hz), E) frequency spectrum of synthetic seismogram ($F_{dom}$ = 120 Hz), F) frequency spectrum of synthetic seismogram ($F_{dom}$ = 400 Hz).

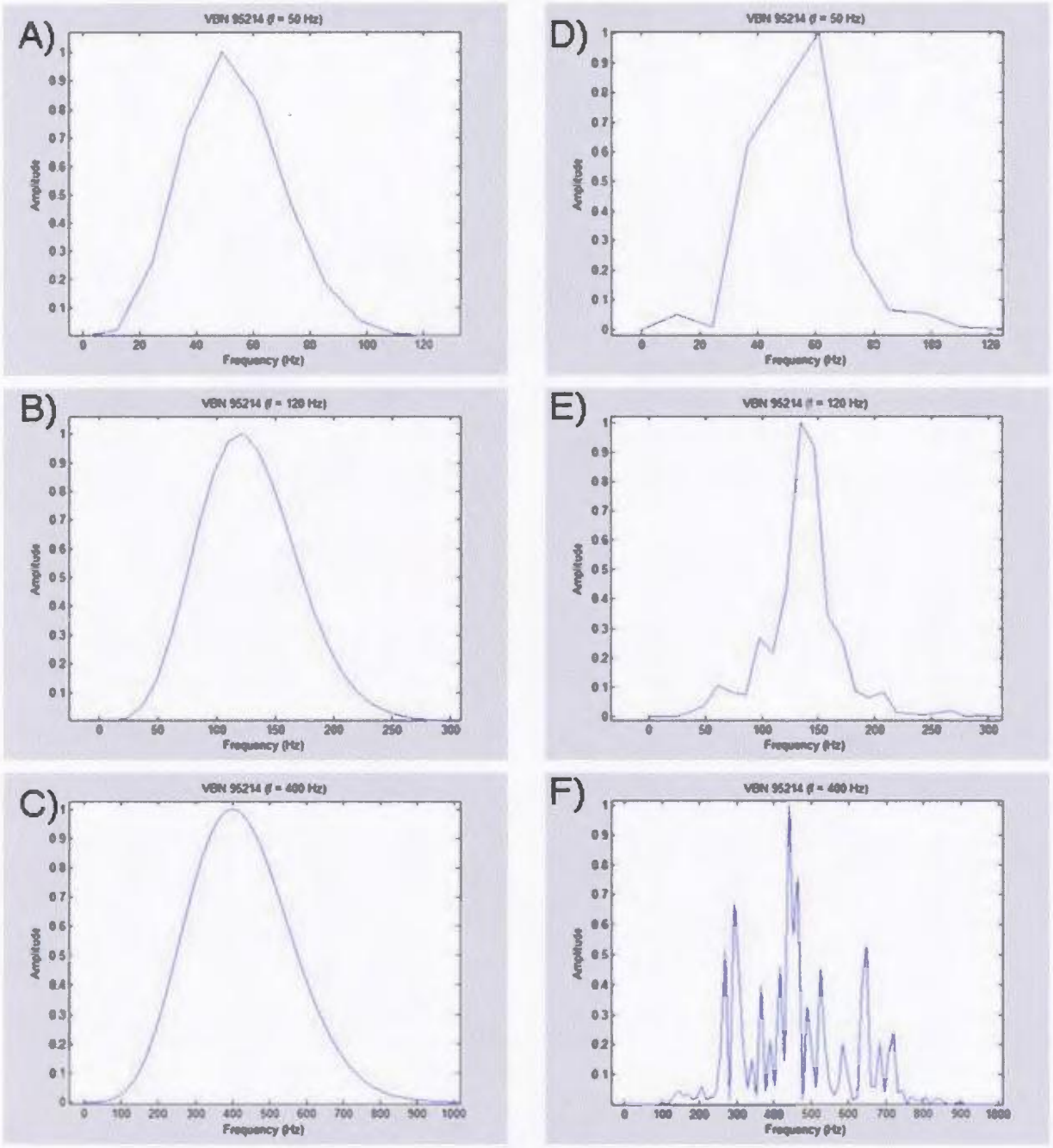


Figure 2.4.11: Eastern Deeps zone borehole VB-95214. A) frequency spectrum of wavelet ($F_{dom}$ = 50 Hz), B) frequency spectrum of wavelet ($F_{dom}$ = 120 Hz), C) frequency spectrum of wavelet ($F_{dom}$ = 400 Hz), D) frequency spectrum of synthetic seismogram ($F_{dom}$ = 50 Hz), E) frequency spectrum of synthetic seismogram ($F_{dom}$ = 120 Hz), F) frequency spectrum of synthetic seismogram ($F_{dom}$ = 400 Hz).

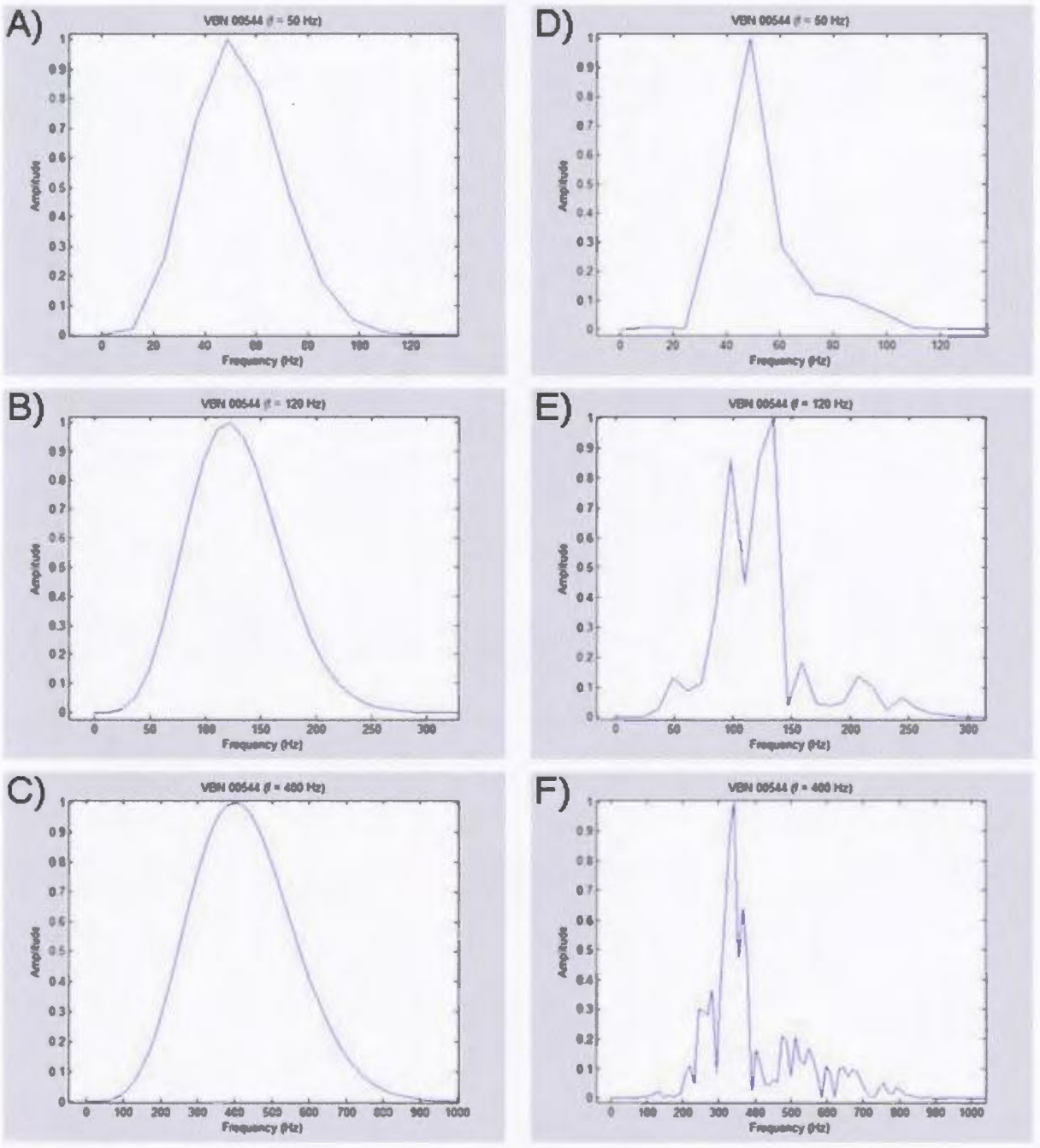


Figure 2.4.12: Eastern Deeps zone borehole VB-00544. A) frequency spectrum of wavelet ($F_{dom}$ = 50 Hz), B) frequency spectrum of wavelet ($F_{dom}$ = 120 Hz), C) frequency spectrum of wavelet ($F_{dom}$ = 400 Hz), D) frequency spectrum of synthetic seismogram ($F_{dom}$ = 50 Hz), E) frequency spectrum of synthetic seismogram ($F_{dom}$ = 120 Hz), F) frequency spectrum of synthetic seismogram ($F_{dom}$ = 400 Hz).

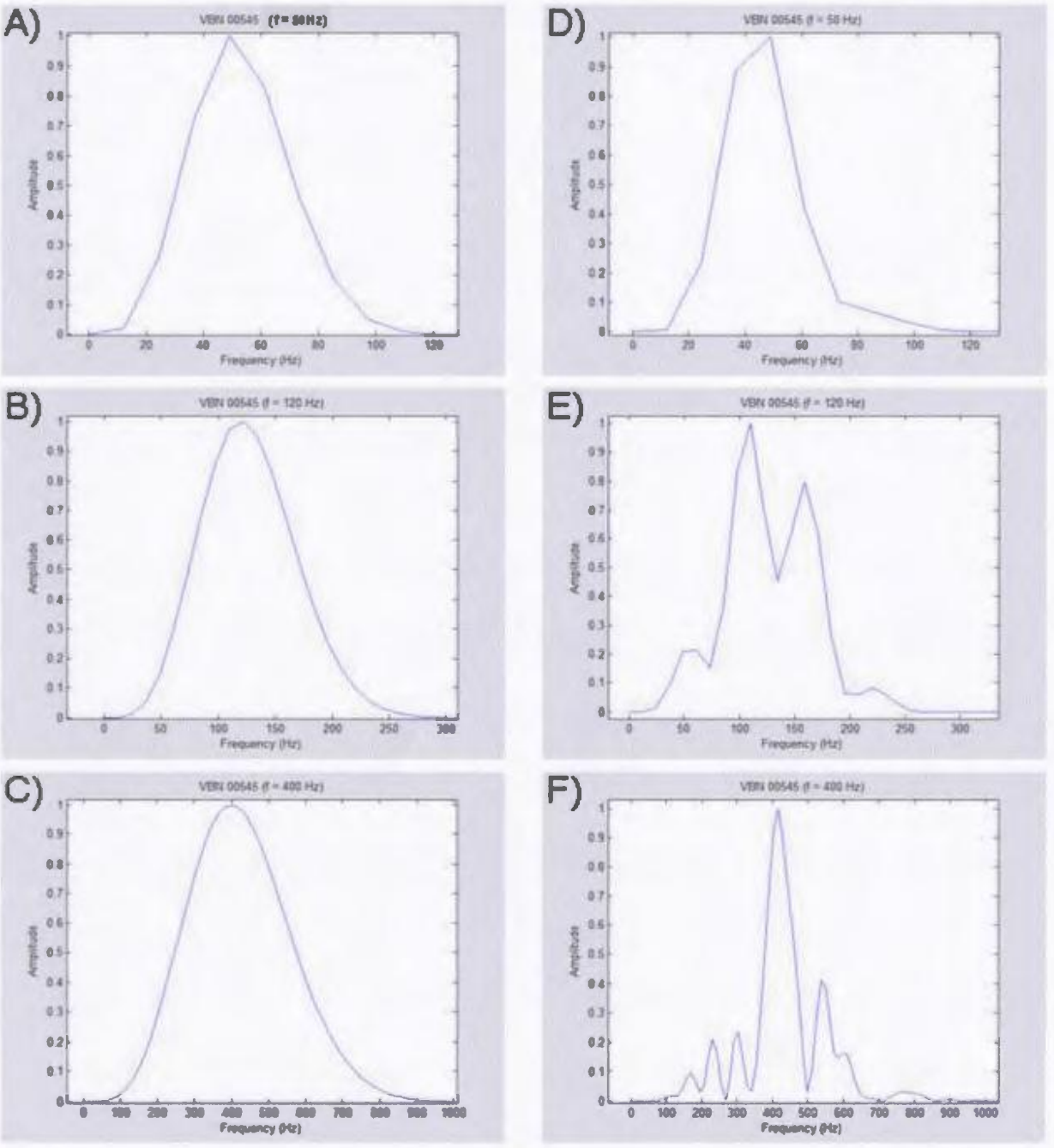


Figure 2.4.13: Eastern Deeps zone borehole VB-00545. A) frequency spectrum of wavelet ($F_{dom}$ = 50 Hz), B) frequency spectrum of wavelet ($F_{dom}$ = 120 Hz), C) frequency spectrum of wavelet ($F_{dom}$ = 400 Hz), D) frequency spectrum of synthetic seismogram ($F_{dom}$ = 50 Hz), E) frequency spectrum of synthetic seismogram ($F_{dom}$ = 120 Hz), F) frequency spectrum of synthetic seismogram ($F_{dom}$ = 400 Hz).

obtained but bandpass filtering can be applied to the data afterwards to focus only on the frequencies of interest. Either way, there is always a trade-off between depth penetration and minimum resolution when selecting a source.

## 2.5 Conclusions

The choice of seismic techniques applied to characterize an ore zone must be tailored to that specific environment and the quality of the seismic interpretation depends on the level of knowledge of the physical properties of the pertinent rocks (Eaton et al, 2003a). Analysis of a large number of velocity and density data derived from borehole logs and core samples from the Voisey's Bay site demonstrates that there is a modest velocity contrast between the gneiss that is the predominant country rock and the troctolitic intrusion that hosts the sulphide mineralization. However, the velocity contrasts between the gneiss and massive sulphide, and the troctolite and massive sulphide, is significant for both areas. On the other hand, there are moderate to large acoustic impedance contrasts between the gneiss and troctolite, and the gneiss and massive sulphide, while the contrast between the troctolite and massive sulphide is slightly smaller as a consequence of the presence of a mineralized troctolitic halo. Analysis of the acoustic impedance logs for specific wells in both the Reid Brook and Eastern Deeps zones further verifies these acoustic impedance contrasts and the insignificant effect of the velocity gradients caused by the mineralized halo.

In general, the average potential reflection coefficients for the lithology contrasts of troctolite and gneiss, troctolite and granite, troctolite and massive sulphide, and gneiss

and massive sulphide are significant in the Reid Brook and Eastern Deeps zones. One exception is the average potential reflection coefficient for troctolite and massive sulphide in the Eastern Deeps zone which is less than 0.04. Analysis of reflection coefficient logs for specific boreholes in both the Reid Brook and Eastern Deeps zones reinforces the potential reflection coefficients predicted for the various contrasting lithologies. Since the reflection coefficient for troctolite and massive sulphide in the Eastern Deeps zone is somewhat weaker the upper bound of the massive sulphides when it falls in contact with the troctolite is not expected to be imaged. The lower bound which normally falls into contact with gneiss is expected to be imaged.

Synthetic seismograms generated for specific boreholes in both the Reid Brook and Eastern Deeps zones demonstrate that the massive sulphide zones may be detected at low to moderate frequencies (< 120 Hz) but only low resolution data would be attained using such long wavelengths. A source that could generate a broad bandwidth of frequencies would provide a wide variety of detail. The frequencies of interest could be focused upon afterwards by filtering the data appropriately. Nevertheless, there is always a trade-off between depth penetration and minimum resolution when selecting a source.

Overall, these data indicate that at the Eastern Deeps zone, velocity-sensitive techniques such as borehole-borehole tomography are most appropriate for direct characterization of the ore bodies themselves and impedance-based techniques such as reflection seismology are more appropriate for characterization of the magmatic system and structural mapping. However, the data do support significant potential for impedance driven ore body detection depending upon the specific setting of the ore body in the

Eastern Deeps zone. On the other hand, impedance-based techniques would be appropriate for characterization of the ore bodies, the magmatic system, and structural mapping in the Reid Brook zone. Consequently, this suggests that minor variations in the host rock type and/or ore mineral combinations may control whether a system responds better to impedance-based techniques and/or velocity-sensitive techniques. Hence, physical properties analysis of the study area becomes a crucial component for any seismic exploration in mining.

# CHAPTER 3: 2-D Seismology

## 3.1 Introduction

Due to the relative geometric complexity and heterogeneity of the geology typical of many ore deposits, the reflection wave field is generally dominated by scattering rather than specular reflection. In general, massive sulphide bodies that are considered economically viable for mining have length scales roughly equivalent to the Fresnel zone associated with the source frequencies (200-300 Hz range) used and deposit depth, and as such fall into the range of frequency independent or Mie scattering regimes (Eaton et al., 2003b). Consequently, signal-to-noise ratios tend to be modest and out-of-plane events and near-critical reflections may be significant components of the wave field. Due to the complexity of the wave field, past attempts at applying 2-D exploration seismic techniques for direct detection of massive sulphide bodies have met with only limited success. However, 2-D surveys have been quite successful in providing information on the structural context of the ore deposits and for mapping regional tectonostratigraphic markers (e.g., Sudbury, Manitouadge) (Milkereit et al., 1996; Eaton et al., 2003b).

The Voisey's Bay site offers a wide range of viable seismic targets of differing complexity that can be used to develop suitable acquisition and processing techniques for mineral exploration. A 2-D forward model-based study was designed to aid in the investigation of 2-D reflection seismic techniques in hardrock environments. I have developed a velocity model that incorporates the geometry and geologic complexity of the Voisey's Bay area for the purposes of seismic modeling. From the simplest form of

this model (i.e., constant velocities), progressing to greater complexities (i.e., heterogeneity and velocity gradients), the objectives are:

- to delineate the magmatic plumbing system at Voisey's Bay,
- to delineate both structure and fault control at Voisey's Bay,
- to fine-tune both the acquisition and processing parameters for a 2-D seismic survey at Voisey's Bay,
- and to provide a basic template for interpretation of the reflection data.

### 3.2 Study Area Geology

The Voisey's Bay area is located on the northeast coast of Labrador and occurs in the proximity of both the tectonic contact between the Nain-Churchill Provinces and the Nain Plutonic Suite. Voisey's Bay hosts one of the most important recent mineral discoveries in Canada – the Voisey's Bay Ni-Cu-Co deposit (Figure 3.2.1). Through previous work, it is now known that there are three main mineralized zones in the Voisey's Bay area: the Western Extension, the Ovoid, and the Eastern Deeps (Figure 3.2.2).

The Western Extension encompasses both the Reid Brook and the Discovery Hill Zones (RBZ and DHZ, respectively). The RBZ is a blind deposit (i.e., it does not intersect the surface), which is located near the surface and plunges to depths of approximately 1500 m below the surface and has an exceptionally complex shape (Kerr, 2003). It lies to the west of the Discovery Hill and consists of a south-dipping feeder

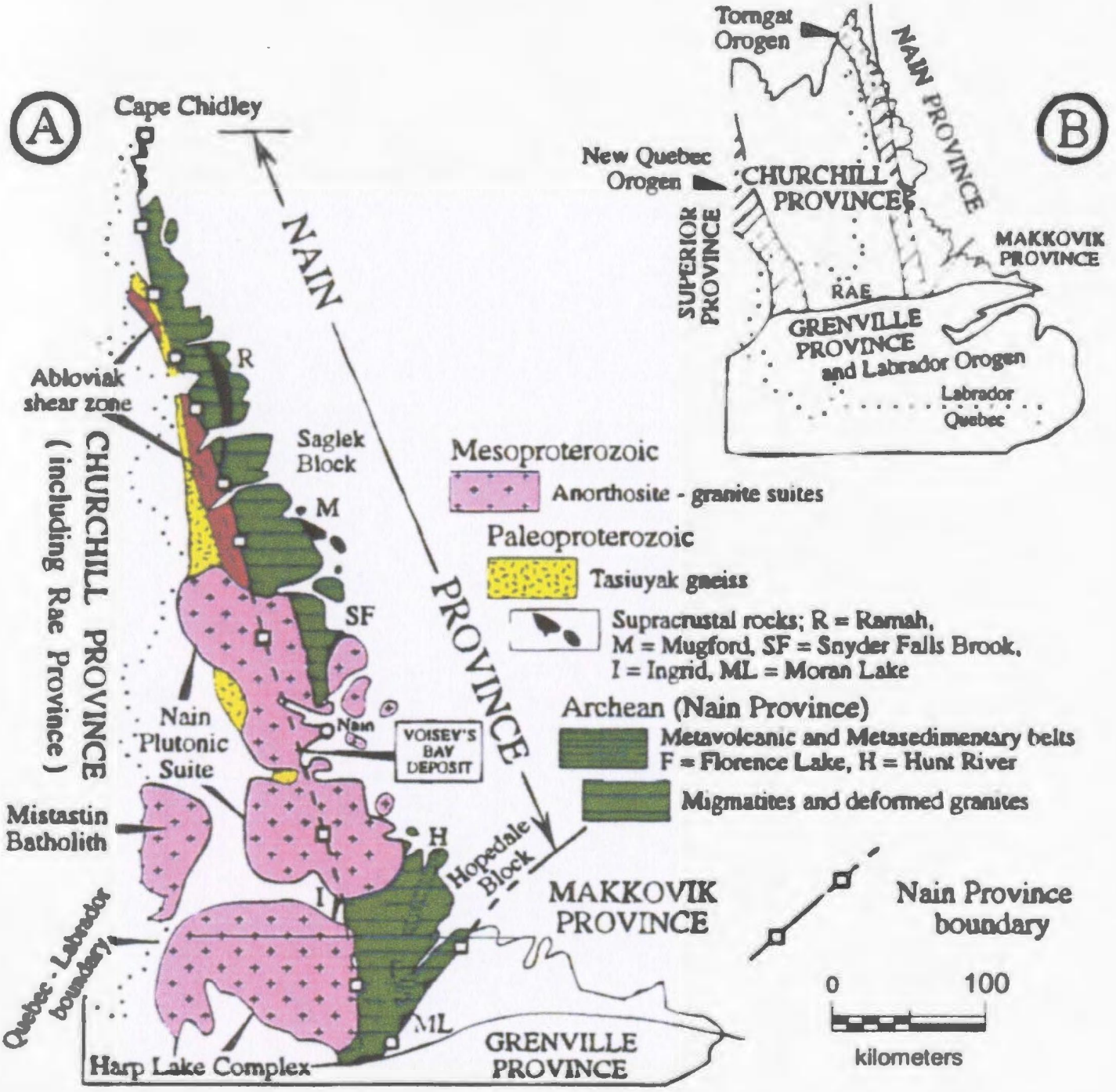


Drawn by VBNC

Figure 3.2.1: Regional Geology of Northern Labrador (after International Geological Correlation Programme Projects No. 290 and No. 315, 1994). (A) Regional geology of Labrador. (B) Regional Framework of Labrador illustrating the Nain and Churchill Provinces and their tectonic contact known as the Torngat Orogen.

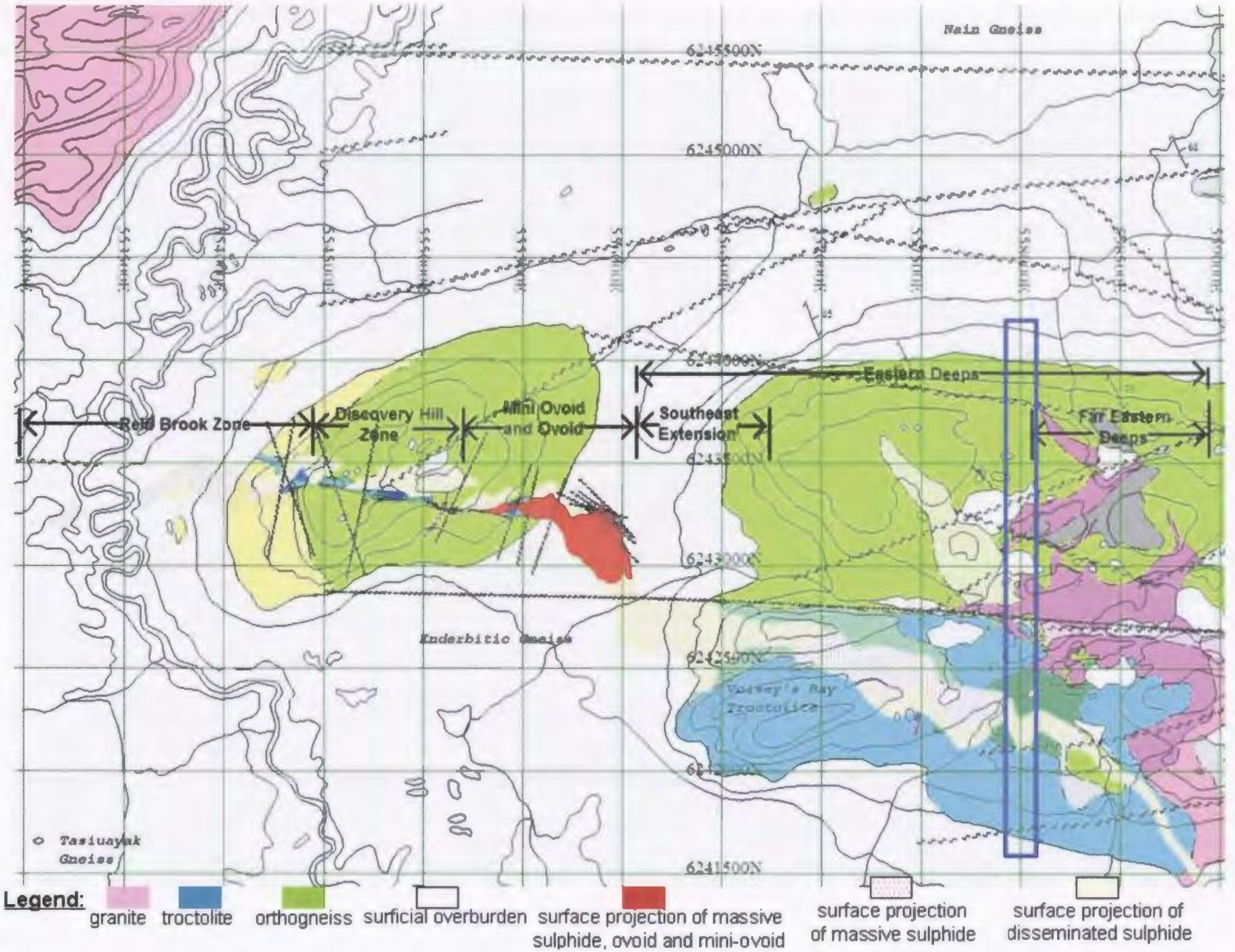


Figure 3.2.2: Geology map illustrating the three main mineralized zones in the Voisey's Bay area: the Western Extension (comprised of the Reid Brook and Discovery Hill zones), the Ovoid, and the Eastern Deeps. The blue box displays the location of the cross-section used for the primary 2-D model. (Modified from VBNC).

sheet which widens with depth into a troctolitic intrusion emplaced within Proterozoic Tasiuyak gneiss. The DHZ consists of a mineralized 30-100 m thick east-west trending, steeply north- to south-dipping pinch-and-swell troctolitic dyke intruded into enderbitic gneisses (Ryan, 2000). Geologically, the RBZ is distinct from the DHZ because it is at a lower position in the conduit stratigraphy and thus, actually plunges beneath the DHZ (Evans-Lamswood, 1999).

The Ovoid sits approximately 20 m below the surface and resembles a bowl, 600 by 350 m and 100 m deep in the center, filled with massive iron, nickel, and copper sulphides (Kerr, 2003: Ryan, 2000). The Ovoid is contained within a magmatic conduit system that is continuous from east to west. Therefore, due to its central location and vast accumulation of sulphides, it can be interpreted as a focal point within the magmatic sulphide system (Evans-Lamswood, 1999).

Like the Reid Brook Zone, the Eastern Deeps Zone is a blind deposit. It is located roughly 500 to 1000 m in the subsurface below texturally variable troctolite which rests on Archean gneiss (Kerr, 2003: Ryan, 2000). The mineralized sulphides are dispersed close to an elongate fracture where a shallowly north-dipping, 30 m thick, mineralized troctolitic dyke intersects the base of the larger troctolite body (Ryan, 2000). The EDZ has somewhat of a wedge-shaped appearance due to the presence of an inclined floor and an erosional cut-off (Evans-Lamswood, 1999).

The working model for development of the Voisey's Bay deposit suggests that extension-driven collapse of a hypothesized magma chamber at depth resulted in the injection of troctolitic magma and entrained sulphides into the present configuration as

known from map and borehole data (Cruden et al., 2000). The model suggests that the various ore bodies from east to west along the Voisey's Bay mineralized trend represent increasingly deeper structural levels in the system. The geometry and geologic association of the ore bodies ranges from simple to complex. Thus the Voisey's Bay site offers a variety of viable seismic targets of differing complexity that can be used to develop appropriate acquisition and processing parameters for a 2-D seismic survey.

## 3.3 2-D Model

The primary model designed to help fine tune acquisition and processing parameters for a 2-D survey planned to delineate the structural setting of the Voisey's Bay deposit was based on a borehole-constrained, a N-S cross-section constructed along a portion of 558000E in the Eastern Deeps by VBNC (Figure 3.2.2). Using this cross-section as the foundation for the primary model, the model was then expanded both to the north and south (unconstrained areas) using knowledge of the study area geology and the working model for the development of the Voisey's Bay deposit suggested by Cruden et al. 2000 (Figure 3.3.1.1).

- **3.3.1 Simplified Model**

Figure 3.3.1.1 is also considered to be the simplest form of the 2-D model where each geologic body and fault has a constant velocity. The constant velocities used for each geologic body were determined from the mean analysis of the physical properties for the Eastern Deeps zone in Section 2.3.2. Table 3.3.1.1 indicates the velocities used for the initial model.

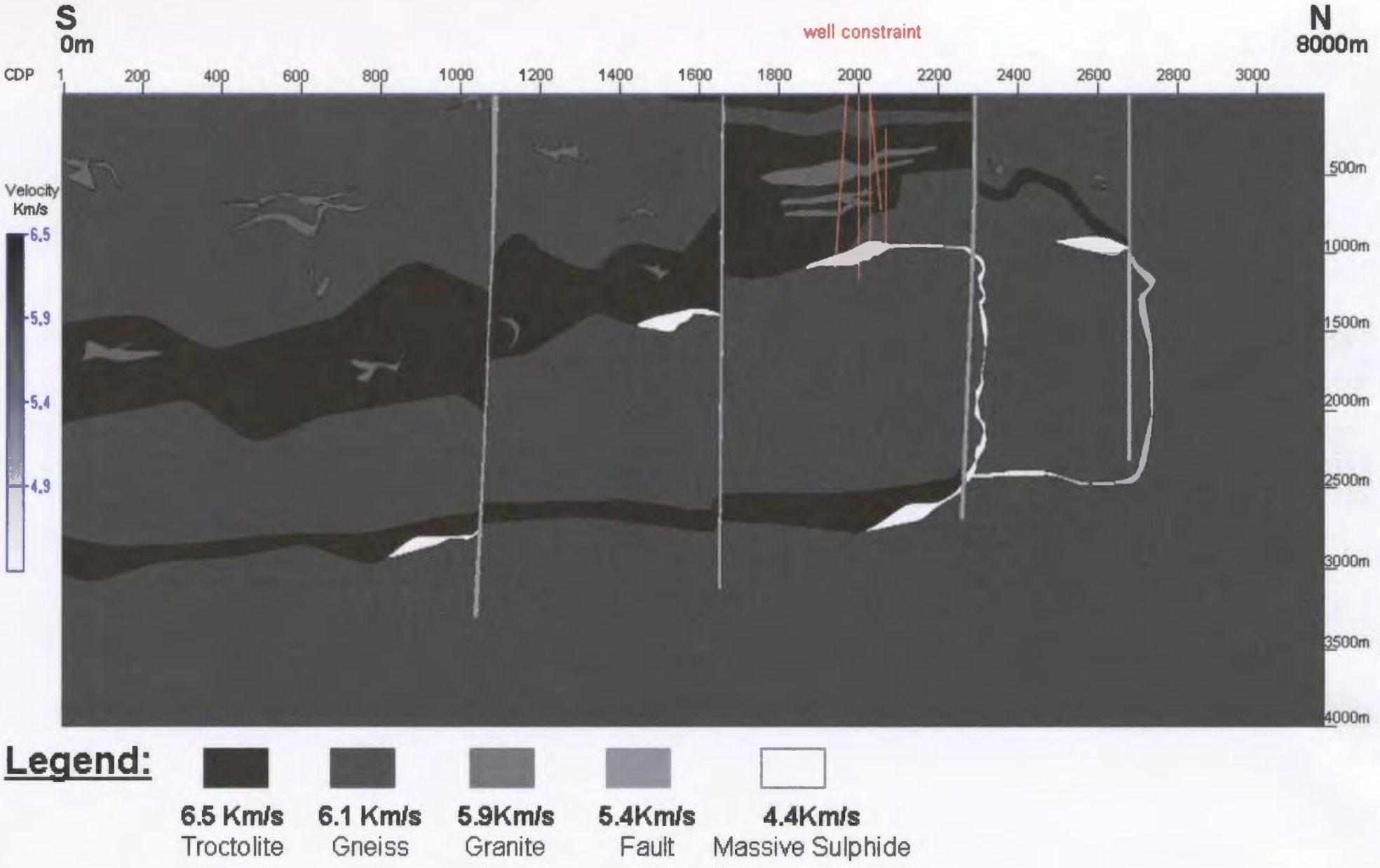


Figure 3.3.1.1: Illustrates the simplified model of the Eastern Deeps area that was used to help fine tune acquisition parameters for a 2-D survey planned to delineate the structural setting of the Voisey's Bay deposit. Figure 3.2.2 shows the location of this cross-section.

Table 3.3.1.1: Constant velocities for the various rock types and faults used in Figure 3.3.1 which are the mean velocity values for the Eastern Deeps zone determined in Section 2.3.2.

| Rock Type | Constant Velocity (m/s) |
|---|---|
| Troctolite | 6500 |
| Granite | 5900 |
| Massive Sulphide | 4400 |
| Gneiss | 6100 |
| Faults | 5400 |

- **3.3.2 Heterogeneity Model**

Models that incorporate geologic heterogeneity at a variety of scales are becoming increasingly popular as opposed to the conventional layer-cake Earth model due to the fact that seismologists want to extract as much information as possible from seismic data (Hurich, 2004). Hurich (2006) has noted that one of the interesting developments from extracting heterogeneity information from seismic reflection data has been the recognition of the potential for mapping nonreflective intrusive bodies and the plumbing systems for shallow intrusions. This is achieved by mapping the difference in the scattering response of the different fabrics in the velocity model (Hurich, 2006). Armed with this knowledge it was decided that a heterogeneity model should be developed to investigate whether or not utilizing this seismic technique will aid in the delineation of the magmatic plumbing system at Voisey's Bay.

In order to incorporate realistic geologic heterogeneity into the simplified model it was first necessary to analyze the structural properties of the rocks in the Eastern Deeps zone. VBNC provided a structural database for the Eastern Deeps zone. From this database, it was evident that there was a strong foliation in the orthogneisses but no fabric in the rest of the rocks. As a result, only the foliation of the orthogneisses was

incorporated into the heterogeneity model. Figure 3.3.2.1 shows the distribution of surface foliation orientation measurements for the orthogneisses in the Eastern Deeps zone.

Stereographic analysis of these orientation values demonstrates that there is one population that fluctuates +/- 30° from vertical (Figure 3.3.2.2). The black squares in Figure 3.3.2.2 represent the poles to the planes for each of the foliation values. These black squares are mostly congregated near the primitive circle thereby revealing that the majority of the planes are steeply dipping. A mean orientation of 70/239 was determined for the foliation planes. Various orientations were considered for acquisition of the model profile. In this particular case we chose to use a northeast-southwest imaging plane where a true dip of 70°S was determined for the foliation in the imaging plane of the model instead of some shallow apparent dip. This steep value was used such that the worst case scenario for imaging could be tested.

A vertical correlation length of 500 m and a horizontal correlation length of 100 m were applied to the gneisses to simulate the structural flattening associated with the foliation. Gneisses are typically layered, generally with alternating felsic and mafic layers. As a result, their velocity range can be considered to be bimodal to the first order. The velocity distribution in the gneiss reflects the assumption of a bimodal lithology. From the histogram for the gneisses in the Eastern Deeps zone in Appendix A it is apparent that there is a range of velocities from 5900-6300 m/s. Therefore, 5900 m/s was used as the low velocity and 6300 m/s was used as the high velocity in the bimodal

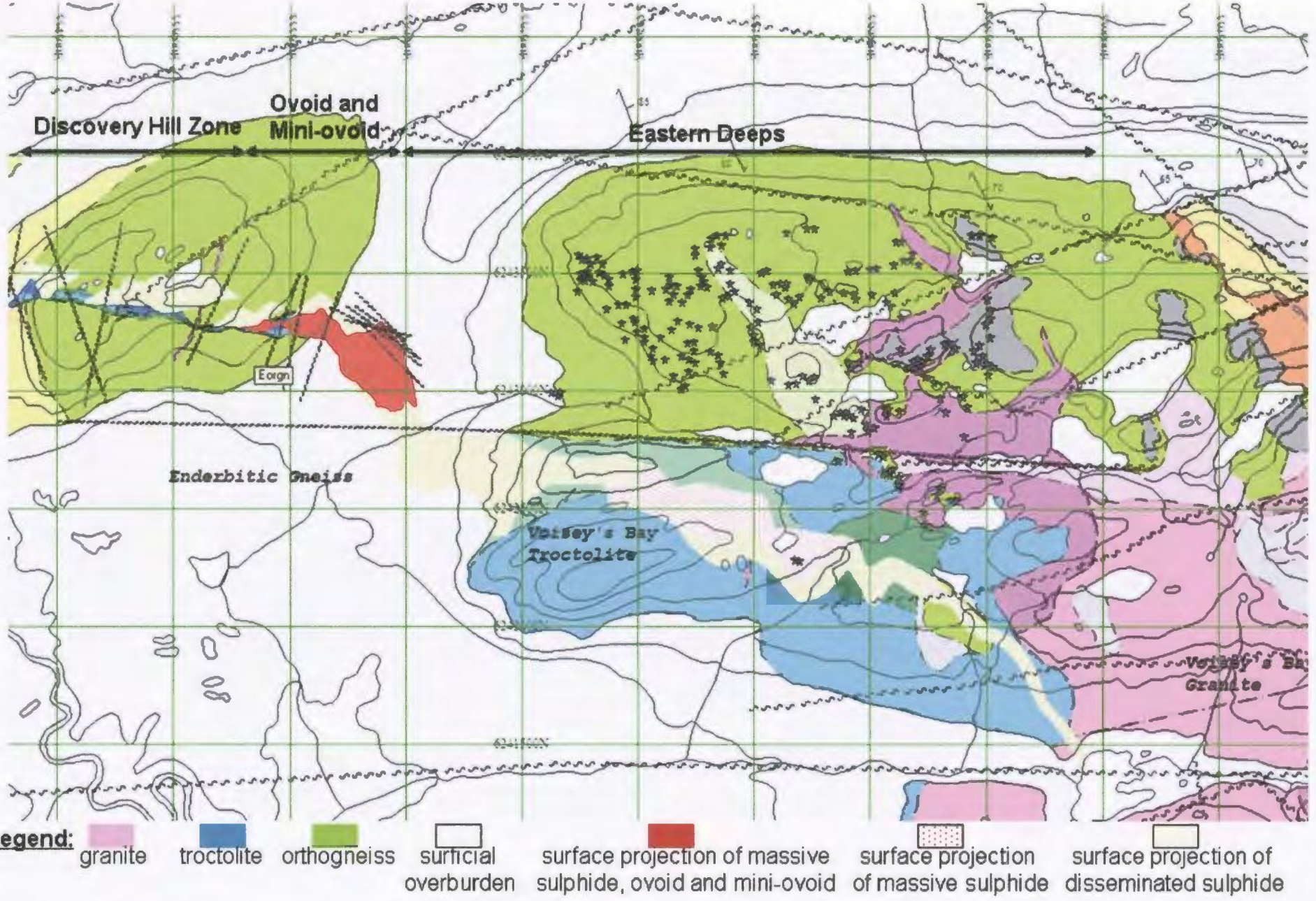


Figure 3.3.2.1: Map illustrating the sampling of the foliation values for orthogneiss in the Eastern Deeps zone. The dark blue stars represent the location of the foliation values. (Modified from VBNC).

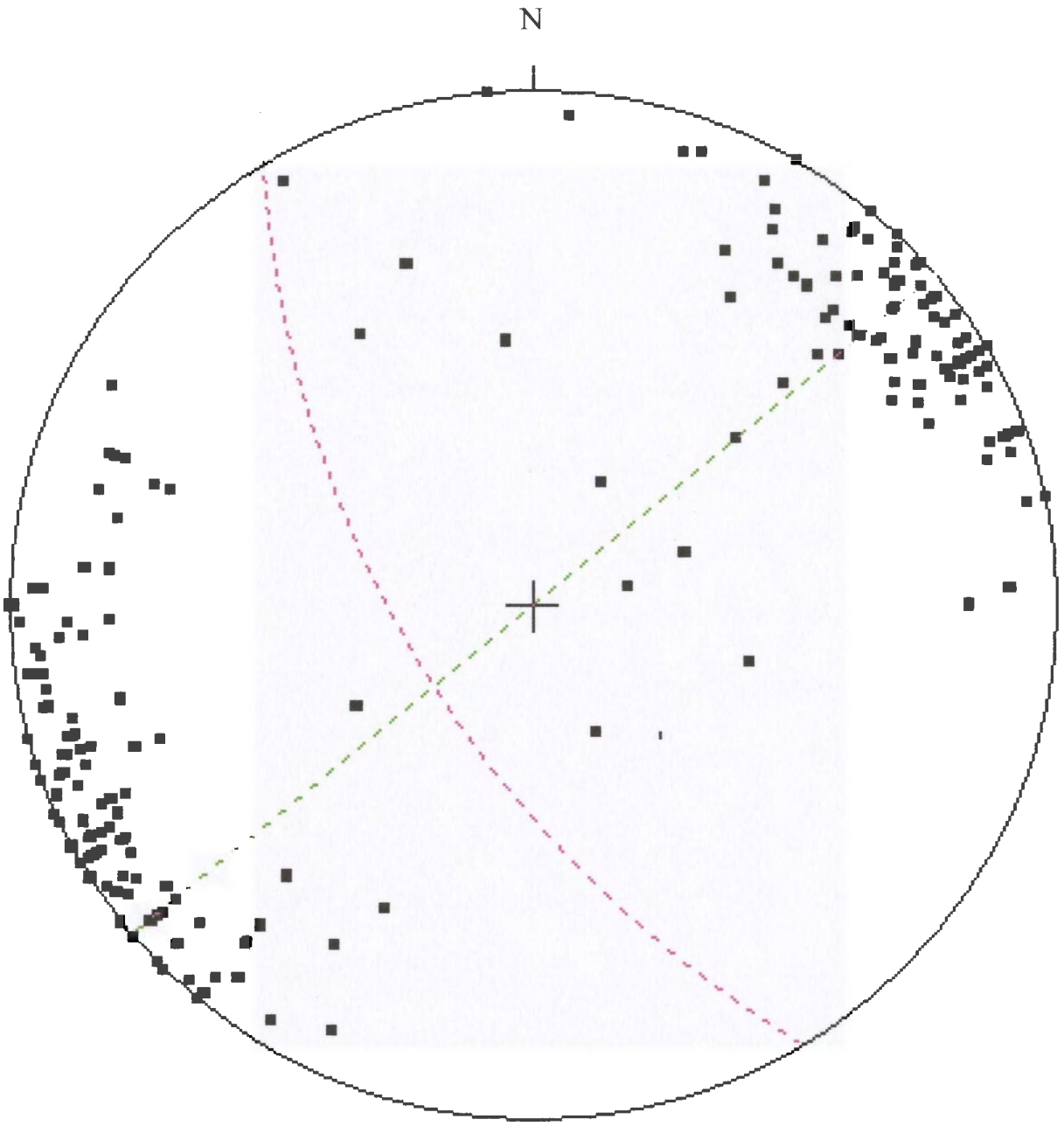


Figure 3.3.2.2: This is a stereogram of foliation for the Eastern Deeps orthogneisses. The black points are poles to the planes. The purple dotted line is the mean orientation (70/239). The green dotted line is the chosen northeast-southwest imaging plane (90/140).

distribution. Figure 3.3.2.3 shows the heterogeneity model used to further fine tune the acquisition and processing parameters for the planned 2-D survey in Voisey's Bay.

- **3.3.3 Velocity Gradient Model**

Surface-surface seismic tomography may be appropriate for delineating the magmatic plumbing system at Voisey's Bay. In order to estimate the depth of penetration of the turning rays in the model a velocity gradient model was developed. Although the model section was originally constructed for the Eastern Deeps zone a similar geologic and structural setting is expected in the Reid Brook zone. Therefore, as a first approximation, this model was also used for the Reid Brook zone. Velocity gradients were determined for both the orthogneisses and the paragneisses, which are located in the Eastern Deeps and Reid Brook zones respectively, using velocity data derived at room temperature and hydrostatic confining pressures ranging from 10-100 MPa for the Voisey's Bay area (Salisbury and Iulucci, 2006). A pressure of 100 MPa corresponds to 4000 m depth, which is the maximum depth of the model. A power trendline ($y = Ax^b$) was fit to the velocity data to determine a non-linear velocity gradient for both the orthogneisses and the paragneisses (Figures 3.3.3.1-3.3.3.3). A program was created in Seismic Unix to only apply the b value (i.e., non-linear velocity gradient) of the power trendline equation to the model. A value of b = 0.027 was used for the orthogneisses (Figure 3.3.3.1) and a value of b =0.044 was used for the paragneisses, which was simply the average of the two b values from Figures 3.3.3.2 and 3.3.3.3. Figures 3.3.3.4 and 3.3.3.5 illustrate the effect

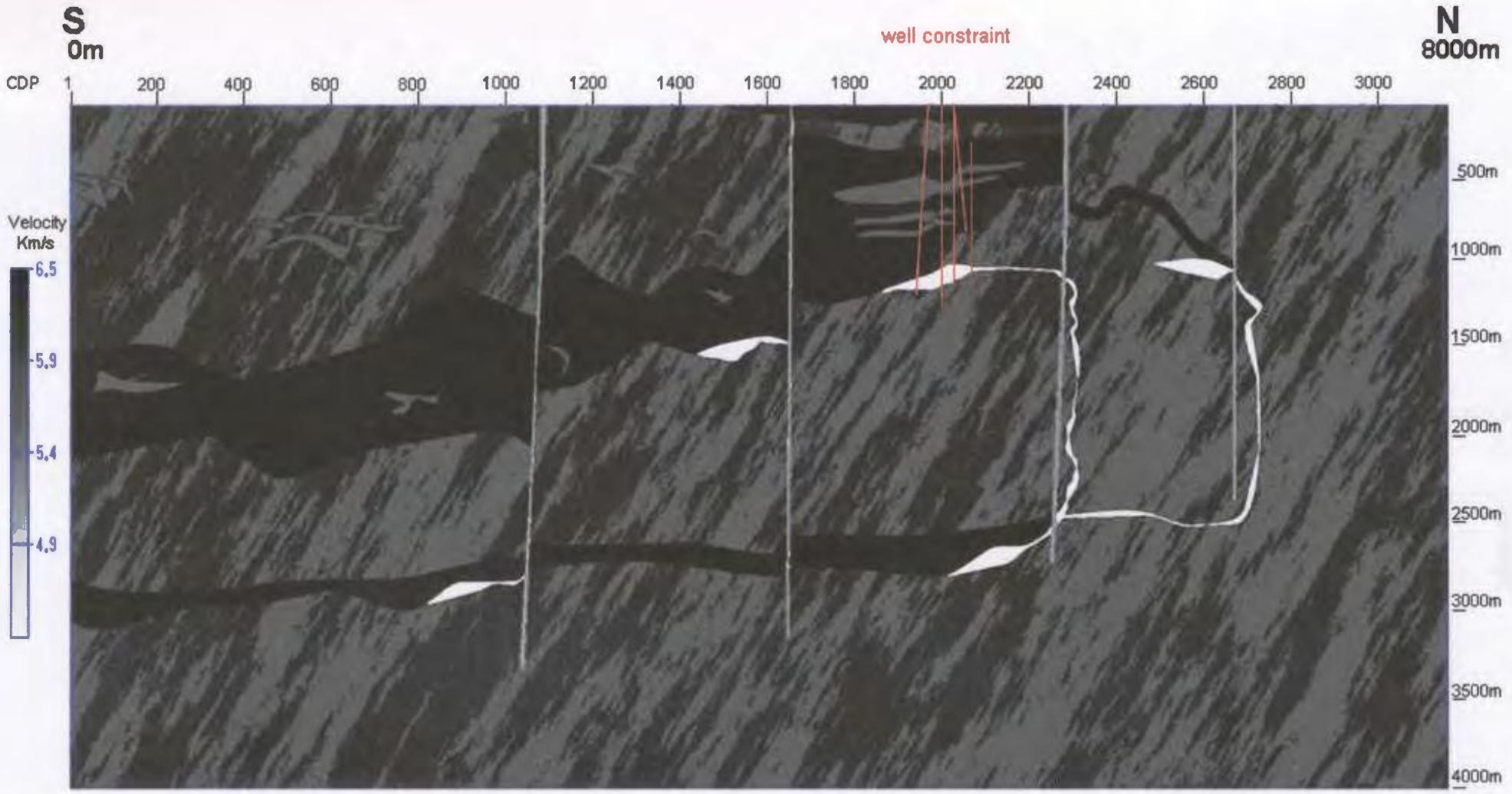


Figure 3.3.2.3: Illustrates the heterogeneity version of the model that was used to further help fine tune the acquisition and processing parameters for a 2-D survey in a hardrock environment with mineralization.

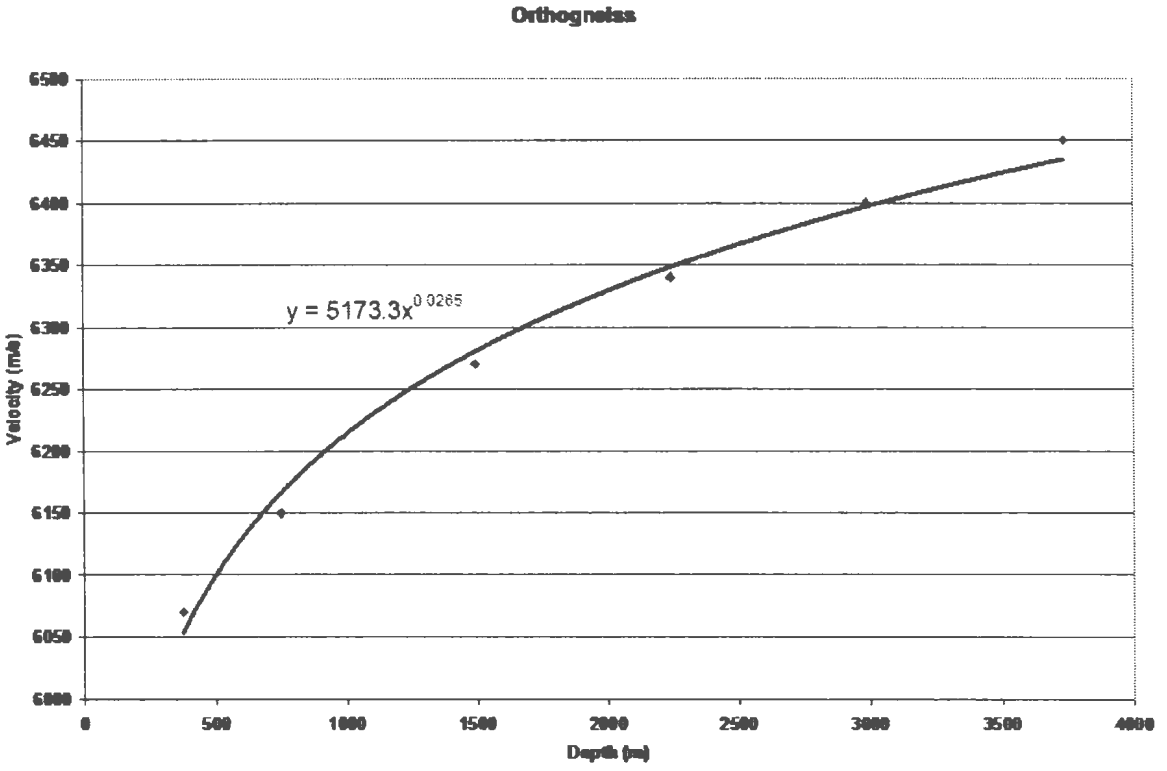


Figure 3.3.3.1: Illustrates the non-linear velocity gradient for the orthogneisses in the Eastern Deeps zone.

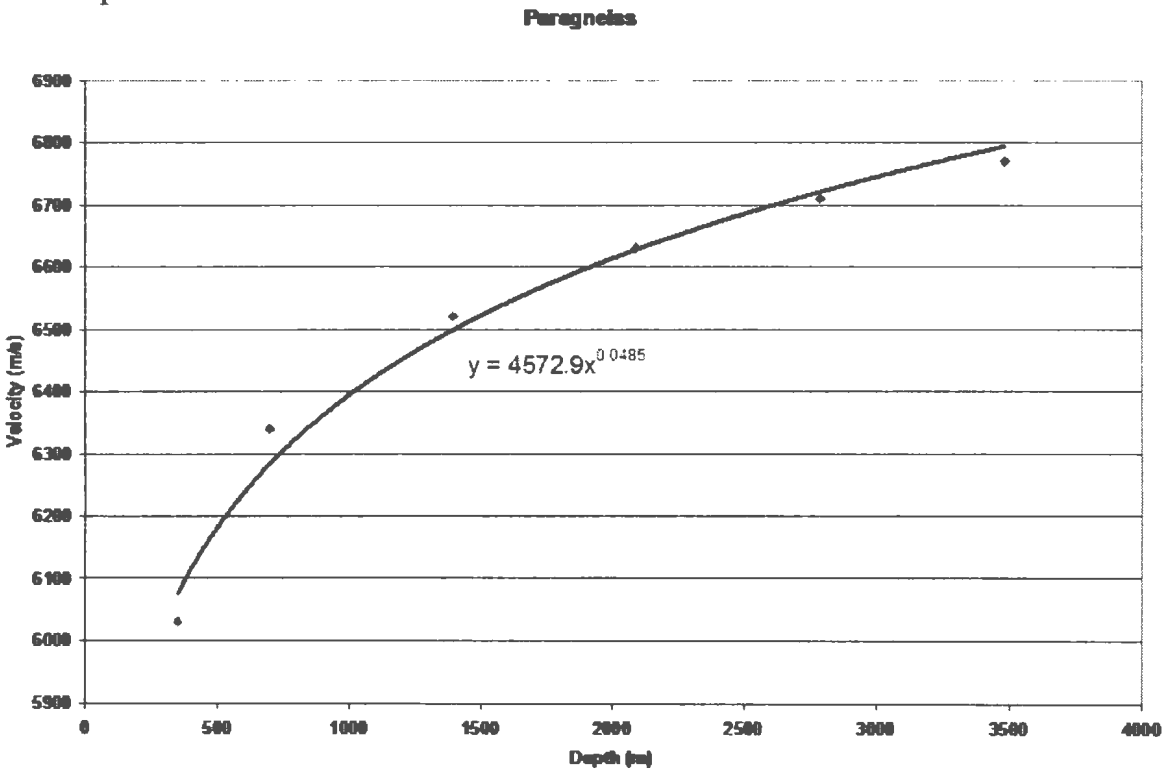


Figure 3.3.3.2: Illustrates one of the non-linear velocity gradients for the paragneisses in the Reid Brook zone.

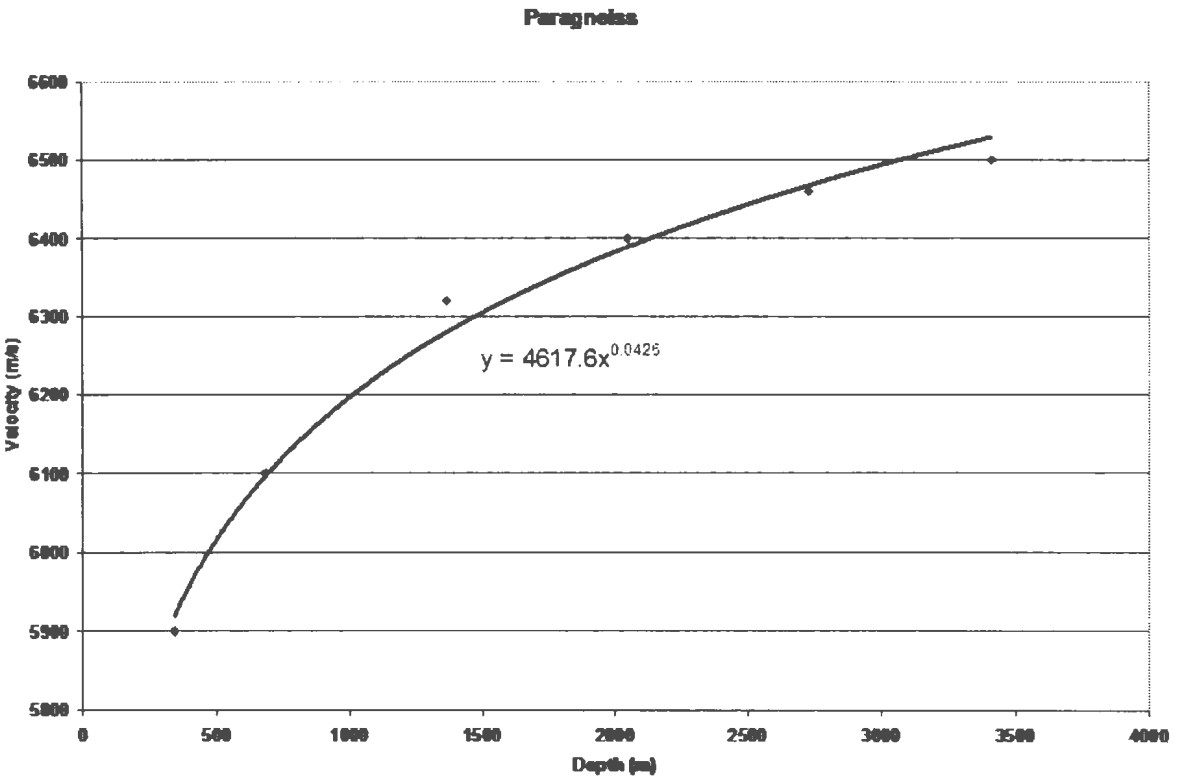


Figure 3.3.3.3: Illustrates another one of the non-linear velocity gradients for the paragneisses in the Reid Brook zone.

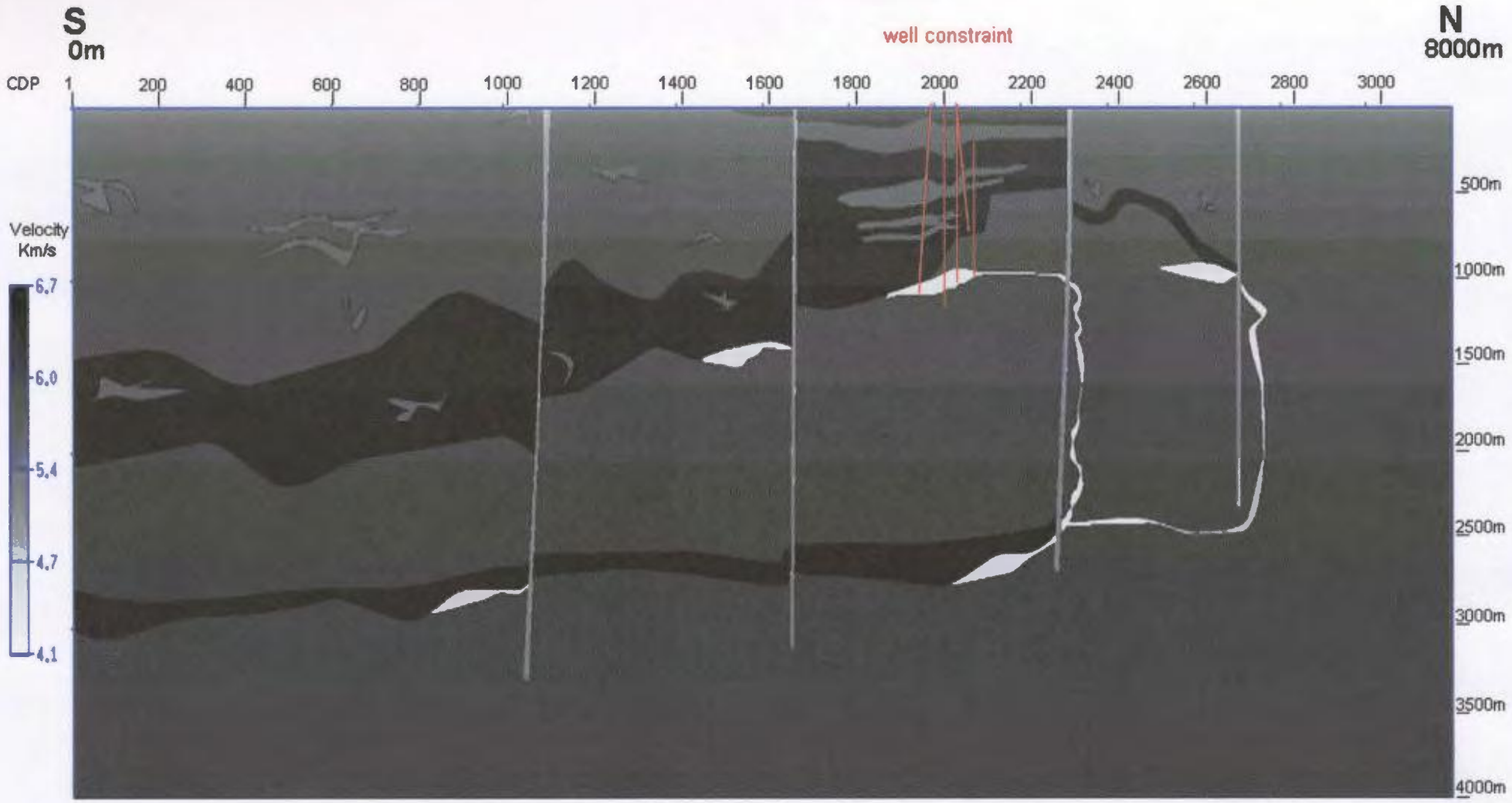


Figure 3.3.3.4: Illustrates the orthogneiss velocity gradient version of the model where a value of b = 0.027 was used.

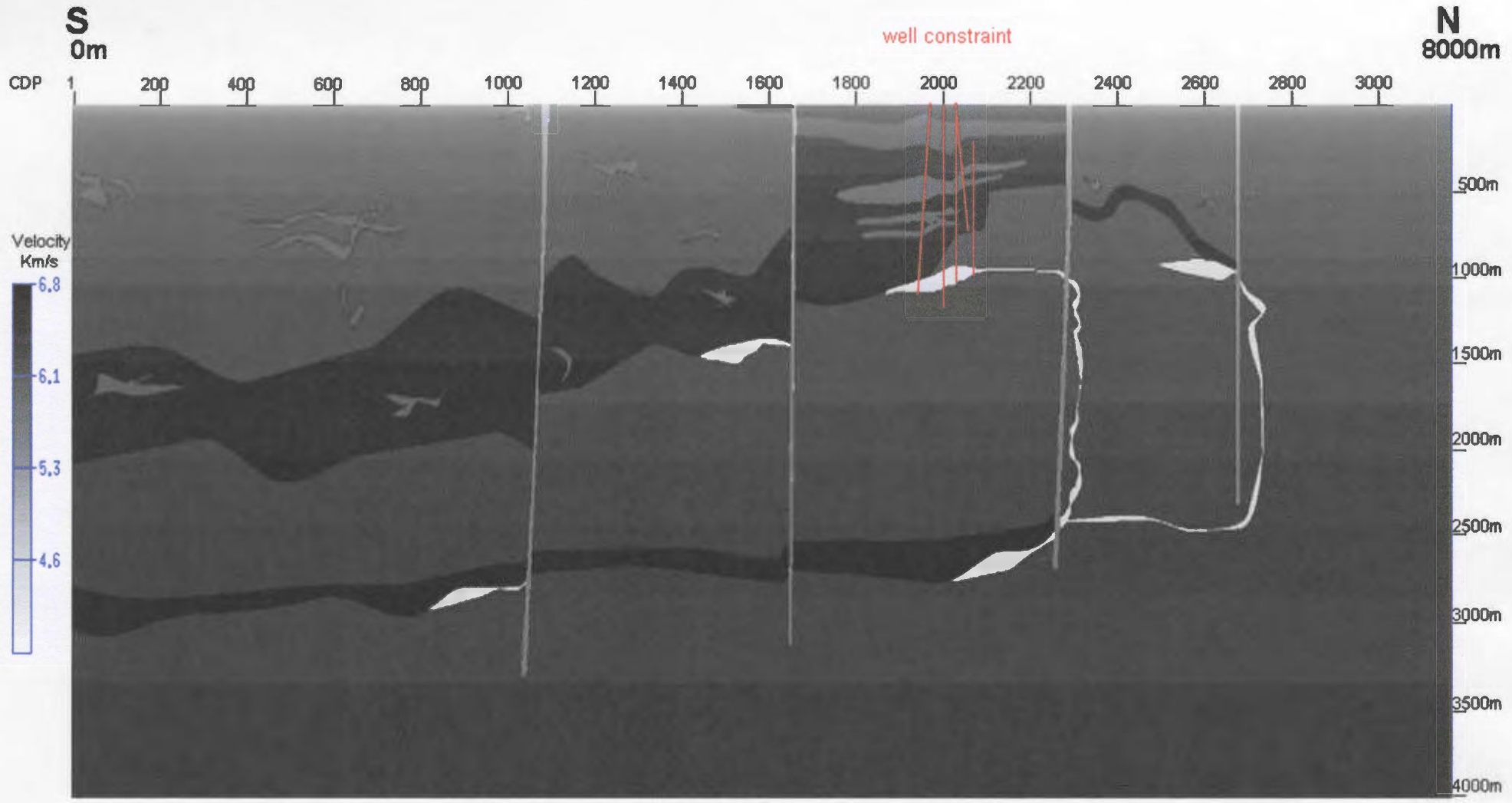


Figure 3.3.3.5: Illustrates the paragneisses velocity gradient version of the model where a value of b = 0.044 was used.

of the non-linear velocity gradients on the model for both the orthogneisses and the paragneisses respectively. It is important to note that the velocity gradients utilized in this model were purely for the orthogneiss and the paragneiss zones and were not associated with the weathering zone in any way.

### 3.4 Acquisition

The same acquisition parameters were used to acquire shot records for each of the models. This allows comparison of their increasingly complex responses (Section 3.6). The data were generated using a 2-D finite-difference program. The 2-D survey was set-up such that both narrow- and wide-aperture data were collected simultaneously. The first shot was located at 0 m and thereafter every 10 m for a total of 800 shots (Figure 3.4.1). The first receiver was also located at 0 m with a receiver spacing of 5 m (Figure 3.4.1). The receivers remained stationary while the shot was incremented sequentially thereby creating an asymmetric spread with both narrow- and wide-aperture data.

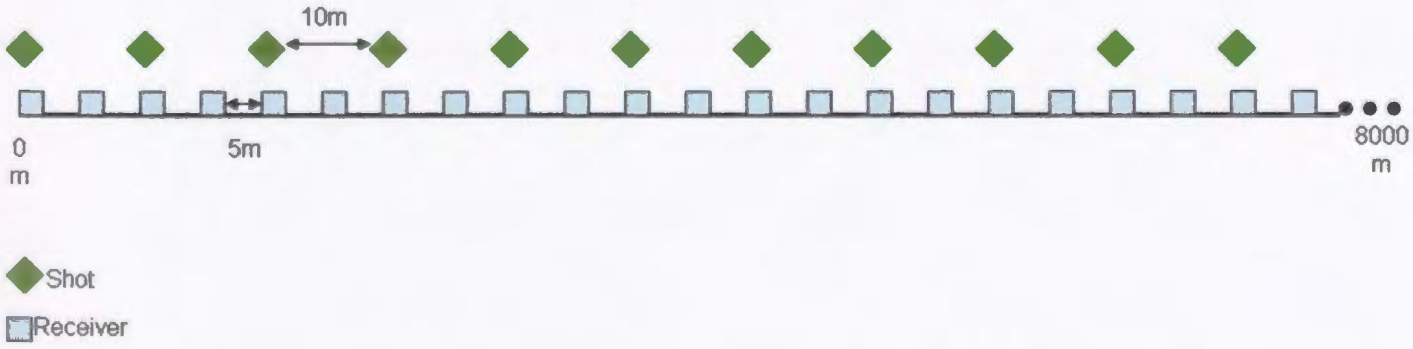


Figure 3.4.1: Diagram illustrating the acquisition parameters used for each 2-D synthetic survey. Refer to Figure 3.3.1.1 for location of 0 m on the model.

The maximum sampling two-way travel time was set at 1.5 s. This was determined from knowing the two-way depth (8000 m) and the average velocity for the model (5700 m/s), which was then substituted into the following equation to determine the maximum sampling two-way travel time:

$$T = \frac{D}{V},$$

where T is maximum sampling two-way travel time, D is two-way depth, and V is the average velocity. The sample rate was set to be 4 ms thus the number of samples was determined to be 375 from the following equation:

$$nt = \frac{T}{dt},$$

where nt is the number of samples, T is the maximum sampling two-way travel time, and dt is the sample rate. The maximum frequency was set to be 90 Hz and was determined by obeying the condition that there must be 10 grid nodes per shortest wavelength in order to maintain the numerical stability of the acoustic finite difference solution. Since the grid node spacing was 5 m the shortest wavelength must be 50 m. Therefore,

$$f_{\max} = \frac{V}{\lambda},$$

where $f_{max}$ is the maximum frequency, V is the lowest velocity in the model, and $\lambda$ is the shortest wavelength.

Theoretically, for an interface to be identified as a specular reflection in the 2-D model it must be at least as wide as the Fresnel Zone, if not, it appears as a diffractor. The width of the Fresnel Zone is determined by:

$$w^2 = 2d\lambda + \frac{\lambda^2}{4},$$

where w is the width of the Fresnel Zone, d is the depth below the source, and λ is the wavelength of the source. Using the fact that the shortest wavelength was determined to be 50 m, it was possible to establish Fresnel Zone widths for various depths within the 2-D model (Table 3.4.1).

Table 3.4.1: Displays the width of the Fresnel Zone for various depths in the 2-D model based on λ = 50m.

| Depth (m) | Width of Fresnel Zone (m) |
|---|---|
| 500 | 225 |
| 1000 | 317 |
| 1500 | 388 |
| 2000 | 448 |
| 2500 | 500 |
| 3000 | 548 |
| 3500 | 592 |
| 4000 | 633 |

Referring back to the simplified 2-D model (Figure 3.3.1.1) it is evident that examples exist of geologic bodies and inclusions that are either narrower or wider than the width of the Fresnel Zone corresponding to their depths. As a result, both specular reflections and diffractions will occur in the synthetic dataset. This wide variety of geologic body size was purposely incorporated into the 2-D model to aid in the simulation of the real complexity of hardrock environments.

## 3.5 Seismological Data Processing

- **3.5.1 Introduction**

Conventional processing schemes generally involve the following steps for seismic data processing: preprocessing, velocity analysis and stack, and migration (Figure 3.5.1.1). This processing scheme will be termed Scheme A for clarity purposes. On the other hand, the processing scheme for seismic data collected in hardrock environments tends to deviate from this conventional processing scheme (Figure 3.5.1.2; Eaton et al., 2003a). This processing scheme will be termed Scheme B for clarity purposes. If adequate, scheme A is favored over Scheme B simply because it is inexpensive and it does not require detailed knowledge of velocities. However Scheme B may be favored because it attempts to deal with well-known issues related to processing seismic data from hardrock environments, such as imaging specular reflections and diffractions simultaneously. The synthetic seismic data generated for both the simplified and heterogeneity models were processed using both Schemes A and B to assess the importance of tailoring the processing scheme to the data and not just applying a 'widely-used' scheme. The purpose of a processing scheme is to improve the quality of the data, thereby aiding in its interpretation.

- **3.5.2 Scheme A**

- Pre-processing

The first step in preprocessing was to input the raw data into the computer in a convenient format (i.e. seg-y). Afterwards, spectral analysis was performed on the raw data to determine the parameters for a bandpass filter. An Ormsby minimum phase bandpass filter with parameters 8-20-80-120 was applied to both the simplified and heterogeneity models to enhance the signal quality of the data (Figures 3.5.2.1 and

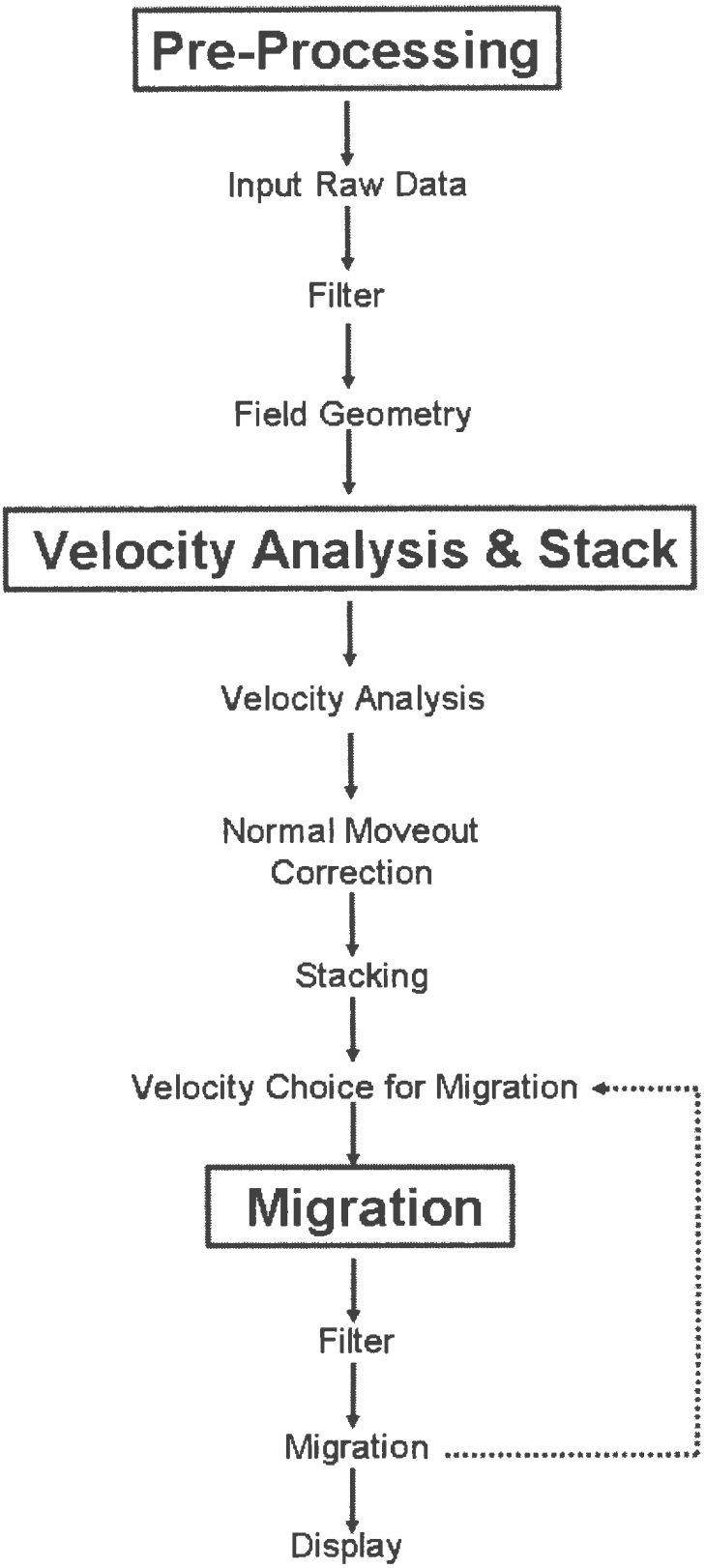


Figure 3.5.1.1: Scheme A: example of a widely-used seismic data processing scheme. Dashed arrow represents a phase in the processing sequence where it may be necessary to return and repeat an earlier process.

3.5.2.2). A top mute was also applied to remove the direct wave so that only the specular reflections and diffractions were focused upon (Figures 3.5.2.3 and 3.5.2.4, respectively).

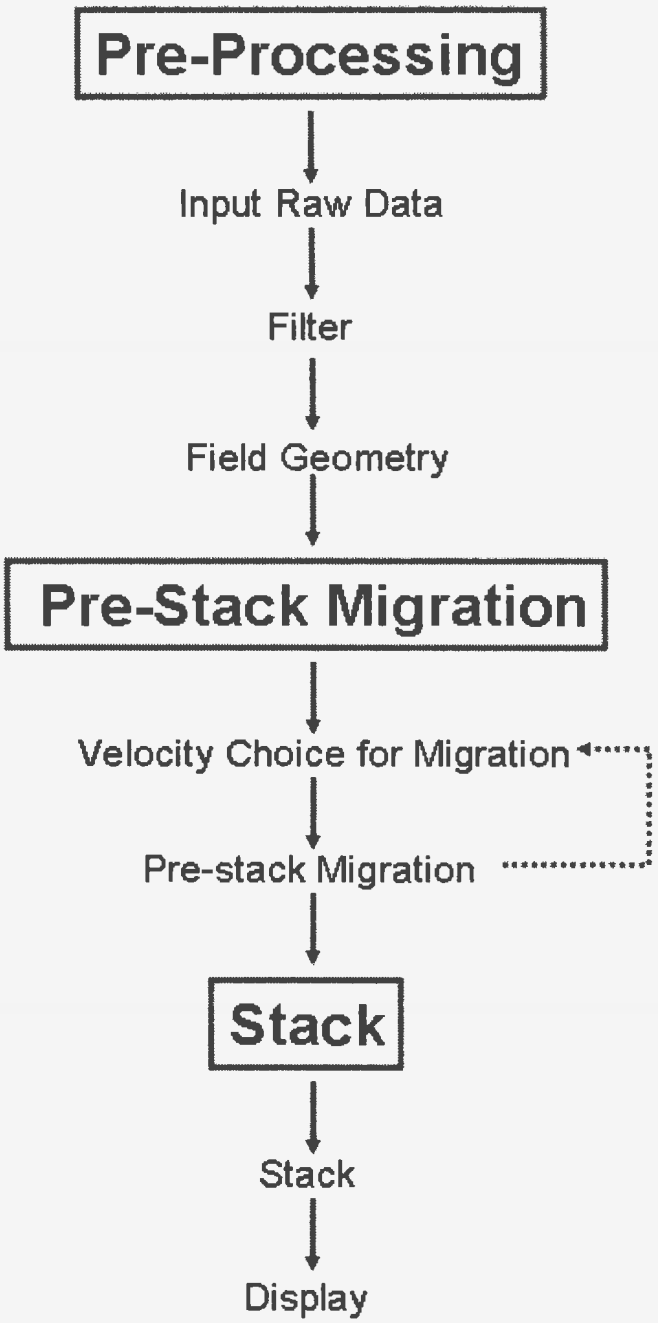


Figure 3.5.1.2: Scheme B: tailored seismic data processing scheme. Dashed arrow represents a phase in the processing sequence where it may be necessary to return and repeat an earlier process.

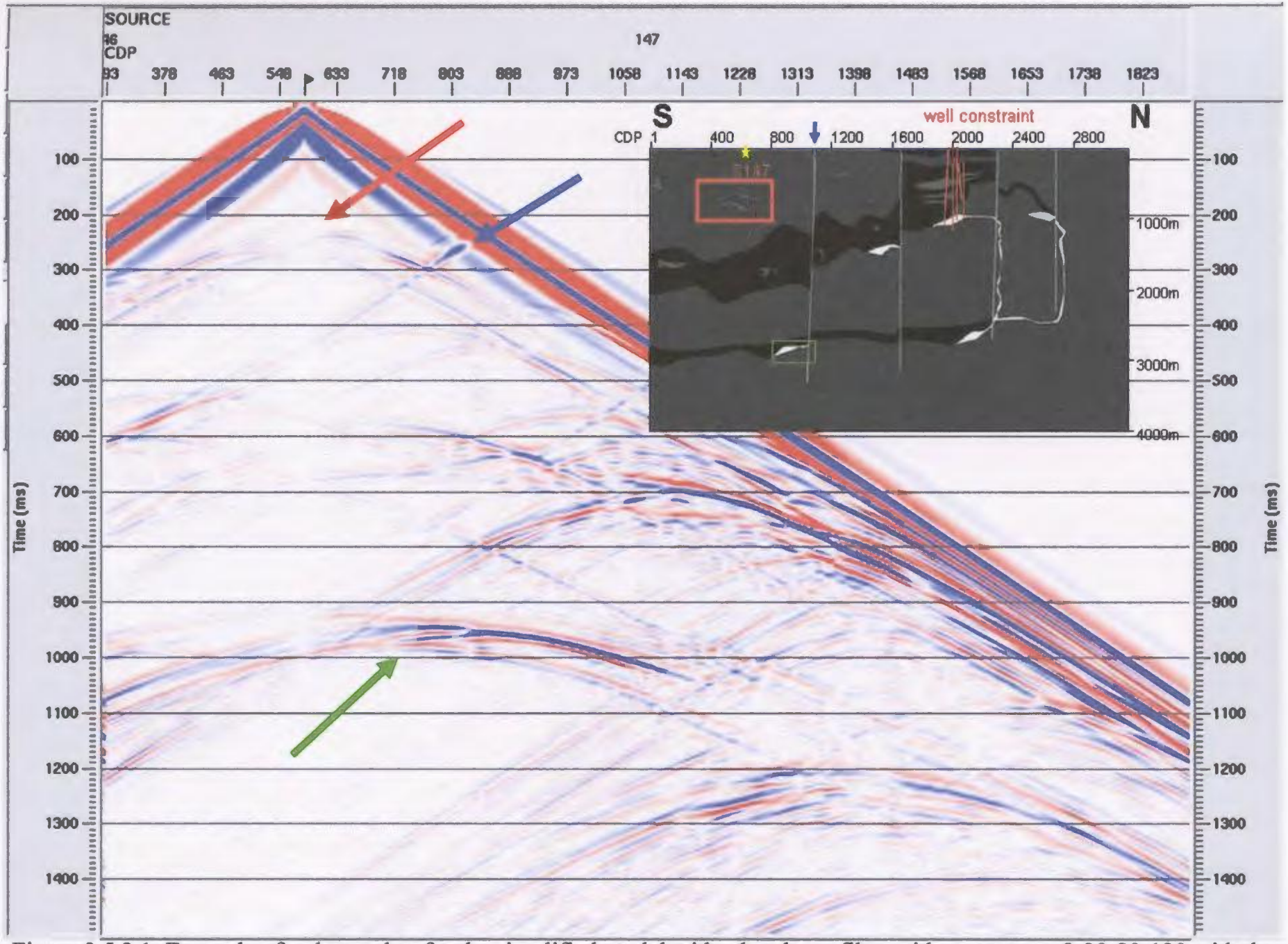


Figure 3.5.2.1: Example of a shot gather for the simplified model with a bandpass filter with parameters 8-20-80-120 with the objects of interest identified by the red (granite body), green (orebody) and blue (fault) arrows. Inset shows where shot gather is located along the cross-section and illustrates the objects of interest.

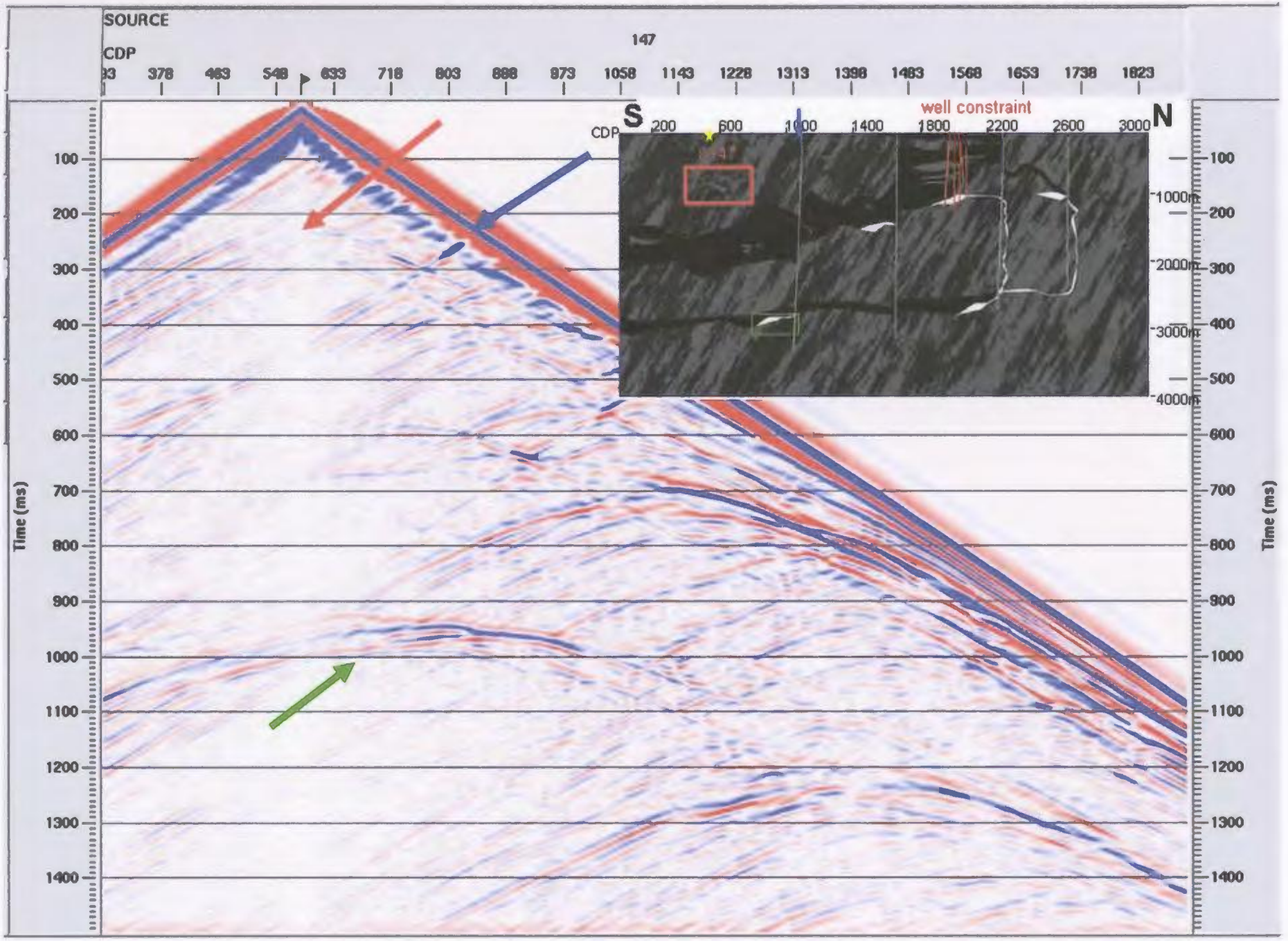


Figure 3.5.2.2: Example of a shot gather for the heterogeneity model with a bandpass filter with parameters 8-20-80-120 with objects of interest identified by the red (granite body), green (orebody), and blue (fault) arrows. Inset shows where shot gather is located along the cross-section and illustrates the objects of interest.

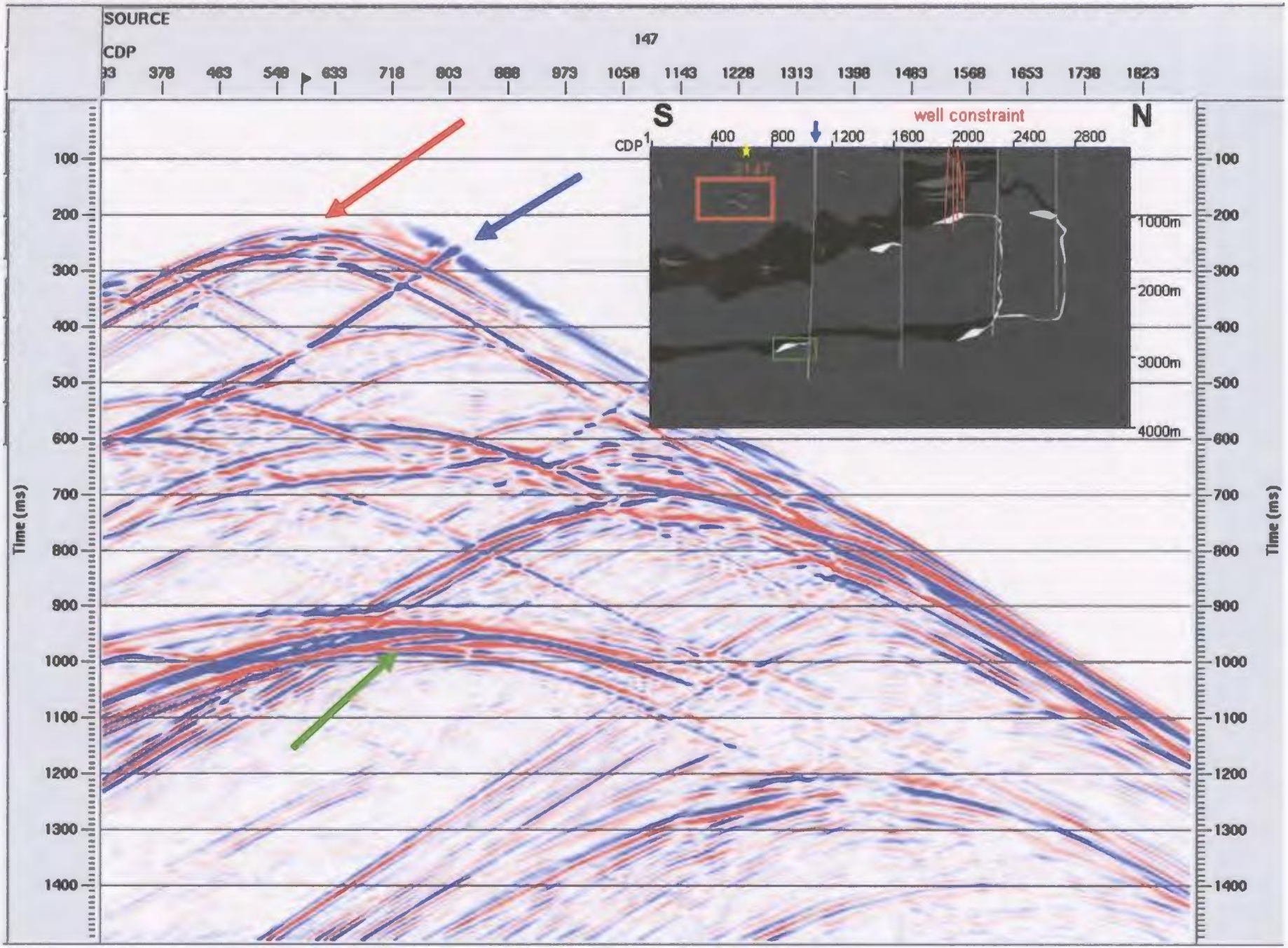


Figure 3.5.2.3: Example of a shot gather for the simplified model with a bandpass filter with parameters 8-20-80-120 and a top mute applied with the objects of interest identified by the red (granite body), green (orebody), and blue (fault) arrows. Inset shows where shot gather is located along the cross-section and illustrates the objects of interest.

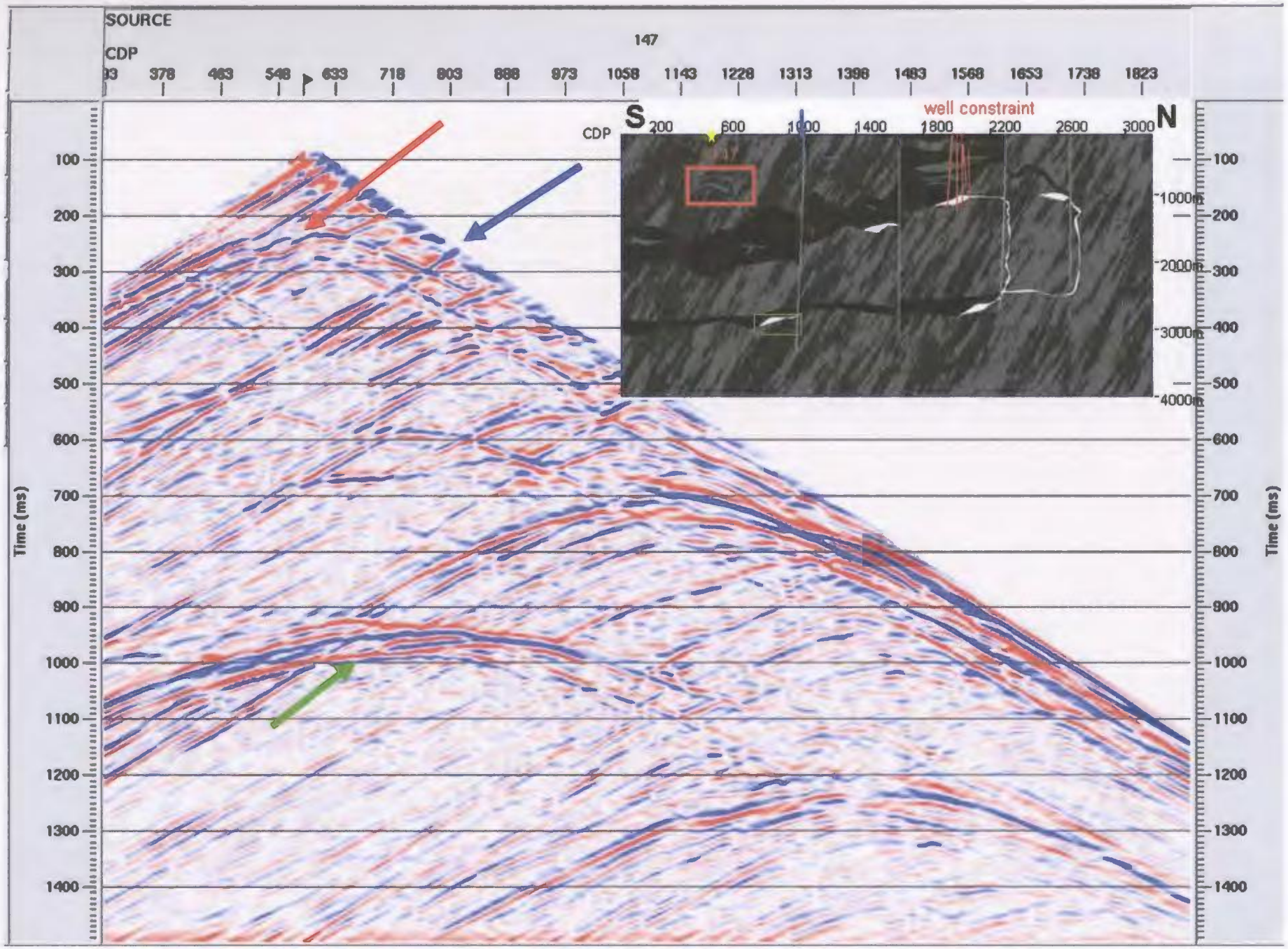


Figure 3.5.2.4: Example of a shot gather for the heterogeneity model with a bandpass filter with parameters 8-20-80-120 and a top mute applied with objects of interest identified by the red (granite body), green (orebody), and blue (fault) arrows. Inset shows where shot gather is located along the cross-section and illustrates the objects of interest.

The filter parameters were kept broad such that as much signal as possible was retained during this early stage of processing. Finally, the field geometry was then incorporated with the seismic data using Promax's 2-D land geometry spreadsheet. The geometry was applied so that the data could be sorted from the source-receiver offset domain to the common depth point (CDP) domain.

- Velocity Analysis and Stack

Velocity analysis was performed on selected CDP gathers using typical semblance peak plots. The main objective in applying the velocity analysis was to determine the amount of normal moveout that should be removed in order to maximize the stacking of the events. Output velocity analysis windows consisted of a semblance plot, an NMO corrected gather, a dynamic stack panel (which shows a representation of a stack generated by the current velocity pick), and a set of constant velocity stacks. It was difficult to perform the velocity analysis using semblance peak plots because of the presence of both specular reflections and diffractions. The peaks were not at all prominent and often did not fall on either a specular reflection or diffraction but rather somewhere in between (Figures 3.5.2.5 and 3.5.2.6). In spite of this, velocities were picked as well as possible for the prominent events. The velocity values rendered from the velocity analysis were then used in a normal moveout correction of the CDP gathers. In theory the offset effect should be removed from the traveltimes and therefore the primary reflection events should become flattened in time across the offset range for both the simplified and heterogeneity models. However, the reflections and diffractions

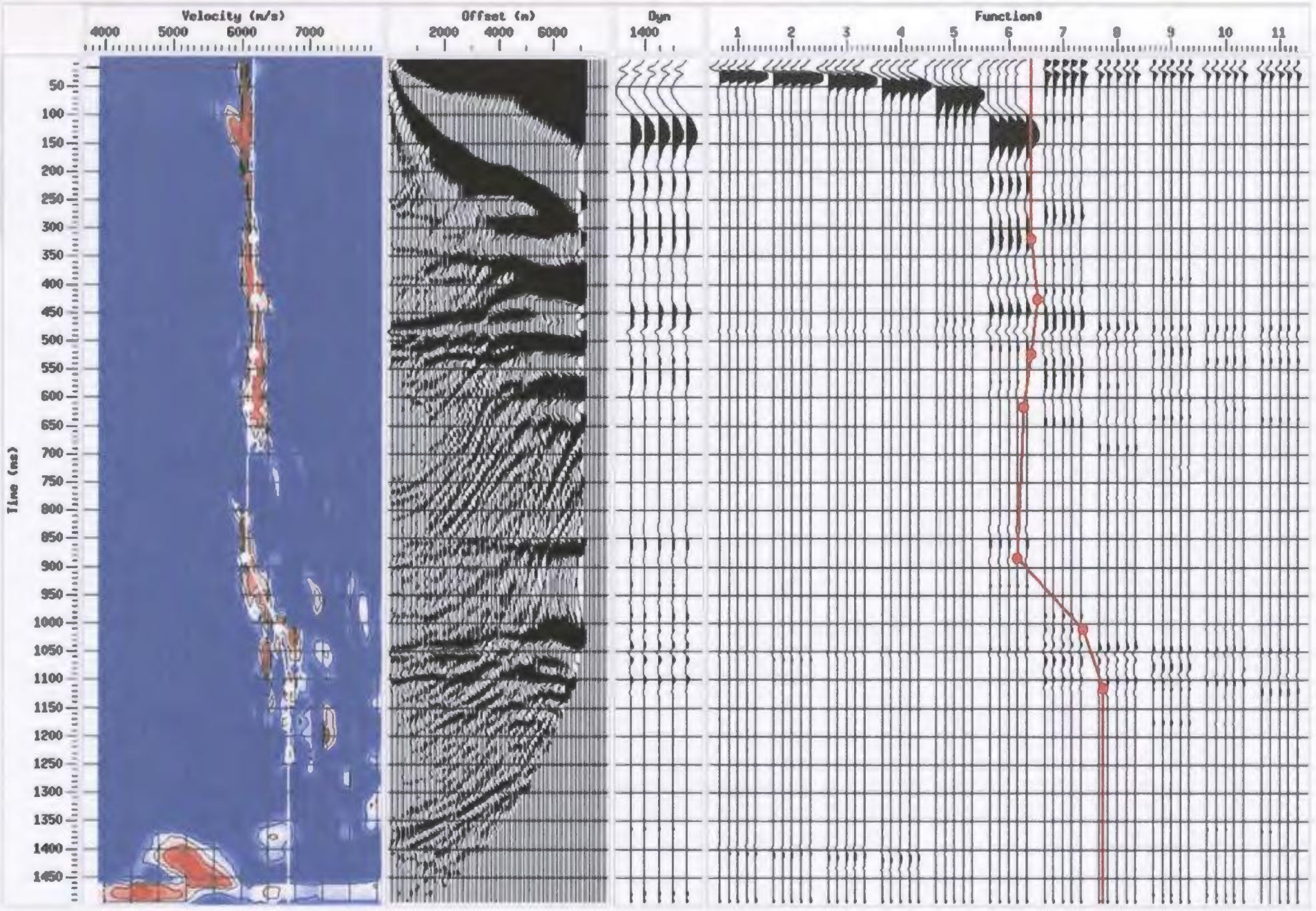


Figure 3.5.2.5: Represented are a semblance plot, an NMO corrected gather, a dynamic stack panel, and a constant velocity stack, which corresponds to the plots from left to right, respectively. These plots are for CDP 1401 for the simplified model illustrating the difficulty in picking velocities and events.

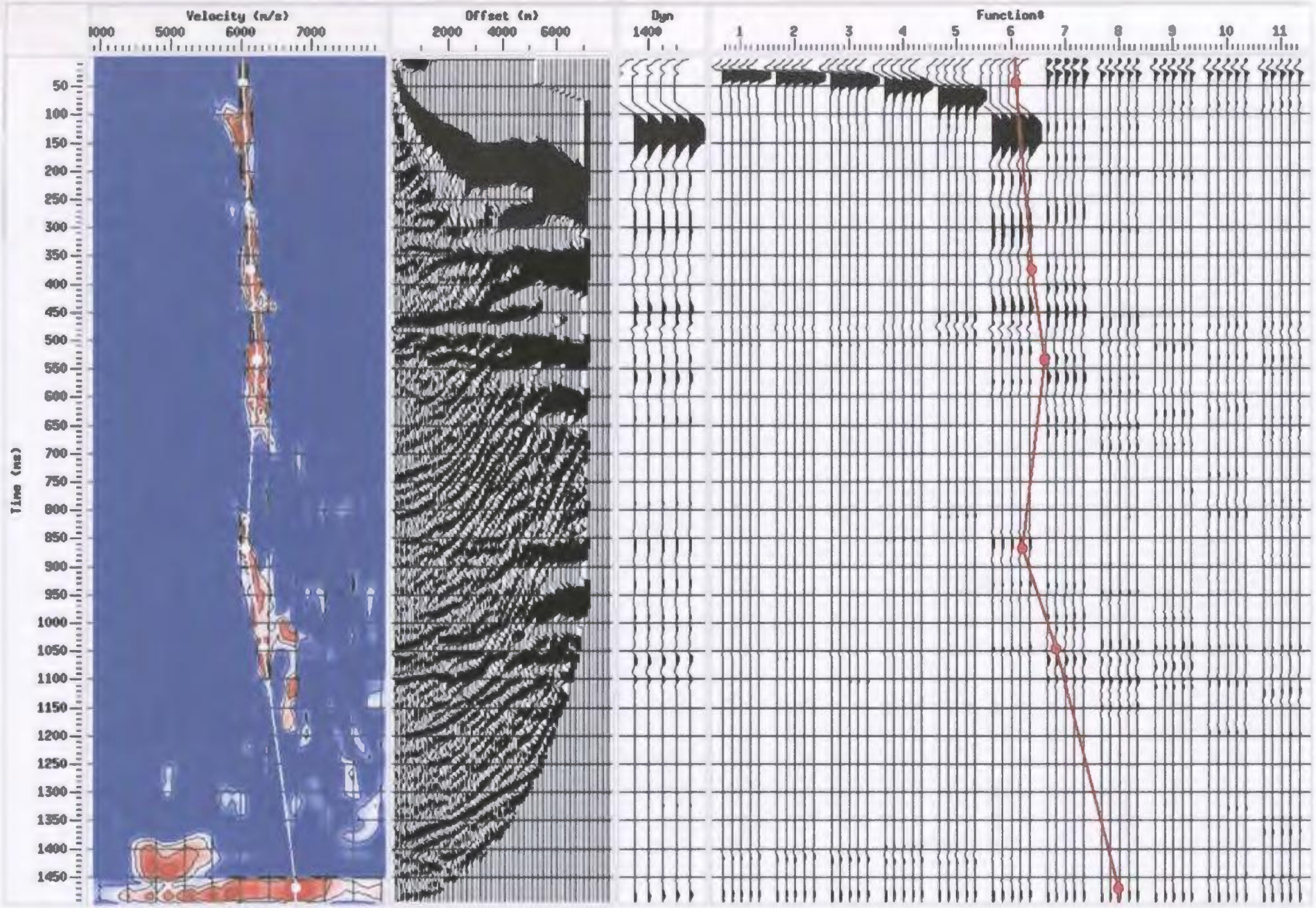


Figure 3.5.2.6: Represented are a semblance plot, an NMO corrected gather, a dynamic stack panel, and a constant velocity stack, which corresponds to the plots from left to right, respectively. These plots are for CDP 1401 for the heterogeneity model illustrating the difficulty in picking velocities and events.

had different stacking velocities and as a result it was impossible to pick every necessary velocity such that every event was stacked properly (Figures 3.5.2.7 and 3.5.2.8). Furthermore, Figures 3.5.2.7 and 3.5.2.8 illustrate that NMO was not suitable for this dataset as it did not flatten the majority of the events and the stretch resulting from the correction also destroyed a lot of the far offset information.

To further aid in the velocity analysis for both the simplified and heterogeneity models, constant velocity stacks were produced for velocities ranging from 4400-6600 m/s at an interval of 200 m/s (Appendices B-1 and B-2 respectively). A suitable interval velocity file was created from the constant velocity stacks by choosing the velocity that best stacked the significant events. This file was then converted to RMS velocities for the purposes of NMO correction and stacking using the velocity manipulation tool in Promax. Figures 3.5.2.9 and 3.5.2.10 again show that the stretch caused by the NMO correction destroyed much of the far offset information and that the NMO correction did not flatten the majority of the events. Comparison of Figures 3.5.2.7 and 3.5.2.8 with 3.5.2.9 and 3.5.2.10 show that there was very little, if any, improvement in the flattening of the primary events with the new velocity analysis. Considering this, the expected outcome of the stacking process is not encouraging.

One of the main downfalls of the conventional NMO correction is that it generates a stretch that increases with offset and decreases with zero-offset time (Perroud and Tygel, 2004). As a consequence, traces generally need to be muted after a certain offset and therefore large-offset traces often do not get incorporated into stacking. This is

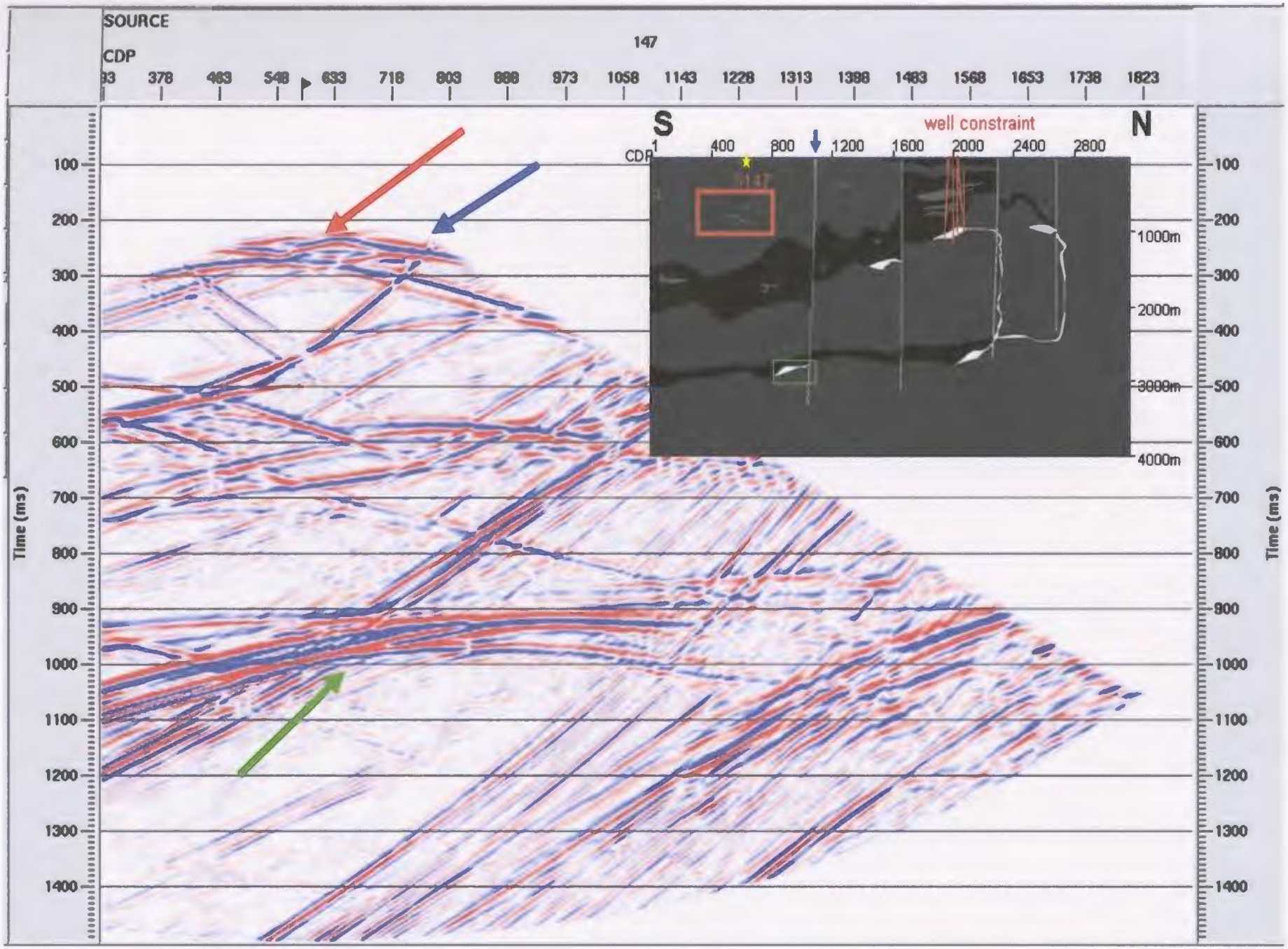


Figure 3.5.2.7: Example of a shot gather for the simplified model with NMO applied (where velocity values were determined by the semblance peak plots) and with objects of interest identified by the red (granite body), green (orebody), and blue (fault) arrows. Inset shows where shot gather is located along the cross-section and illustrates the objects of interest.

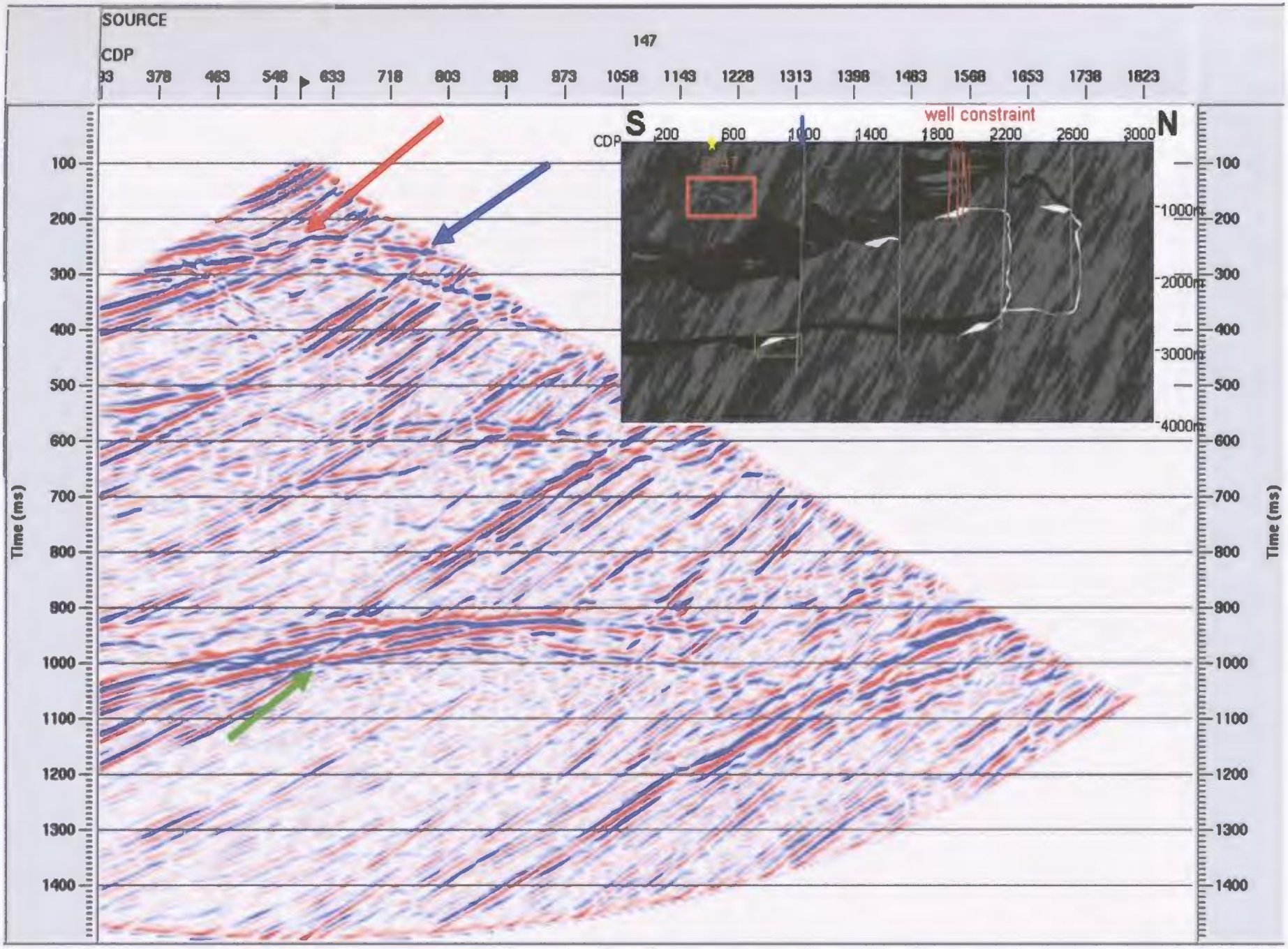


Figure 3.5.2.8: Example of a shot gather for the heterogeneity model with NMO applied (where the velocity values were determined by the semblance peak plots) and with objects of interest identified by the red (granite body), green (orebody) and blue (fault) arrows. Inset shows where shot gather is located along the cross-section and illustrates the objects of interest.

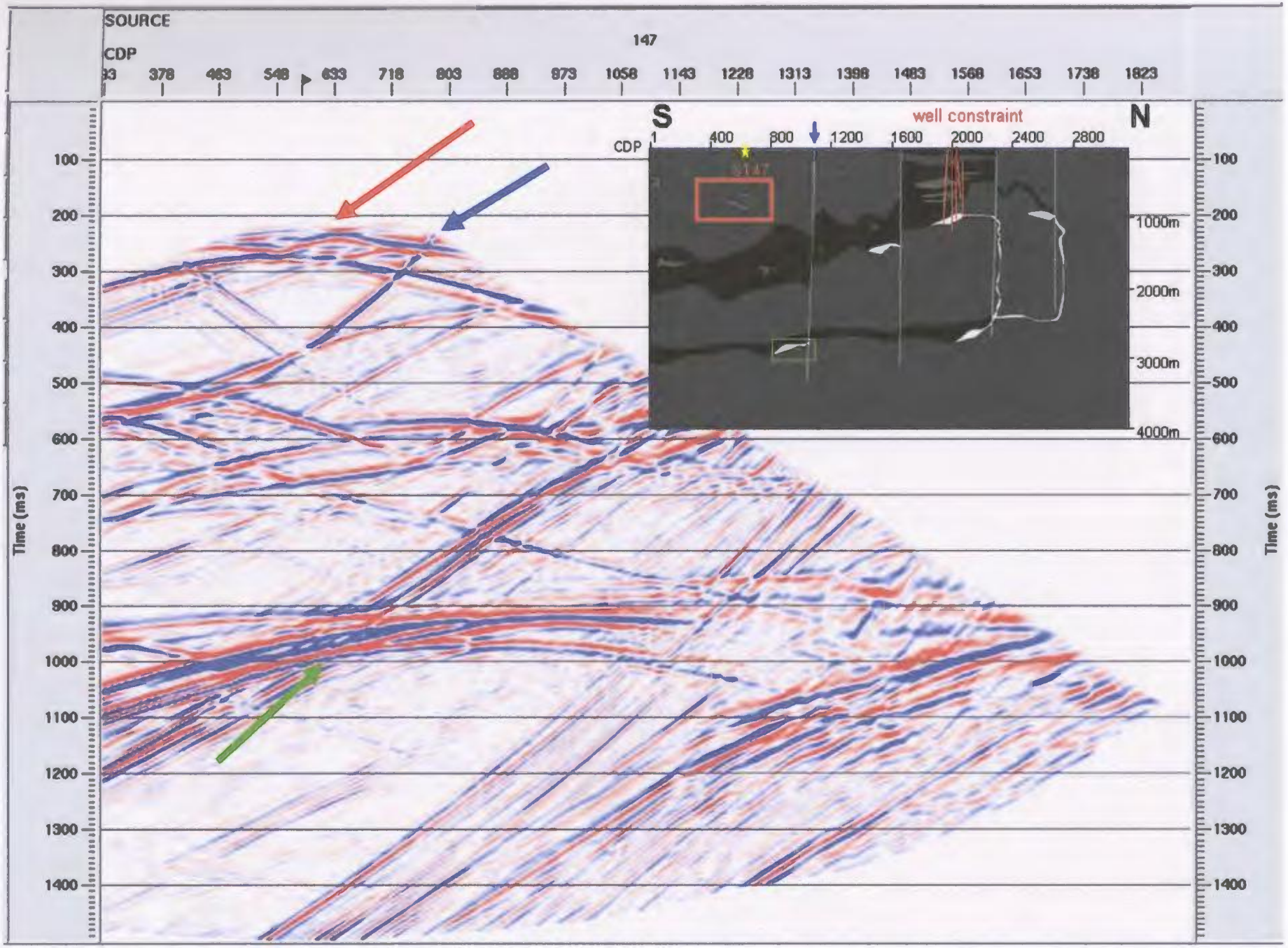


Figure 3.5.2.9: Example of a shot gather for the simplified model with NMO applied (where velocity values were determined by the constant velocity stacks) and with objects of interest identified by the red (granite body), green (orebody) and blue (fault) arrows. Inset shows where shot gather is located along the cross-section and illustrates the objects of interest.

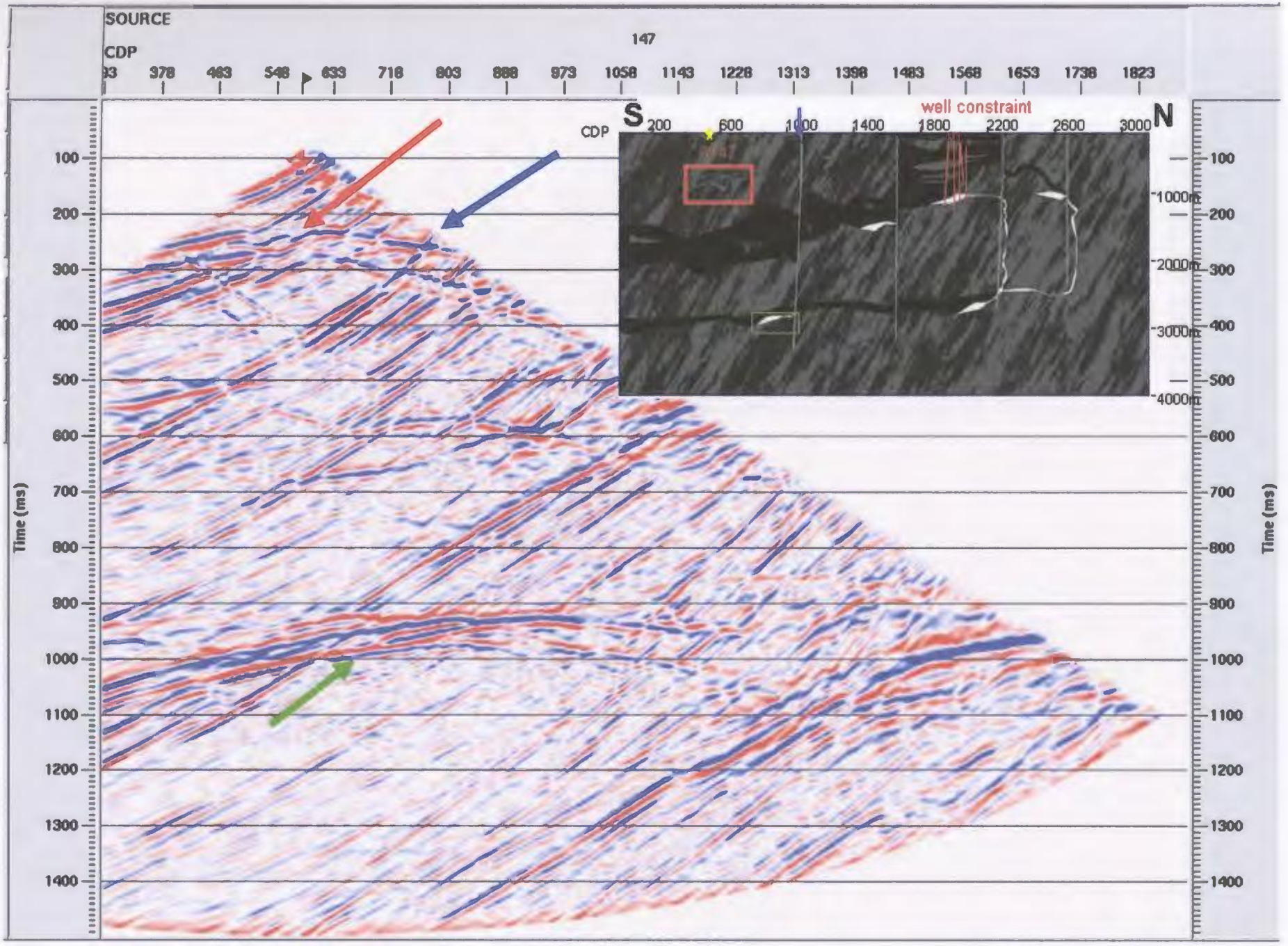


Figure 3.5.2.10: Example of a shot gather for the heterogeneity model with NMO applied (where the velocity values were determined by the constant velocity stacks) and with objects of interest identified by the red (granite body), green (orebody) and blue (fault) arrows. Inset shows where shot gather is located along the cross-section and illustrates the objects of interest.

exceptionally destructive to shallow reflectors, which present reasonably large offsets with respect to depth or traveltime (Perroud and Tygel, 2004).

The NMO-corrected shot gathers for both the simplified and heterogeneity models also display strong diagonal patterns of energy (similar to the fault plane reflections). Interestingly enough the CDP gathers do not exhibit this same phenomenon. Instead the strong diagonal patterns of energy behave similarly to reflections and therefore have a somewhat hyperbolic moveout before NMO correction (Figures 3.5.2.11 and 3.5.2.12) and appear to be flattened after NMO correction (Figures 3.5.2.13 and 3.5.2.14). Larner et al. (1983) have attributed the occurrence of different noise patterns on shot records, CDP gathers, and stacked sections to be a result of energy scattered in the subsurface. Although the data presented in this section are synthetic and do not contain any noise it is possible that the strong diagonal patterns of energy present in the shot gathers may be a result of energy scattered from the shallow complex geologic bodies in the model.

Both the objects of interest identified by the red (granite body) and green (orebody) arrows in Figures 3.5.2.11 and 3.5.2.12 demonstrate the hyperbolic moveout typical of specular reflections which appear flattened in Figures 3.5.2.13 and 3.5.2.14 after NMO correction. However, the event identified by the green arrow (orebody) also exhibits over-correction which further verifies that both the reflections and the diffractions have different stacking velocities and it was impossible to pick both. Another interesting feature is that the fault (blue arrow) appears to be flat before NMO correction (Figures 3.5.2.11 and 3.5.2.12) and over-corrected after NMO correction (Figures

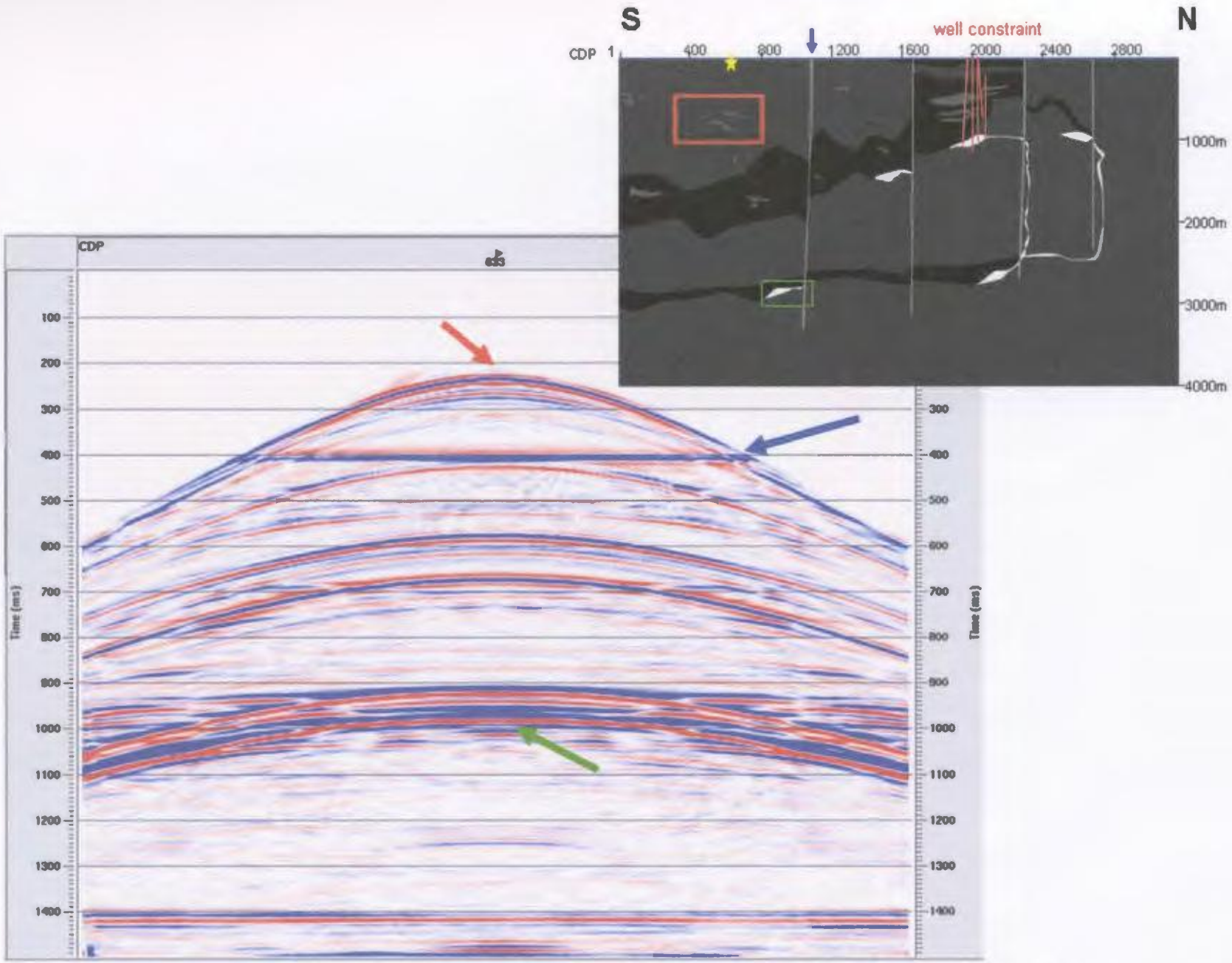


Figure 3.5.2.11: Example of a CDP gather (633) for the simplified model with a bandpass filter with parameters 8-20-80-120 and a top mute applied with objects of interest identified by the red (granite body), green (orebody) and blue (fault) arrows. Inset shows where the CDP gather is located along the cross-section and objects of interest.

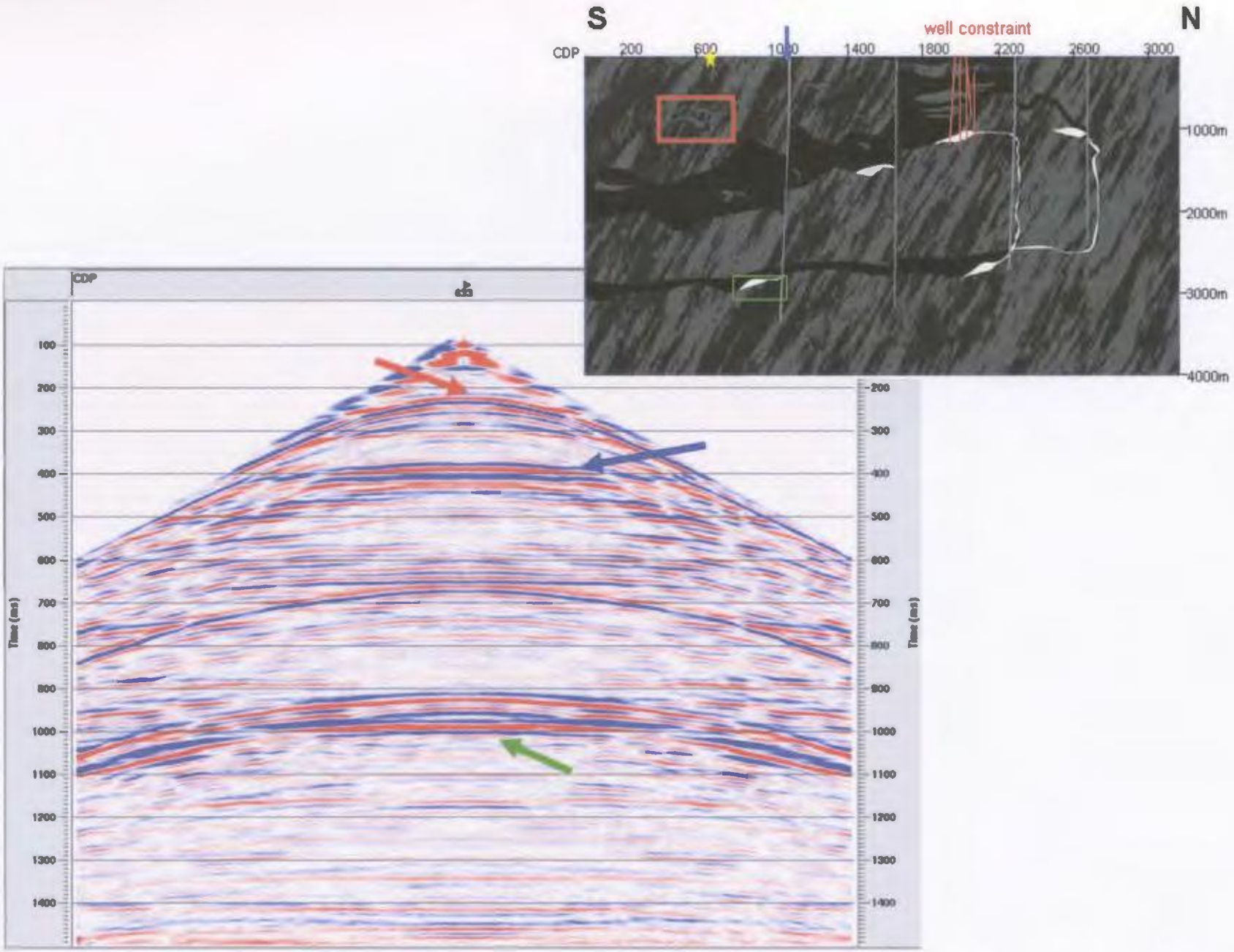


Figure 3.5.2.12: Example of a CDP gather (633) for the heterogeneity model with a bandpass filter with parameters 8-20-80-120 and a top mute applied with objects of interest identified by the red (granite body), green (orebody) and blue (fault) arrows. Inset shows where the CDP gather is located along the cross-section and objects of interest.

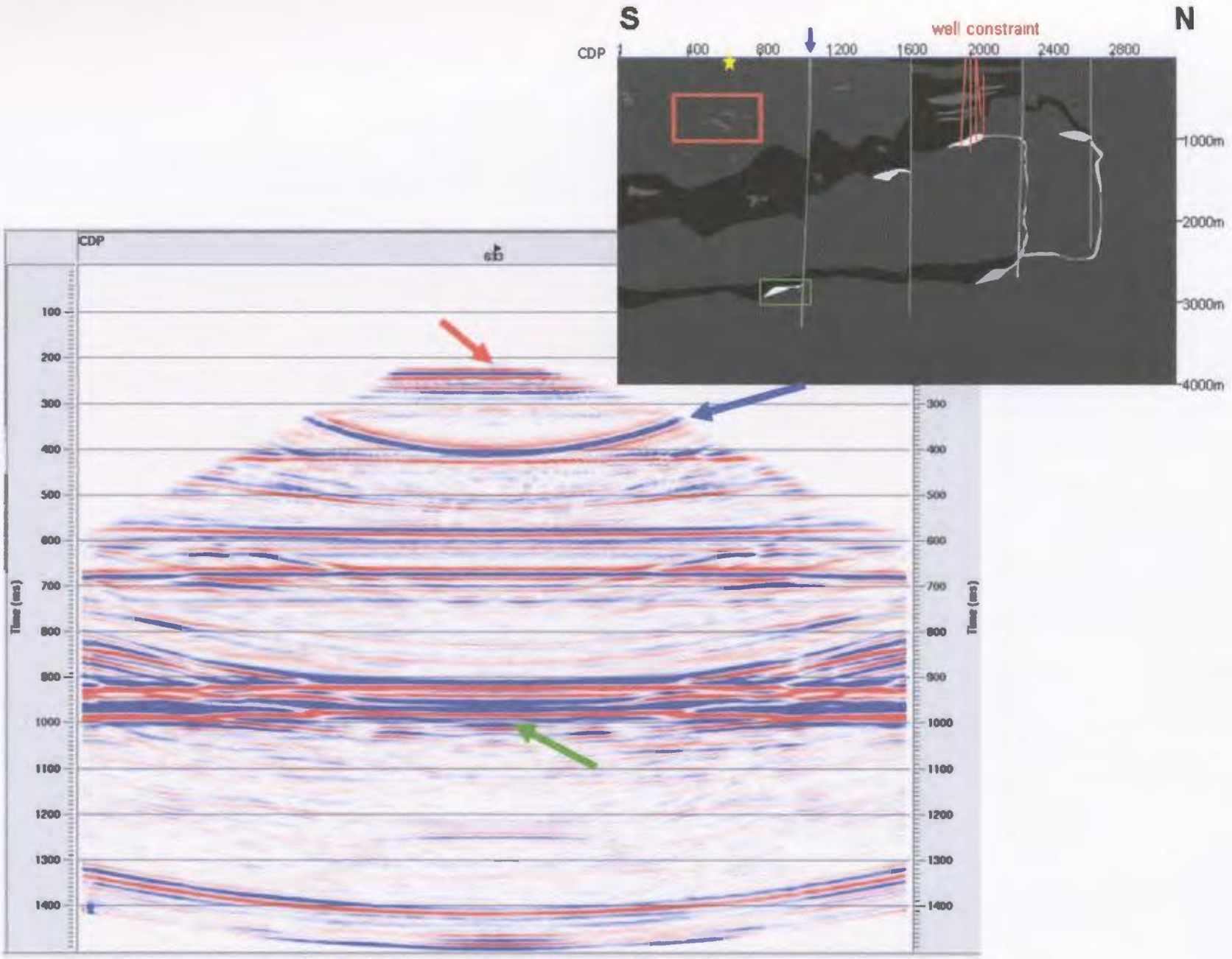


Figure 3.5.2.13: Example of a CDP gather (633) for the simplified model with a bandpass filter with parameters 8-20-80-120, a top mute, and NMO applied with objects of interest identified by the red (granite body), green (orebody) and blue (fault) arrows. Inset shows where the CDP gather is located along the cross-section and objects of interest.

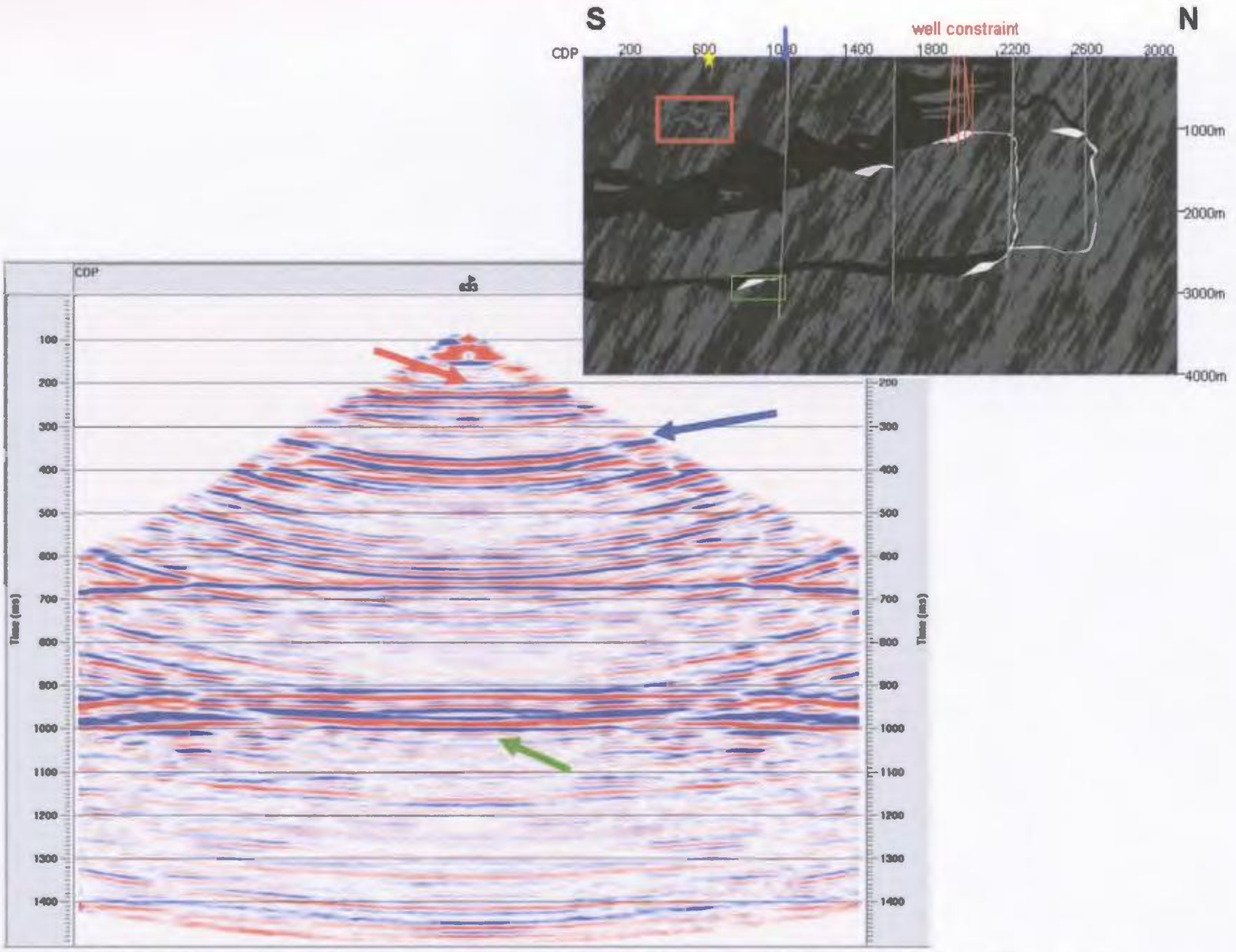


Figure 3.5.2.14: Example of a CDP gather (633) for the heterogeneity model with a bandpass filter with parameters 8-20-80-120, a top mute, and NMO applied with objects of interest identified by the red (granite body), green (orebody) and blue (fault) arrows. Inset shows where the CDP gather is located along the cross-section and objects of interest.

3.5.2.13 and 3.5.2.14). This is a result of applying a hyperbolic NMO to a linear event such as this fault which is a reflected direct arrival. As an aside, it may be possible to enhance the imaging of the faults by simply stacking the dataset without NMO correction since these events are linear and are the only events that appear to already be flattened in the CDP gathers without NMO correction (Figures 3.5.2.11 and 3.5.2.12).

Even though it does not appear that either of the previous two steps have been overly successful, stacking was still attempted in order to produce a complete comparison of post-stack and pre-stack processing schemes on the quality of the final image. CDP stacking involves the summation of several traces to generate one CDP. An arithmetic mean horizontal stacking algorithm was utilized where the main advantage is its simple formula:

$$S_t = \frac{\sum_{i=1}^{i=v} a_{it}}{n},$$

where $S_t$ is the stack value at time t, $a_{it}$ is the amplitude of the $i^{th}$ trace at time t. This formula simply states that mean stacking sums the amplitudes of the traces at all times for all CDP's and then divides the sum by the number of traces. The calibre of the stack is contingent upon the selected stacking velocities therefore it is generally necessary to re-evaluate them and re-stack the data until a suitable stack is produced. Figures 3.5.2.15 and 3.5.2.16 display the final stacks for both the simplified and heterogeneity models respectively. Despite the unreliability of the velocity analysis and the NMO correction virtually all of the features present in the original models (Figures 3.3.1.1and 3.3.2.3) are

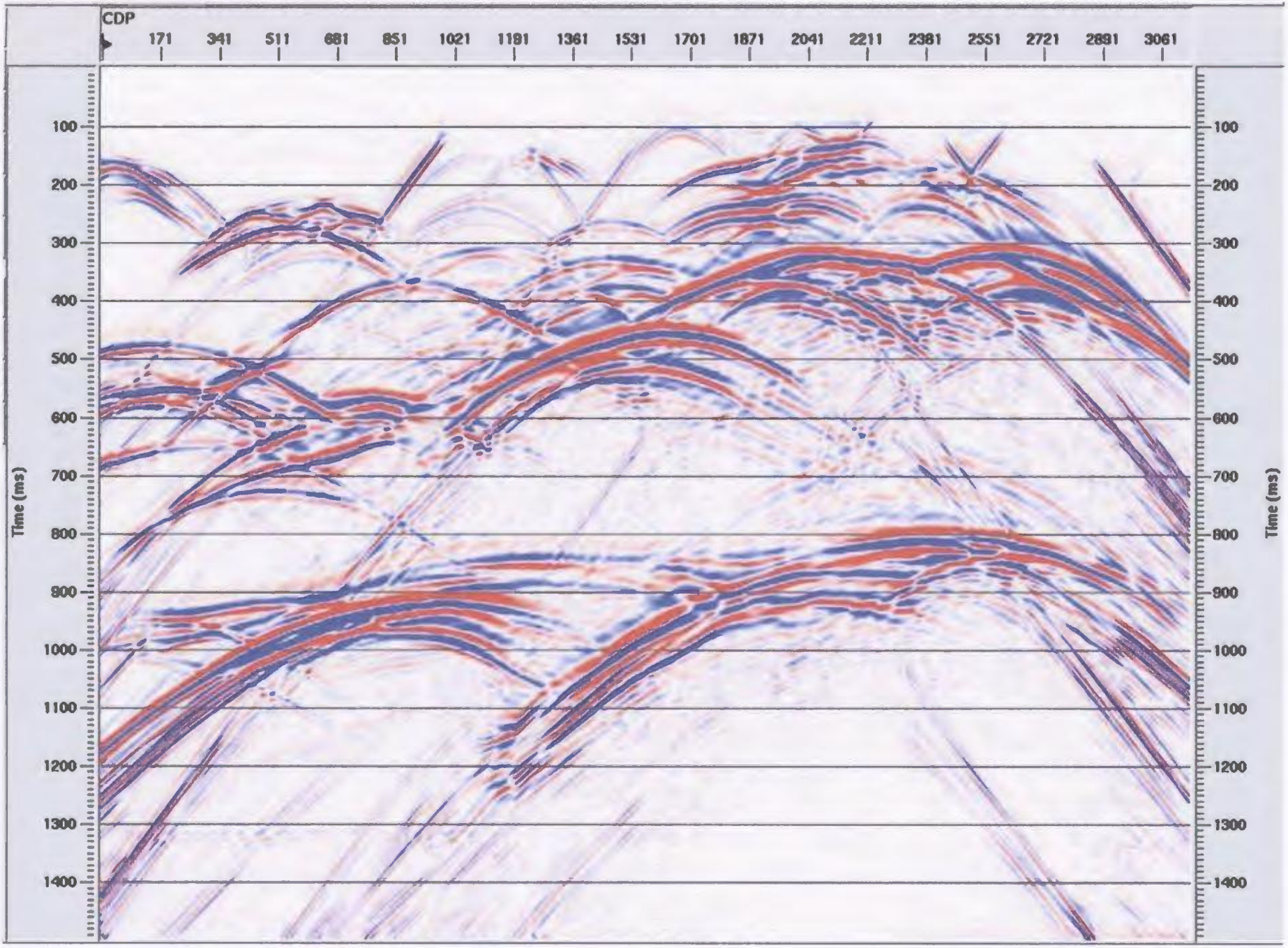


Figure 3.5.2.15: Final stack incorporating all data for the simplified model.

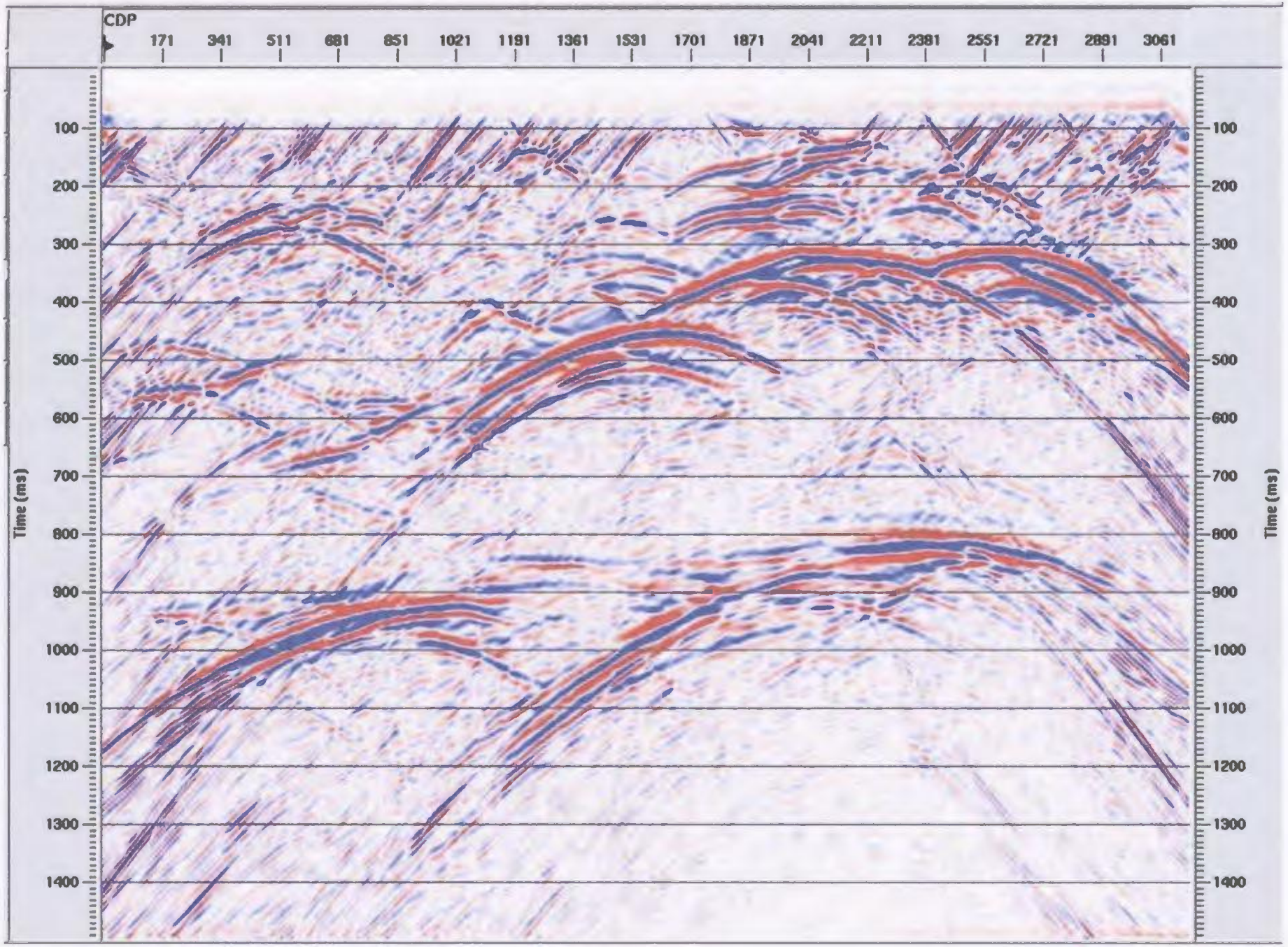


Figure 3.5.2.16: Final stack incorporating all data for the heterogeneity model.

evident in the CDP stacks. This occurrence is most likely a result of the fact that there was no noise present in this dataset to destructively interfere. In general, the first 100-150 ms, which roughly corresponds to offsets of 0-1000 m, of data was lost for both models which stems from the application of the NMO correction.

Incorporating all the data in the stacking process for both models seems to produce more of a vague section than a detailed one. Limited offset stacks with offsets +/- 500 m, +/- 1000 m, and +/- 2000 m were produced for both the simplified and heterogeneity models to illustrate the effects that the near and far offsets have on the quality of the stack (Figures 3.5.2.17-3.5.2.19 and 3.5.2.20-3.5.2.22, respectively). The limited offset stacks with offsets +/- 500 m and +/- 1000 m offer better resolution of the shallower events, particularly between CDP's 1361-2211 in the upper 200 ms, as opposed to the far offset stacks (+/- 2000 m). The stacks including farther offsets closely resemble the original stacks incorporating all offsets. As a consequence, one may conclude that the information contained in the very far offsets (> +/- 2000 m) may be dominating the stack and obscuring the shallower events. The farther offsets may be dominating the stack simply because they are of higher amplitude than the near offsets. Comparison of Figures 3.5.2.23 and 3.5.2.24 with Figures 3.5.2.18 and 3.5.2.21 also illustrate that the very far offsets (+/- 2000-8000 m) do not appear to provide any additional valuable information and therefore should not be included during the stacking process.

- Migration

The preceding processing has demonstrated that velocity analysis was difficult and that the NMO correction does not appear to be effective for this dataset. Despite this

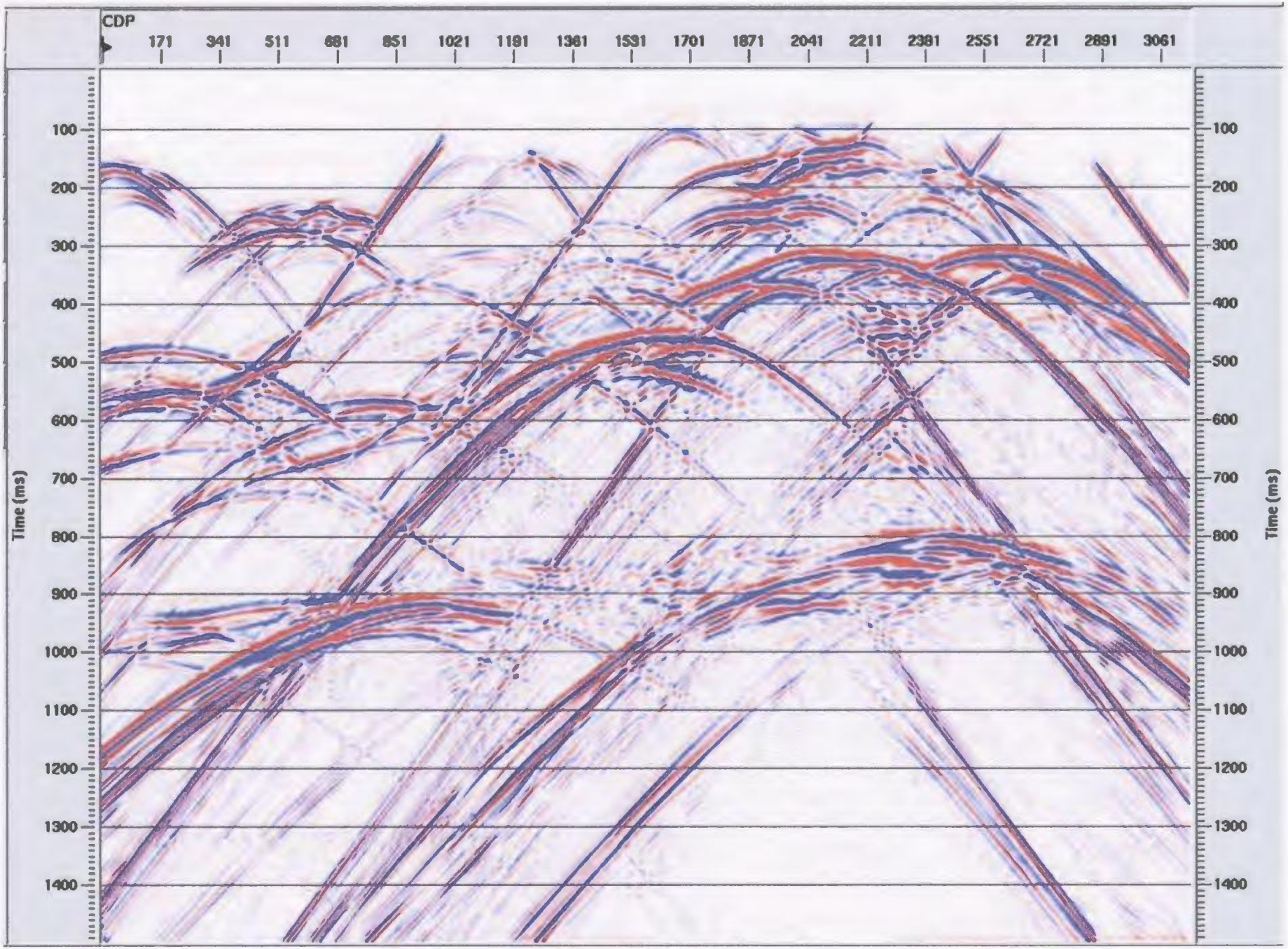


Figure 3.5.2.17: Limited offset stack with offsets +/- 500 m for the simplified model.

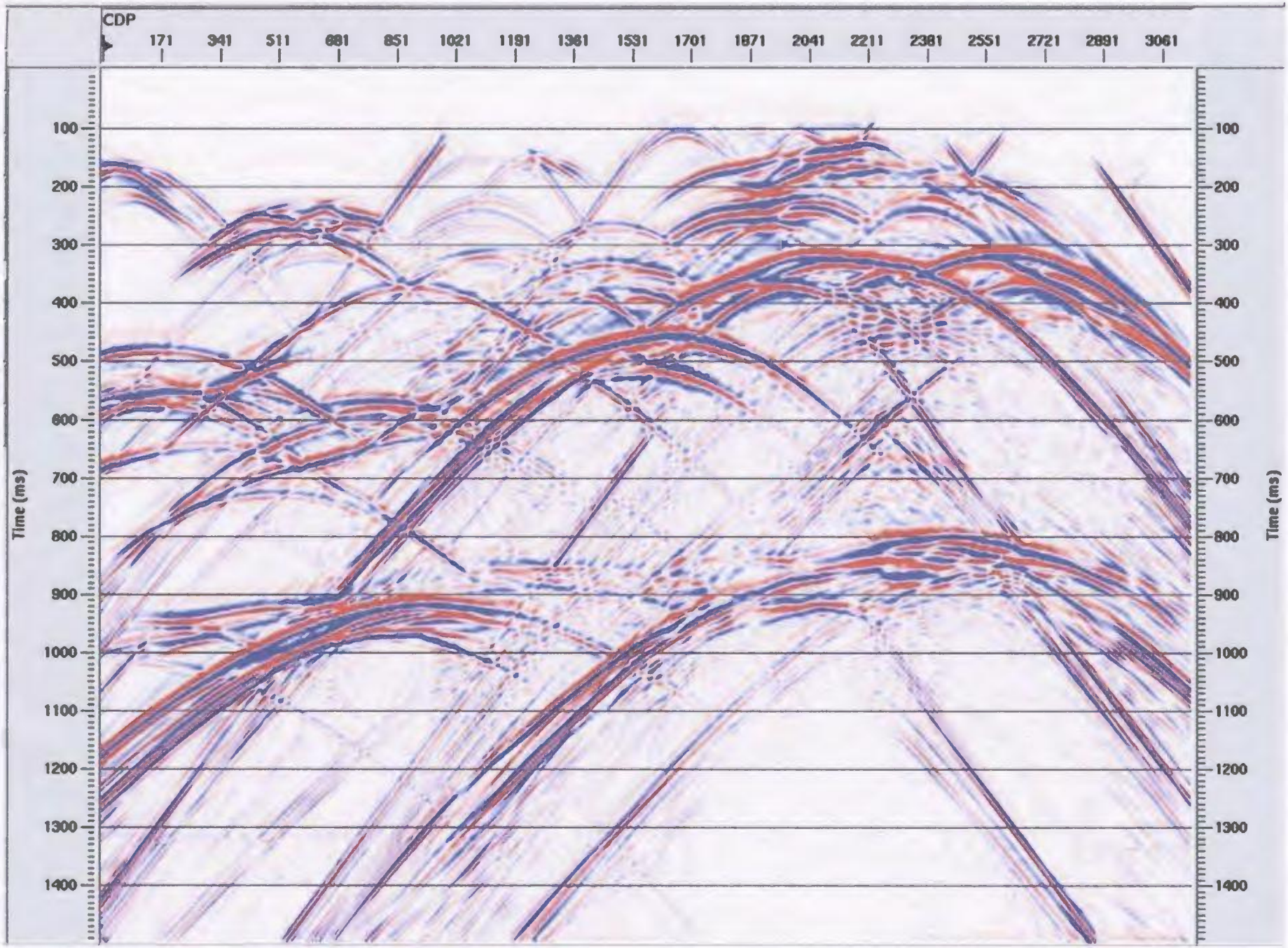


Figure 3.5.2.18: Limited offset stack with offsets +/- 1000 m for the simplified model.

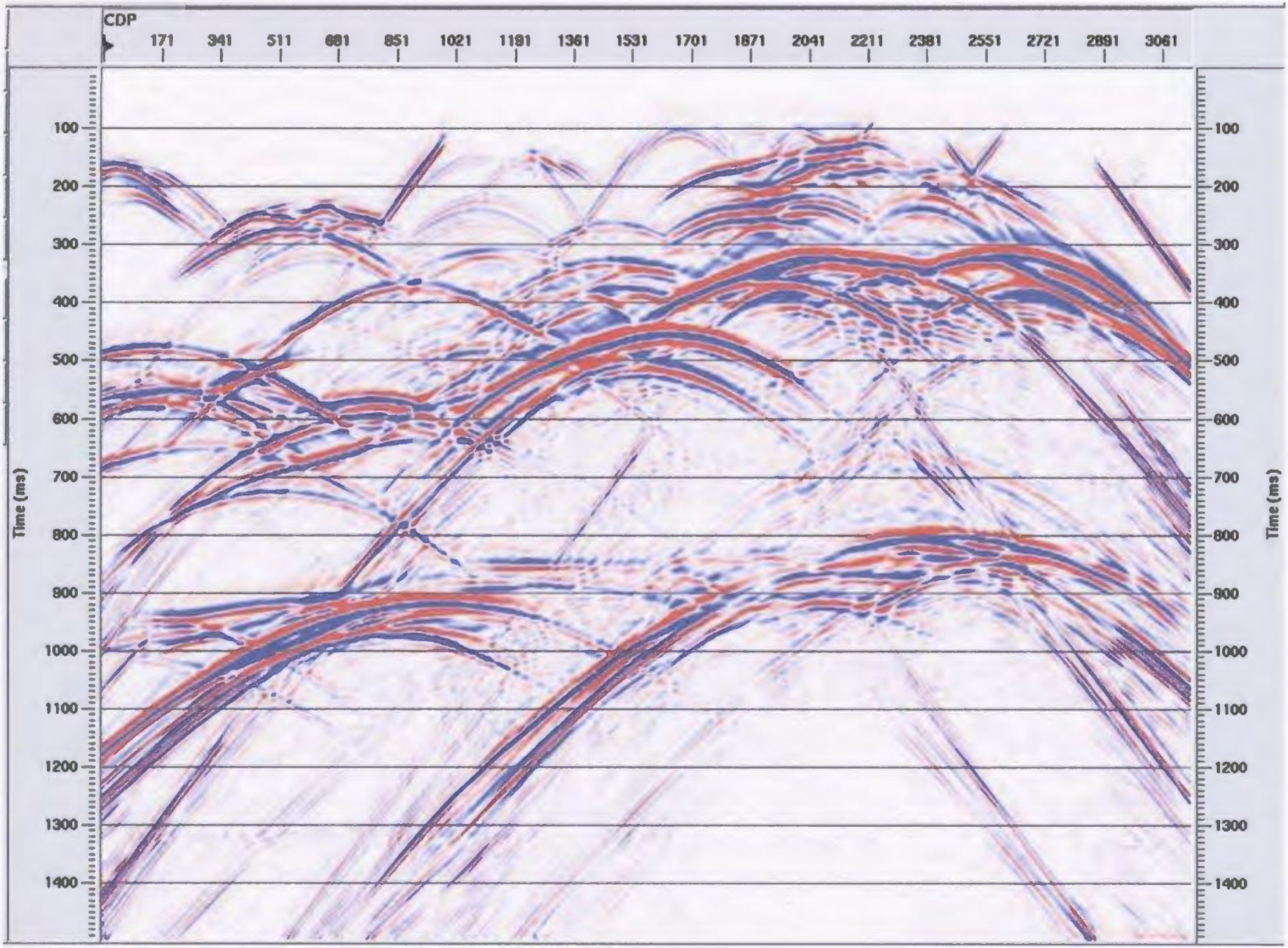


Figure 3.5.2.19: Limited offset stack with offsets +/- 2000 m for the simplified model.

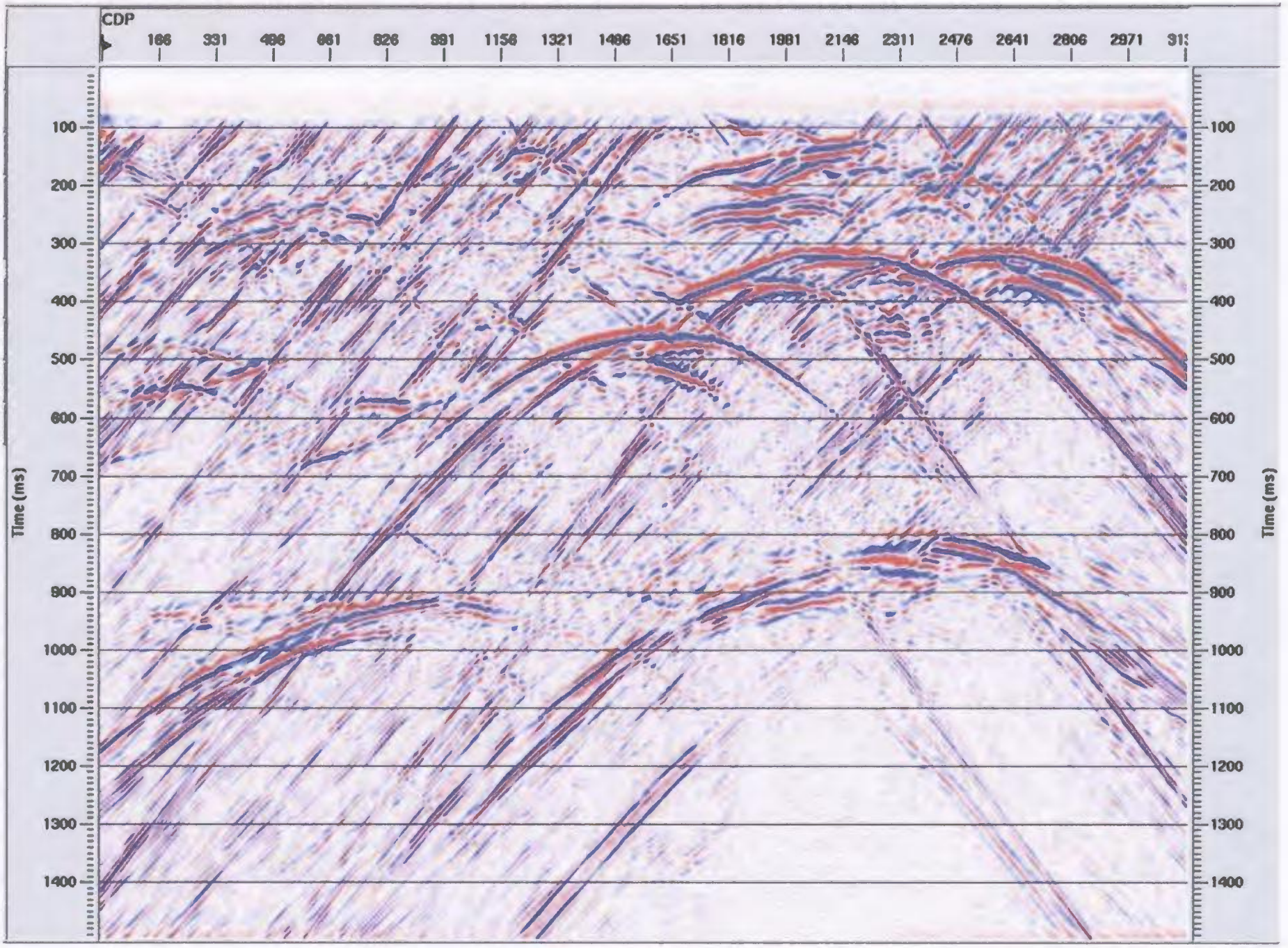


Figure 3.5.2.20: Limited offset stack with offsets +/- 500 m for the heterogeneity model.

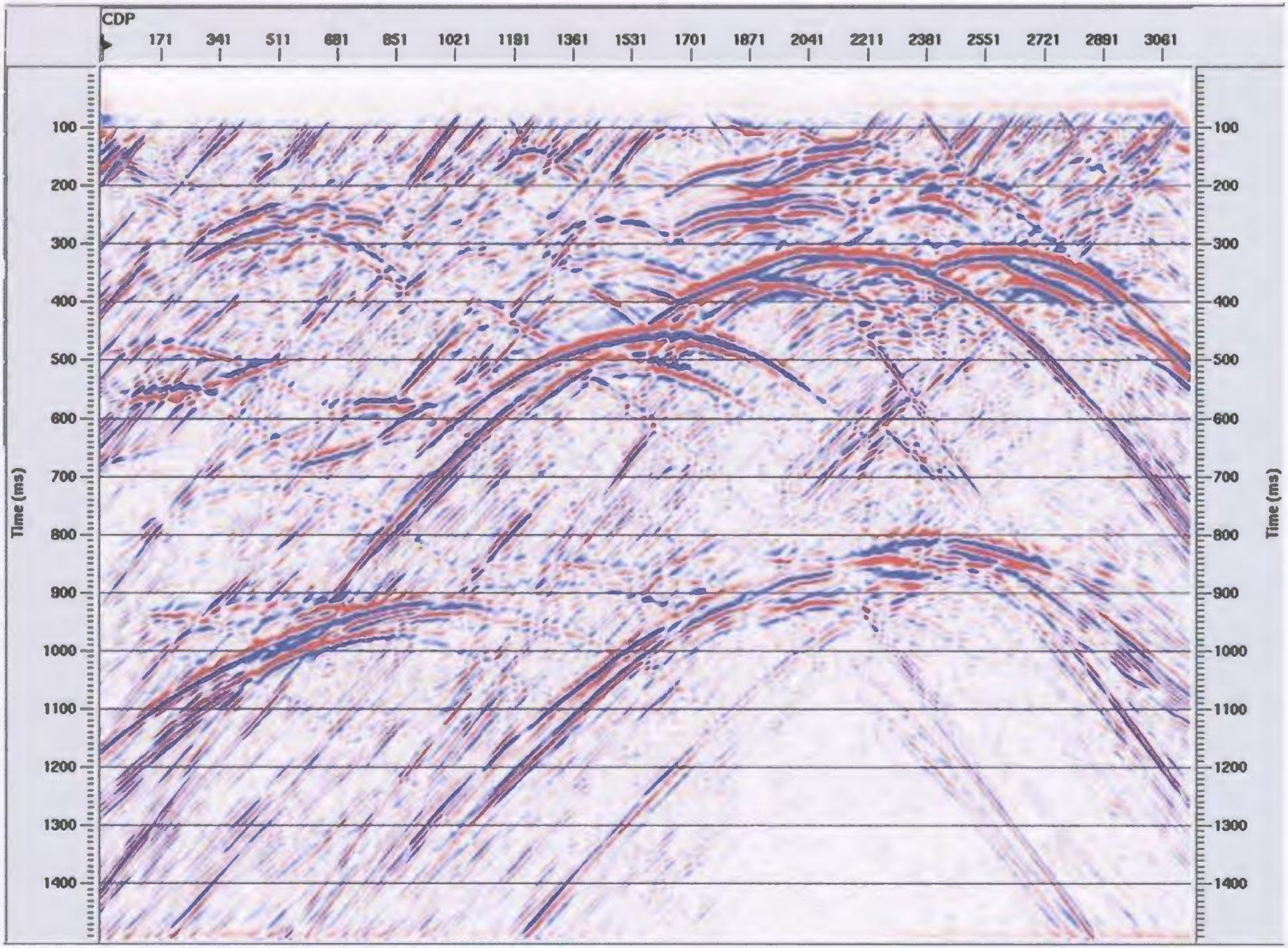


Figure 3.5.2.21: Limited offset stack with offsets +/- 1000 m for the heterogeneity model.

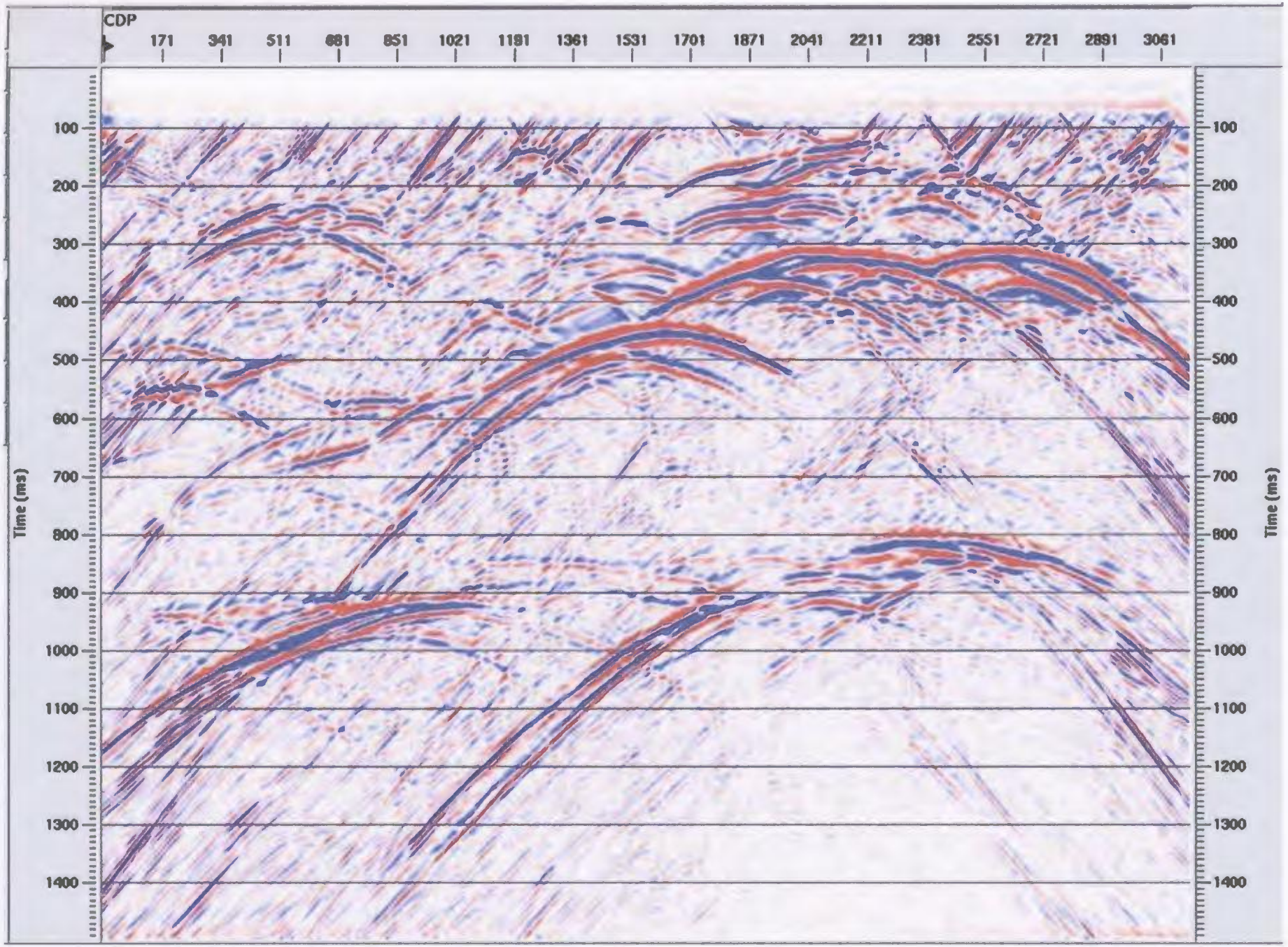


Figure 3.5.2.22: Limited offset stack with offsets +/- 2000 m for the heterogeneity model.

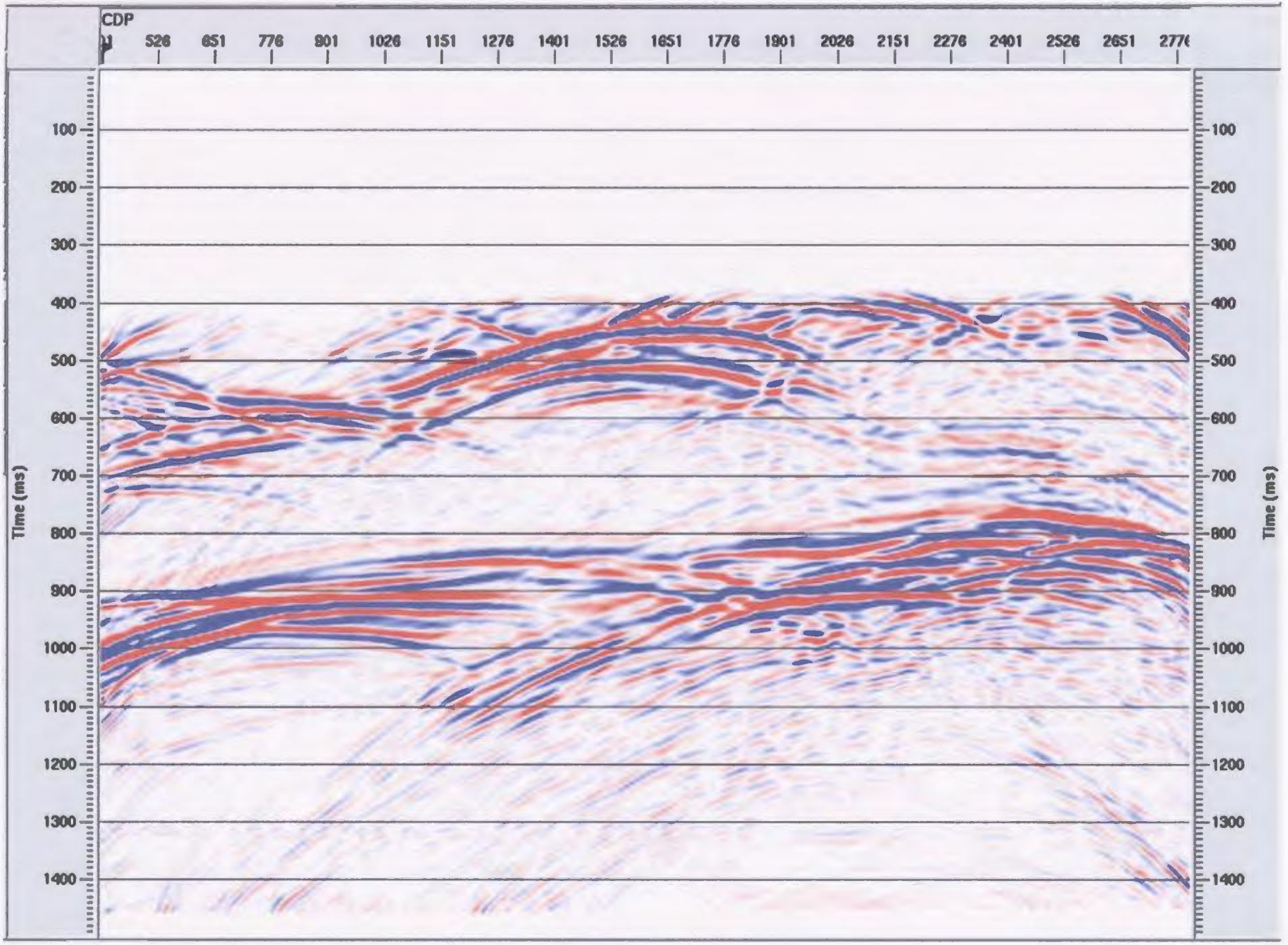


Figure 3.5.2.23: Limited offset stack with offsets +/- 2000-8000 m for the simplified model.

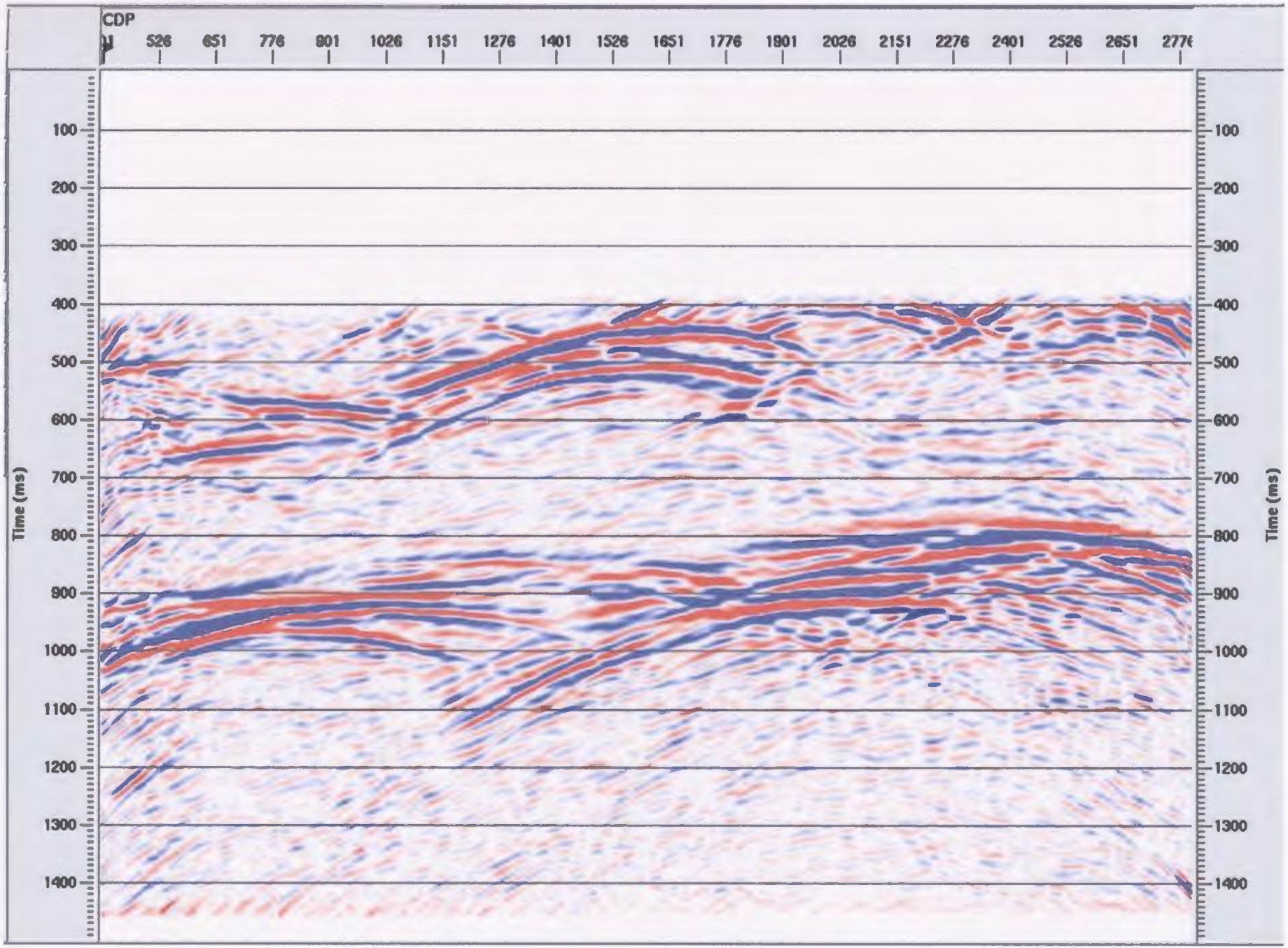


Figure 3.5.2.24: Limited offset stack with offsets +/- 2000-8000 m for the heterogeneity model.

Despite this, stacking the dataset produced encouraging results whereby the majority of the events stacked in; however, this may be a consequence of not having noise present in the dataset. Regardless, velocity analysis was poor for determining the stacking velocities which are then used as the starting point for migration velocities. Therefore, this does not provide a reliable starting point for determining the migration velocities. However, migration was performed on the stacked sections for both the simplified and heterogeneity models to attempt to increase lateral resolution by collapsing the diffractions and moving dipping events to their true subsurface positions (Yilmaz and Doherty, 1987).

A Kirchhoff time migration algorithm was used for this specific processing scheme. This particular algorithm uses the diffraction summation method of migration with correction for amplitude variations. The performance of the Kirchhoff time migration is affected by the aperture width used in summation, the maximum dip to migrate, and velocity errors. An excessively small aperture causes destruction of steeply dipping events while an excessively large aperture can degrade the migration quality in poor signal-to-noise conditions (Yilmaz and Doherty, 2001). The migration aperture was set to default for each model in order to instruct the Kirchhoff time migration algorithm to find the most suitable aperture for each of the models. Specifying the maximum allowable dip may be useful in suppressing steeply dipping coherent noise; however, this dip parameter is also directly related to aperture (Yilmaz and Doherty, 2001). Therefore, the smaller the maximum allowable dip, the smaller the aperture. A maximum allowable dip of +/- $90^{\circ}$ was applied for each model in order to allow all possible dips. The

Kirchhoff time migration algorithm then determined a maximum migration aperture based on these previous two conditions, thereby avoiding a migration aperture that may be too small.

Over and undermigration effects can result through the use of low or high velocities respectively. With increasingly low velocities, the diffraction hyperbola is collapsed less and less taking the shape of a frown which is known as undermigration (Yilmaz and Doherty, 2001). With increasingly high velocities, the diffraction hyperbola is inverted more and more taking the shape of a smile which is known as overmigration (Yilmaz and Doherty, 2001). Consequently it is beneficial to have an acceptable starting point for the migration velocities.

As a first attempt, the stacking velocities previously determined were used for the migration velocities. Considering that there was difficulty in determining the stacking velocities for both the simplified and heterogeneity models, the first attempt at migrations produced very modest results (Figures 3.5.2.25 and 3.5.2.26). The migration velocities were then fine-tuned by analyzing the first attempt and adjusting the velocities in areas that were either over or undermigrated. Several iterations of migrations for each model were necessary using this procedure. A suitable migration velocity file was achieved for both the simplified and heterogeneity models when it was no longer possible to adjust the migration velocities and still improve the quality of the migration (Figures 3.5.2.27 and 3.5.2.28). In spite of this, both under and overmigration effects are still evident, especially on events with complex structures (Figures 3.5.2.27 and 3.5.2.28).

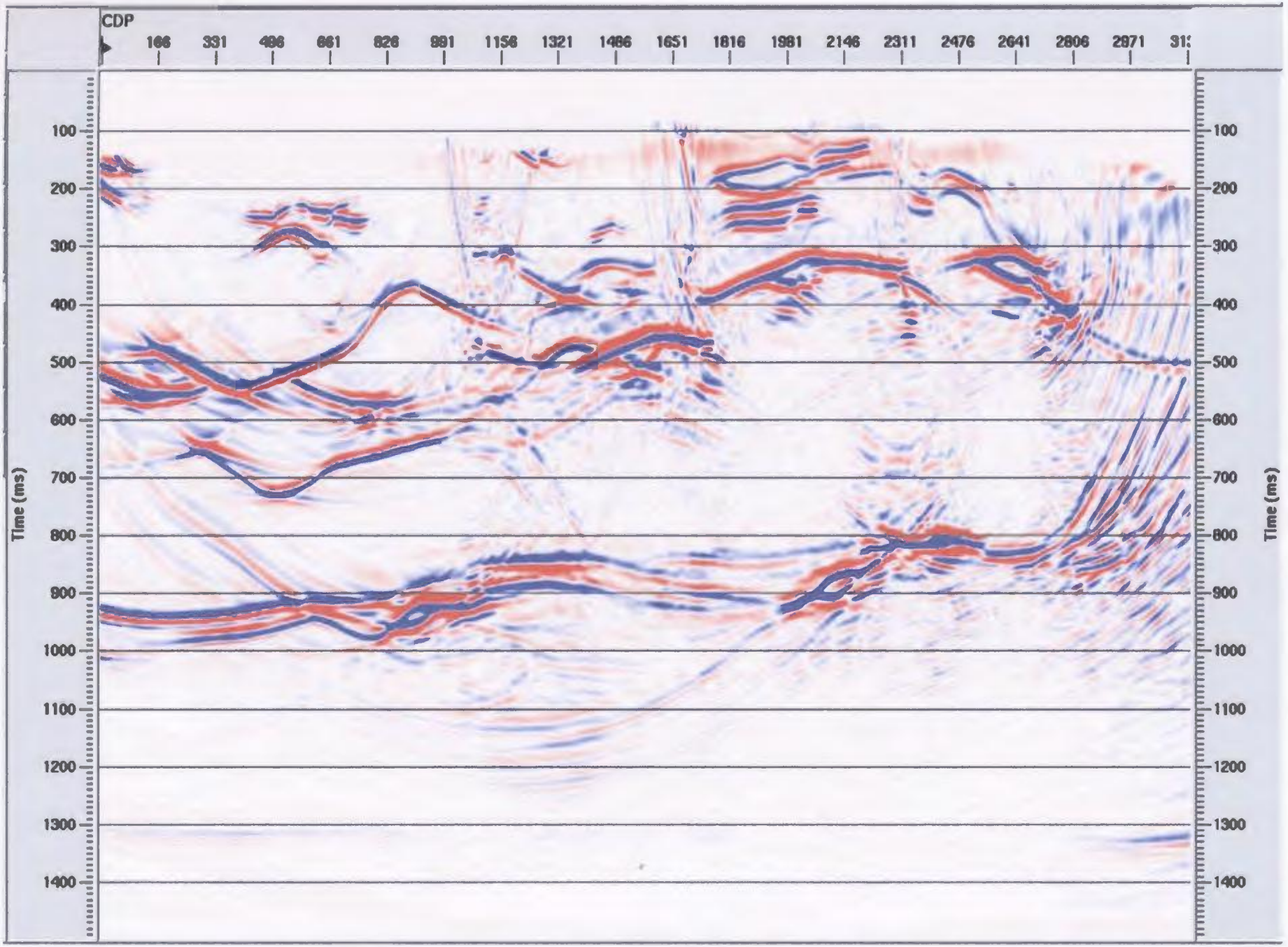


Figure 3.5.2.25: Illustrates the first attempted post-stack time migration for the simplified model with all offsets using the stacking velocities.

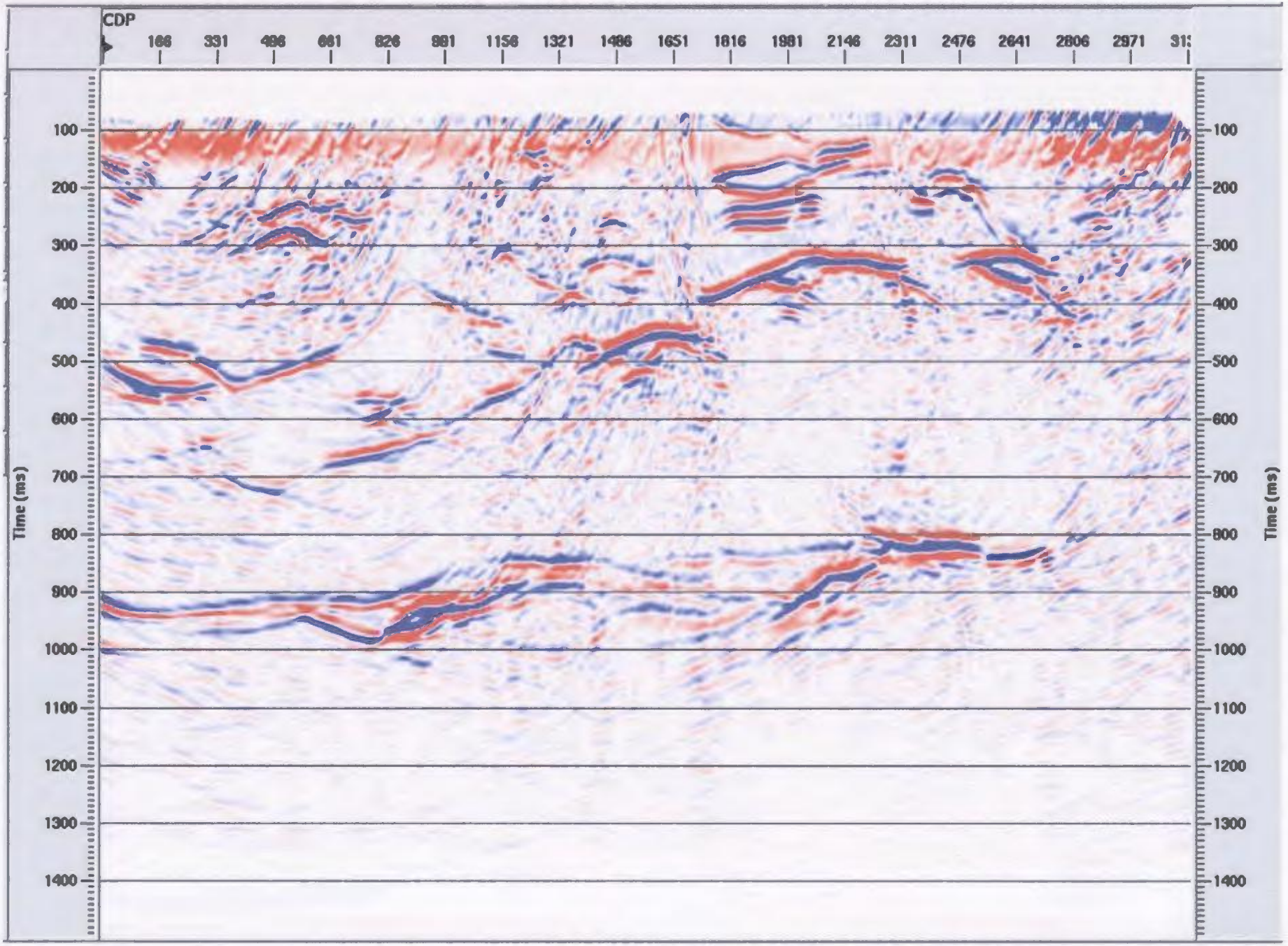


Figure 3.5.2.26: Illustrates the first attempted post-stack time migration for the heterogeneity model with all offsets using the stacking velocities.

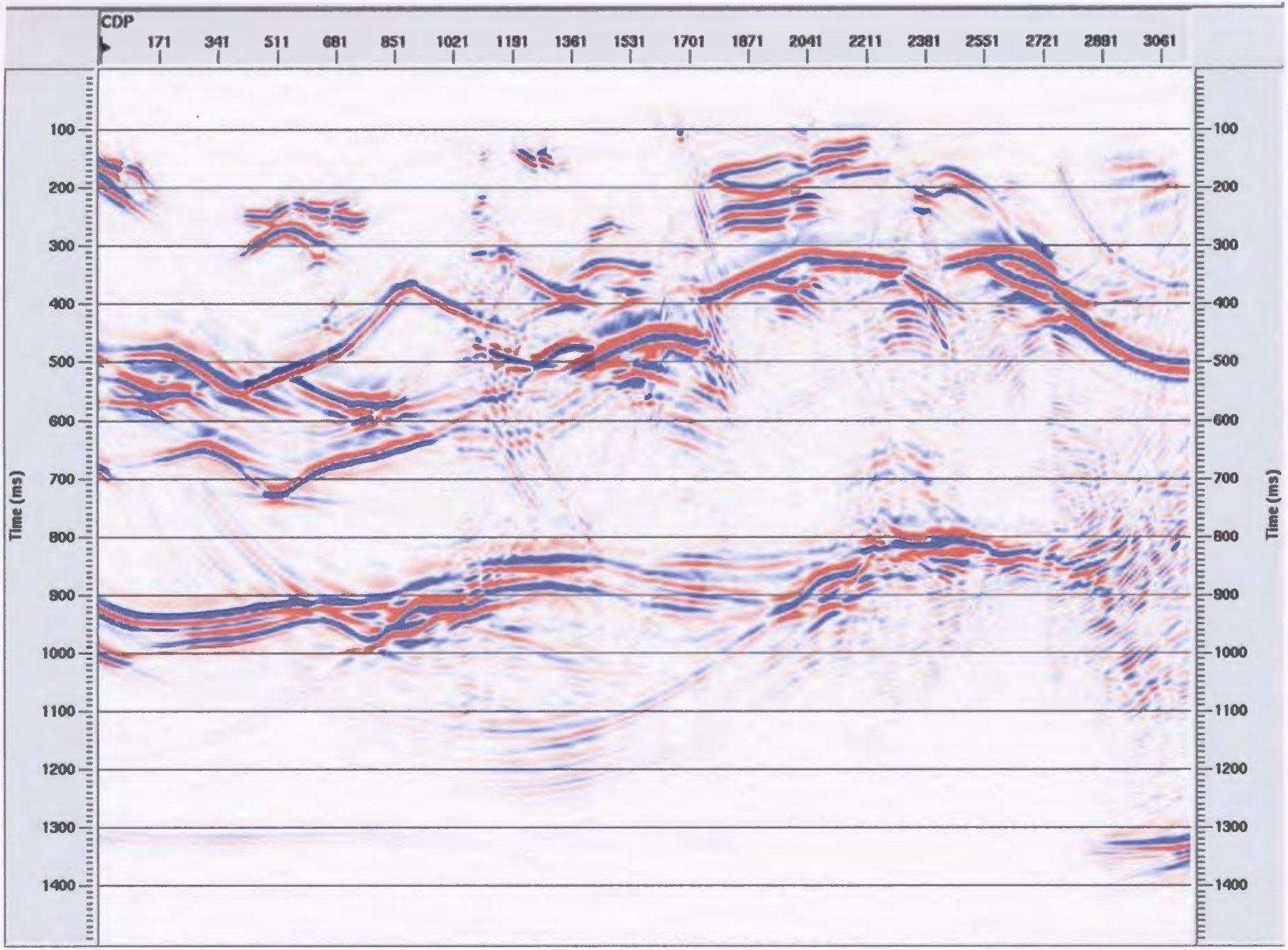


Figure 3.5.2.27: Illustrates the final post-stack time migration for the simplified model with all offsets.

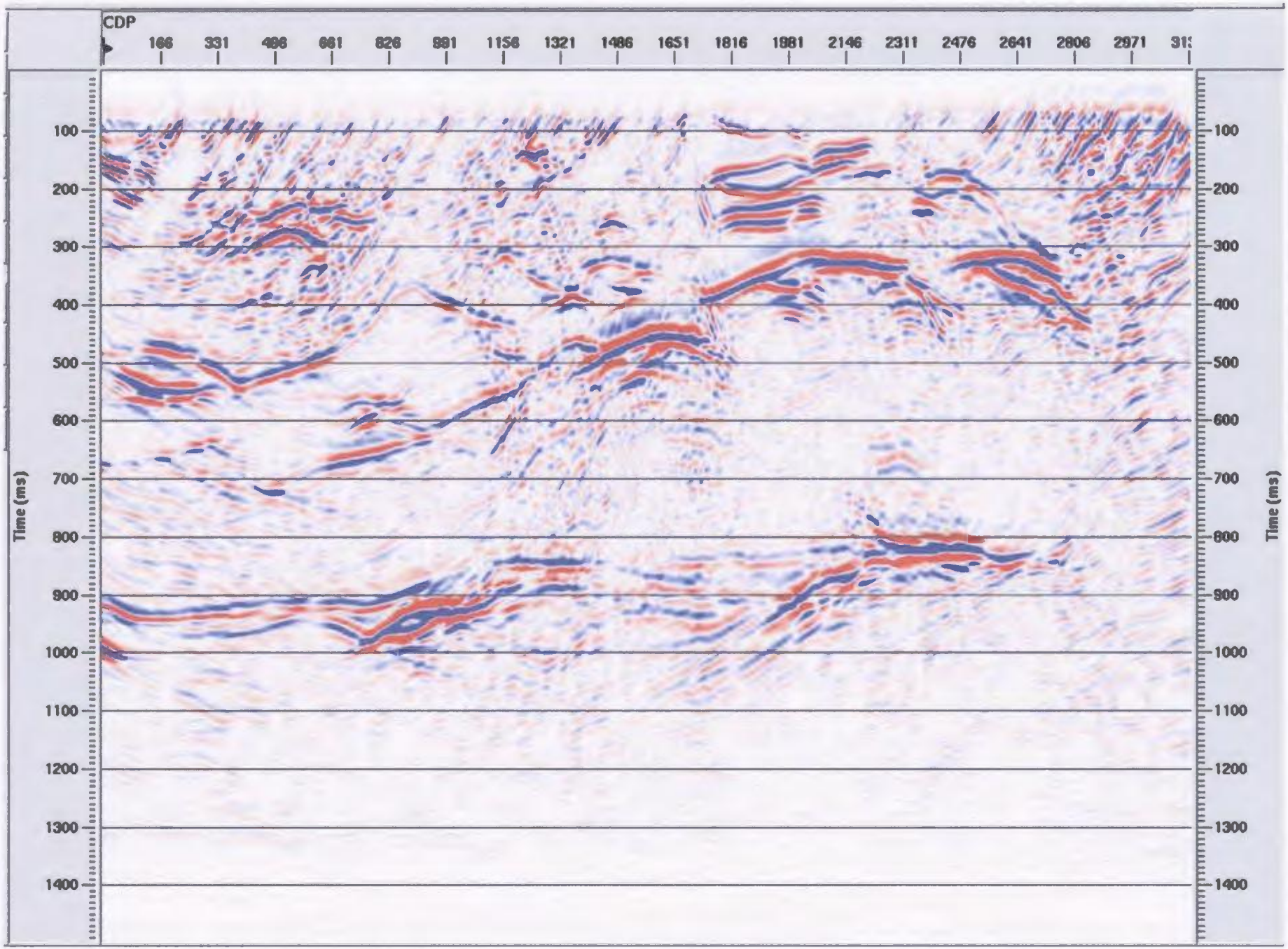


Figure 3.5.2.28: Illustrates the final post-stack time migration for the heterogeneity model with all offsets.

Limited offsets of +/- 500 m, +/- 1000 m, and +/-2000 m were also migrated for both the simplified and heterogeneity models since there was modest success regarding imaging with the limited offset stacks (Figures 3.5.2.29-3.5.2.31 and 3.5.2.32-3.5.2.34, respectively). Overall, limiting the offsets incorporated into the migration resulted in slightly better imaging of all the events however the energy from the majority of theevents does not focus properly. Post-stack migration algorithms are designed to produce an image that will be an approximate zero-offset section and consequently are inadequate for imaging complex structures with large lateral velocity variations, steep dips, and wide apertures (Raiaskaran and McMechan, 1995).

Proper stacking depends on appropriate NMO functions being applied to all CDP gathers so that the delay times of reflection events line up. NMO corrections usually assume the uncorrected reflection events lie along hyperbolic curves, which is only true if the Earth is a constant velocity medium above the reflector and is only partially true for layered media (Kessinger, 2005). According to Kessinger (2005), for complex structures the events may not lie on a hyperbola and therefore will not move-out and stack properly. Kessinger (2005) also suggests that events can appear on CDP gathers at the same travel time, but with different stacking velocities as was seen in Figures 3.5.2.13 and 3.5.2.14.

Since migration after stack is not suitable for dealing with this problem perhaps migration should be performed on the individual seismic traces before stacking (Yilmaz and Doherty, 1987). In general, both the lateral resolution and the signal-to-noise quality of the seismic image are simultaneously improved by pre-stack migration since all the data contained in the individual traces are available during imaging. Stacking, however

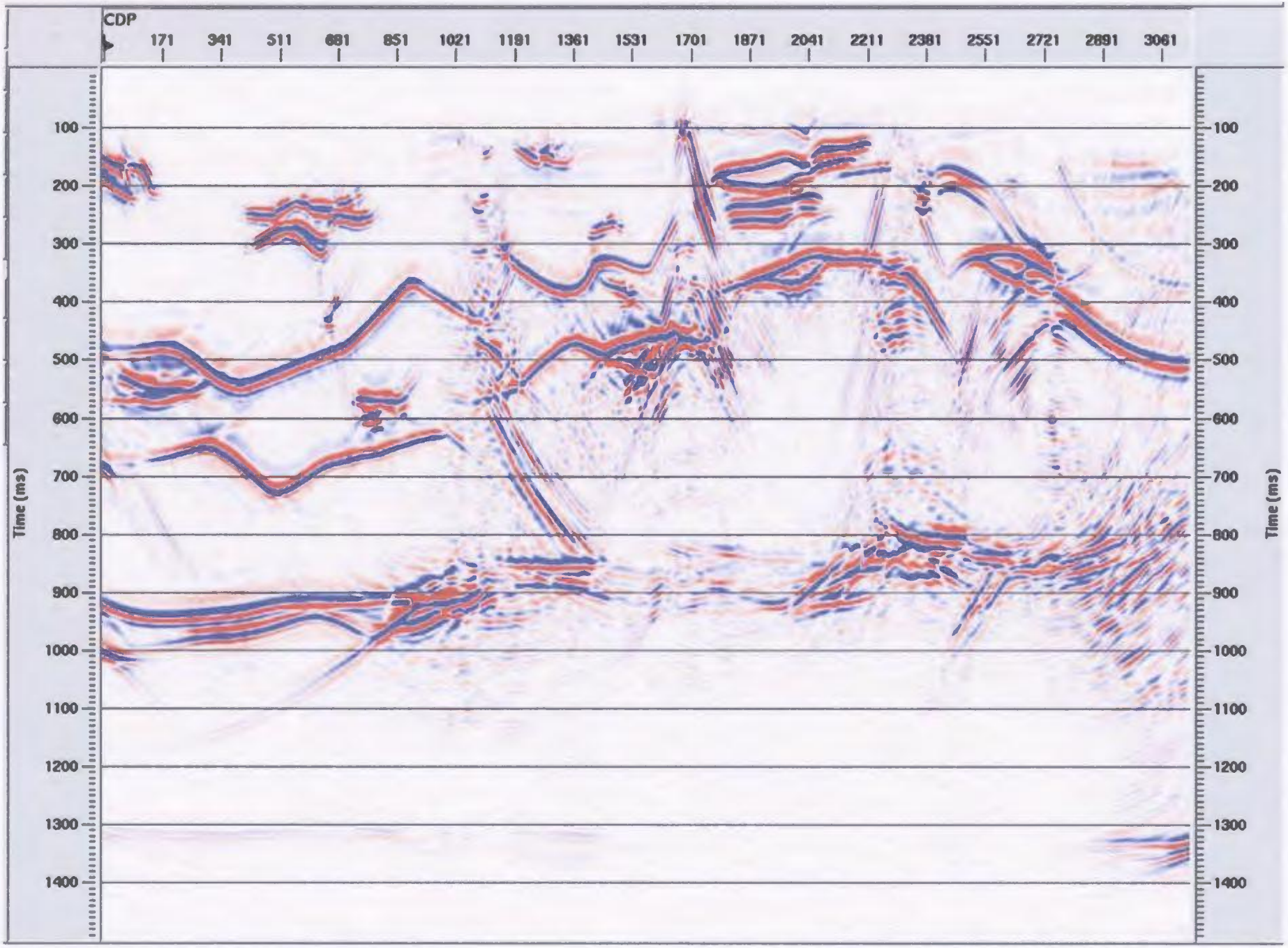


Figure 3.5.2.29: Illustrates the final post-stack time migration for the simplified model with offsets +/-500 m.

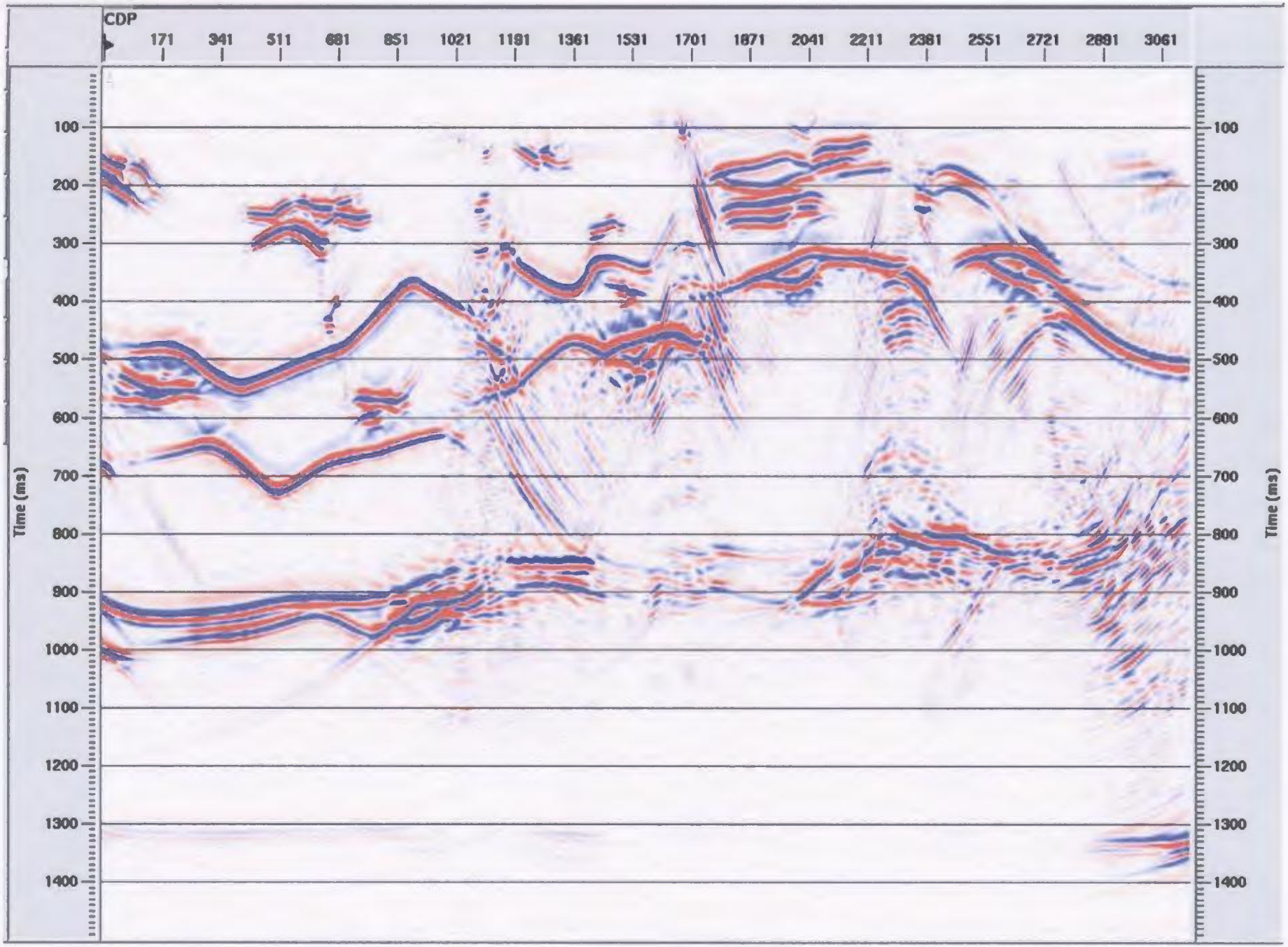


Figure 3.5.2.30: Illustrates the final post-stack time migration for the simplified model with offsets +/-1000 m.

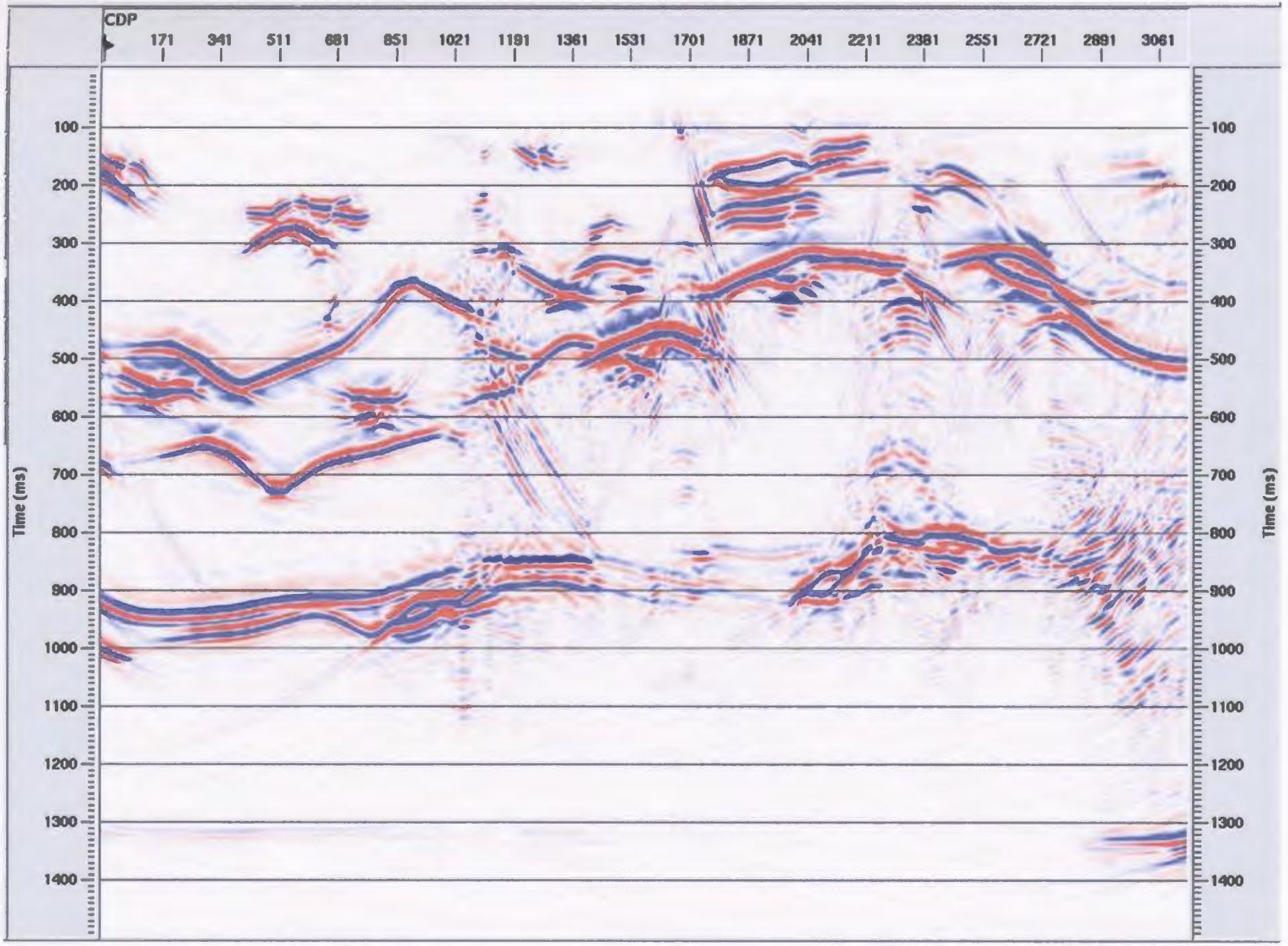


Figure 3.5.2.31: Illustrates the final post-stack time migration for the simplified model with offsets +/-2000 m.

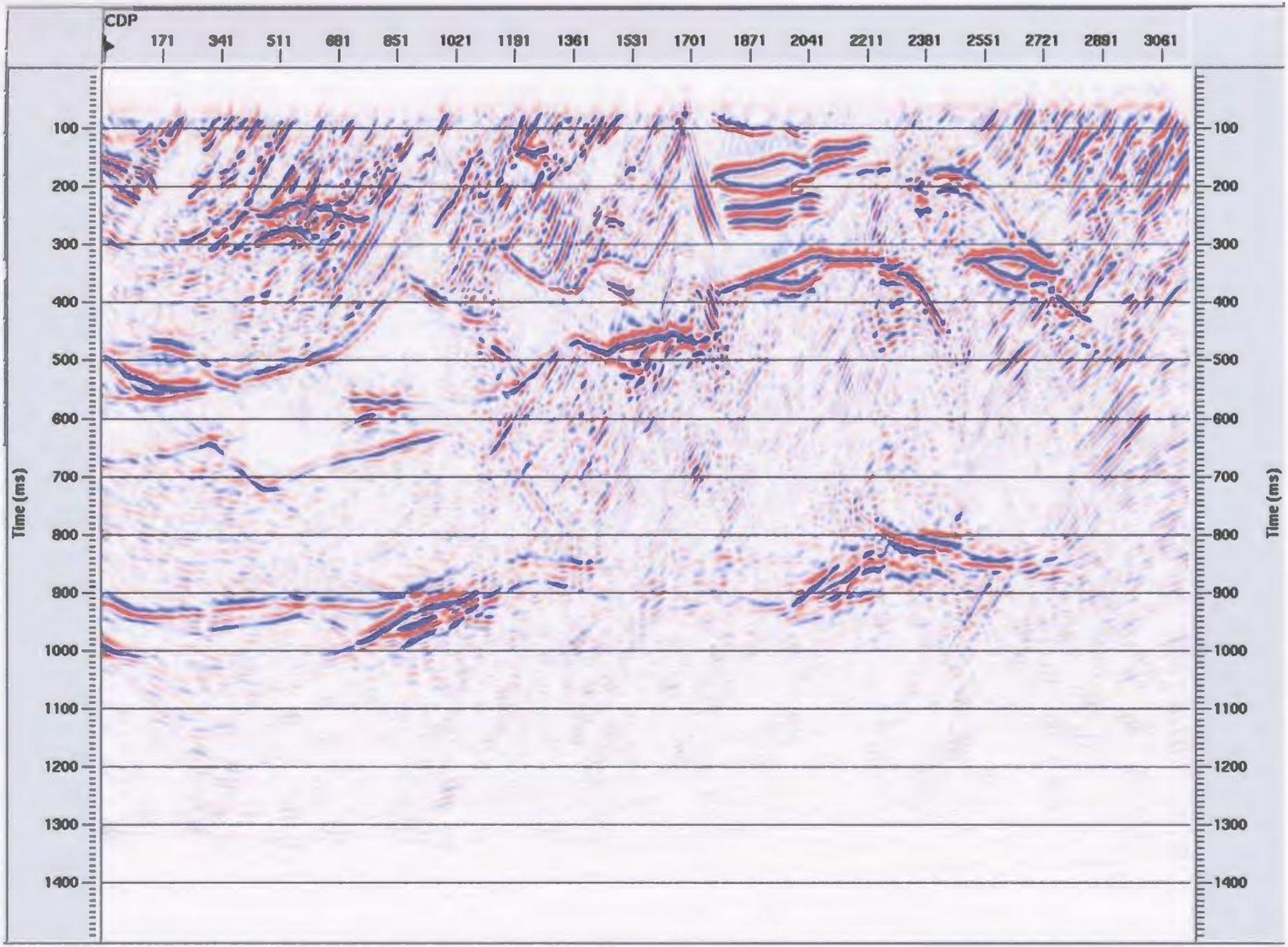


Figure 3.5.2.32: Illustrates the final post-stack time migration for the heterogeneity model with offsets +/-500 m.

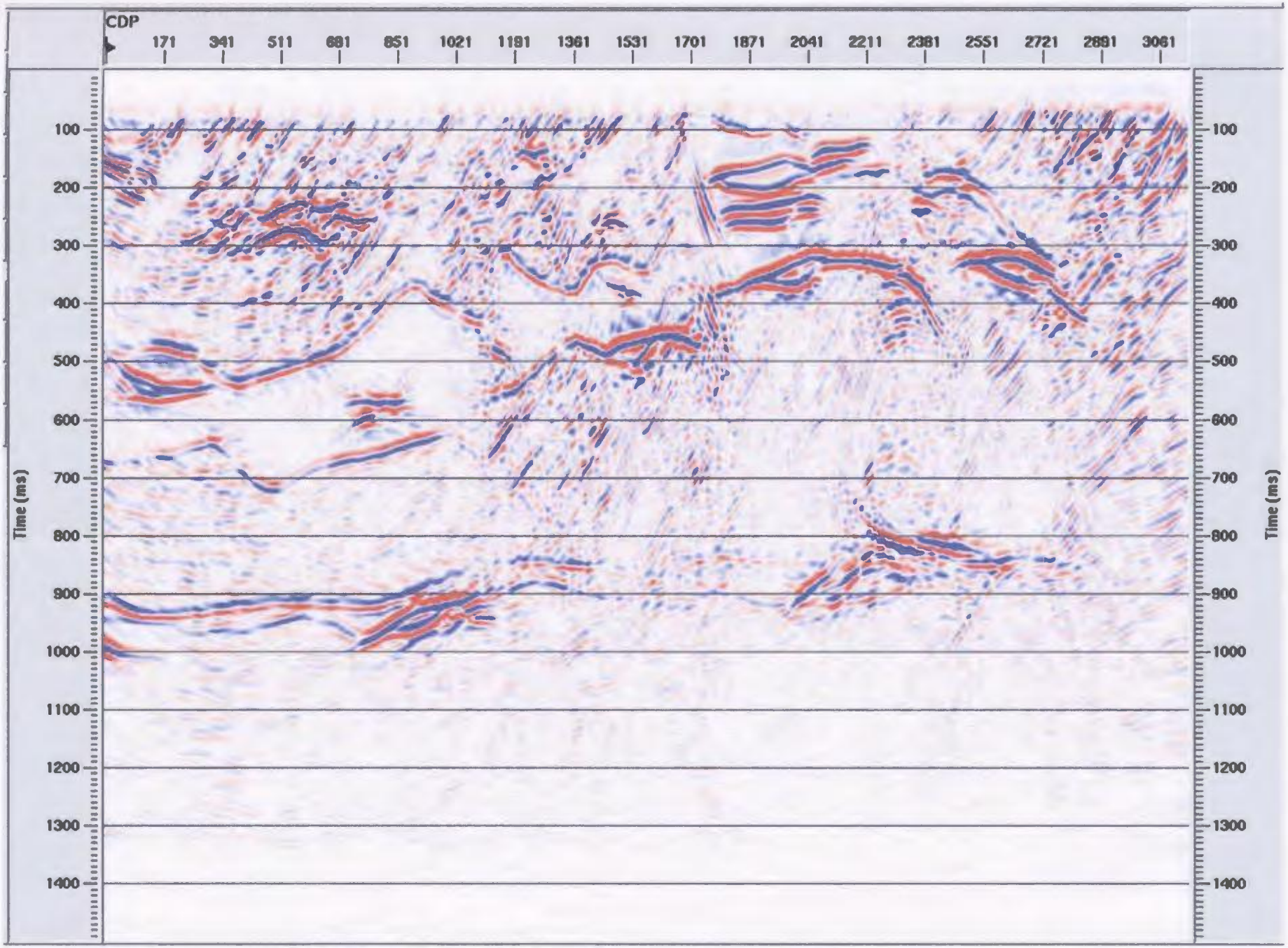


Figure 3.5.2.33: Illustrates the final post-stack time migration for the heterogeneity model with offsets +/-1000 m.

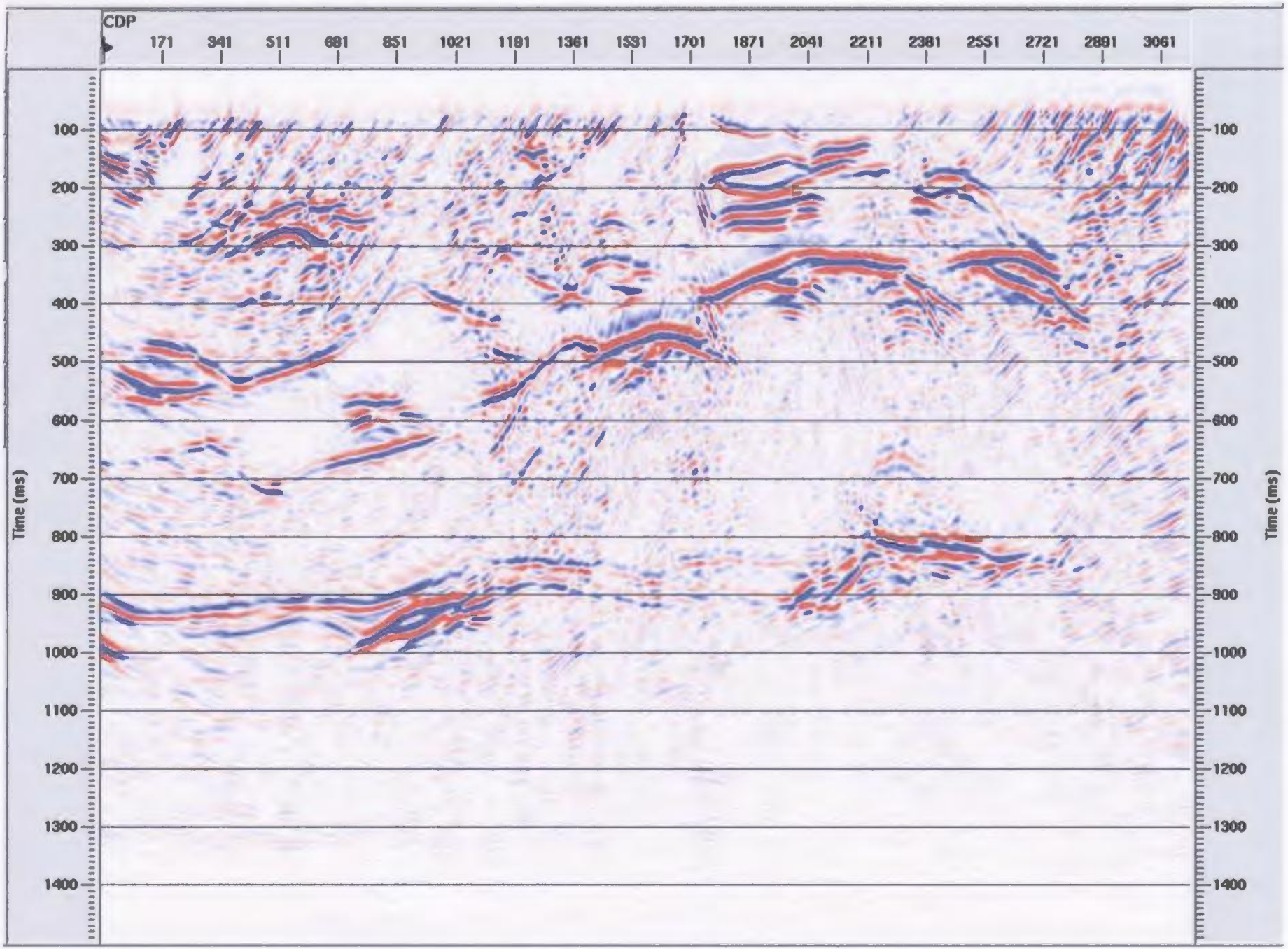


Figure 3.5.2.34: Illustrates the final post-stack time migration for the heterogeneity model with offsets +/-2000 m.

may destroy information that appears only at certain offsets, such as the far offsets in this case (for example: Figures 3.5.2.9 and 3.5.2.10; Kessinger, 2005). Consequently both the functions of stacking and post-stack migration are replaced by pre-stack migration, which may be a more appropriate method of dealing with 2-D surface seismic data from hardrock environments.

- **3.5.3 Scheme B**

- Pre-Processing

The same pre-processing scheme used in Section 3.5.2 was also utilized for this section.

- Pre-stack Migration

Pre-stack depth migration is superior to pre-stack time migration when structures are complex and large variations in lateral velocity occur; however, it does require a more accurate velocity model (Albertin et al., 2002). Pre-stack depth migration requires a more accurate approximation of the velocity field for the model than either post-stack and pre-stack time migration in order to accurately image reflections and diffractions. Creation of an appropriate velocity model requires appropriately detailed knowledge of the local geology and can be time consuming depending on the degree of complexity of the geology (Albertin et al., 2002). An interval velocity versus depth file was created based on knowledge of the geology for the Voisey's Bay area and the working model for the development of the Voisey's Bay deposit (Cruden et al., 2000) (Figure 3.5.3.1). This file was then used to create pre-stack depth migrations for both the simplified and heterogeneity models.

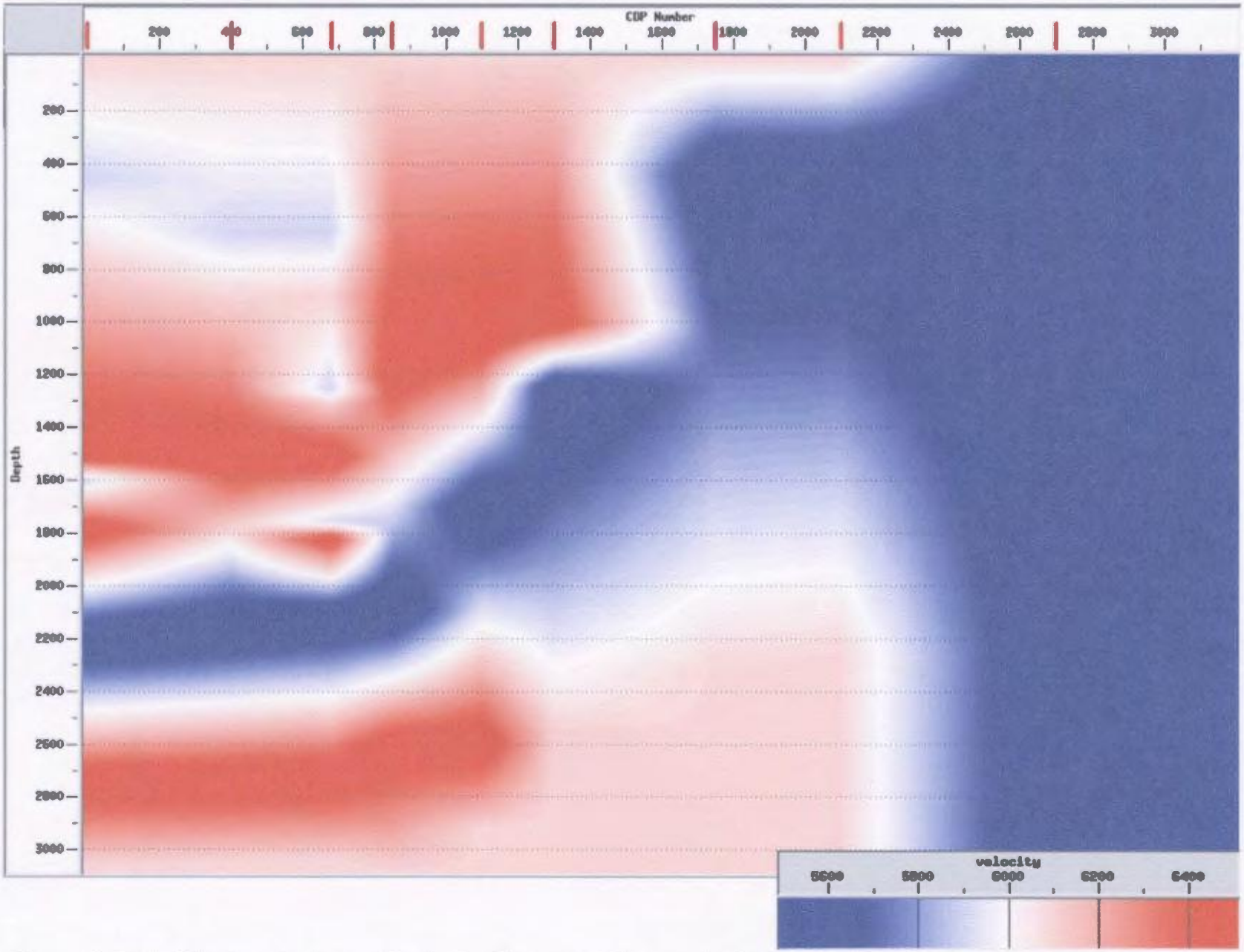


Figure 3.5.3.1: Displays the interval velocity file created for use in the pre-stack depth migration algorithm.

The main difference between post-stack and pre-stack migration is that post-stack assumes that the data are zero-offset whereas pre-stack assumes the data are nonzero-offset (Yilmaz and Doherty, 1987). Instead of summing along the zero-offset diffraction hyperbolas as is done for post-stack migration, amplitudes are summed along the nonzero-offset traveltime trajectories for pre-stack migration (Yilmaz and Doherty, 1987). Pre-stack Kirchhoff depth migration performs a migration by applying a Green's function to each CDP location using a traveltime map, which relates the time from each surface location to a region of points in the subsurface. This algorithm was applied to common-offset gathers for this particular dataset but can also be applied to shot gathers. An implicit eikonal solver method was used for the traveltime map computation. This particular method is fast since it only computes the first arrival and does not calculate amplitudes. If a very strong gradient existed problems could potentially arise; however, that is not the case for this particular dataset. Since aperture width, which determines the width of the traveltime maps to the left and right of a given surface location, can greatly affect the performance of the Kirchhoff depth migration the migration aperture was set to default for each model such that the algorithm retrieves the most suitable aperture. In addition, since the Kirchhoff depth migration is strongly dependent upon the velocity model, several iterations were necessary to fine-tune the velocity model. Several CDP gathers were analyzed for both the simplified and heterogeneity models to assess the accuracy of the velocity model (Figures 3.5.3.2-3.5.3.3 and 3.5.3.4-3.5.3.5, respectively). In order to keep

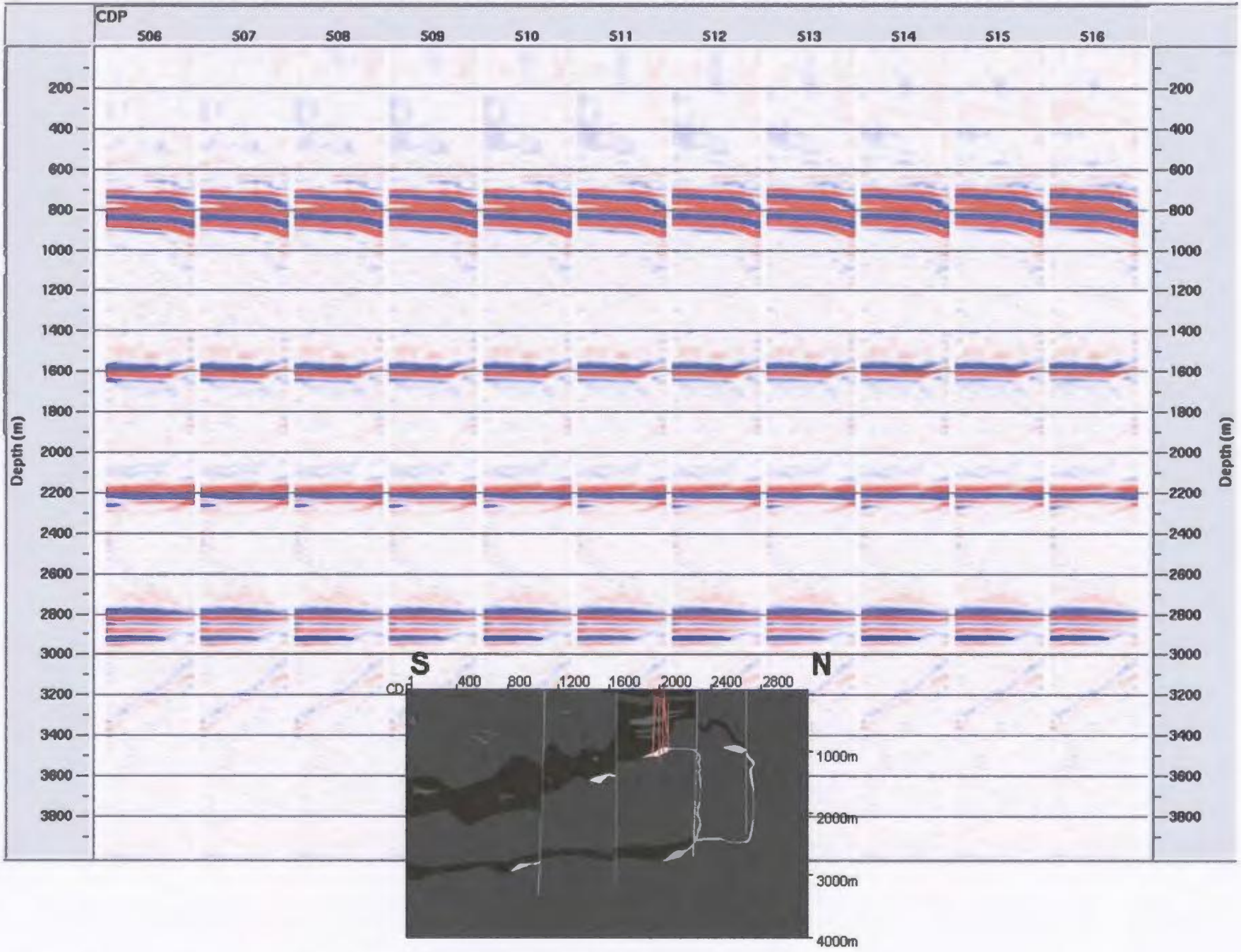


Figure 3.5.3.2: Displays CDP gathers 506-516 for the simplified model.

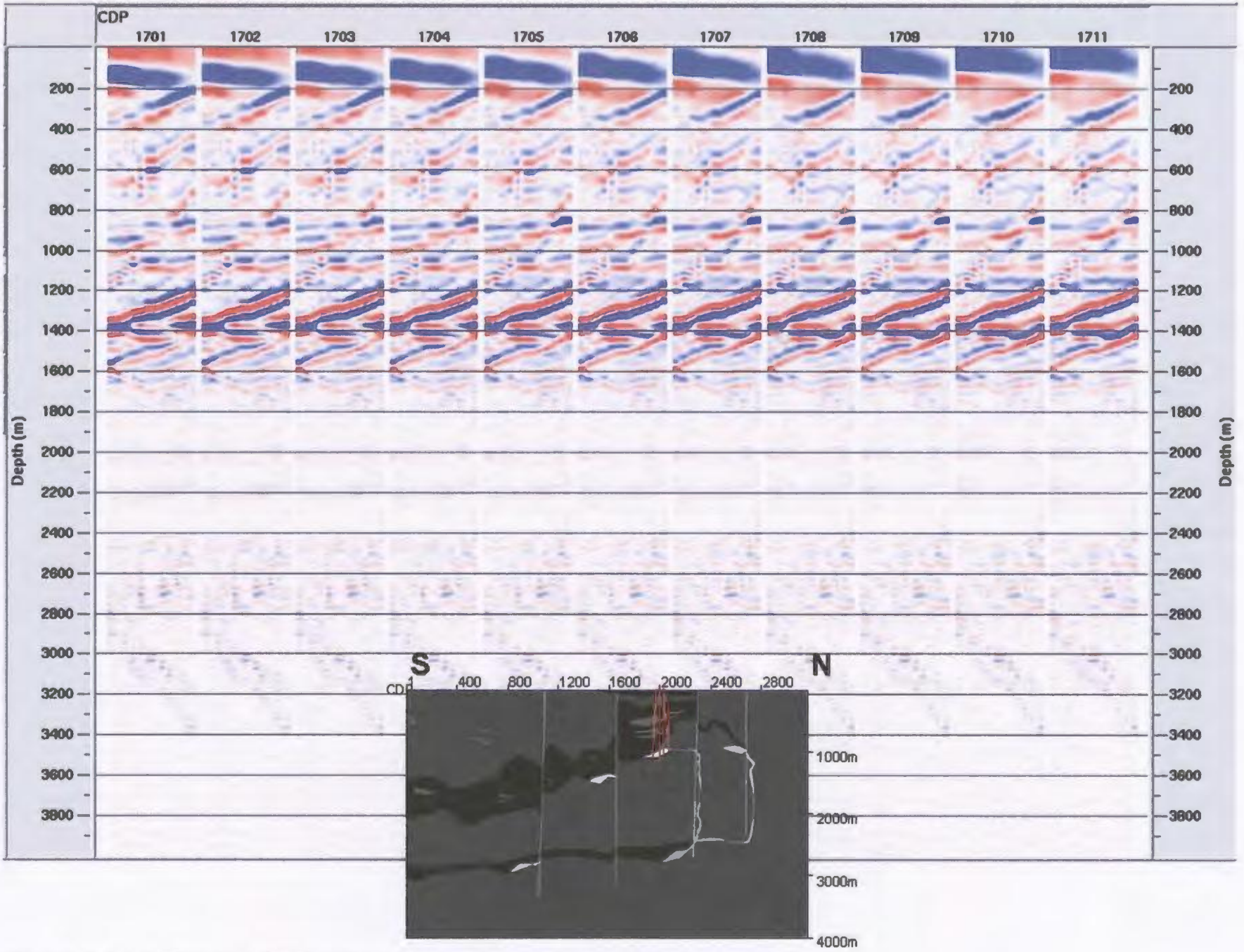


Figure 3.5.3.3: Displays CDP gathers 1701-1711 for the simplified model.

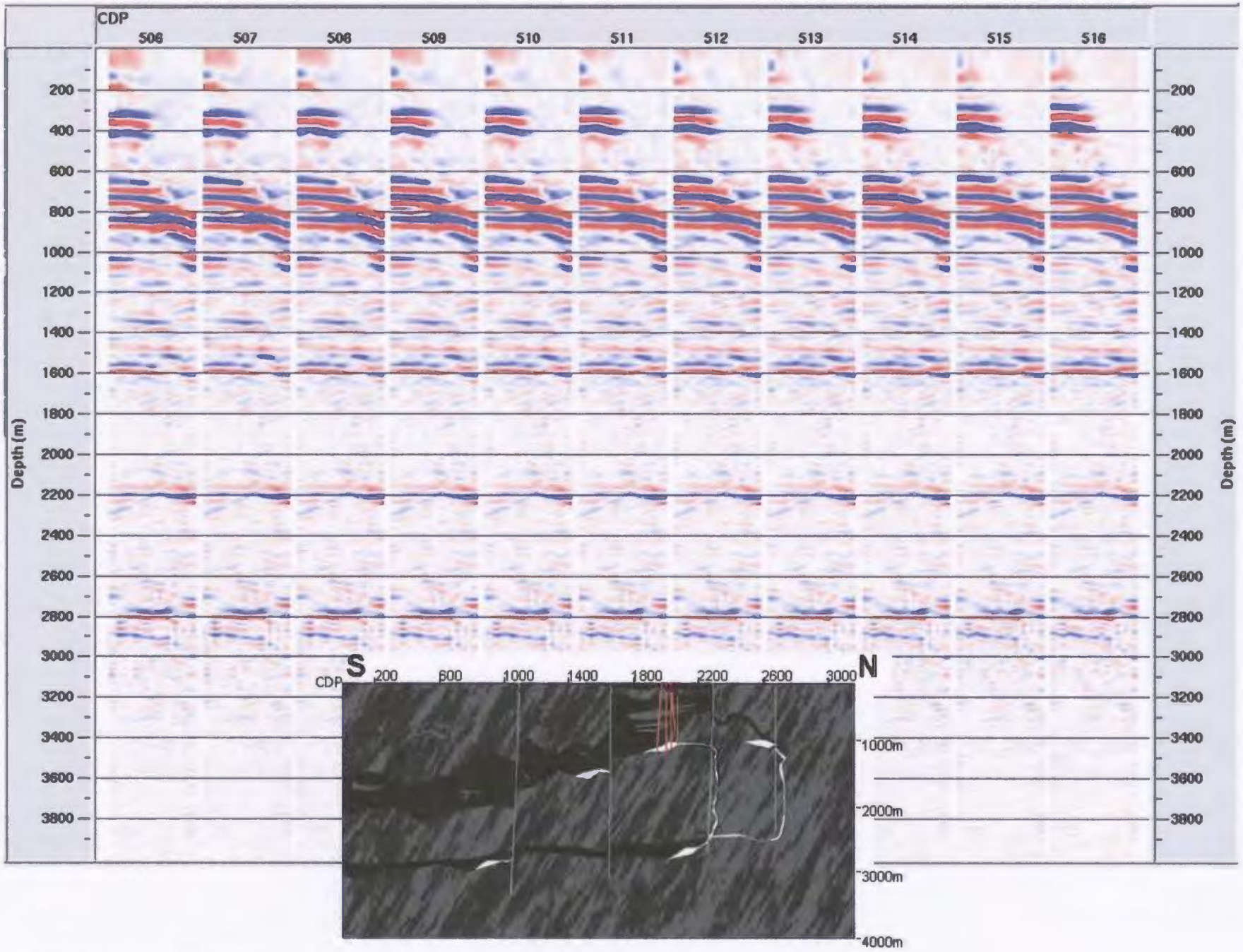


Figure 3.5.3.4: Displays CDP gathers 506-516 for the heterogeneity model.

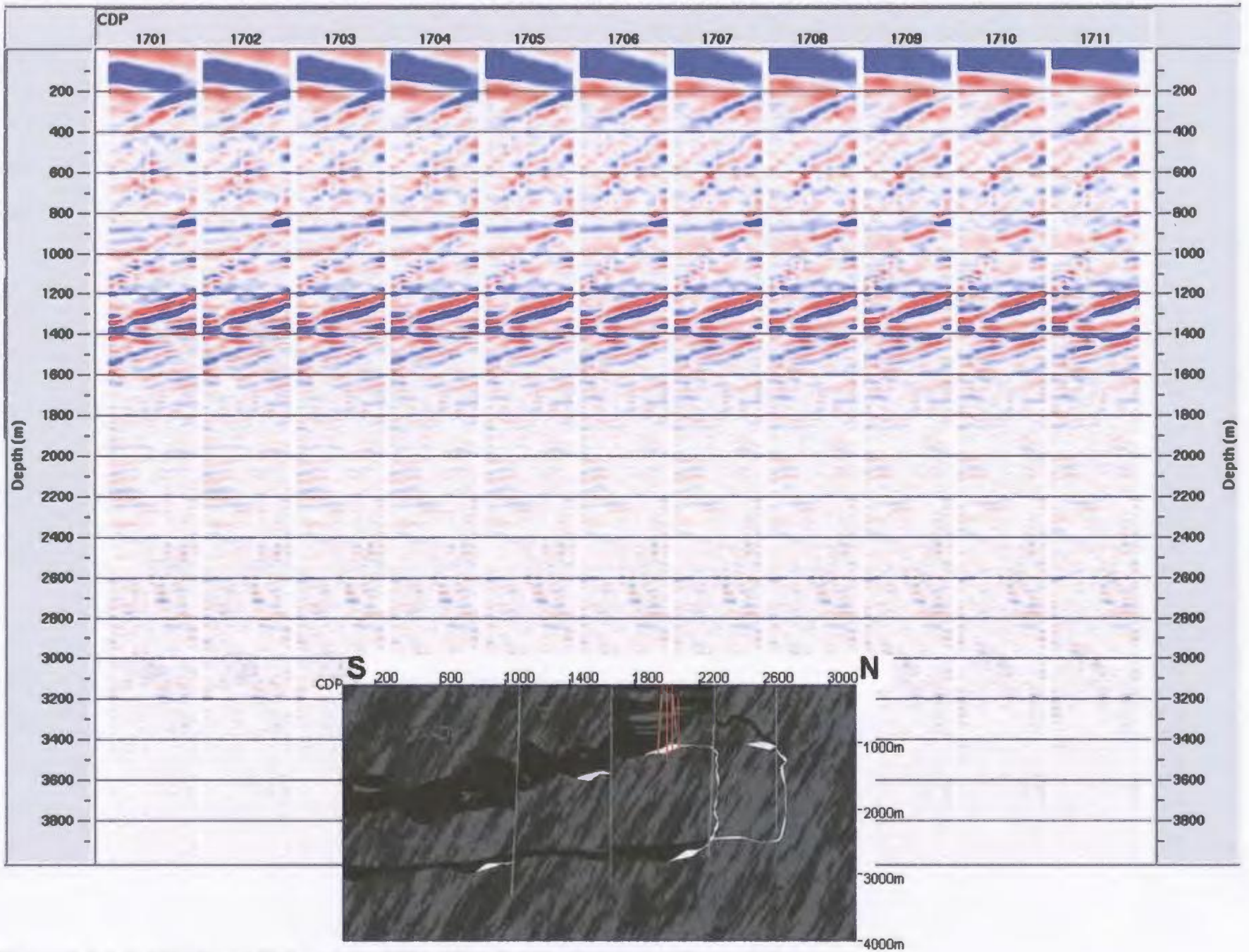


Figure 3.5.3.5: Displays CDP gathers 1701-1711 for the heterogeneity model.

processing costs down and since limited offsets have proved to be valuable for this dataset, pre-stack migration was performed on limited offsets of 0-2000 m with a 200 m increment for both the simplified and heterogeneity models. Figure 3.5.3.2 shows that the velocity model worked well for the majority of the events in this area except for the first prominent event at 800 m which appears to be slightly under-corrected. This indicates that too high of a velocity was used. Figure 3.5.3.3 shows that the velocity model was not very accurate in this area and a lot of the events are over-corrected. This indicates that too low a velocity was used. Figures 3.5.3.4 and 3.5.3.5 illustrate that these same problems are evident for the heterogeneity model as well. The CDP gathers for the heterogeneity model also show that the velocity model has dealt reasonably well with the foliation of the gneiss (Figures 3.5.3.4 and 3.5.3.5).

- Stack

Once pre-stack migration was completed the data were then sorted from offset gathers back to CDP gathers such that CDP stacking could be completed. An arithmetic mean horizontal stacking algorithm was utilized for stacking as discussed in Section 3.5.2. Figures 3.5.3.6 and 3.5.3.7 demonstrate that pre-stack migration compared to post-stack migration (Figures 3.5.29-3.5.34) dealt better with the conflicting velocities for the diffractions and specular reflections that were present in this typical mineral exploration dataset. In particular, the energy from the majority of the events including the faults focuses more appropriately.

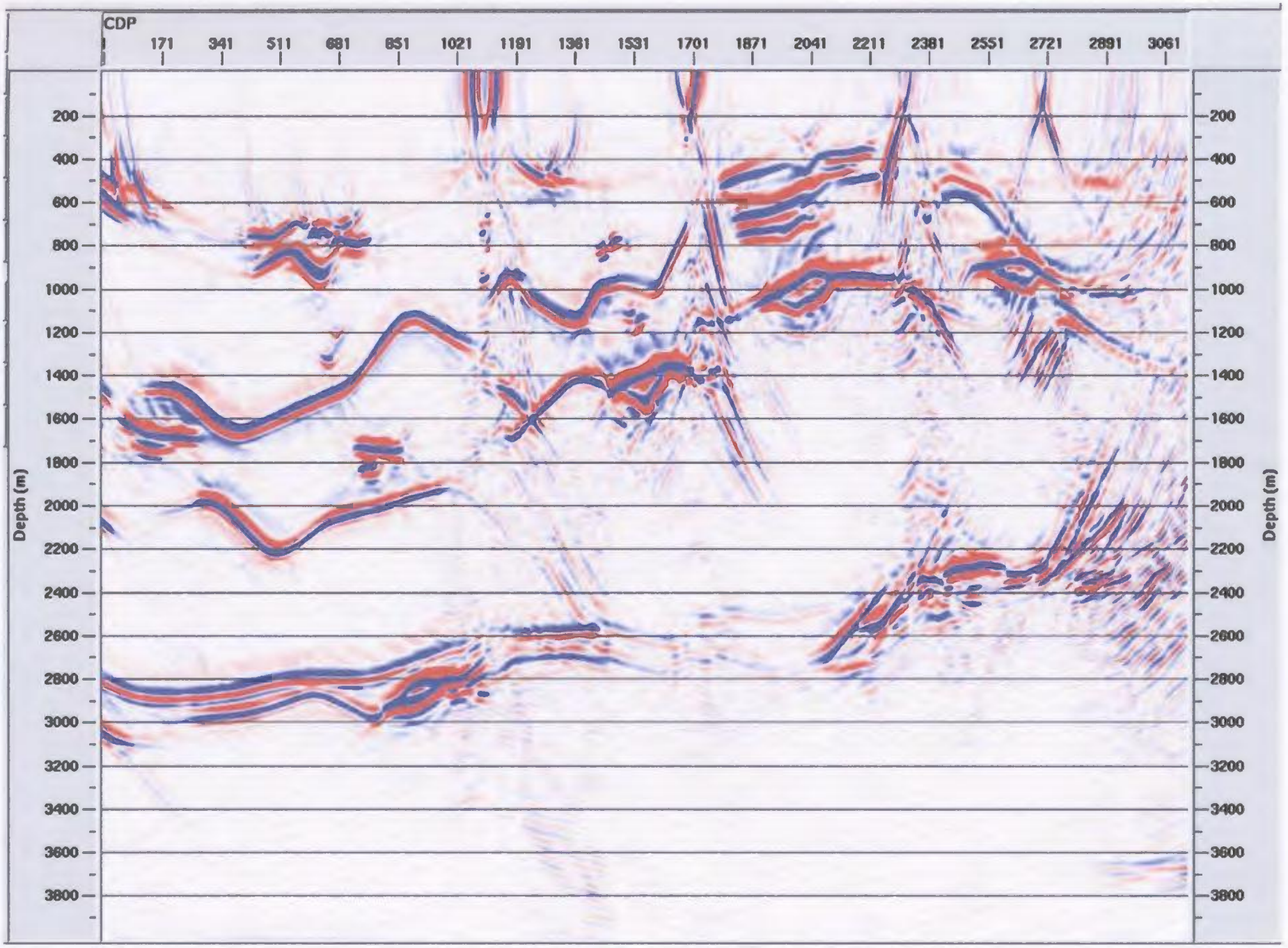


Figure 3.5.3.6: Final stacked pre-stack depth migration for simplified model.

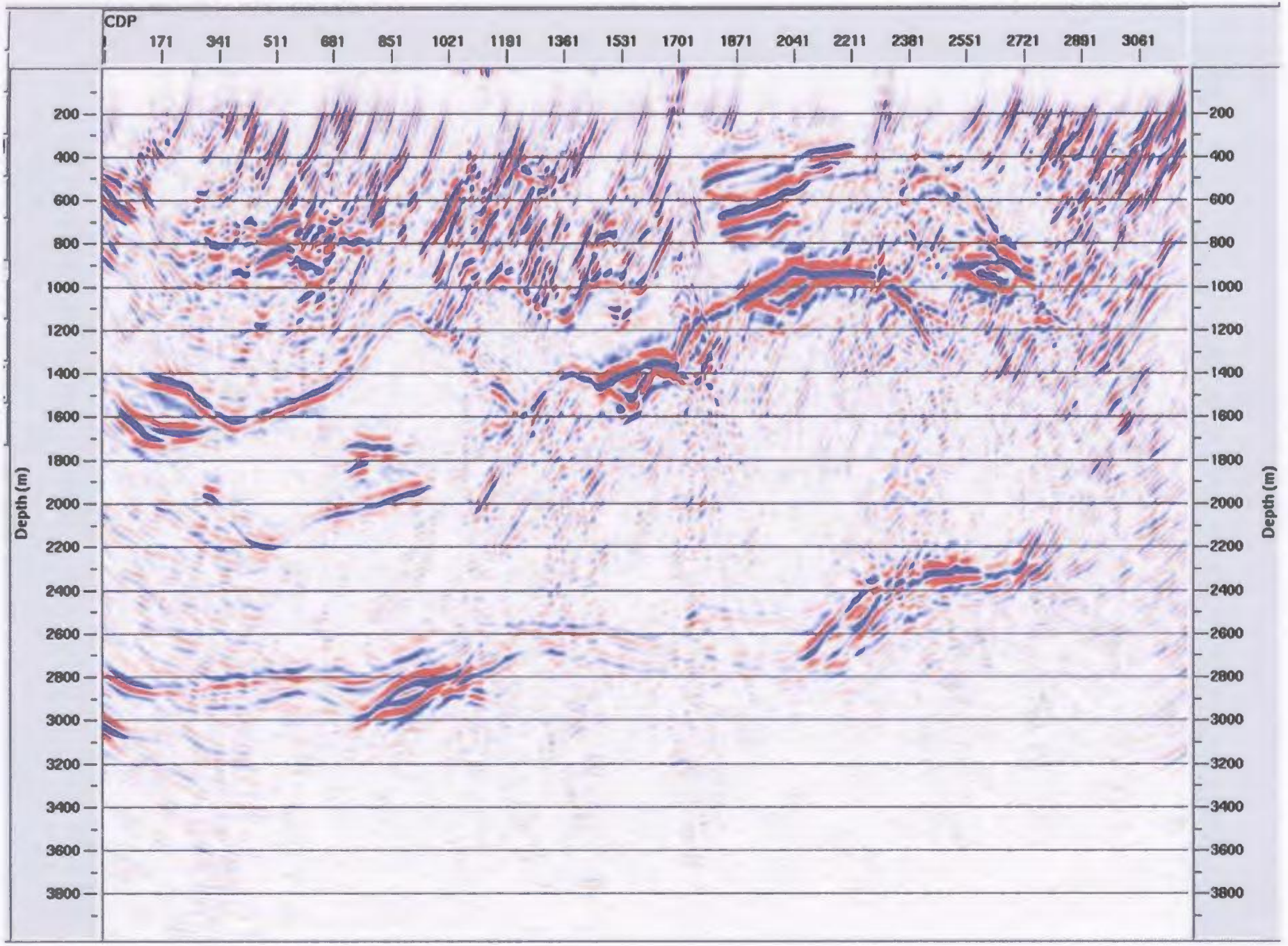


Figure 3.5.3.7: Final stacked pre-stack depth migration for the heterogeneity model.

In spite of this, every event was not migrated flawlessly because the pre-stack migration algorithm is extremely velocity-sensitive. Previous analysis of the CDP gathers demonstrated that the velocity model utilized for these particular pre-stack migrations could use further fine-tuning. Therefore further iterations could potentially produce an even better pre-stack image; however, since the purpose of undertaking pre-stack migration was to assess the validity of the technique for mineral exploration datasets, fine-tuning of the velocity model was not pursued.

Processing of this synthetic dataset has confirmed that the reflection wave field is generally dominated by scattering rather than specular reflection in areas with relative geometric complexity and heterogeneity, which is the geologic environment typical of many ore deposits. As a result, past attempts at applying 2-D exploration seismic techniques for direct detection of massive sulphide bodies have met with only limited success. However, this 2-D synthetic survey has demonstrated that by applying appropriate processing techniques tailored to deal with the issues resulting from attempting to retain both specular reflections and diffractions in a dataset, it should be possible to use reflection seismic techniques successfully in a mineral exploration environment.

### 3.6 Velocity Gradients

Surface-to-surface seismic tomography may be appropriate for delineating the magmatic plumbing system at Voisey's Bay. Figures 3.3.3.4 and 3.3.3.5 show both the orthogneiss and paragneiss velocity gradient models respectively. Visual inspection of

the wave fields for both these models for all offsets revealed that the depth of penetration of the turning rays was only approximately 500 m for the orthogneiss and 1000 m for the paragneiss. In addition, this maximum depth of penetration was only achieved near the middle of the models (near CDP range 1700-1900) thus there will be little ray coverage for the entire model. Extending the length of the seismic line may help create better ray coverage but it would also increase the cost of the survey. Considering that the previous section did not seem to benefit from the far-offset data, this may not be a very economical approach. The specified velocity gradients are laboratory-based and principally rely on the closure of micro-cracks with increasing pressure. As a result, the specified velocity gradients can be considered minima and therefore the average velocity gradients for both the orthogneisses and paragneisses are most likely higher. Unfortunately, at present there is no way of knowing how much higher they may be. Consequently, based on this information alone, surface seismic tomography is most likely not beneficial for delineating the magmatic plumbing system at Voisey's Bay due to the weak velocity gradients in both the Eastern Deeps and Reid Brook zones.

In spite of the previous conclusion, examination of the wave fields illustrated that many of the geologic features in the model were detected in the wave field (Figure 3.6.1(a-g)). In particular, features in the southern portion of the model were detected, such as two of the faults and four of the massive sulphide bodies. However the wave field in the most northern portion of the model was intensely scattered and therefore difficult to distinguish any of the features. This intense scattering response could be related to the vertical massive sulphide feeders which are only present in the northern portion of the model.

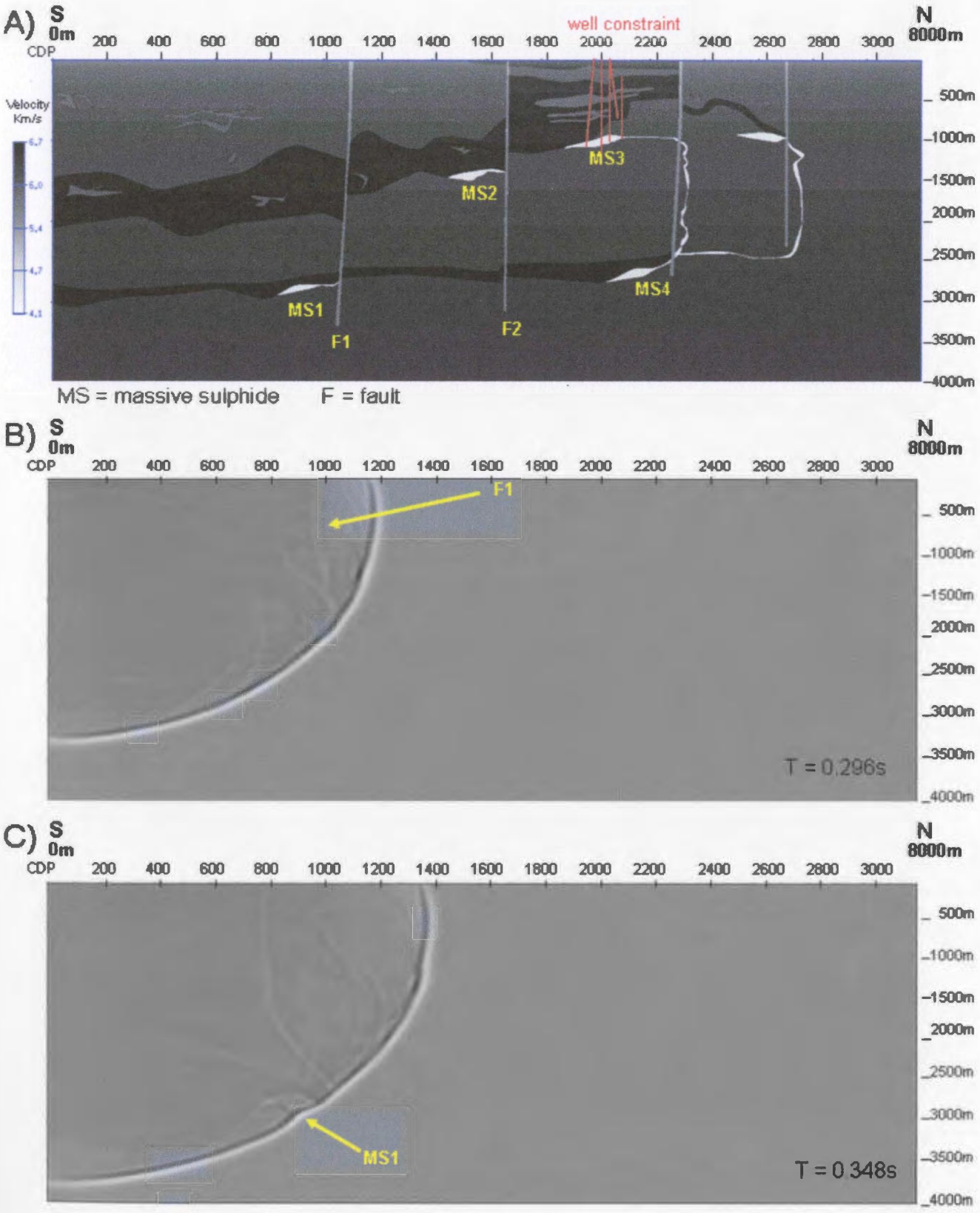
A)
S
0m
N
8000m
CDP
200 400 600 800 1000 1200 1400 1600 1800 2000 2200 2400 2600 2800 3000
well constraint
Velocity
Km/s
6,7
6,0
5,4
4,7
4,1
MS1
MS2
MS3
MS4
F1
F2
500m
1000m
1500m
2000m
2500m
3000m
3500m
4000m
MS = massive sulphide
F = fault
B)
S
0m
N
8000m
CDP
200 400 600 800 1000 1200 1400 1600 1800 2000 2200 2400 2600 2800 3000
F1
T = 0.296s
500m
1000m
1500m
2000m
2500m
3000m
3500m
4000m
C)
S
0m
N
8000m
CDP
200 400 600 800 1000 1200 1400 1600 1800 2000 2200 2400 2600 2800 3000
MS1
T = 0.348s
500m
1000m
1500m
2000m
2500m
3000m
3500m
4000m

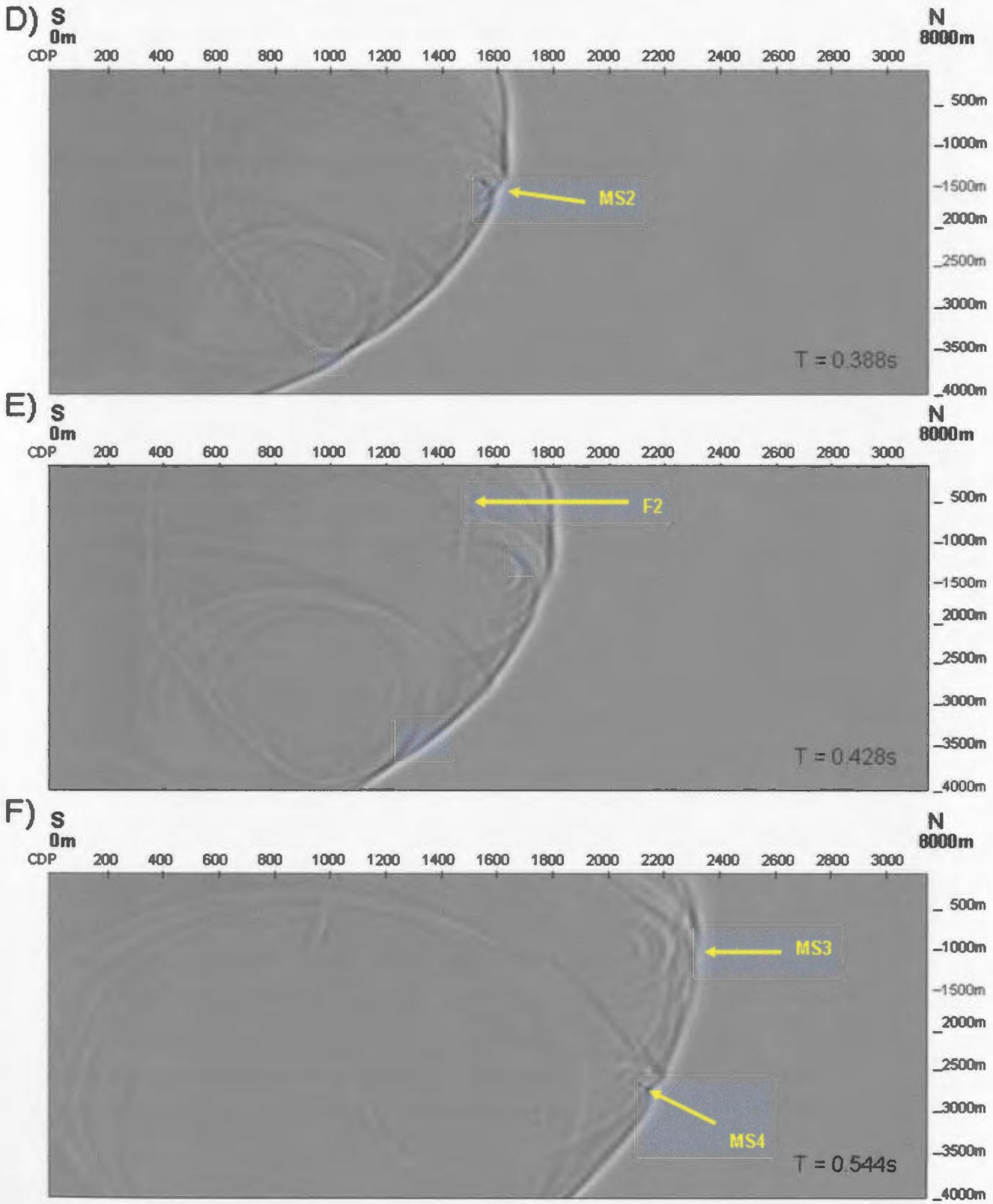
D)
S
0m
N
8000m
CDP
200
400
600
800
1000
1200
1400
1600
1800
2000
2200
2400
2600
2800
3000
500m
1000m
1500m
2000m
2500m
3000m
3500m
4000m
MS2
T = 0.388s
E)
S
0m
N
8000m
CDP
200
400
600
800
1000
1200
1400
1600
1800
2000
2200
2400
2600
2800
3000
500m
1000m
1500m
2000m
2500m
3000m
3500m
4000m
F2
T = 0.428s
F)
S
0m
N
8000m
CDP
200
400
600
800
1000
1200
1400
1600
1800
2000
2200
2400
2600
2800
3000
500m
1000m
1500m
2000m
2500m
3000m
3500m
4000m
MS3
MS4
T = 0.544s

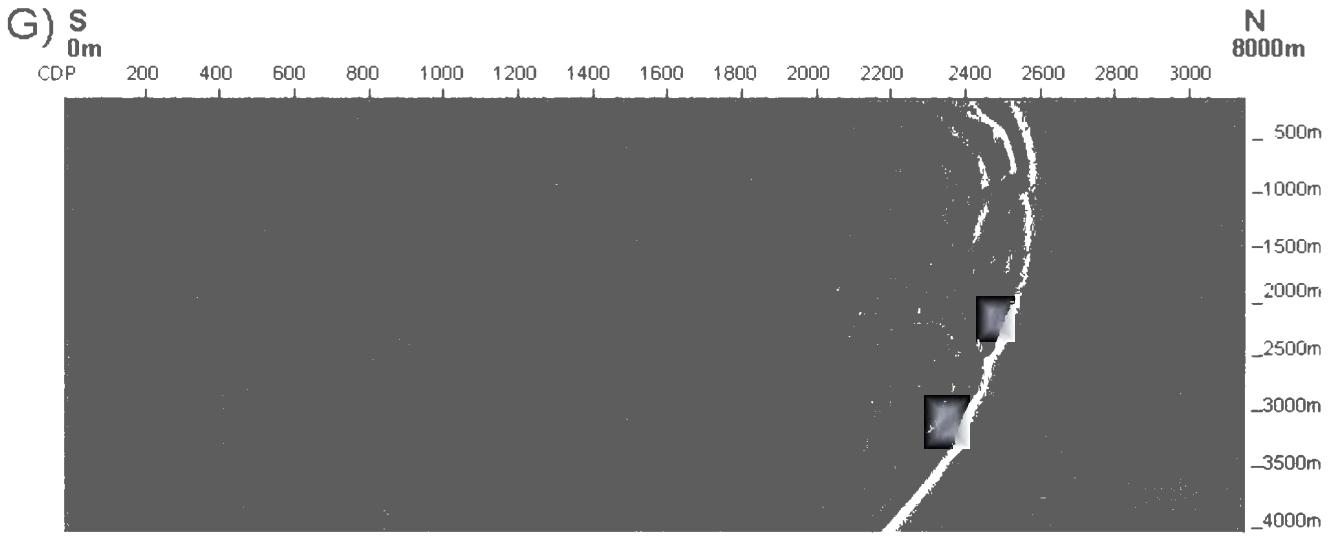


Figure 3.6.1: A) orthogneiss velocity gradient model, B) wave field illustrating F1, C) wave field illustrating MS1, D) wave field illustrating MS2, E) wave field illustrating F2, F) wave field illustrating MS3 and MS4, and G) complex wave field. The same features were exhibited for the paragneiss velocity gradient model and thus were not shown due to redundancy.

## 3.7 Heterogeneity Mapping

- **3.7.1 Introduction**

A contrast exists in the petrofabric between the foliated gneiss which is the country rock and the troctolitic intrusion which hosts the sulphide mineralization. This contrast may be detectable using reflection seismic techniques and as result there may be potential to delineate the magmatic plumbing system at Voisey's Bay by exploiting this contrast. Resolution and localization of heterogeneity has the greatest potential with high-resolution seismic techniques such as reflection seismic as opposed to other various low-resolution techniques such as potential fields (Hurich, 2004). In particular, a technique based on heterogeneity mapping, which localizes subtle variations in the reflection wave field, will be investigated (Hurich, 2007 (in review)).

Geologic heterogeneity has been found through spatial statistics and physical property analyses to commonly be discontinuous or modal with self-similar spatial properties (Hurich, 2004). As a result, geologic heterogeneity is often parameterized as a von Kármán process. The von Kármán process is described by variance, correlation length, and Hurst number (Goff and Jordan, 1988). The correlation length represents the distance beyond which the wave field decays from a scaling process to an uncorrelated process or white noise (Hurich, 2007 (in review)). The Hurst number defines the exponent of the power law that characterizes the scaling characteristics at distances less than the correlation length. In general, the correlation length and the Hurst number express noticeably different features of the wave field. However, for the purposes of geologic description they can be combined into a single parameter to define a third parameter F* (Hurich, 2003; Hurich, 2007 (in review)). F* can be considered a description of the fabric of the wave field that in general is related to the macro-scale petrofabric of a rock body.

Hurich, 2007 (in review) has demonstrated that heterogeneity mapping produces detailed maps of the statistical parameters (correlation length, Hurst number, and F*) by mapping the data with a sliding analysis window. The advantage of this mapping procedure is that it can detect and localize nonstationarity in the reflection wave field and therefore highlight variations that are related to geology. The size of the local analysis window and the amount of overlap between individual windows are what establishes the resolution of the heterogeneity mapping technique. As a rule of thumb, the analysis window should only be as small as one that still allows stable estimates of all of the

statistical attributes. It is essential that heterogeneity mapping be used with the same attention to data quality as required by any other interpretation process because non-stationary noise and variations in amplitude and/or reflection coherence will cause variability in the heterogeneity maps.

- **3.7.2 Maps**

Heterogeneity mapping was applied to the seismic wave field of the heterogeneity model after pre-stack depth migration (Figure 3.7.2.1) by using an analysis window with dimensions of 250 m by 75 m. The analysis window slid with increments of 25 m laterally and vertically until the seismogram was completely mapped. The spatial statistics determined by this procedure were established by autocorrelation whereby the analyses presented in this section were based on methods determined by Hurich and Kocurko (2000). His method derives the autocorrelation matrix by a Fourier transform-based estimation of the 2-D power spectrum to obtain the autocorrelation. The observed autocorrelation was then fit to the Von Kármán model through a least-squares optimization procedure. The heterogeneity mapping program was also set up to allow for dips between -70° and 70° which was the average dip of the fabric of the gneisses. A dip factor of 1.5 was then used for this synthetic data as a smoothing operator to ensure that the autocorrelation function was anisotropic. Essentially, the dip factor measures the orientation of the long axis of the autocorrelation function and provides an estimation of the apparent dip of the dominant energy in x-t space (Figure 3.7.2.2; Hurich, 2003). This

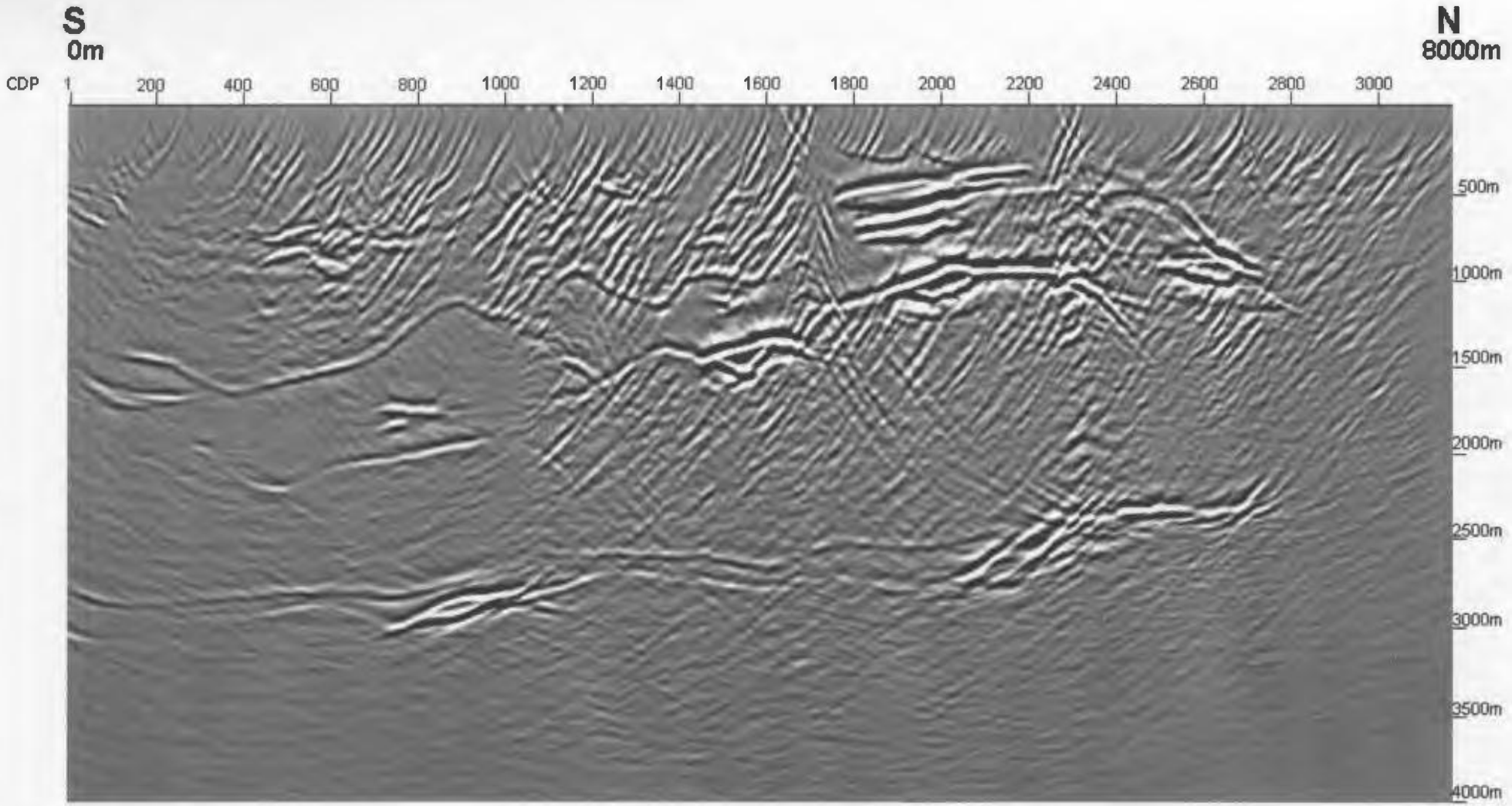


Figure 3.7.2.1: Final pre-stack depth migration for the heterogeneity model.

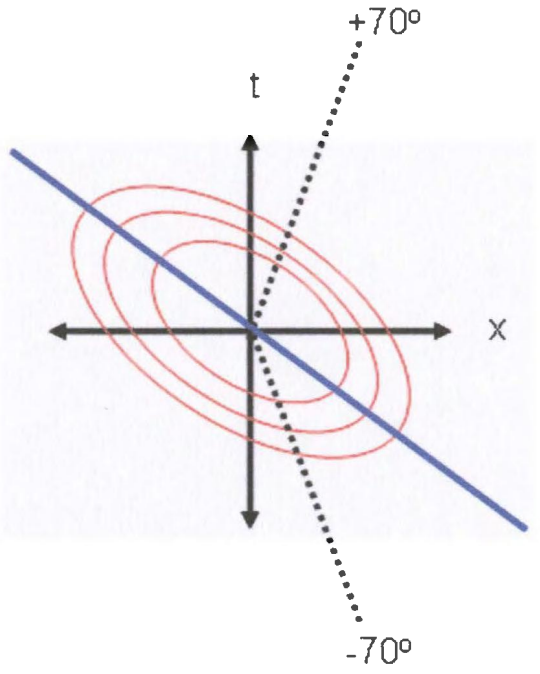


Figure 3.7.2.2: Diagram illustrates the theory behind the dip factor. The red circles correspond to the contours of the 2-D autocorrelation function. The blue line corresponds to the longest axis of the 2-D autocorrelation function.

was then related to the geologic dip present in the dataset such that if the longest axis was not more than 1.5 times the mean of all of the other possibilities between -70° – 70° then it was rejected. Figure 3.7.2.3 illustrates that the general dip trend for the model was approximately 70° which was the average fabric of the gneisses. The maximum frequency content for this dataset was 90 Hz which provides low resolution and affects the dimensions of the analysis window making them somewhat smaller than ideal.

Neither the correlation length map, the Hurst number map nor the F* map provide much discrimination of the variations in the character of the reflectivity due to fabric variations (Figures 3.7.2.4-3.7.2.6, respectively), a result contradictory to our expectations based on the seismic data (Figure 3.7.2.1). We suspect that the reason for these disappointing results was that the mapping technique was relatively insensitive to

amplitude variations. Since the autocorrelation for each window was independently normalized, coherent energy of very low amplitudes may be dominating the response of the windows that visually appear to have little or no reflected or back-scattered energy. It was likely that the coherent energy in these windows was a numerical noise resulting from the finite-difference modeling scheme or was the result of incomplete migration of dipping events. To test this idea, random noise was added to the migrated seismic data in an attempt to de-correlate the low amplitude portions of the seismogram.

Noise with an S/N ratio of 25 with a Gaussian noise probability distribution was added to Figure 3.7.2.1 using a program in Seismic Unix (Figure 3.7.2.7). The S/N ratio was a function of the program and was characterized as follows:

$$Output = signal + [(scale)(noise)]$$

where,

$$scale = \left(\frac{1}{S/N}\right)\left[\frac{\left(\frac{abs\max\_signal}{\sqrt{2}}\right)}{\sqrt{energy\_per\_sample}}\right]$$

where S/N was the signal-to-noise ratio and absmax_signal was the absolute maximum signal present in the data. As a result, the specified S/N ratio entered into the program does not actually provide any direct indication of the actual S/N ratio for the data. A comparison between the seismogram with and without noise demonstrates that the applied S/N served to de-correlate only the lowest amplitude events in the seismogram (Figures 3.7.2.1 and 3.7.2.7, respectively).

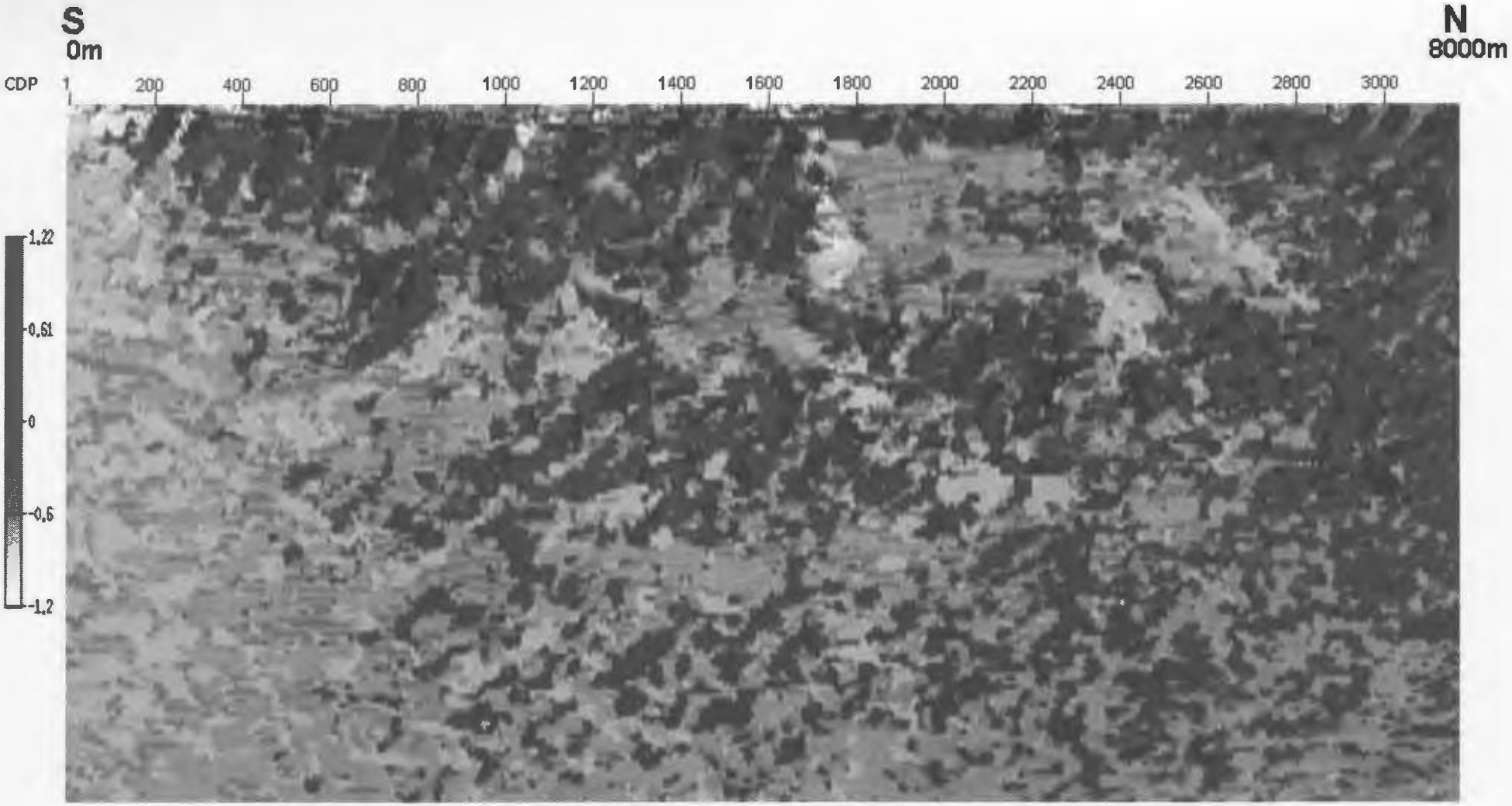


Figure 3.7.2.3: Dip map illustrating the dip trend mapped in the model. Legend scale is in radians where maximum corresponds to 70° and the minimum corresponds to -70°.

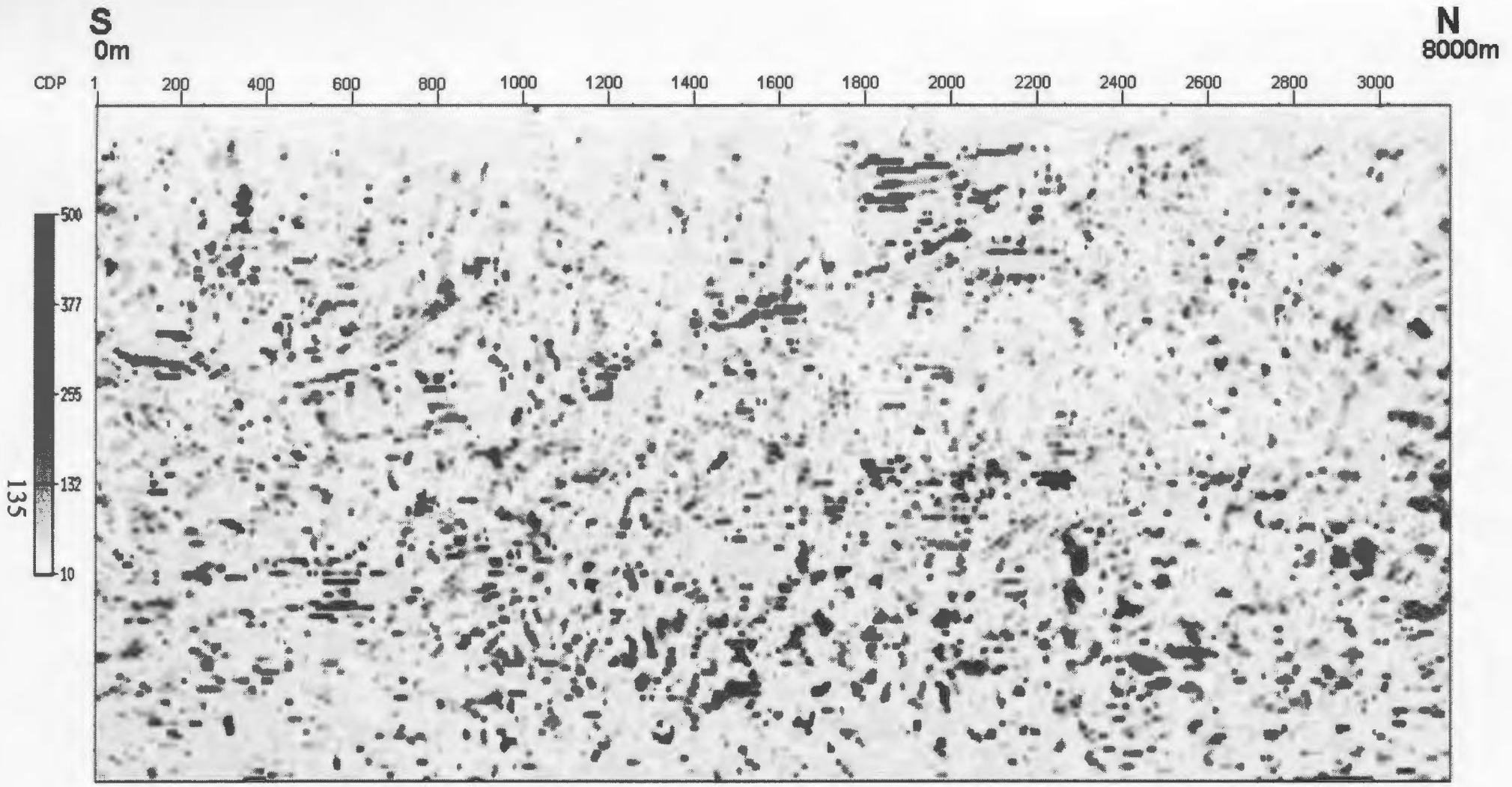


Figure 3.7.2.4: Correlation length map. Legend scale is in metres.

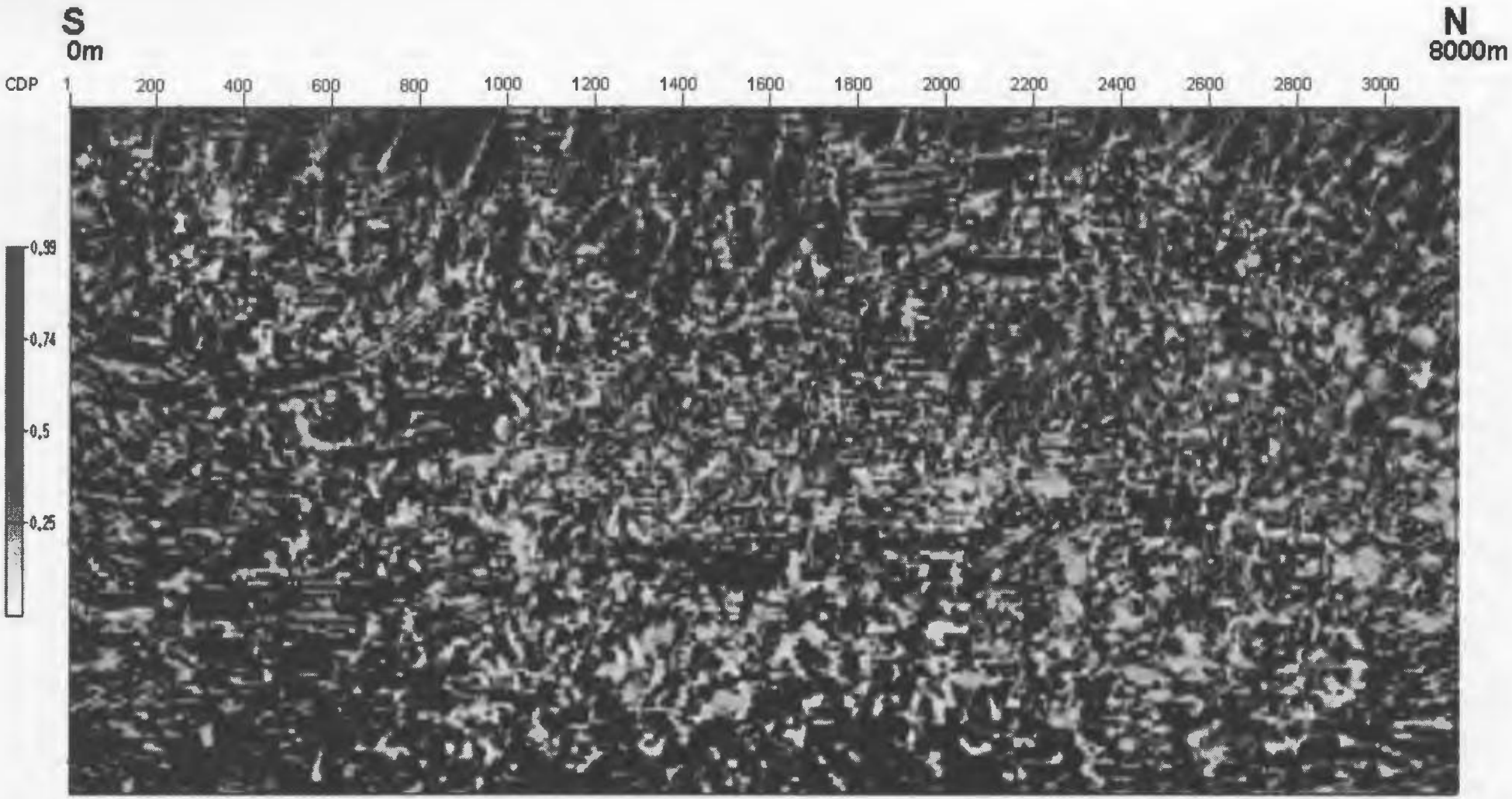


Figure 3.7.2.5: Hurst number map.

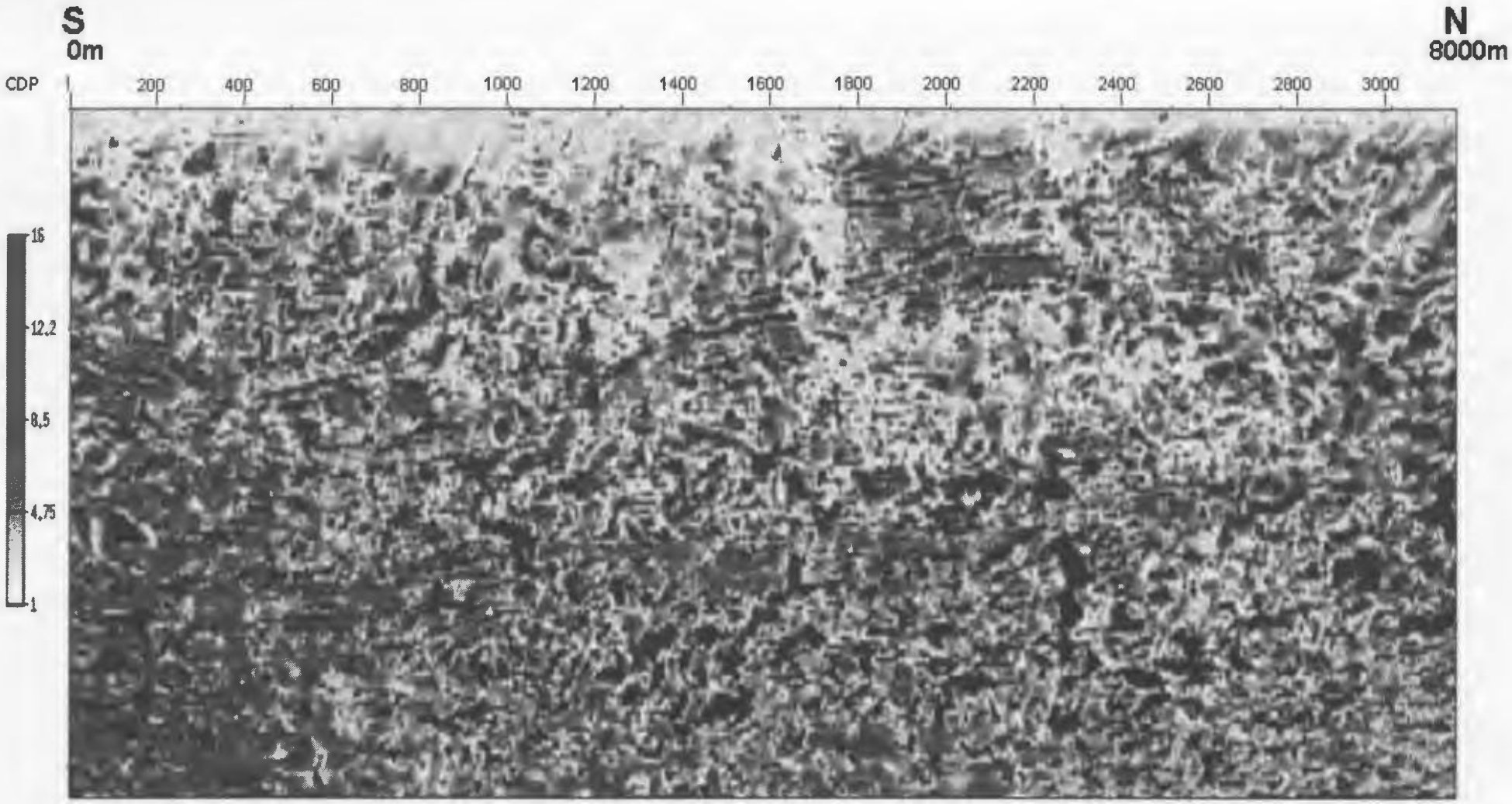


Figure 3.7.2.6: F* map.

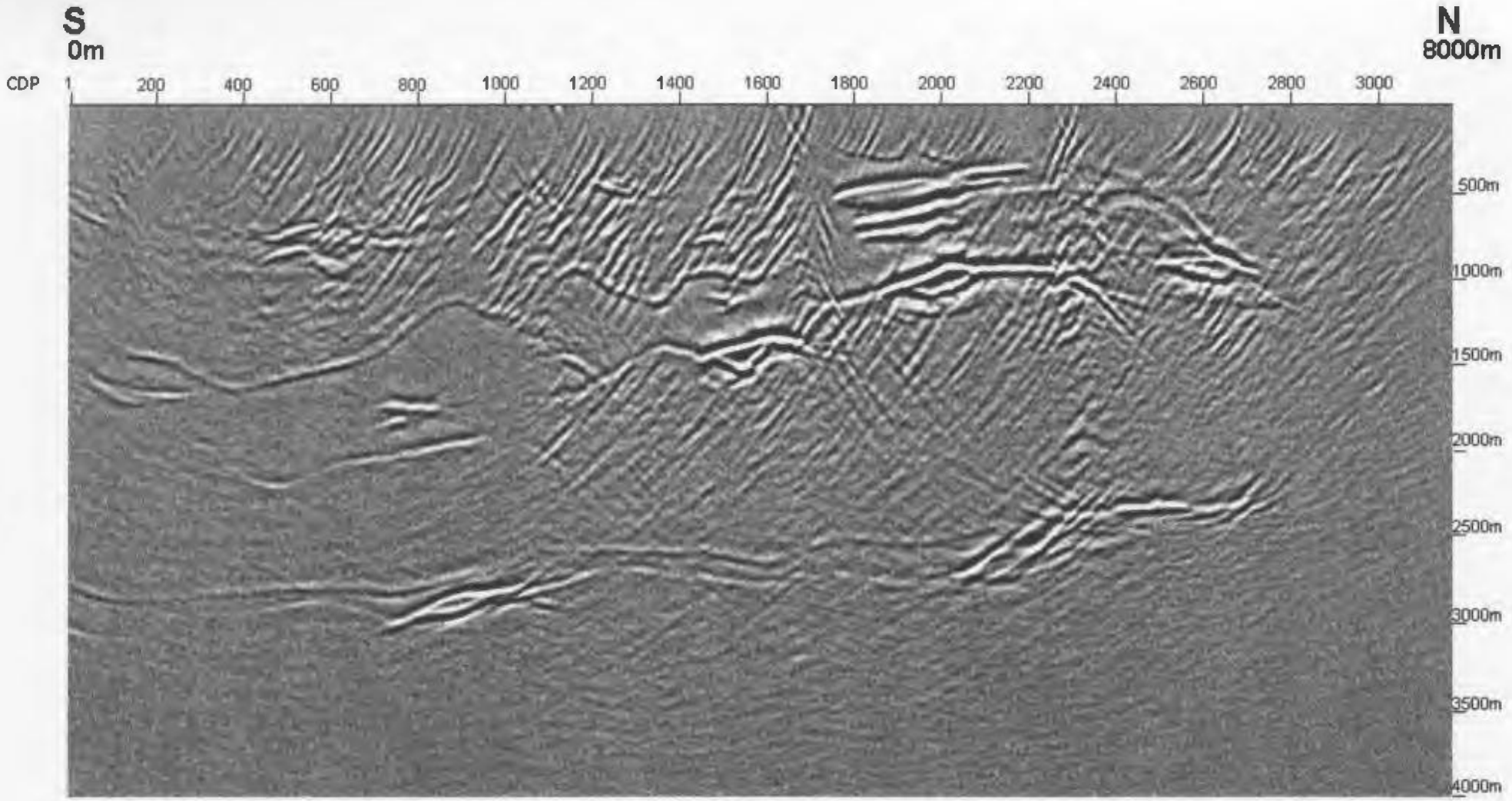


Figure 3.7.2.7: Final pre-stack depth migration for the heterogeneity model with noise based on a specified S/N of 25 added.

Heterogeneity mapping was again applied to the seismogram using the same window analysis and dip parameters as previously used. Figure 3.7.2.8 illustrates that, as in the previous example the dip of the strong events was recovered. In comparison to Figures 3.7.2.4-3.7.2.6, Figures 3.7.2.9-3.7.2.11 provide much better definition of the variations in the character of the reflectivity. Both the correlation length and the F* maps provide the same amount of detail with regards to the troctolite and the foliated gneiss while the Hurst number map appears to provide slightly more detailed mapping (Figures 3.7.2.9-3.7.2.11). Each of the statistical parameter maps were successful in distinguishing between the troctolite and the foliated gneiss in the southern portion of the model but were unsuccessful in the northern portion (Figures 3.7.2.9-3.7.2.11). Difficulty in distinguishing between the troctolite and the foliated gneisses in the northern portion of the model may be attributed to the fact that the troctolite packages in that area were thinner and fall below the resolution of the heterogeneity mapping and to the failure of the migration to completely move dipping events into the correct location.

## 3.8 Conclusions

The Voisey's Bay site offers a wide range of viable seismic targets of differing complexity which will be used to develop suitable acquisition and processing techniques for minerals exploration. 2-D forward modeling studies designed to study and fine-tune the acquisition and processing sequence best-suited for hardrock environments provides the basis for design of the field experiments.

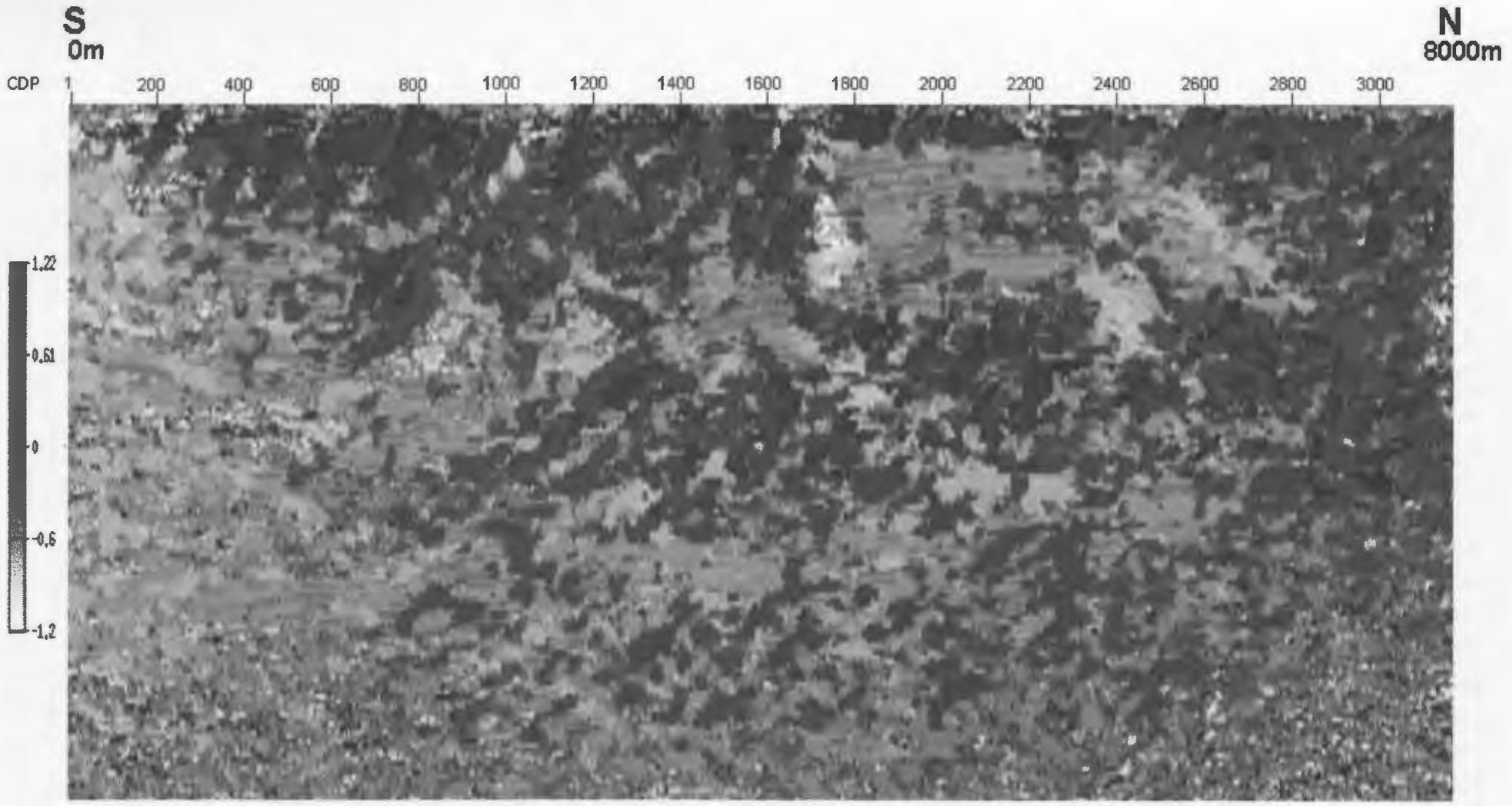


Figure 3.7.2.8: Dip map illustrating the dip trend mapped in the model with noise. Legend scale is in radians where maximum corresponds to 70° and the minimum corresponds to -70°.

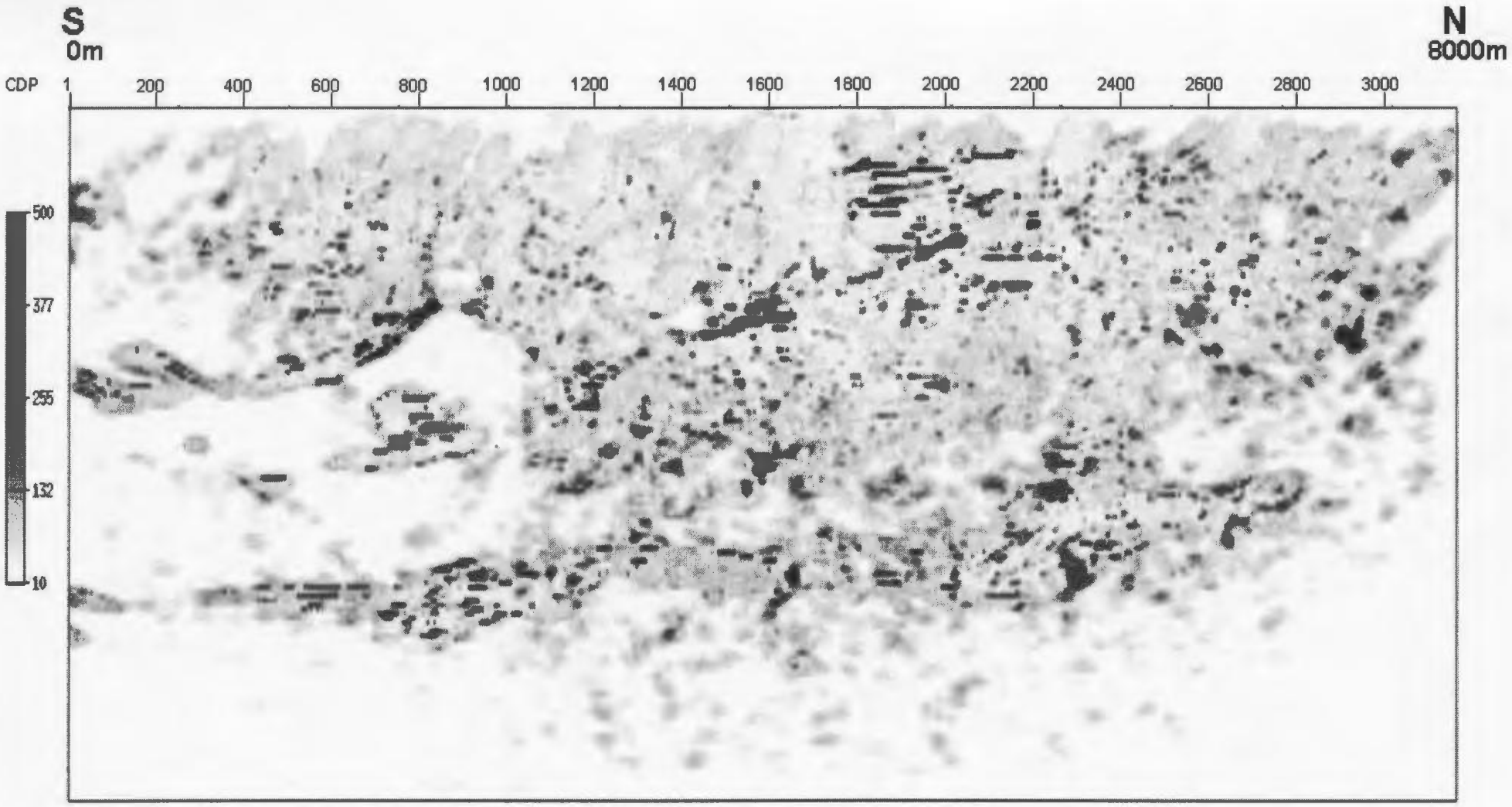


Figure 3.7.2.9: Correlation length map for the model with noise. Legend scale is in metres.

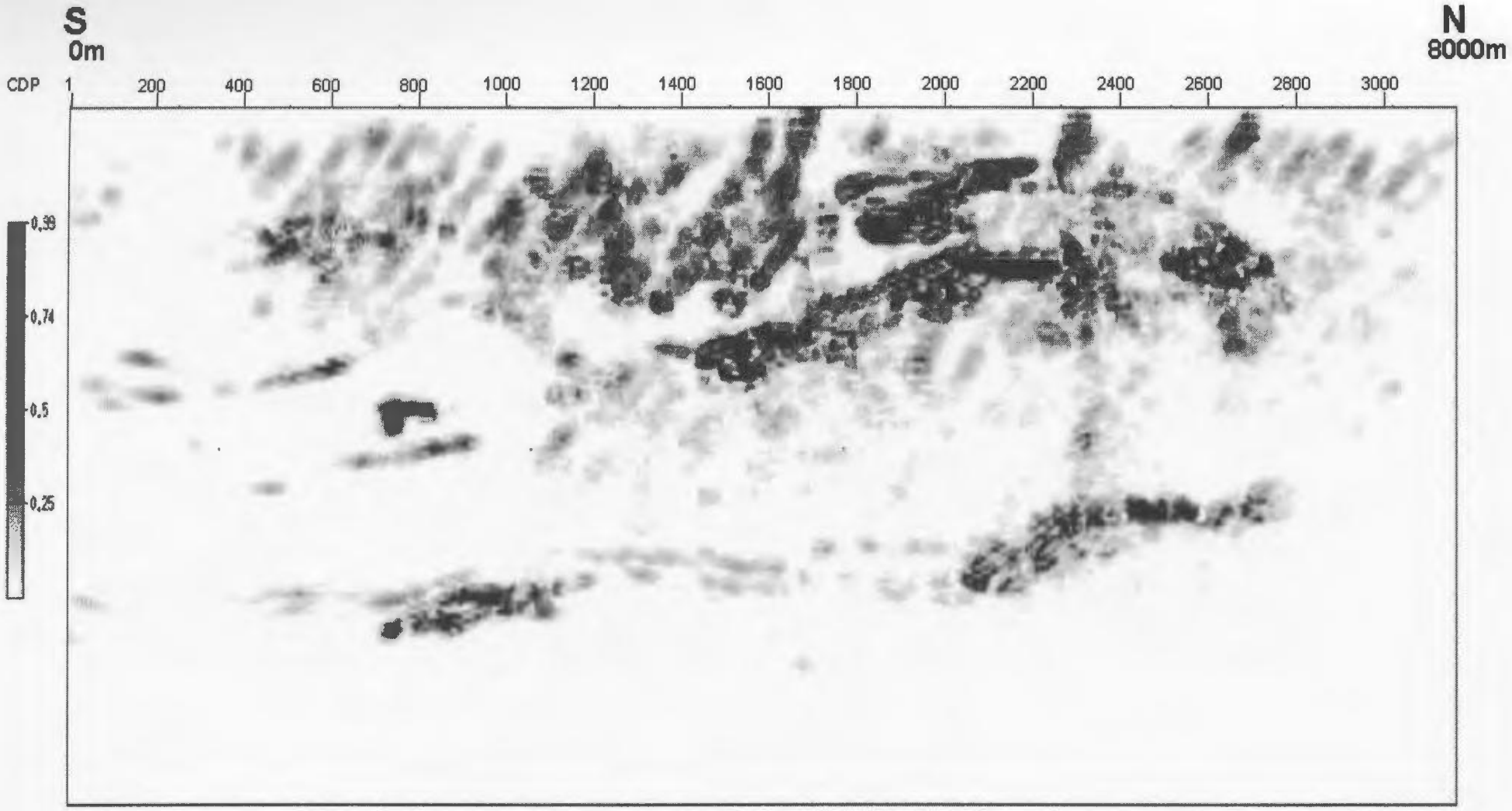


Figure 3.7.2.10: Hurst number map for the model with noise.

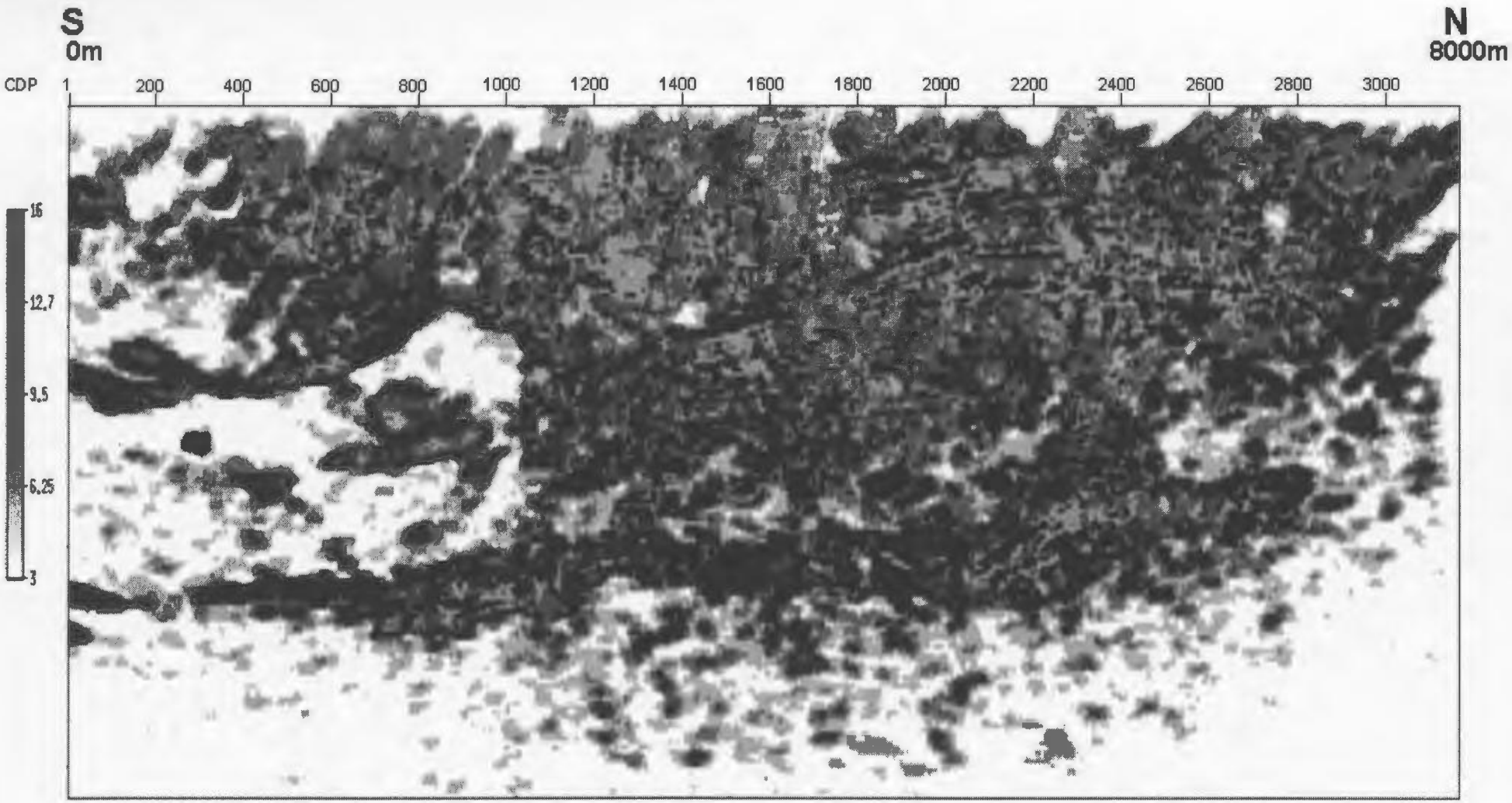


Figure 3.7.2.11: F* map for the model with noise.

The processing strategy that many seismologists apply to collected seismic data has been mainly designed for data collected in sedimentary basins and not in hardrock environments. For that reason it is not necessarily a very effective processing strategy when the wave field contains both specular reflections and diffractions and the information content of both modes is equally important. Evaluation of the seismic data determined that the main processing challenge was related to determining the initial velocity model. The conventional processing scheme involving stack and post-stack migration was performed on the dataset but the key issue was trying to establish an acceptable velocity model to use to perform the NMO correction and as the basis for the stacking velocities. Attempts at establishing an acceptable velocity model included both semblance peak plot and constant velocity analyses. Neither attempt allowed the velocity model to retain velocity information for both the specular reflections and diffractions. Instead it was necessary to pick a velocity that highlighted either the specular reflections or the diffractions but not both. As a result, it was not possible to stack and migrate all of the important events which, in turn produced a poor final image. In an attempt to resolve this issue of dealing with a wave field that contains both equally important specular reflections and diffractions a tailored processing scheme involving pre-stack migration was performed on the dataset. Normally, pre-stack migration improves both the lateral resolution and the signal-to-noise quality of the seismic image since all the data contained in the individual traces are available during imaging (Kessinger, 2005). Again, one of the major issues with pre-stack migration was determining the initial velocity model which was primarily based on knowledge of the local geology. The velocity model was then

iteratively adjusted by analyzing the CDP gathers after pre-stack migration. Since this dataset was synthetic and contained no noise it was easy to determine which events were corrected properly and which were not and to alter the velocities accordingly. However, a real dataset will contain noise and therefore the success of analyzing events in the CDP gathers will depend on the S/N ratio of the dataset. Nevertheless, it was easier to establish an accurate velocity model that incorporated information for the entire wave field using this method which was further verified in the end by the final pre-stack migration image. As a result, pre-stack migration was preferred over post-stack migration since it replaced both the functions of stacking and post-stack migration more effectively.

The effect of velocity gradients in the Voisey's Bay area was examined in order to ascertain whether or not surface-to-surface seismic tomography may be a viable technique for this area. Preliminary results show that the velocity gradients for the Voisey's Bay area are not strong enough to produce turning rays at great enough depths for effective delineation of the magmatic plumbing system. However, these velocity gradients can be considered a minimum approximation because they were based on laboratory data and the resulting velocity gradients must be predominantly the result of micro-crack closure. As a result, further work comprised of field investigation and measurement may provide more accurate velocity gradient results and therefore the viability of surface-surface tomography for the Voisey's Bay area should be re-evaluated.

Heterogeneity mapping was also performed on the seismic dataset to maximize the benefits of 2-D reflection seismic data for hardrock environments. Although, this particular hardrock environment did not give rise to the 'ideal' conditions for

heterogeneity mapping some success was still achieved for the modeled data. The statistical parameter maps, produced as a function of the heterogeneity mapping process, were successful in distinguishing between the troctolite and the foliated gneiss in the southern portion of the model but unsuccessful in the northern portion. Even though heterogeneity mapping was not successful in mapping the entire troctolite system for the synthetic dataset it still has potential for aiding in the delineation of the magmatic plumbing system at Voisey's Bay.

Extensive analysis of the 2-D forward modeling study for the Voisey's Bay area shows that surface seismic reflection techniques are viable for minerals exploration. Characterization of the ore bodies, the magmatic system and structural mapping are all possible for the Voisey's Bay area using reflection seismology techniques. In general, this model-based study helped to foresee acquisition and processing issues before implementation of a field-based 2-D seismic reflection experiment. For that reason, this information will allow for the design of a high quality – high return experiment in an environment where surface seismic reflection methods have rarely been used.

# CHAPTER 4: Alternative to 3-D Seismology

## 4.1 Introduction

Classical 3-D seismic techniques have been proved to be valuable for imaging ore bodies (e.g., Adam et al., 2003). However mining companies are not confident that the cost of 3-D seismic acquisition and processing is worth the perceived benefits. My research in this area is based on three observations. First, between 50-70 % of the cost of a classical 3-D seismic survey on land is associated with the seismic source; second, contacts in the mining industry indicate that detection of potential ore bodies as drill targets is of more interest than imaging for geometric information; and third, the most diagnostic signature of individual scattering bodies in 3-D seismic data is the 'bulls-eye' pattern observed in time slices of unmigrated seismic volumes (Lalestang, 2001). Based on these observations, I have investigated an approach that combines dense 2-D receiver and sparse source arrays to locate strong scatterers in the subsurface. This approach should decrease the cost of 3-D seismic and make the technology more cost-effective for mineral exploration.

Diffractions, which give rise to the 'bulls-eye' pattern observed in time slices, are "produced by any irregularity in a structure that is comparable in scale to the wavelength of the signal" (Fowler, 2005). Ore bodies are characterized by complex shapes and rarely occur in simple stratigraphic settings or sheet-like forms (Eaton et al., 2003b). As a result, they lack the distinct lateral continuity of prominent seismic reflectors (Milkereit et al., 1996) and therefore are better observed through seismic scattering expressed as diffractions. Since ore bodies often have complex 3-D shapes they frequently give rise to

point or edge diffractors in seismic data. The Eastern Deeps zone has a relatively simple ore body geometry while the Reid Brook zone has a more complex geometry. As a result, the Voisey's Bay area presents a range of geometric complexities relating to ore bodies which therefore will provide good test sites for a first assessment of this technique.

Forward modeling, aimed at a first evaluation of this technique, demonstrates the potential of using sparsely illuminated seismic volumes and animated time slicing to detect the distinctive scattering pattern associated with ore body sized targets. This approach to 3-D seismic acquisition has the ability to operate as a cost-effective exploration tool as well as a development tool, by improving possible drill target locations.

### 4.2 Model/Acquisition

A single scatterer (1:10,000 scale) physical model was investigated in this thesis. The single scatterer was represented by a rectangular piece of aluminum with dimensions 4 x 1 x 0.2 cm (scales to 400 x 100 x 20 m) and was attached to a larger square piece of aluminum with dimensions 12 x 12 cm (scales to 1200 x 1200 m) that acted as a reflector (Figure 4.2.1). The scatterer was chosen to be this size because it is approximately 1.5 Fresnel zones in length and less than one Fresnel zone in width which simulates a complex scatterer that may be observed in a real environment. The scatterer has a dip slightly less than vertical due to the fact that it was difficult to place it exactly vertical. This model was placed in a modeling tank where the coupling medium is water. Since shear waves do not propagate in fluids this experiment considers only the acoustic case.

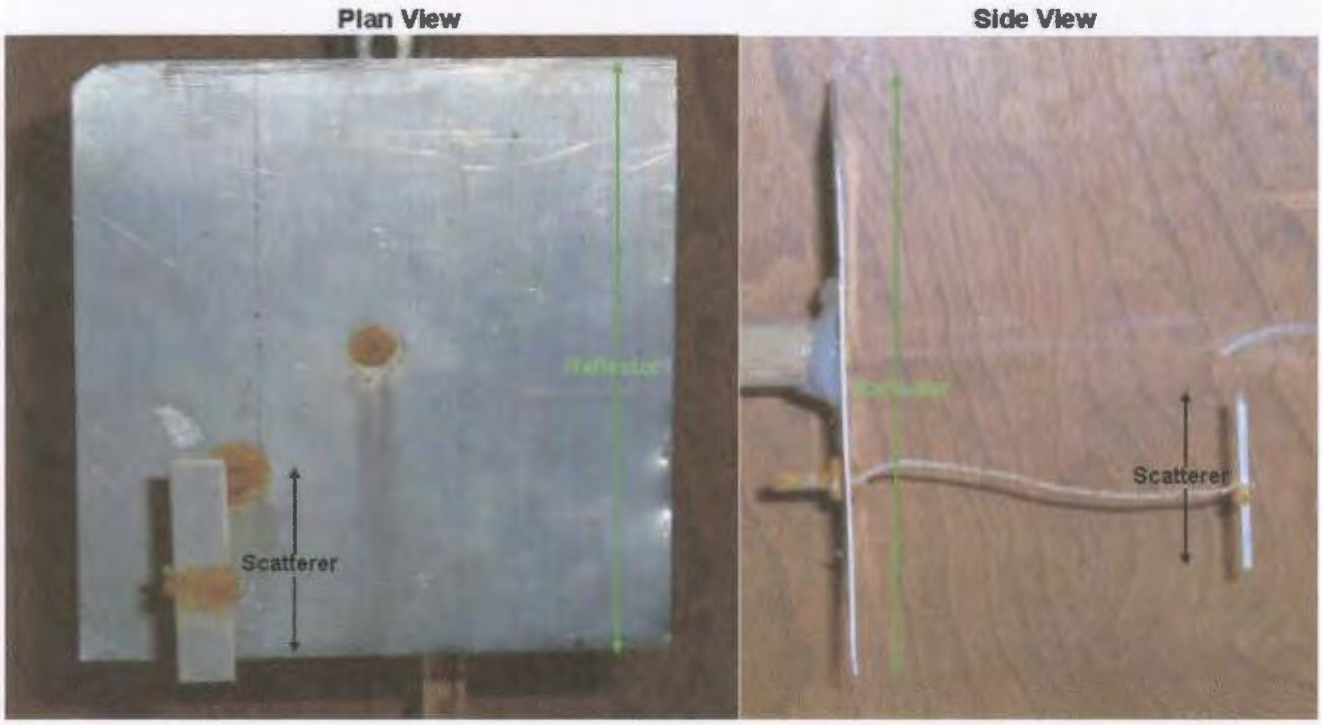


Figure 4.2.1: Illustrates the physical model used in this experiment which consists of a scatterer, reflector and weights to keep the model stationary in the wave tank.

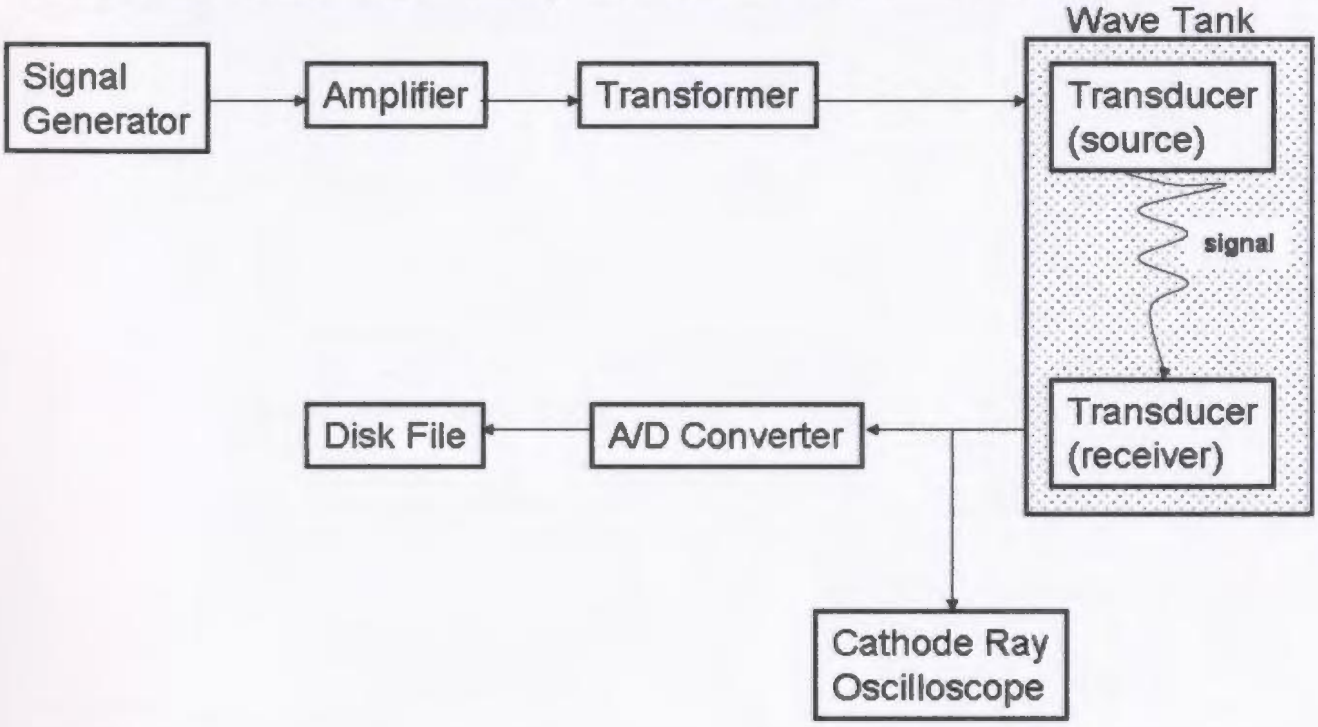


Figure 4.2.2: Flow chart demonstrating the set-up for the data acquisition for the single scatterer physical model.

However, the results offer adequate enough information for the purpose of the experiment.

Data acquisition equipment for this physical model comprised both source and receiver transducers, a signal source, an amplifier, and a recording unit. Figure 4.2.2 shows a flow chart demonstrating the set-up for the data acquisition. The source and receiver are both lead zirconate titanate (PZT) P-wave piezo-electric transducers that have a resonant frequency of approximately 300 kHz (scales to 30 Hz). These transducers were mounted on computer driven stepper motors. The source was programmed to remain stationary while the receiver was programmed to move both vertically and horizontally. This allowed for the recording of offset 3-D receiver gathers. The source was fired nine times for each receiver location so that each trace could be stacked vertically to increase the signal-to-noise ratio. The receiver was moved one group interval[1] at a time vertically until the receiver line was completed which consisted of a total of 60 receiver locations (Figure 4.2.3). Then the receiver was moved one group interval horizontally to the next receiver line and the previous procedure was repeated (Figure 4.2.3). This sequence was repeated for a total of 60 receiver lines, thus the survey was a 60 x 60 receiver array (3600 channels). Four separate surveys were completed with this set-up where the source was located in a different corner of the array each time so that there would be sparse illumination of the scatterer from all quadrants. Figure 4.2.3 shows the set-up of the receiver array and the location of the source for each of the four surveys. The model was submerged in the middle of the wave tank and was kept down

[1] Group interval is equal to 2 mm in the wave tank which simulates 20 m in an actual seismic survey.

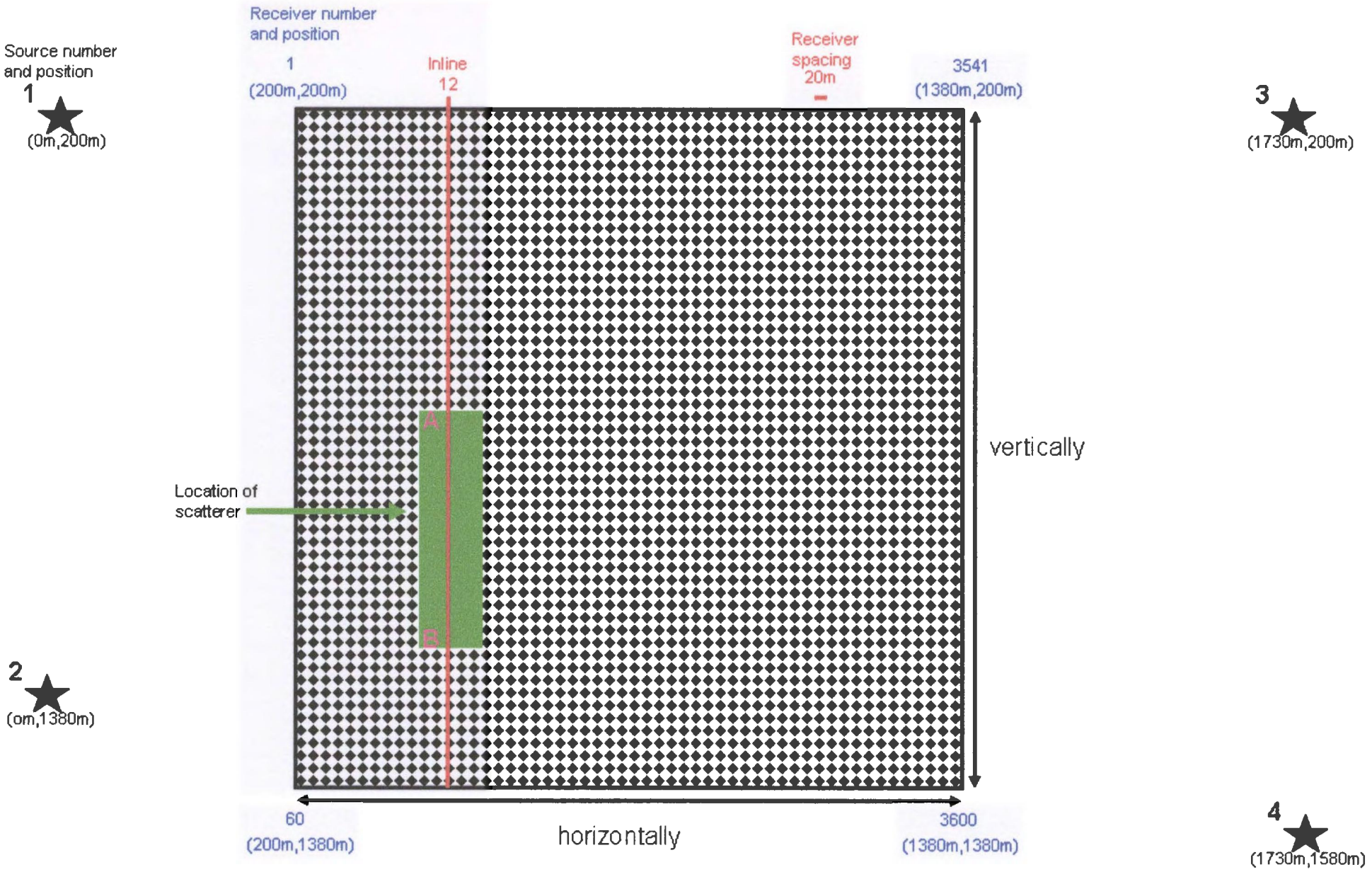


Figure 4.2.3: Shows the set-up of the receiver array and the location of the source for each of the four scale surveys. Opposite ends of the scatterer have been arbitrarily labeled A and B for discussion purposes. The coordinates are given for field scale (1:10, 000).

with weights to help avoid any turbulence that may be caused by the movement of the receiver transducer.

## 4.3 Individual Sources

- **4.3.1 Data Processing**

The data from each different common-source survey were processed individually using the processing scheme detailed in Table 4.3.1.1. This processing scheme prepares the data for interpretation as in-lines, cross-lines, and horizontal time slices.

Table 4.3.1.1: Individual data processing sequence. All times are scaled.

| | |
|---|---|
| Geometry | Apply 3-D Land Geometry |
| NMO | Apply NMO with zero stretch mute and constant velocity 1460 m/s |
| Statics | Correct for statics using event alignment on the reflection (Appendix C-1) |
| Inverse NMO | Remove previous NMO |
| Hand Statics | Apply hand statics to shift the receiver closest to the scatterer to a specified datum (Appendix C-2) |
| Mute | Surgical mutes to remove both the direct wave and the reflections |
| Deconvolution | Apply minimum phase predictive with a 200 ms operator length and a 35 ms operator predictive distance |
| Filter | Apply a bandpass filter with parameters 5-10-40-50 Hz |

| | |
|---|---|
| AGC | Apply AGC with 100 ms length |
| Display | In-lines, cross-lines, and time slices |

In general, the different steps detailed in the processing scheme in Table 4.3.1.1 are basic processing functions commonly used with the processing of seismic data and therefore do not need further explanation except for perhaps the purpose of the hand statics. In order to compare each source survey a hand static was applied to shift the receiver closest to the scatterer (i.e. shortest travel time) to the same datum of 1000 ms for each of the four sources (refer to Figure 4.4.1.1). This way, diffractions on the same traces for each source survey would not be shifted in time, producing irregular and incoherent events.

- **4.3.2 Results/Observations**

Analysis of each of the separate source surveys shows that despite the effectiveness of the deconvolution the data is still modestly ringy. It is evident by the number of different diffraction moveouts that the scattering response contains diffractions originating from different points spatially (Figure 4.3.2.1). These different diffractions may be caused by an interaction with the wire that is wrapped around the scatterer and also connected to the reflector or may simply be a result of the location of the source with respect to the scatterer (Figures 4.2.1 and 4.2.3). Consequently, the first arriving wave for each of the different source surveys does not originate from the same scattering point. Figure 4.3.2.1 also illustrates that different portions of the scatterer are better illuminated

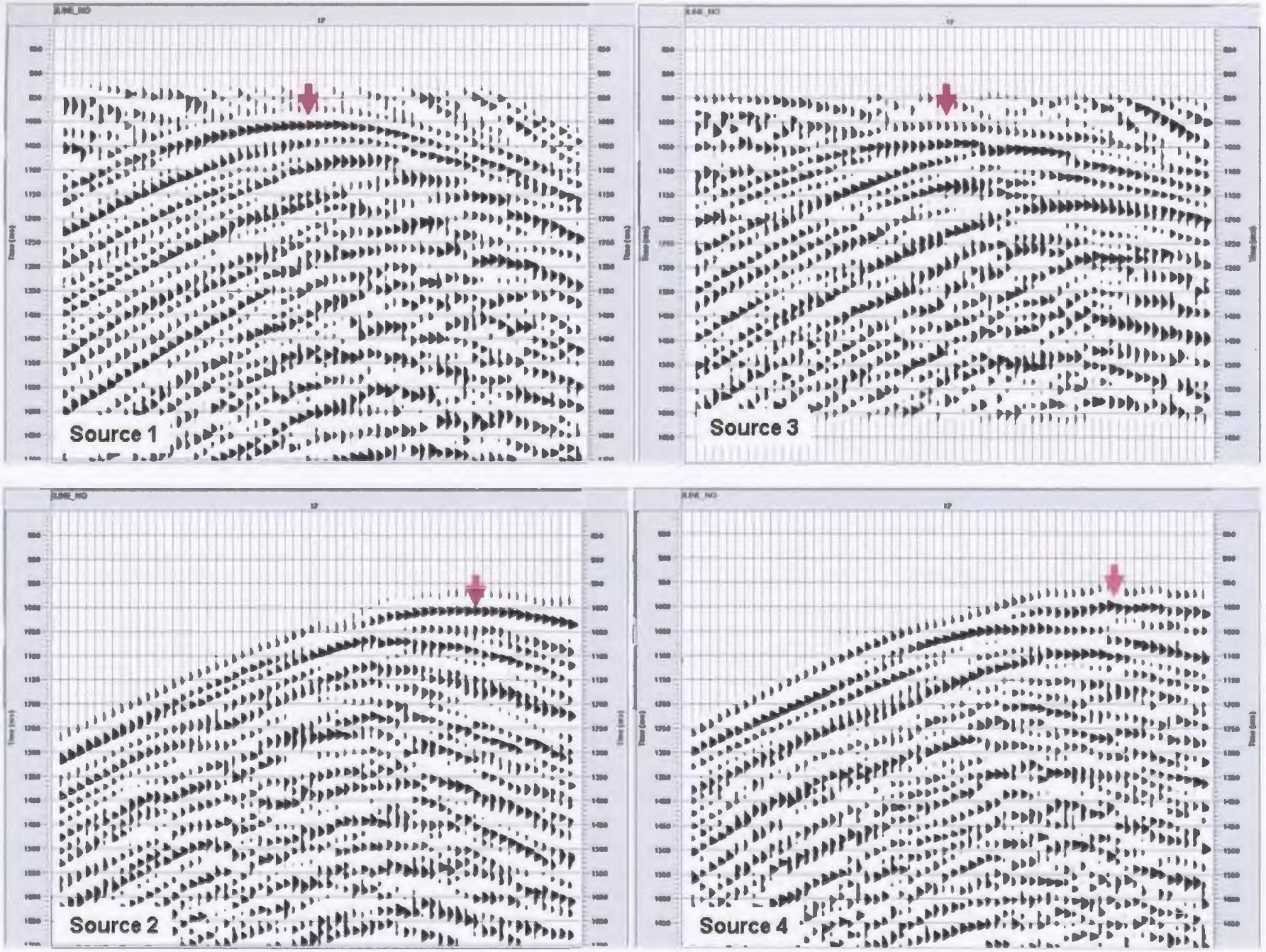


Figure 4.3.2.1: Illustrates in-line 12 for each source survey. Pink arrows show where the scatterer is better illuminated for each source survey which have been datumed to 1000 ms.

depending upon the location of the source. In-line 12 (Figure 4.2.3) was chosen to analyze since it crosses approximately through the middle of the scatterer and theoretically (if there is no dip) the strongest amplitudes along the diffraction hyperbola should all be located in the same place for each different source survey but they are not. These observations were further confirmed by analyzing and comparing horizontal time slices for each separate source survey (Figure 4.3.2.2). It is evident from Figure 4.3.2.2 that the complex diffracting pattern from the scatterer is best visualized by screen captures of the horizontal time slices and animation of the horizontal time slices (Appendix D). Time-slicing of the "pseudo 3-D" synthetic seismic data for each source survey also images the "bulls-eye" pattern that is normally characteristic of scatterers in 3-D volumes. Thus, it is possible to use a sparse source array with a dense receiver array as an alternative to 3-D seismic. However, there is only illumination from each quadrant with this type of survey set-up. The next section examines whether or not stacking the four sources may be more beneficial by producing more complete illumination of the scatterer.

## 4.4 Stacked Sources

- **4.4.1 Stacking Theory**

To stack the four common source gathers, a correction for the different travel times associated with the four source locations is required. Because the position of the scatterer and the receiver locations are the same for all four shots only the location of the source changes. Thus the variations in travel time must be associated with variation in the

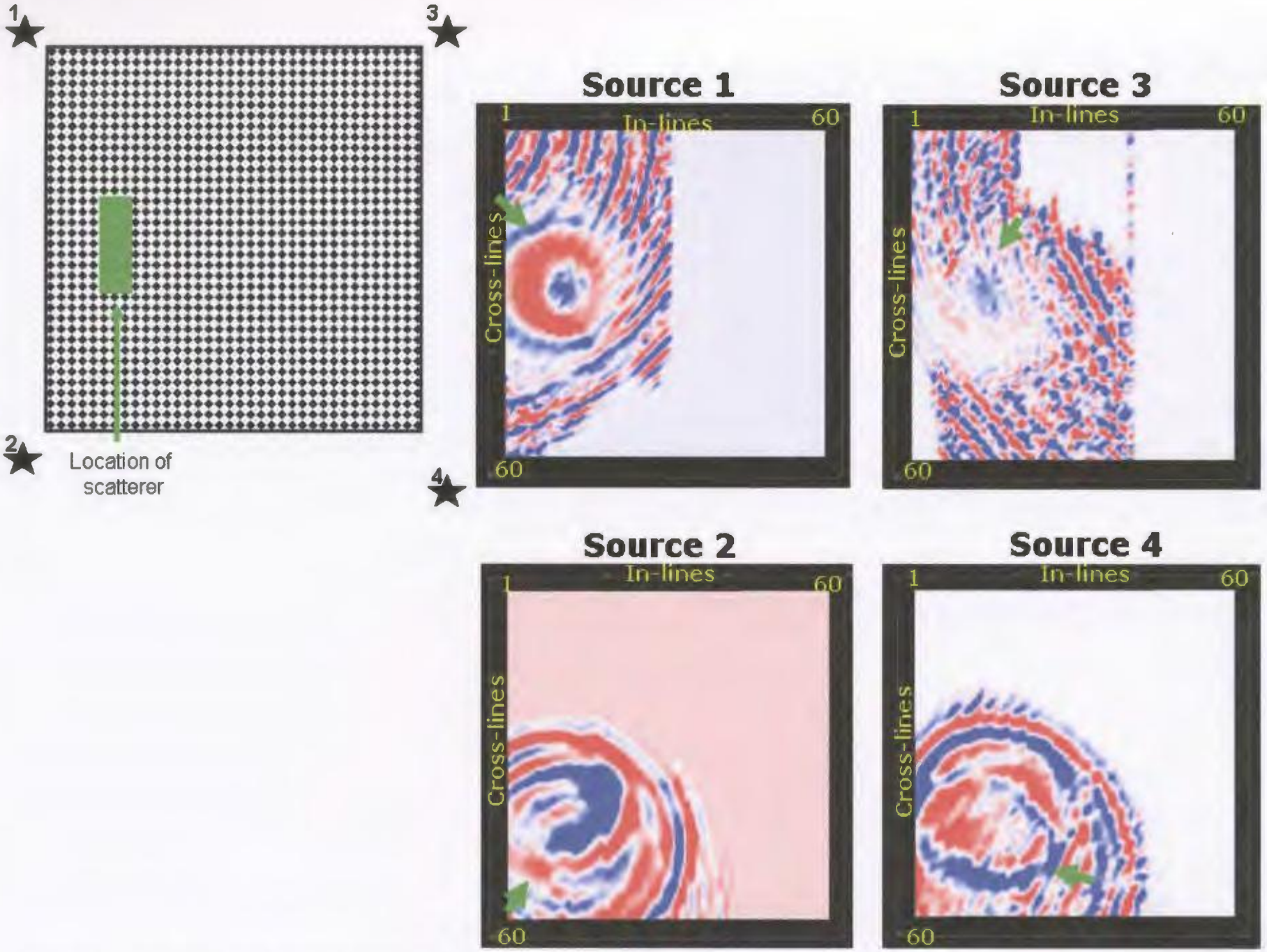


Figure 4.3.2.2: Illustrates horizontal time slices for t=1080ms for each source survey. The green arrow shows where the scatterer is best illuminated. Small inset shows location of the sources with respect to the location of the scatterer.

time involved in the source to scatterer travel path. Figure 4.4.1.1 displays the case for two sources offset from a diffracting point.

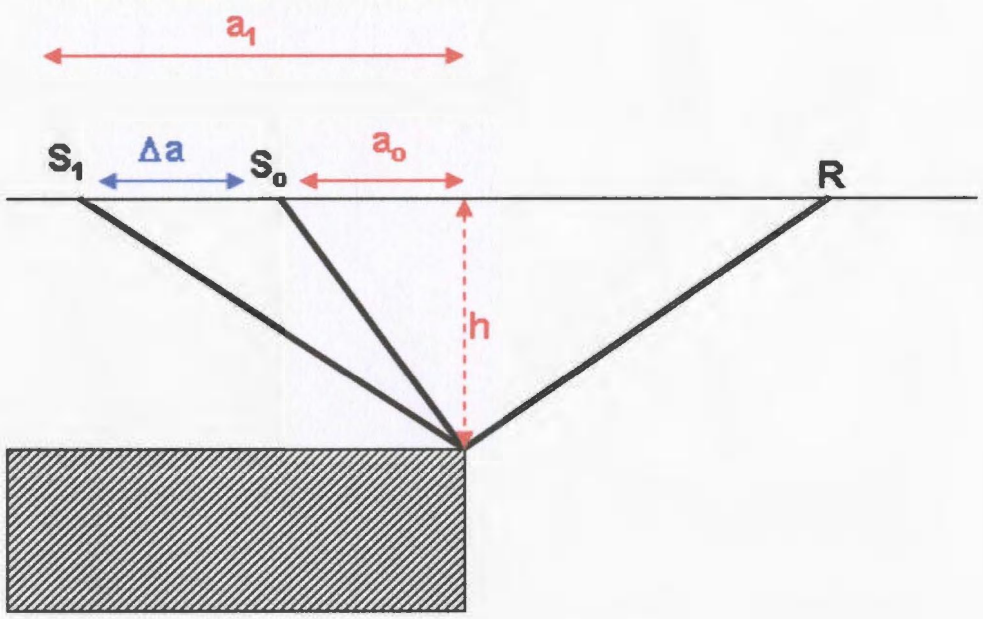


Figure 4.4.1.1: Two sources offset from a diffracting point. $S_0$ is the datum source, $S_1$ is first offset source, R is the receiver, h is the height from the diffractor to the surface, $a_o$ and $a_1$ are the distances from the datum and first offset sources respectively to the point vertically over the diffractor, and $\Delta a$ is the difference in the distance between the two sources (adapted from Sheriff and Geldart, 1995).

The source portion of the diffraction traveltime curve for $S_o$ is given by:

$$t_o = \frac{1}{V}\sqrt{a_o^{\,2} + h^2}\,, \quad (4.0)$$

which can be rearranged to:

$$(t_o V)^2 = a_o^{\,2} + h^2\,. \quad (4.1)$$

Because the position of the nearest receiver and the diffractor do not change as a function of the shot location, the source portion of the diffraction traveltime curve for $S_1$ is given by:

$$t_1 = \frac{1}{V}\sqrt{a_1^{\,2} + h^2}\,, \qquad (4.2)$$

which can be rearranged to:

$$t_1 = \frac{1}{V}\sqrt{(a_o + \Delta a)^2 + h^2} = \frac{1}{V}\sqrt{a_o^{\,2} + h^2 + 2a_o\Delta a + \Delta a^2}\,, \qquad (4.3)$$

substituting equation 4.0 into the equation 4.3 we get the following relationship between the two sources:

$$(t_1 V)^2 = (t_o V)^2 + 2a_0\Delta a + \Delta a^2\,. \qquad (4.4)$$

Therefore, the diffraction traveltime curves from $S_0$ and $S_1$ are related to each other by a simple time shift associated with the difference in their locations. Thus, once each source survey has been corrected to the same datum, the moveout of the diffractions should be the same which will allow for them to be stacked. This theory is based upon the assumption that the velocity function is homogeneous and isotropic; however, if it is inhomogeneous and/or anisotropic there may be complications related to the velocity equations that need further attention.

- **4.4.2 Data Processing**

The same data processing sequence in Section 4.3.1 was also used here to prepare the four individual sources for stacking. The four sources were stacked together using a mean receiver stack. Figure 4.4.2.1 illustrates that there was a significant error in the stacking process because the diffractions from all four source surveys do not add together constructively. Instead, in-lines from both sources 1 and 3 and then 2 and 4 have the same first arrival diffraction moveout thereby illuminating ends A and B of the scatterer

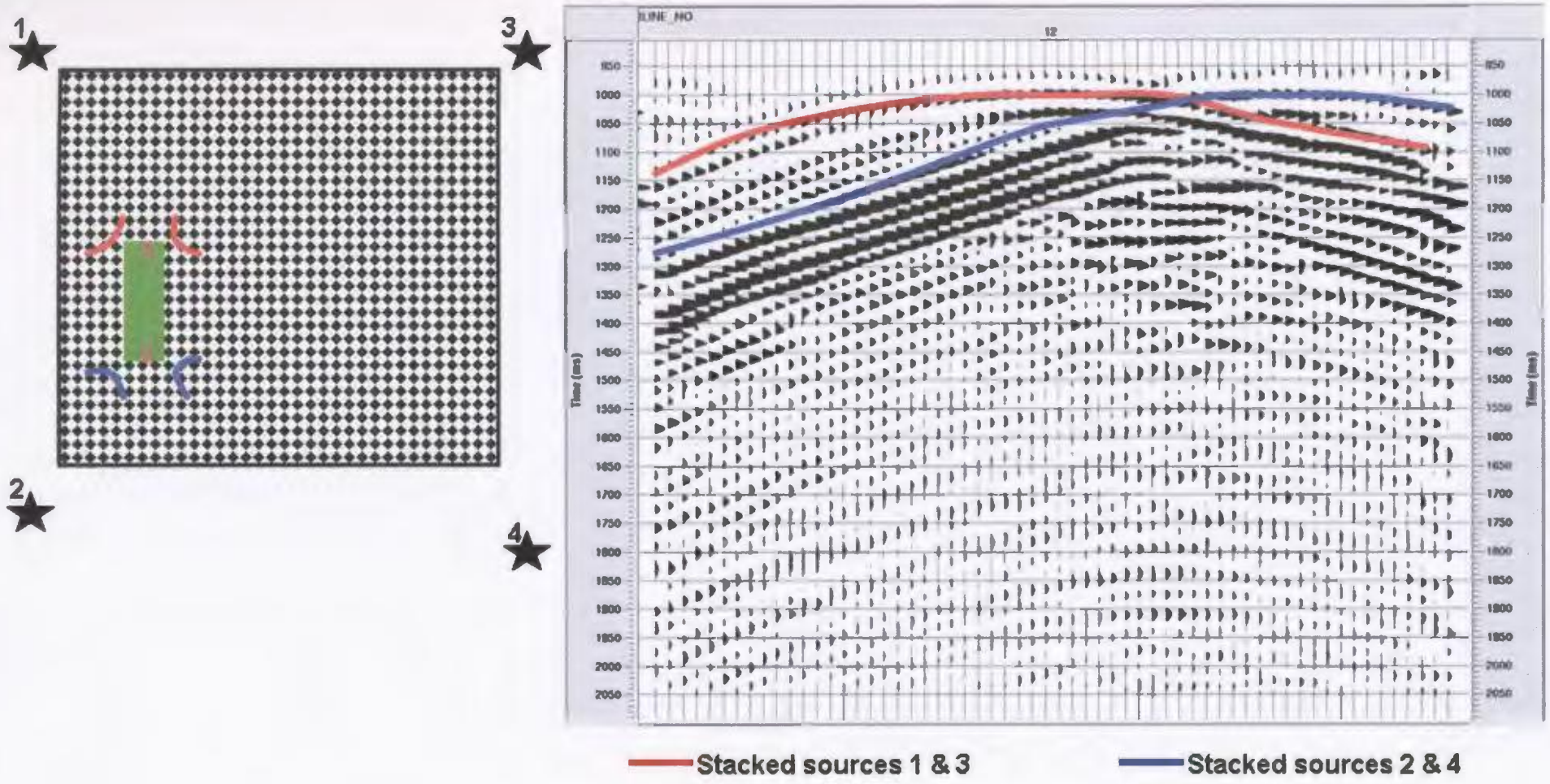


Figure 4.4.2.1: Illustrates that the four shots do not stack together properly. Instead sources 1and 3 have the same diffraction moveout and so do sources 2 and 4. Inset shows that end A of the scatterer is illuminated by sources 1 and 3 while end B is illuminated by source 2 and 4.

respectively (Figure 4.4.2.1). Since the scatterer is approximately 1.5 Fresnel zones in length both ends A and B are distinguishable. The width of the scatterer is less than one Fresnel zone and therefore does not affect the stacking of the cross-lines because the edges are not detected as separate features but instead only as one (Figure 4.4.2.2). As a consequence, it is no longer logical to stack all four common source gathers together because two different features are being detected in the in-line orientation. Instead, it is more appropriate to deal with ends A and B of the scatterer as separate features and thus try to improve the representation of the scatterer by illuminating these two portions. Table 4.4.2.1 displays the new processing sequence used for stacking.

Table 4.4.2.1: Data processing sequence used for stacking. All times are scaled.

| | |
|---|---|
| Geometry | Apply 3-D Land Geometry |
| NMO | Apply NMO with zero stretch mute and constant velocity 1460 m/s |
| Statics | Correct for statics using event alignment on the reflection (Appendix C-1) |
| Inverse NMO | Remove previous NMO |
| Hand Statics | Apply different hand statics to shift the receiver closest to the scatterer to a specified datum for both ends A and B of the scatterer (Appendix C-3) |
| Mute | Surgical mutes to remove both the direct wave and the reflections |
| Merge | Merge data files for shots 1 and 3 together and 2 and 4 together. |
| Stack | Mean receiver stack separately on merged files |

| | |
|---|---|
| Deconvolution | Apply minimum phase predictive with a 200 ms operator length and a 35 ms operator predictive distance |
| Filter | Apply a bandpass filter with parameters 5-10-40-50 Hz |
| AGC | Apply AGC with 100 ms length |
| Merge | Merge stacked files for ends A and B of scatterer together |
| Stack | Mean receiver stack previous merged file |
| Display | In-lines, cross-lines, and time slices |

As before in Section 4.3.1, the different steps detailed in the processing scheme in Table 4.2.1.1 are basic processing functions commonly used with the processing of seismic data and therefore do not need further explanation except for perhaps the purpose of re-doing the hand statics. In order to stack each source survey a hand static was applied to shift the receiver closest to the scatterer (i.e. trace with the shortest travel time) to the same datum. This way, diffractions on the same traces for each source survey would not be shifted in time, producing irregular and incoherent events. Sources 1 and 3 were referenced to a 1080 ms datum while sources 2 and 4 were referenced to a 1000 ms datum. This was done so that the different time arrivals of the two events were maintained in the stacking process.

- **4.4.3 Results/Observations**

Analysis of in-line 12 shows that the data files for both ends A and B of the scatterer (sources 1&3, 2&4, respectively) stack in-phase when processed separately (Figures 4.4.3.1 and 4.4.3.2, respectively) as opposed to Figure 4.4.2.1. It was then

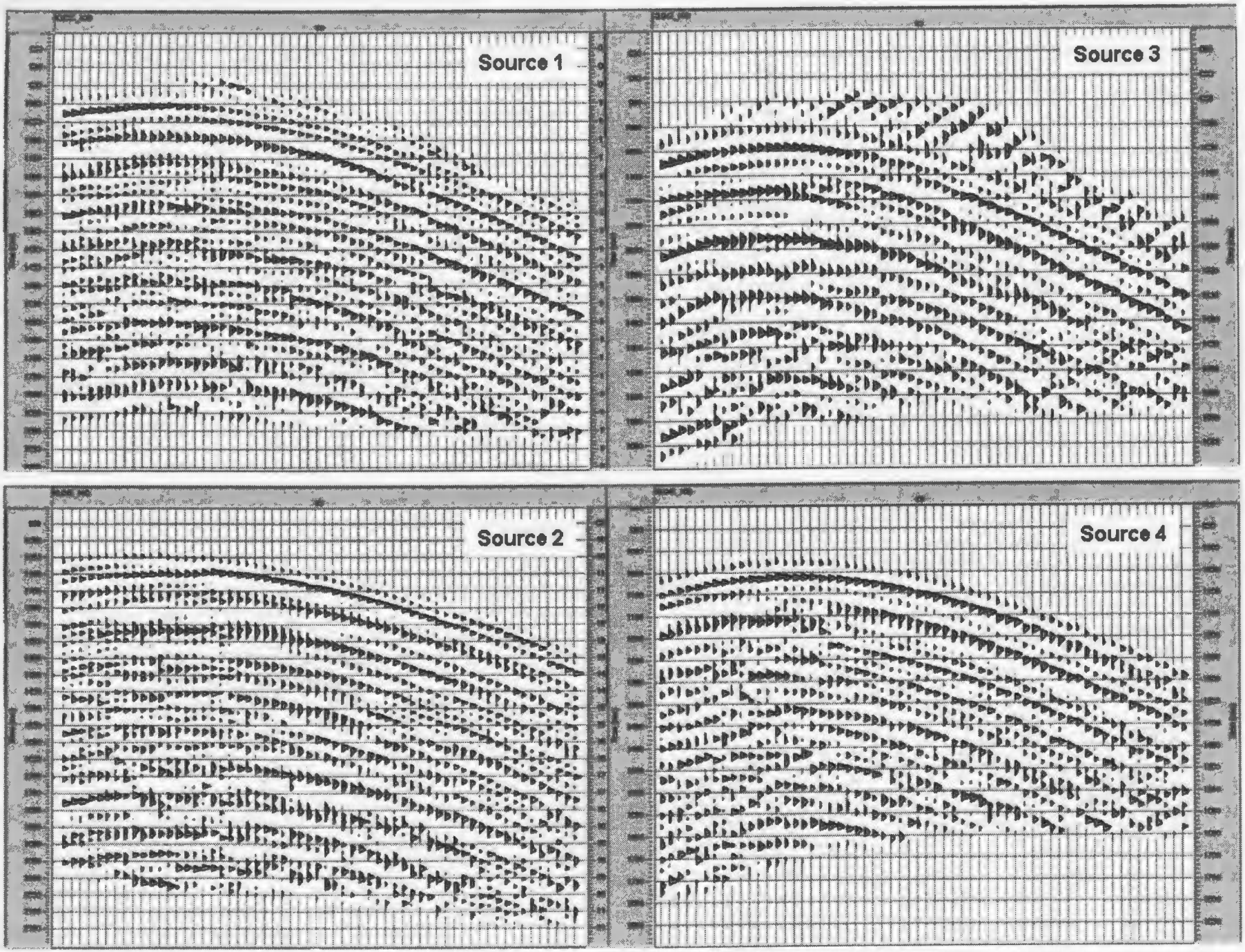


Figure 4.4.2.2: Shows that the moveout on the diffractions is the same for each source for the cross-lines. Cross-line 30 was used as an example.

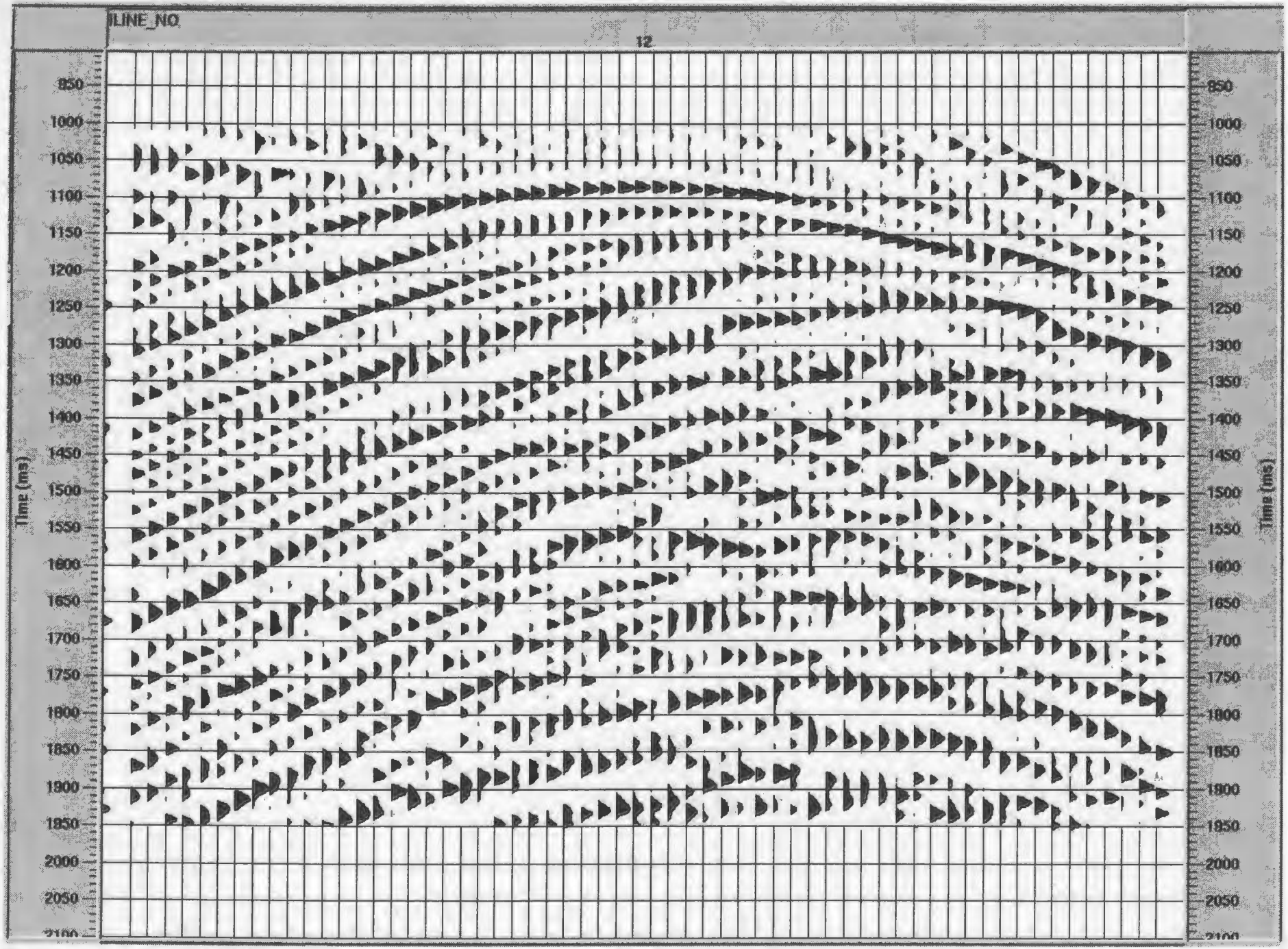


Figure 4.4.3.1: Illustrates that shots 1 and 3 stack together in-phase to illuminate end A of the scatterer.

Figure 4.4.3.2: Illustrates that shots 2 and 4 stack together in-phase to illuminate end B of the scatterer.

possible to produce a final stack by merging and stacking Figures 4.4.3.1 and 4.4.3.2 (Figure 4.4.3.3).

The scattering response is still modestly ringy even when the data is stacked which is most likely associated with the ringy source wavelet or the response of the wire that supports the scattering body.

The complex interfering diffraction pattern from the scatterer is best visualized as horizontal time slices. Horizontal time slices through both the stacked versions of ends A and B of the scatterer reveal that stacking the data improved the overall illumination of the scatterer (Figures 4.4.3.4 and 4.4.3.5, respectively). Horizontal time slices through the final stack demonstrate that both the 'bull-eyes' patterns for ends A and B of the scatterer are recognizable as expected. This indicates that dependent upon the size of the ore body it may be possible to image various portions of the ore body thereby generating an even better target for drilling. Animation of the horizontal times slices for the stacked ends A and B and for the final stack can be found in Appendix D.

- **4.4.4 Noise**

Figure 4.4.4.1a illustrates the case where there is no noise present in the data. This is obviously the ideal case and does not disclose whether or not the 'bulls-eye' patterns would be recognizable in the presence of noise in a real environment. Seismic noise may be either coherent or incoherent depending upon whether or not the noise can be followed across a few traces or not at all (Sheriff and Geldart, 1995). This experiment illustrates

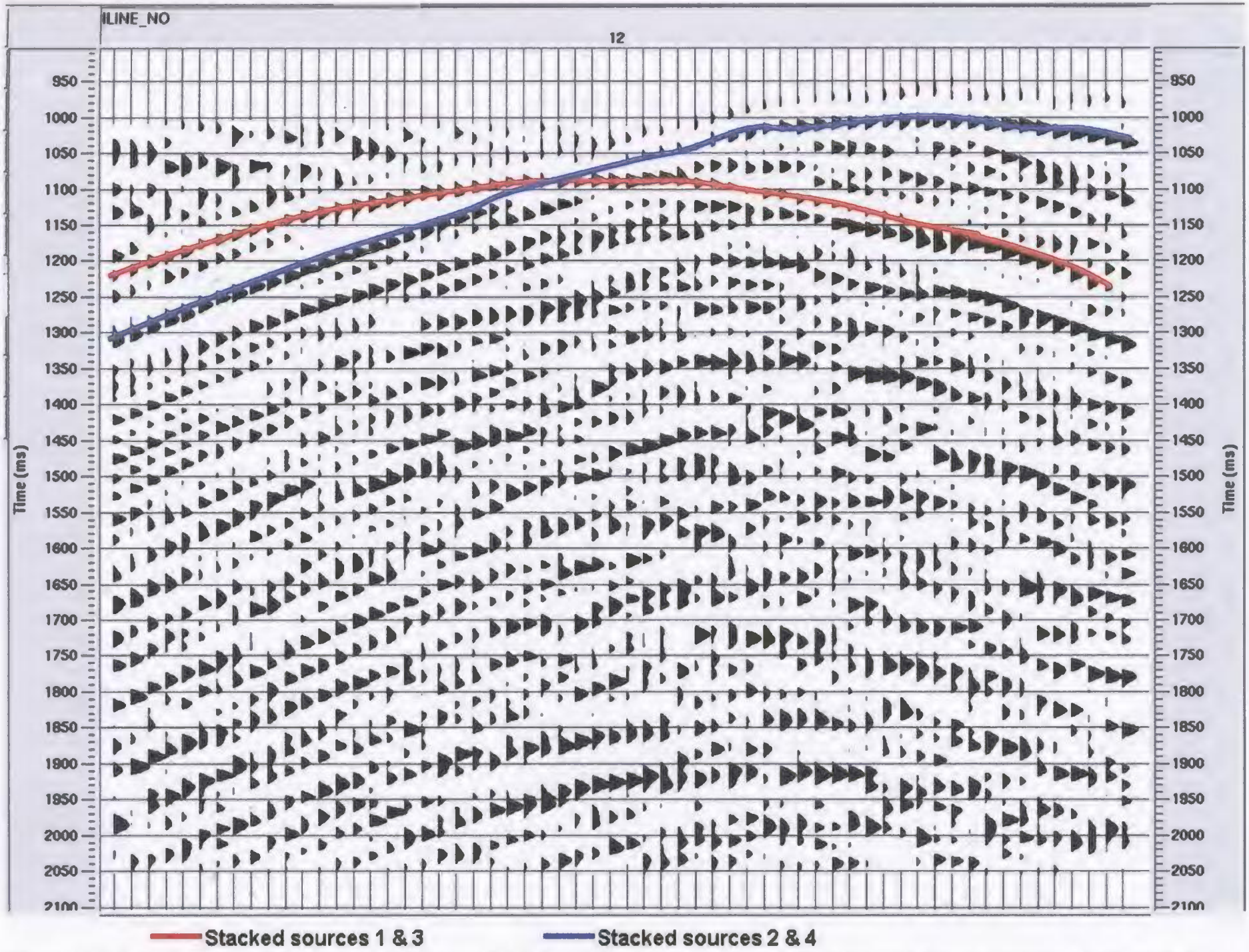


Figure 4.4.3.3: Illustrates the stacking of Figures 4.4.3.1 and 4.4.3.2 to produce a final stacked image including both ends A and B of the scatterer.

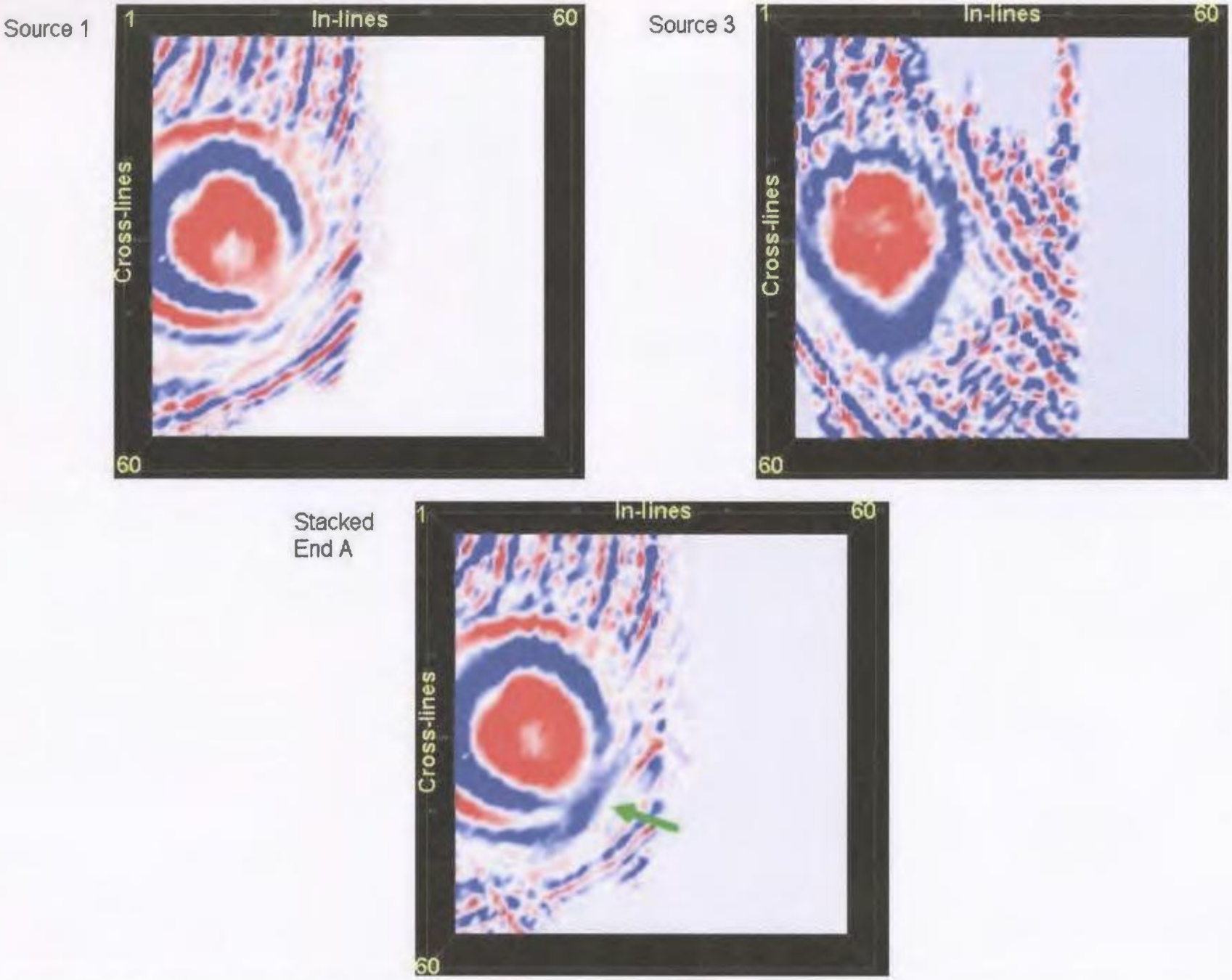


Figure 4.4.3.4: Illustrates that stacking was beneficial for illuminating end A of the scatterer. The green arrow on stacked end A time slice illustrates where illumination of the scatterer benefited from stacking. Time slices for t = 1110 ms are displayed as an example.

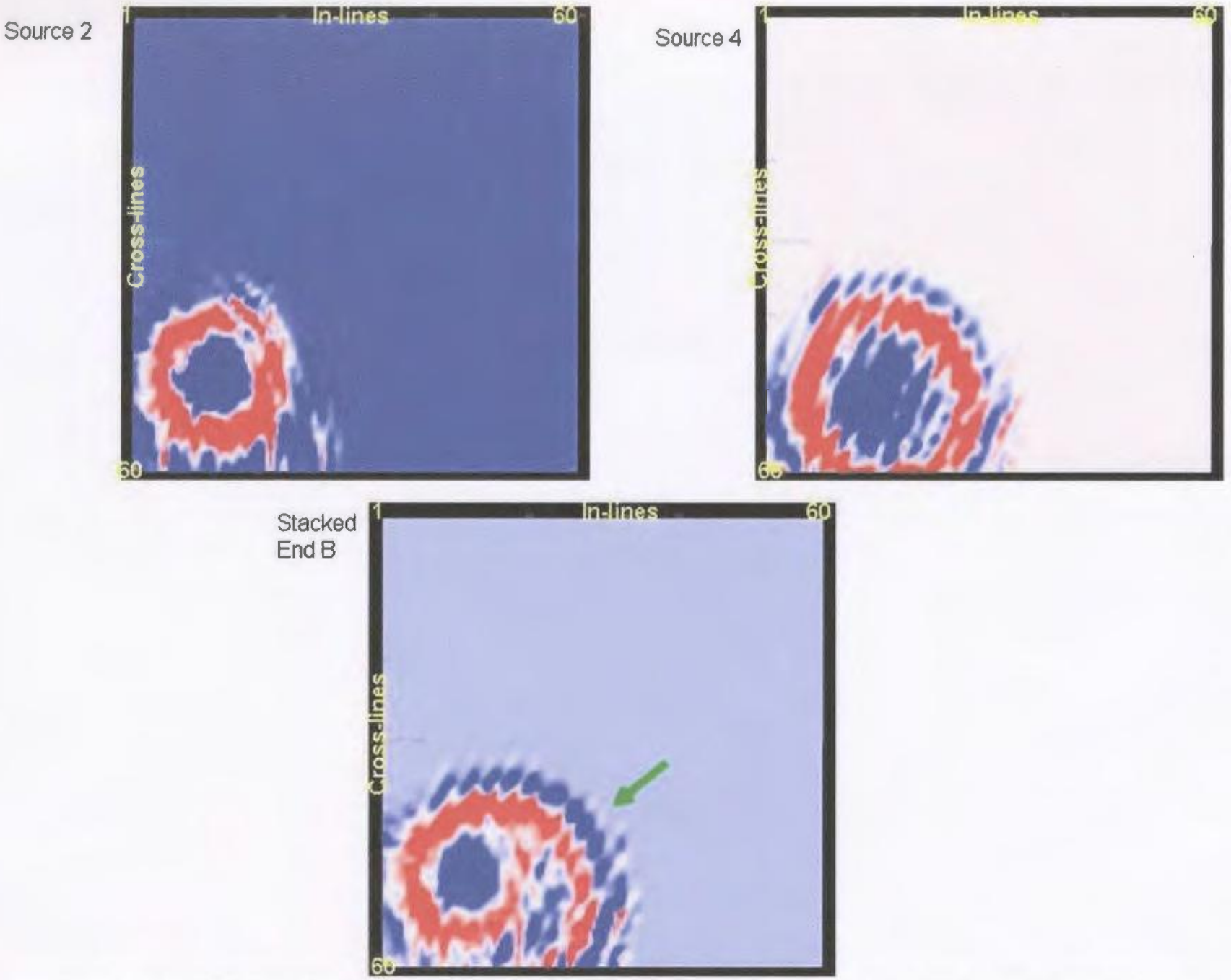


Figure 4.4.3.5: Illustrates that stacking was beneficial for illuminating end B of the scatterer. The green arrow on the stacked end B time slice illustrates where illumination of the scatterer benefited from stacking. Time slices for t = 1000 ms are used as an example.

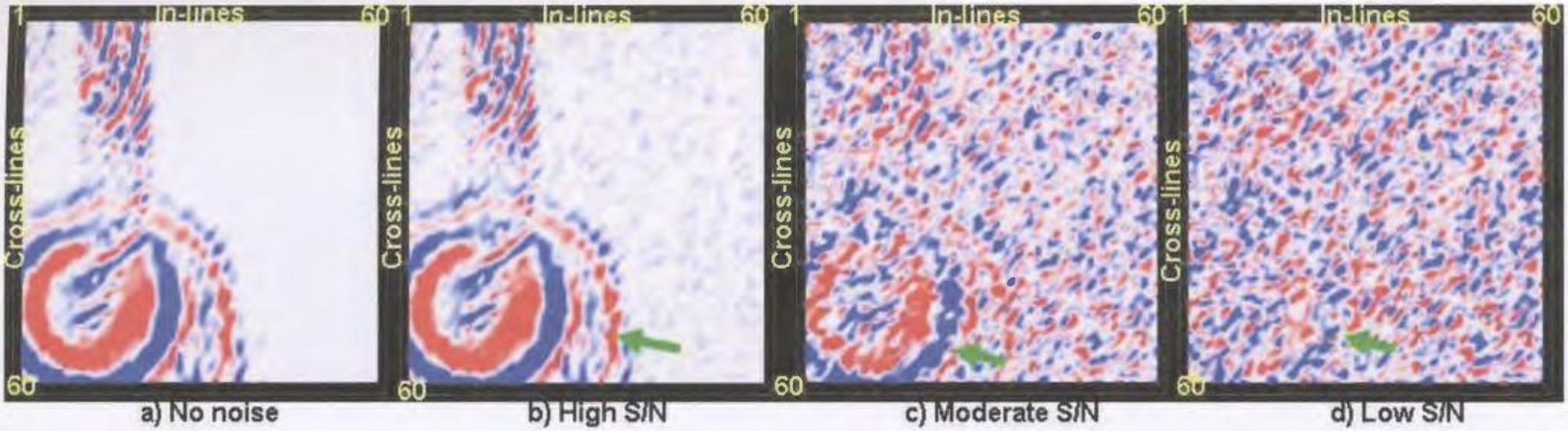




Figure 4.4.4.1: Illustrates that the 'bulls-eye' pattern is still evident when varying amounts of noise are present. The green arrows highlight the 'bulls-eye' locations for t = 1040 ms. The eye focuses better upon the 'bulls-eye' pattern when the time slices are animated.

the use of both coherent and incoherent noise. The coherent noise is already present in the data in the form of the ringy source wavelet while the incoherent noise, often known as random noise, is computer generated and is added to the data. In general, the quality of a seismic record is often determined by its signal-to-noise ratio (S/N), which is the ratio of signal in a specified portion of the record to the total noise in the same portion (Sheriff and Geldart, 1995). Varying amounts of noise, based on a specified S/N ratio, with a Gaussian noise probability distribution were added to the final stack using a program in Seismic Unix. S/N ratios of 5, 3, and 1 were used to illustrate high, moderate, and low S/N conditions respectively (Figures 4.4.4.1b, c, and d, respectively). These S/N ratios are a function of the program and are characterized as follows:

$$Output = signal + [(scale)(noise)]$$

where,

$$scale = \left(\frac{1}{S/N}\right)\left[\frac{\left(\frac{abs\max\_signal}{\sqrt{2}}\right)}{\sqrt{energy\_per\_sample}}\right]$$

where S/N is the signal-to-noise ratio and absmax_signal is the absolute maximum signal present in the data. As a result, the specified S/N ratios entered into the program do not provide any direct indication of the actual S/N ratio for the data. Since the detection of the 'bulls-eye' pattern is based upon coherency, further investigation into the accurate S/N ratios was not deemed necessary. A bandpass filter with parameters 5-10-40-50 Hz was applied to the data to enhance the image. Figure 4.4.4.1b which is a screen capture of the horizontal time slice at t = 1040 ms for the case of a high signal-to-noise ratio shows

that the 'bulls-eye' pattern is evident as expected. For the case of a moderate signal-to-noise ratio the 'bulls-eye' pattern is still highly recognizable (Figure 4.4.4.1c). For the case of a low signal-to-noise ratio the 'bulls-eye' pattern is barely recognizable (Figures 4.4.4.1d). This is not surprising since record quality normally deteriorates rapidly as the S/N decreases to less than unity (Sheriff and Geldart, 1995). However, the 'bulls-eye' pattern is more evident when the time slices are assembled together and animated because the human eye tends to focus on the coherent 'bulls-eye' pattern instead of the incoherent noise (Appendix D). This is true for all three different cases of S/N.

## 4.5 Migration

3-D migration was performed on the previous stacked sections to ascertain whether or not better localization of the scatterer could be obtained. Since the scatterer is only sparsely illuminated it is most likely that it will not be possible to collapse the diffractions entirely as intended by the migration algorithm. Stolt 3-D migrations were performed using constant migration velocities of 1400 m/s, 1460 m/s, and 1500 m/s in order to determine the appropriate migration velocity for this data. The data migrated most effectively with a migration velocity of 1460 m/s, which was the same as the stacking velocity used in Section 4.4. The diffractions are essentially collapsed to a small area located at the apex of the diffraction hyperbola by the 3-D migration (Figure 4.5.1, animated time slices in Appendix D).

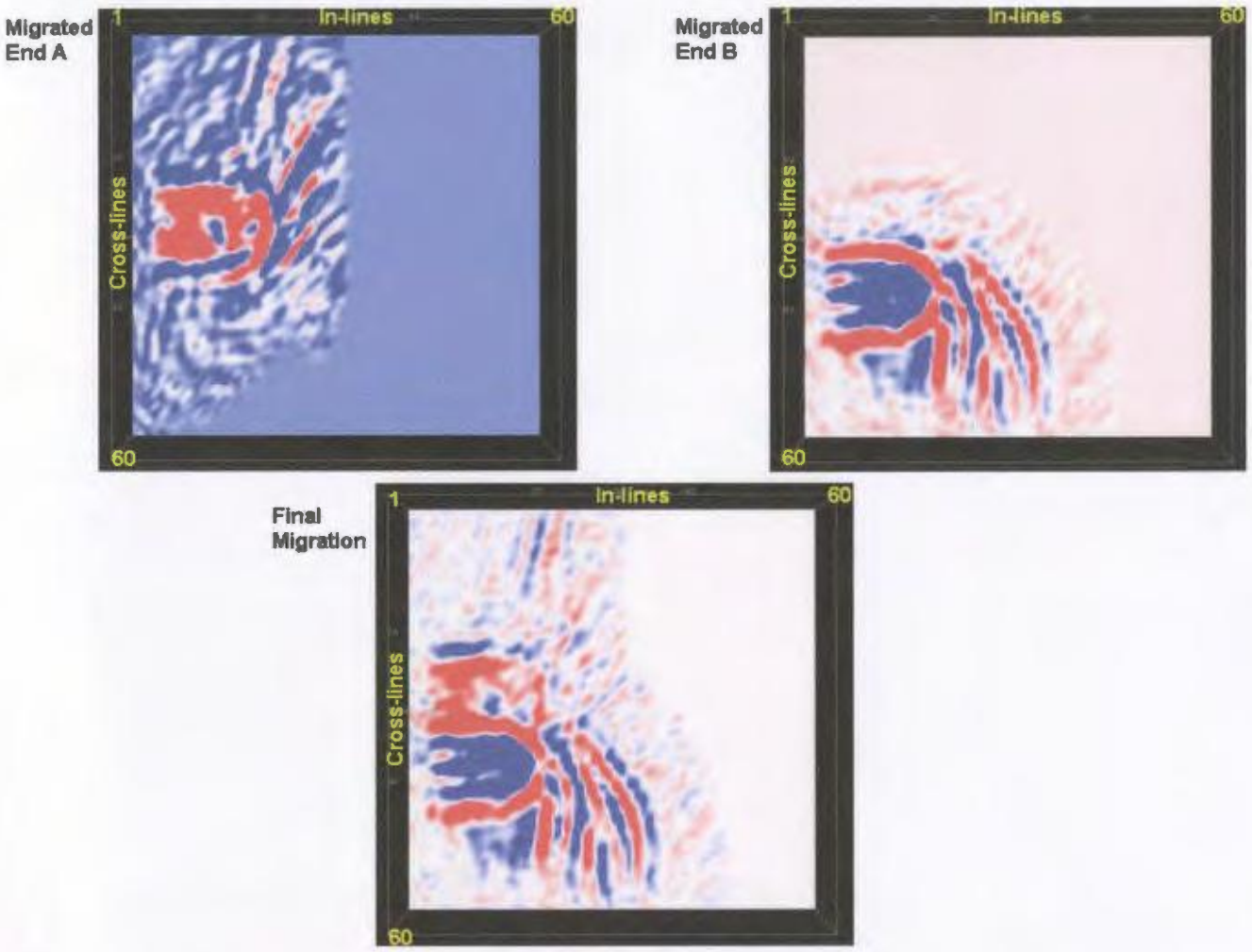


Figure 4.5.1: Illustrates the collapse of the diffractions caused by 3-D migration and the smaller size of the anomalies for both ends A and B of the scatterer for t = 1080 ms.

Comparison of the unmigrated and the migrated horizontal time slices reveals that the anomalies are in general smaller in size on the migrated horizontal time slices (Figure 4.5.2 and 4.5.3 respectively). Also, as time increases the diffractions appear to not collapse as efficiently which may be a result of both the ringiness still present in the data and the sparse illumination of the scatterer. Therefore, localization of the scatterer becomes slightly more obscured with time (Figure 4.5.3). However, at this time the migrated data provides better localization of the scatterer whereas the unmigrated data provides more effective detection of the diffractions.

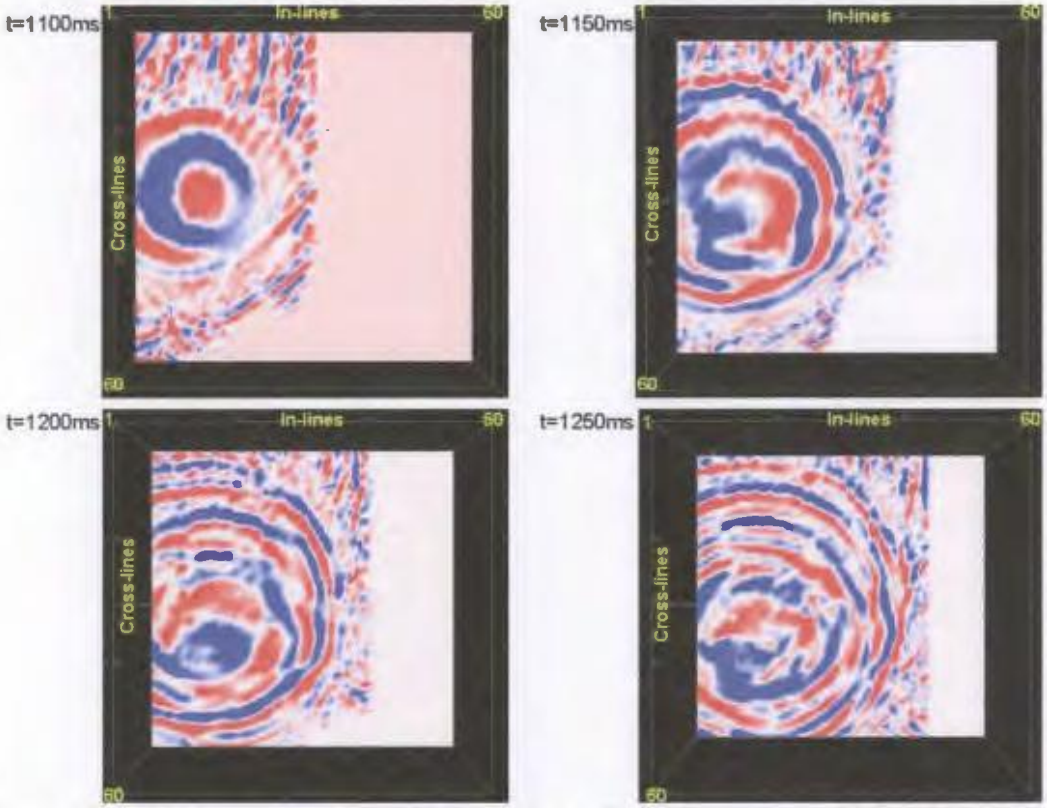


Figure 4.5.2: Unmigrated horizontal time slices for end A of the scatterer illustrating the progressive 'bulls-eye' pattern.

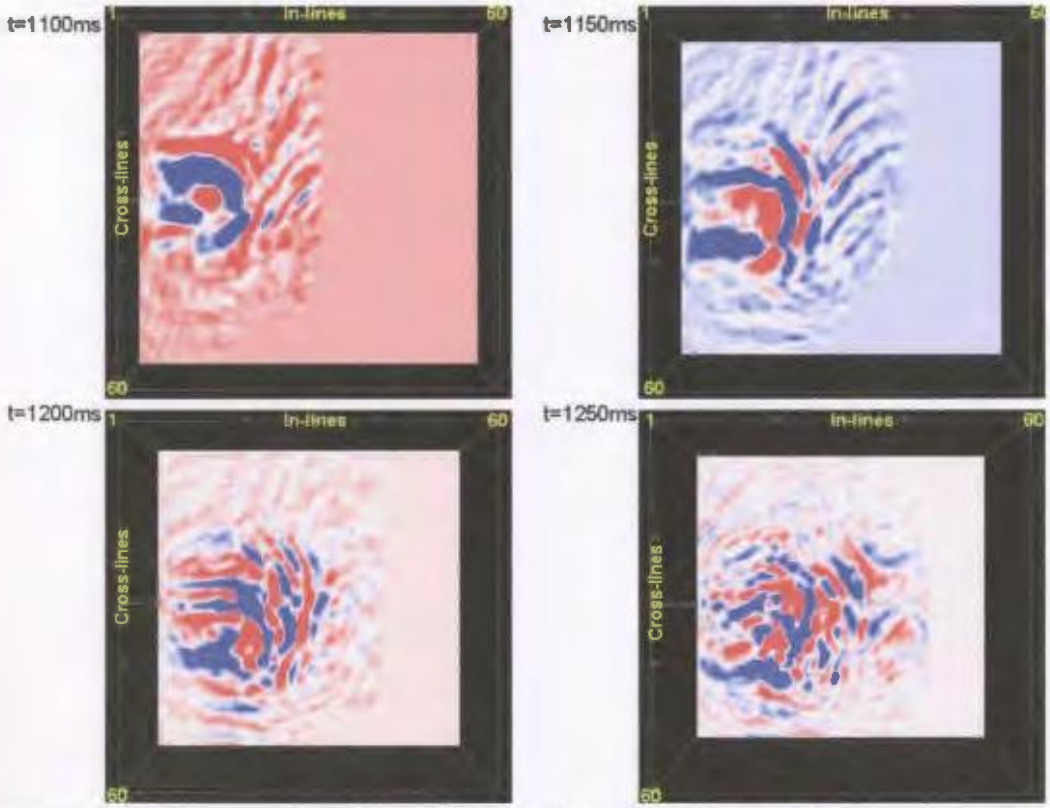


Figure 4.5.3: Migrated horizontal time slices for end B of the scatterer illustrating the non-distinctive pattern.

## 4.6 Conclusions

Processing and analysis of both the individual source surveys and the stacked source surveys revealed that the 'bulls-eye' pattern characteristic of individual scattering bodies in classical 3-D seismic is clearly evident in the 'pseudo 3-D' seismic. As a result, the dense 2-D receiver array and sparse source array technique investigated in this chapter can be considered a more economical method of 3-D seismic in hardrock environments but with essentially the same benefits.

Stacking the four different sources together to compose a common source gather proved valuable because it illustrated that there were in fact diffractions emanating from both ends A and B of the scatterer instead of just from the scatterer as a whole as originally expected. As a consequence, it was necessary to re-stack the data and treat both ends A and B of the scatterer individually. In particular, the complex interfering diffraction pattern from the individual scatterer was best visualized as horizontal time slices instead of as receiver gathers. Comparison of the horizontal time slices for the individual source surveys and for the stacked sections revealed that stacking provided more effective full illumination of the scatterer. To simulate actual seismic data, Gaussian noise was added to the final stacked section. This demonstrated that the horizontal time slices still exhibit the diagnostic 'bulls-eye' pattern in low signal-to-noise conditions. However, the pattern is most evident when the time slices are animated because the eye focuses on the coherent 'bulls-eye' pattern and not the incoherent noise.

3-D migration of the stacked sections simply established that detection of the individual scatterers is best visualized in the horizontal time slices of the unmigrated

sections. 3-D migration caused the diffractions to collapse to a small area at the apex of the diffraction hyperbola and therefore the anomalies were smaller in size and not as clearly distinguishable as the strong 'bulls-eye' pattern in the unmigrated sections. Nevertheless, 3-D migration of the 'pseudo 3-D' data does provide better localization of the scatterer once its existence has been detected.

Focusing on simply detecting the ore bodies rather than imaging them has allowed for the development of a more cost-effective method than classical 3-D seismic in hardrock environments. Developing the technique of a dense 2-D receiver array and a sparse source array will allow for detection of strong scatterers (i.e. ore bodies) in the subsurface more cost-effectively in hardrock environments. However, using a sparse number of sources may cut down on the cost of the survey but it only provides low resolution data. Hence, this technique may benefit the drilling program by providing better localization of prospective targets but it does not provide any detailed information on the size or dip of the ore body. Also, since ore bodies can be quite complex in their shape there may be numerous diffractions emanating from various points along the ore body. Consequently, this may increase the complexity of the first response from the ore body. As a result of this and the low resolution of the data, it may be difficult to distinguish whether or not more than one ore body is being detected. However, this technique will still aid the drilling program by helping to determine areas of interest and eliminating areas unlikely to be of interest. Depth control on the targets may be provided if there is a velocity model for the area. A velocity model may be determined for the area by conducting extensive physical rock properties studies which are an important

prerequisite for any seismic exploration in crystalline basement. In general, the previous modeling results in this study have shown that both the acquisition procedures and the processing schemes related to this technique are not overly labor-intensive or time-consuming. Therefore, mining companies should find this technique to be more suitable to both their exploration and economic needs.

# CHAPTER 5: CONCLUSIONS

Mineral exploration is currently focused on discovering and developing deeper deposits as the known shallow deposits become depleted. Seismic techniques show promise for minerals exploration but conventional acquisition, processing and interpretation techniques require significant modification for the techniques to be effective and economic for the complex targets encountered in hardrock environments. This work has investigated a range of issues related to the application of 2-D and 3-D seismology to exploration for massive sulphides. This preliminary work was completed in preparation for a series of field experiments that will be carried out at the Voisey's Bay nickel-copper-colbalt deposit in Labrador. The objectives of this research were:

1. study and analysis of the seismic properties of the ores and host rocks at Voisey's Bay,
2. investigation of the processing approaches necessary for a 2-D survey planned to delineate the structural setting of the deposit,
3. investigation of an alternative approach to 3-D acquisition and processing.

Analysis of the seismic properties of the ores and host rocks at Voisey's Bay illustrated that their seismic response is greatly affected by composition, metamorphic grade, and fractures. Analysis of velocity, density, acoustic impedance, potential reflection coefficients, and synthetic seismograms for both the Reid Brook and Eastern Deeps zones of the Voisey's Bay area yielded important insights that will dictate the choice of seismic technique utilized in the different zones. The data indicate that

impedance-based techniques would be appropriate for characterization of the ore bodies, the magmatic system, and structural mapping in the Reid Brook zone. However, at the Eastern Deeps zone, velocity-sensitive techniques such as borehole-borehole tomography are most appropriate for direct characterization of the ore bodies themselves, whereas impedance-based techniques such as reflection seismology are more appropriate for characterization of the magmatic system and structural mapping. Nonetheless, the data also support significant potential for impedance driven ore body detection depending upon the specific setting of the ore body in the Eastern Deeps zone. Ultimately the physical properties work demonstrates that minor variations in the host rock type and/or ore mineral combinations may control whether a system responds better to impedance-based techniques and/or velocity-sensitive techniques. Hence, physical properties analysis of the study area becomes a crucial component for any seismic exploration in mining.

Drill-hole data from the Voisey's Bay site indicates a wide range of seismic targets of differing complexity. Based on information from the physical properties analysis and from the working model for development of the Voisey's Bay deposit suggested by Cruden et al. (2000) a velocity model was developed for the purposes of seismic modeling. Initially, the model was created in its simplest form (i.e. constant velocities) and then progressed to greater complexity (i.e. heterogeneity and velocity gradients) in order to study and fine-tune the processing sequence best-suited for hardrock environments such as Voisey's Bay. One of the most important issues that needed to be considered when determining a processing strategy for this mineral

exploration dataset was that the wave field contained both specular reflections and diffractions. The information content of both modes was equally important. Initial evaluation of the seismic data determined that the main processing challenge was related to determining the initial velocity model. Conventional processing, which consisted of stack and post-stack migration, was deemed inferior for this type of dataset. This was primarily because of a velocity conflict between the specular reflections and diffractions. The conventional processing scheme only allowed for either the specular reflections or the diffractions to be stacked completely but not both. As a result, the final migration image was incomplete and important information was missing. A processing scheme involving pre-stack migration was also attempted in order to resolve this issue of conflicting velocities. Again, one of the major issues with pre-stack migration was determining the initial velocity model, which was primarily based on knowledge of the local geology. Tweaking of the velocity model was only accomplished by analyzing the CDP gathers after pre-stack migration. For this synthetic case it was uncomplicated because there was no noise but this may not be the case for a real dataset. In spite of this, it was easier to establish a more accurate velocity model that incorporated information for the entire wave field using this method. This was further verified in the end by the final pre-stack migration image. As a result, a processing scheme involving pre-stack migration was preferred over post-stack migration for this typical mineral exploration dataset. This was mainly because it was able to handle the conflicting velocities for the specular reflections and diffractions more effectively.

The effect of velocity gradients in the Voisey's Bay area was also examined in order to ascertain whether or not surface-surface seismic tomography may be a viable technique for imaging the troctolite intrusions. Preliminary results showed that the velocity gradients for the Voisey's Bay area were not strong enough to produce turning rays at great enough depths (>1500 m) for effective delineation of the magmatic plumbing system. Instead, a maximum depth of only 500 m was determined for the orthogneisses while a maximum depth of 1000 m was determined for the paragneisses. However, these velocity gradients are considered to be a minimum approximation because they were based on laboratory data and the resulting velocity gradients must be predominantly the result of micro-crack closure. As a result, further work comprised of field investigation and measurement may provide more accurate velocity gradient results and therefore the feasibility of surface-surface tomography for the Voisey's Bay area should be re-evaluated.

Heterogeneity mapping was evaluated as another technique exploiting the benefits of 2-D reflection seismic data for hardrock environments. The advantage of heterogeneity mapping is that it produces detailed statistical parameter maps that can map variations in the reflection wave field related to macro-scale fabrics and emphasize variations related to geology. For this particular dataset the statistical parameter maps were partially successful in distinguishing between the troctolite, which hosts the sulphide mineralization, and the foliated gneiss, which is the predominant country rock, for the Voisey's Bay area. However, this particular hardrock environment did not give rise to the 'ideal' conditions for heterogeneity mapping which was demonstrated by the fact that this

procedure was unable to map the entire troctolite system. Despite this, heterogeneity mapping is a technique that has the potential to aid in the delineation of the magmatic plumbing system at Voisey's Bay.

An alternative approach to 3-D acquisition and processing was investigated by focusing on simply detecting the ore bodies rather than imaging them which then allowed for the utilization of a technique based on a dense 2-D receiver array and a sparse source array. This technique allows for the potential detection of strong scatterers (i.e. ore bodies) in the subsurface more cost-effectively in hardrock environments than conventional 3-D seismic. Processing and analysis of the individual datasets revealed that the 'bulls-eye' pattern characteristic of individual scattering bodies in classical 3-D seismic volumes is clearly evident in the 'pseudo 3-D' seismic horizontal time-slices. Stacking of the individual datasets provided more complete illumination of the scatterer as opposed to the localized illumination from the individual source surveys and demonstrated that scattering occurs from multiple source points on the scattering body. 3-D migration of the stacked sections illustrated that although diffractions were partially collapsed, the imaging was incomplete due to the sparsity of the source points. Comparison between the unmigrated and migrated time-slices revealed that the unmigrated data were more effective for diffraction detection while the migrated data provided better localization of the scatterer. Although this technique is more cost-effective, it only provides low resolution data which as a result provides limited information on the size or dip of the ore body. This will also affect whether or not

multiple ore bodies can be distinguished from each other. In addition, depth control on the targets may only be provided if there is a velocity model for the area.

Overall, the issues discussed in each of the preceding chapters demonstrated that seismic techniques show promise for mineral exploration. Imaging and detection of ore bodies in a hardrock environment requires extensive analysis of the physical properties of the pertinent rocks in the study area. Only then can an informed estimate of the appropriate data acquisition and processing parameters be made before implementation of field-based seismic experiments. This will help to foresee any acquisition and processing issues which, in turn will allow for the design of both high quality – high return 2-D and 3-D experiments in an environment where seismic reflection methods have rarely been used.

## References


Adam, E, Perron, G., Arnold, G., Matthews, L., and Milkereit, B., 2003, Hardrock Seismic Exploration: 3D Seismic Imaging for VMS Deposit Exploration, Matamagi, Quebec. Society of Exploration Geophysicists, Geophysical Developments, No. 10, pp. 229-246.

Albertin, U., Kapoor, J., Randall, R., Smith, M., Brown, G. Soufleris, C. Whitfield, P., Dewey, F., Fansworth, J., Grubitz, G., and Kemme, M., 2002, The Time for Depth Imaging. Oilfield Review, Spring, pp. 1-15.

Bohlen, T., Muller, C., and Milkereit, B., 2003, Hardrock Seismic Exploration: Elastic Seismic-Wave Scattering from Massive Sulfide Orbodies: On the Role of Composition and Shape, Society of Exploration Geophysicists, Geophysical Developments, No. 10, pp.70-89.

Cruden, A.R., Burrows, D.R. and Evans-Lamswood, D., 2000, Structural, tectonic and fluid mechanical controls on emplacement of the Voisey's Bay troctolite and its Ni-Cu-Co mineralization. GAC_MAC Abstract.

Eaton, D., Milkereit, B., and Salisbury, M., 2003a, Hardrock Seismic Exploration: Mature Technologies Adapted to New Exploration Targets, Society of Exploration Geophysicists, Geophysical Developments No. 10, pp. 1-6.

Eaton, D., Milkereit, B., and Salisbury, M., 2003b, Seismic methods for deep mineral exploration: Mature technologies adapted to new targets. The Leading Edge, June, pp. 580-585.

Evans-Lamswood, D. M., Butt, D.P., Jackson, R.S., Lee, D.V., Muggridge, M.G. and Wheeler, R.I., 2000, Physical Controls Associated with the Distribution of Sulfides in the Voisey's Bay Ni-Cu-Co Deposit, Labrador. Economic Geology, Vol. 95, pp. 749-769.

Evans-Lamswood, D., 1999, Physical and Geometric Controls on the Distribution of Magmatic and Sulphide-Bearing Phases within the Voisey's Bay Nickel-Copper-Cobalt Deposit, Voisey's Bay, Labrador. M.Sc. Thesis, Memorial University of Newfoundland.

Fowler, C.M.R., 2005, The Solid Earth: An Introduction to Global Geophysics. Cambridge University Press: Cambridge, p. 157.

Goff, J.A., and Jordan, T.H., 1988, Stochastic modeling of seafloor morphology: Inversion of Sea Beam data fir second-order statistics, J. Geophys. Res., Vol. 93, No. 13, pp. 589-13608.

Hurich, C.A., 2007, In Review, Heterogeneity mapping of deep seismic profiles: Review, validation and examples, Tectonophysics.

Hurich, C.A., 2006. Seismic Mapping of Intrusive Systems, web article: http://www.mun.ca/earthsciences/Hurich/Mapping.php

Hurich, C.A., 2004, Seismology and the Characterization of Lithospheric Heterogeneity, Extended Abstract, CCSS Fall 2004, Virginia Tech.

Hurich, C.A., 2003, The nature of crustal seismic heterogeneity: A case study from the Grenville Province, in J.A. Goff and K. Holliger, eds., Heterogeneity in the Crust and Upper Mantle, Kluwer Academic, New York, pp. 299-320.

Hurich, C.A., Deemer, S.J., Indares, A., and Salisbury, M., 2001, Compositional and metamorphic controls on velocity and reflectivity in the continental crust: An example from the Grenville Province of eastern Quebec. Jour. Geophys. Res., Vol. 106, No. B1, pp. 665-682.

Hurich, C.A., and Kocurko, A., 2000, Statistical approaches to interpretation of seismic reflection data. Tectonophysics, Vol. 329, pp. 251-267.

Kessinger, W., 2005. Exploration Seismology, web article: http://walter.kessinger.com/index1.html.

Laletsang, K., 2001, Seismic Exploration for Metallic Mineral Deposits. Ph.D. Thesis, Memorial University of Newfoundland.

Larner, K., Chambers, R., Yang, M., Lynn, W., and Willon, W., 1983. Coherent noise in marine seismic. Geophysics, Vol. 48, No. 7, pp.854-886.

Li, C., and Naldrett, A.J., 1999, Geology and petrology of the Voisey's Bay intrusion: Reaction of olivine with sulfide and silicate liquids. Lithos, V. 27, pp. 1-32.

Ludwig, J., Nafe, J., and Drake, C., 1971, Seismic refraction, in Maxwell, A.E., Ed., The sea, V.4: Wiley, pp.53-84.

MacDonald, J.G., Burton, C.J., Winstanley, I., and Lapidus, D.F., Collins Dictionary: Geology. New ed. 2003.

Milkereit, B., Eaton, D., Wu, J., Perron, G., Salisbury, M., Berrer, E.K. and Morrison, G., 1996, Seismic Imaging of Massive Sulfide Deposits: Part II. Reflection Seismic Profiling. Economic Geology, Vol. 91, No. 5, pp. 829-834.

Naldrett, A.J., Singh, J., and Li, C., 2000, The Mineralogy of the Voisey's Bay Ni-Cu-Co Deposit, Northern Labrador, Canada: Influence of Oxidation State and Textures and Mineral Compositions. Economic Geology, Vol. 95, pp. 889-900.

Perroud, H., and Tygel, M., 2004, Nonstretch NMO. Geophysics, Vol. 69, No. 2, pp. 599-607.

Raiaskaran, S., and McMechan, G.A., 1995, Prestack processing of land data with complex topography. Geophysics, Vol. 60, No. 6, pp. 1875-1886.

Reynolds, J.M., 1997, An Introduction to Applied and Environmental Geophysics. John Wiley & Sons: New York, pp. 374-375.

Ryan, B., 2000, The Nain-Churchill Boundary and the Nain Plutonic Suite: A Regional Perspective on the Geologic Setting of the Voisey's Bay Ni-Cu-Co Deposit. Economic Geology, Vol. 95, pp. 703-724.

Salisbury, M., and Iulucci, R., 2006. GSC Atlantic/Dalhousie University Rock Properties Database: Web article: http://gsca.nrcan.gc.ca/pubprod/rockprop/index_e.php

Salisbury, M., Harvey, C., Matthews, L., 2003, Hardrock Seismic Exploration: The Acoustic Properties of Ores and Host Rocks in Hardrock Terranes, Society of Exploration Geophysicists, Geophysical Developments No. 10, pp. 9-19.

Salisbury, M., Milkereit, B., Ascough, G., Adair, R., Matthews, L., Schmitt, D.R., Mwenifumbo, J., Eaton, D.W. and Wu, J., 2000, Physical properties and seismic imaging of massive sulfides. Geophysics, Vol. 65, No. 6, pp. 1882-1889.

Salisbury, M.H., Milkereit, B. and Bleeker, W., 1996, Seismic Imaging of Massive Sulfide Deposits: Part I. Rock Properties. Economic Geology, Vol. 91, No. 5, pp. 821-828.

Sheriff, R.E., and Geldart, L.P., 1995, Exploration Seismology. Cambridge University Press: Cambridge, pp. 146-150, 183.

Yılmaz, Öz., Doherty, S.M., 2001. Seismic Data Analysis. Society of Exploration Geophysicists, Tulsa, Ok., Investigations in Geophysics, Vol. 1.

Yilmaz, Öz., Doherty, S.M., 1987. Seismic Data Processing. Society of Exploration Geophysicists, Tulsa, Ok., Series 1 – Investigations in Geophysiscs, Vol. 2.

# Appendix A

This appendix illustrates the density, velocity, and acoustic impedance histograms for both the host rocks and the ores for both the Reid Brook (RBZ) and Eastern Deeps (ED) zones. Information regarding the mean distribution, standard deviation of the distribution, and the number of samples in the distribution was also provided for each respective histogram. These histograms were used to aid in the analysis of the statistical distribution of the physical properties for the Voisey's Bay area in Section 2.3.2 of Chapter 2.

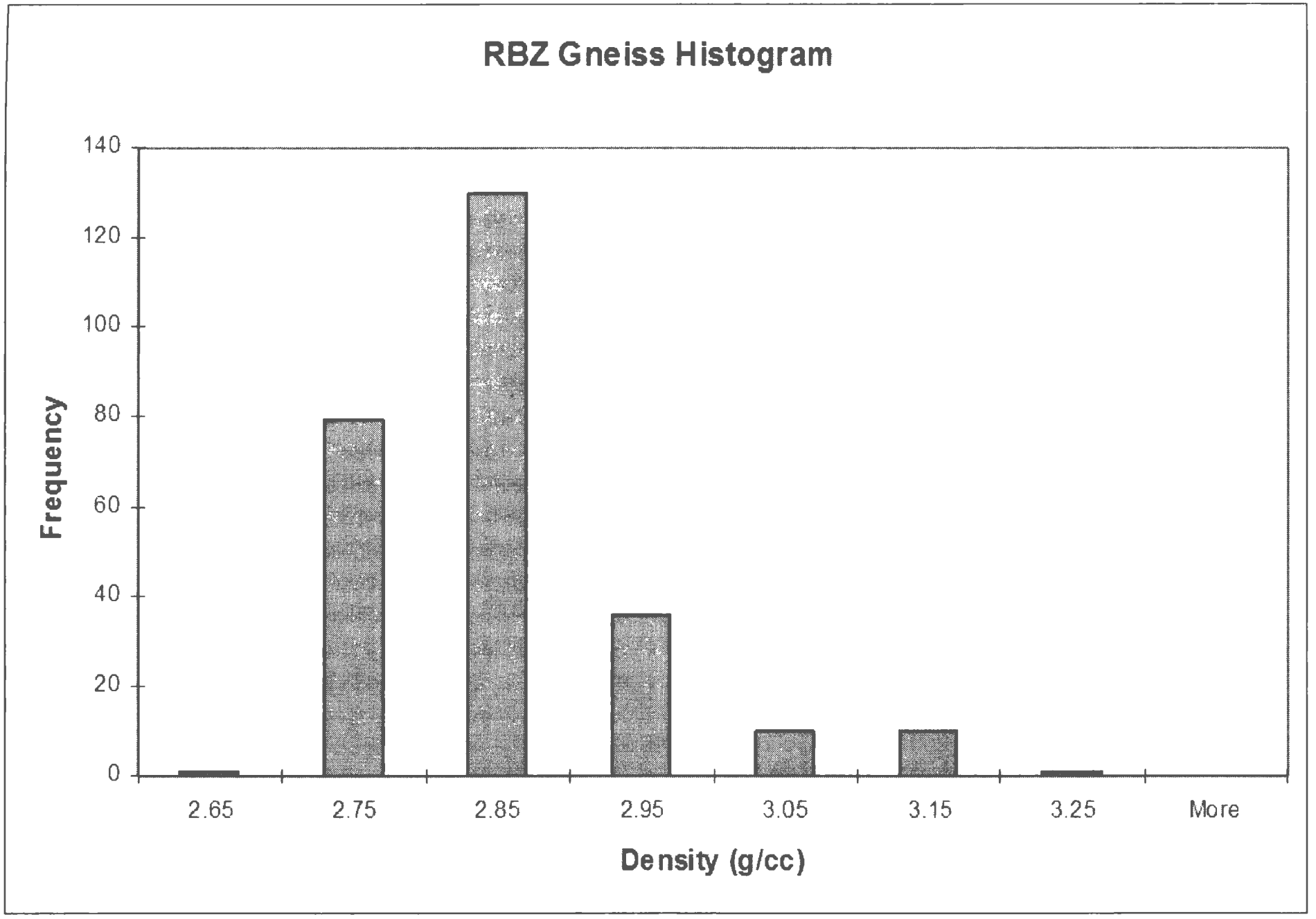


| | |
|---|---|
| Average Density | 2.80 |
| Standard Deviation | 0.00968 |
| Number of Samples | 267 |

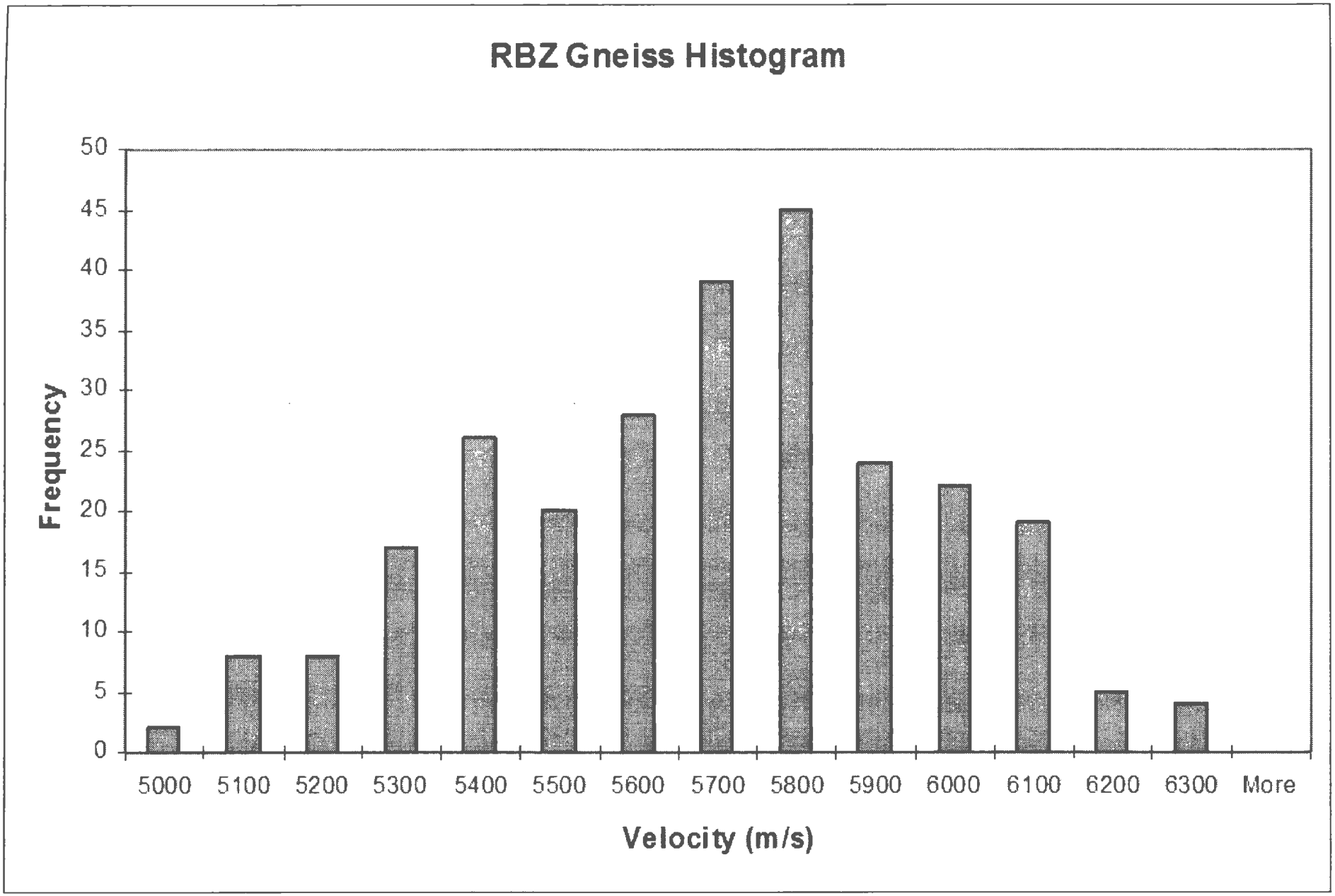


| | |
|---|---|
| Average Velocity | 5642 |
| Standard Deviation | 279 |
| Number of Samples | 267 |

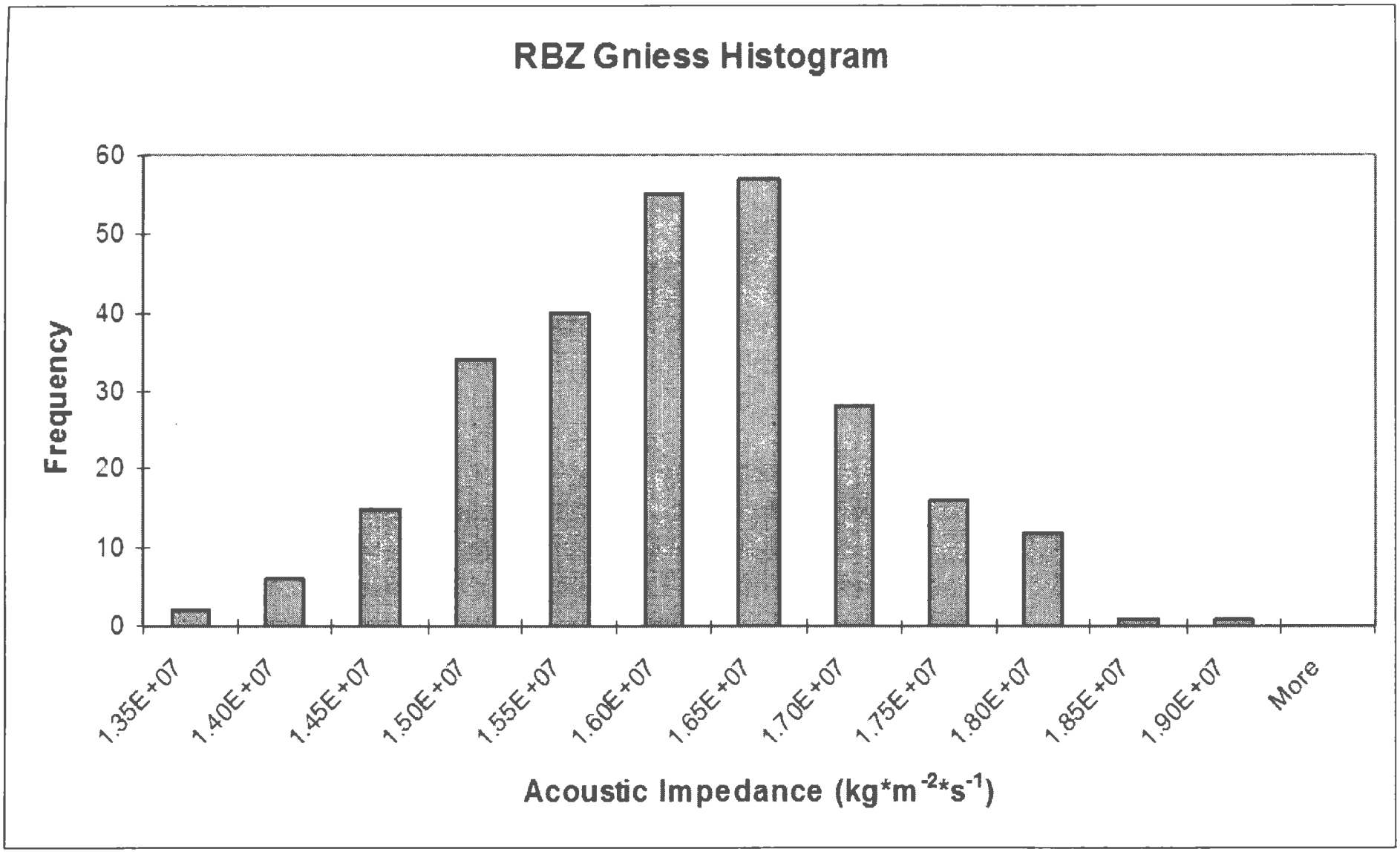


| | |
|---|---|
| Average Acoustic Impedance | 1.58 E+07 |
| Standard Deviation | 9.64 E+05 |
| Number of Samples | 267 |

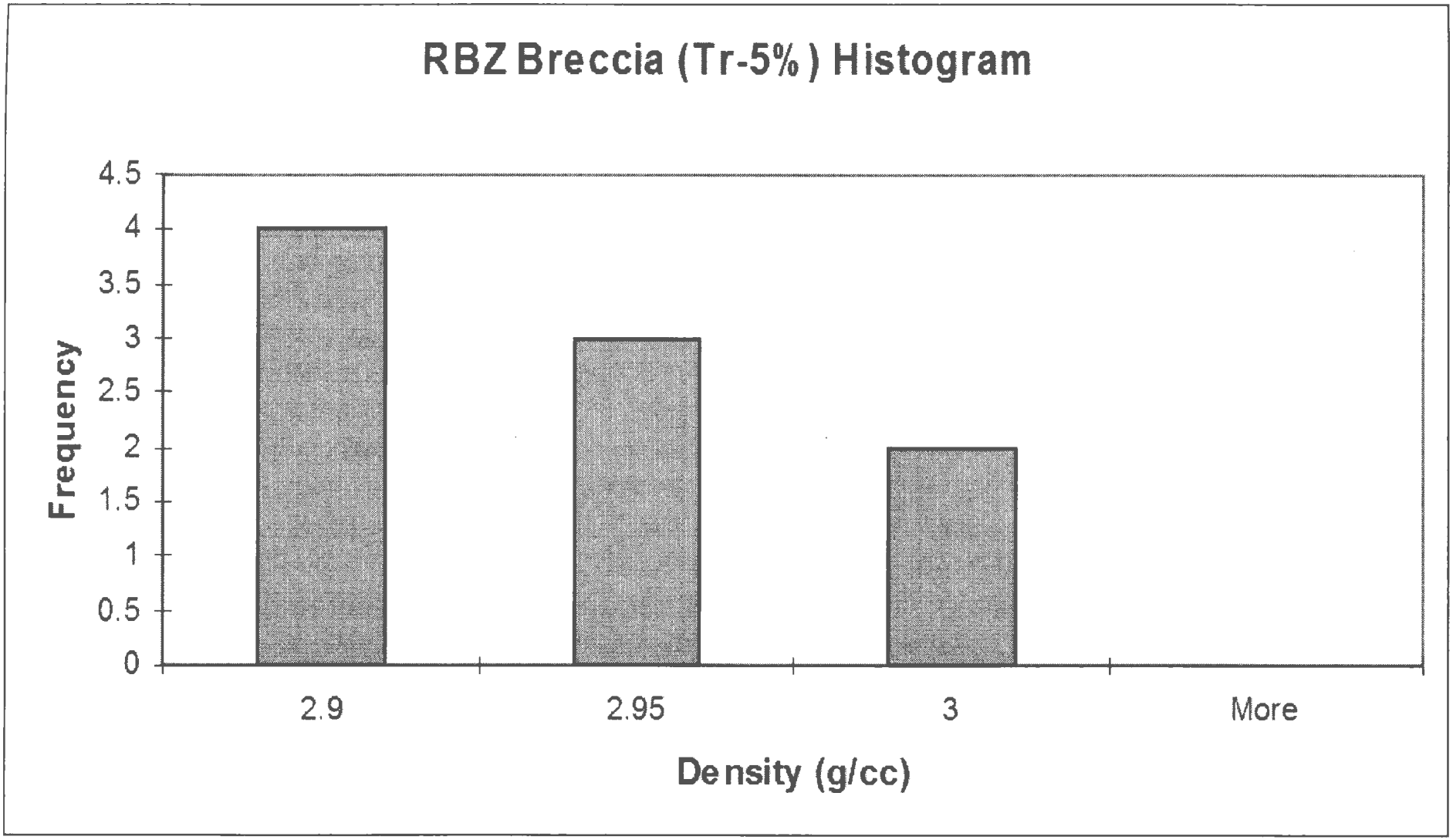




| | |
|---|---|
| Average Density | 2.92 |
| Standard Deviation | 0.0319 |
| Number of Samples | 9 |

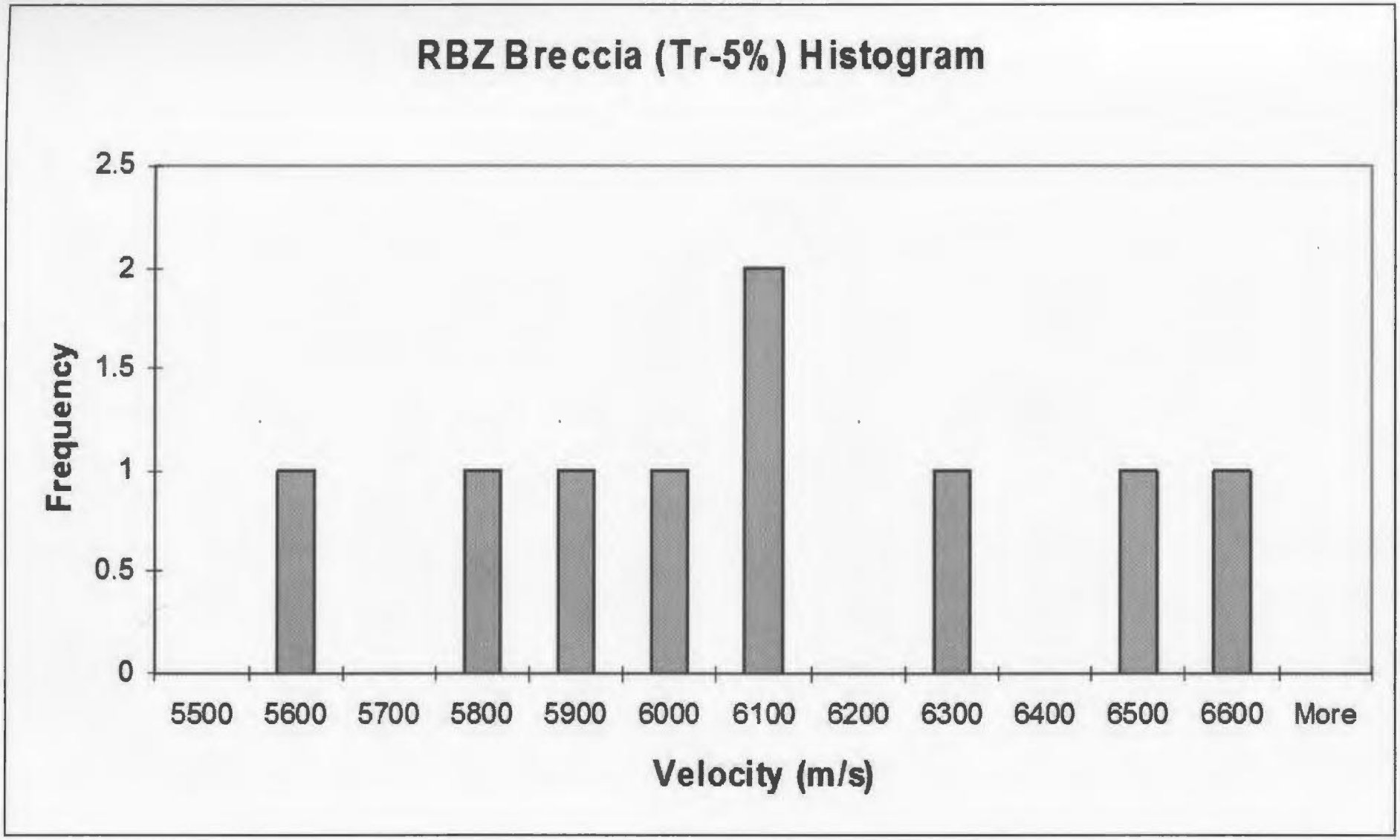


| | |
|---|---|
| Average Velocity | 6050 |
| Standard Deviation | 342 |
| Number of Samples | 9 |

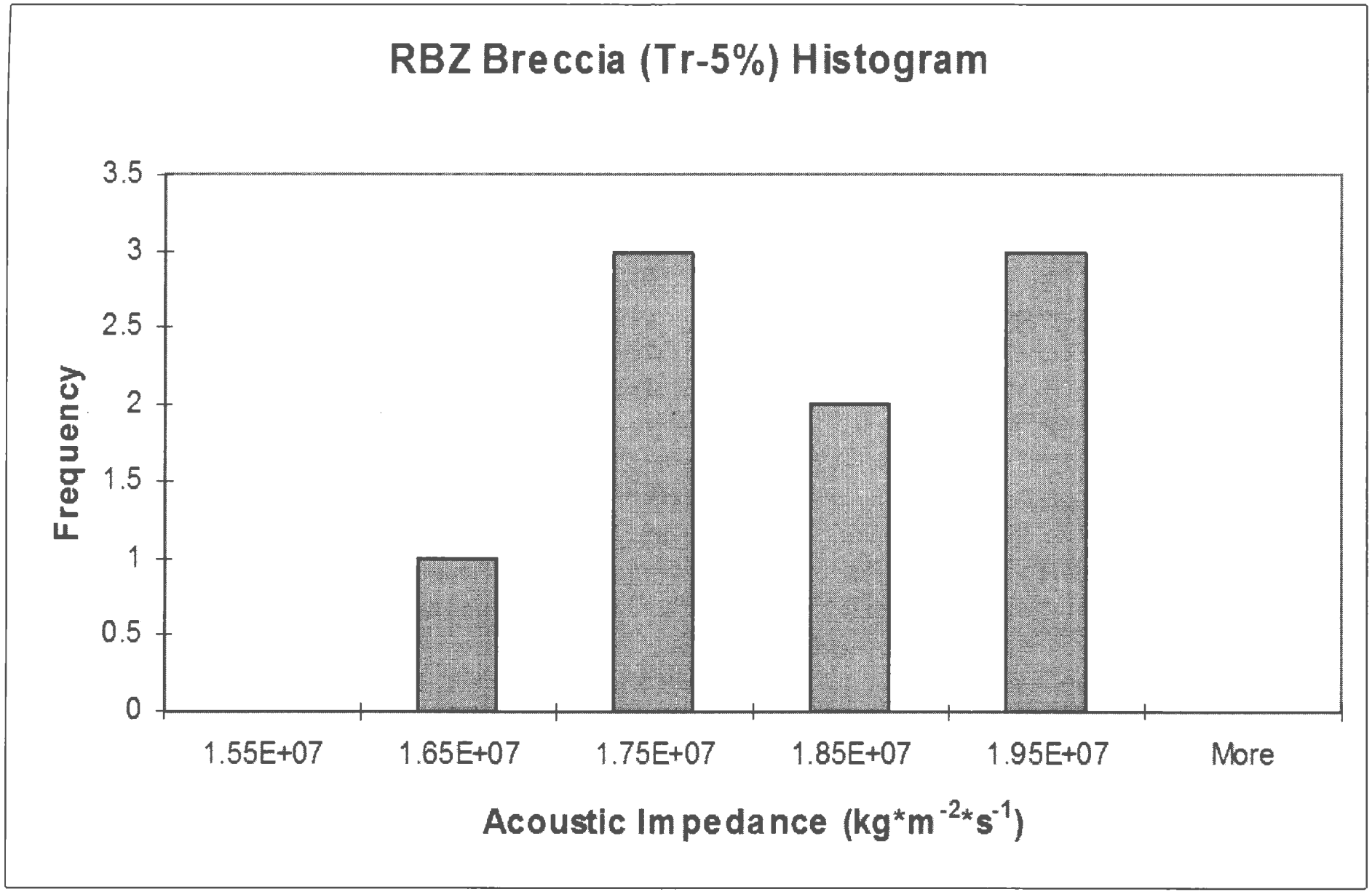


| | |
|---|---|
| Average Acoustic Impedance | 1.77 E+07 |
| Standard Deviation | 1.08 E+06 |
| Number of Samples | 9 |

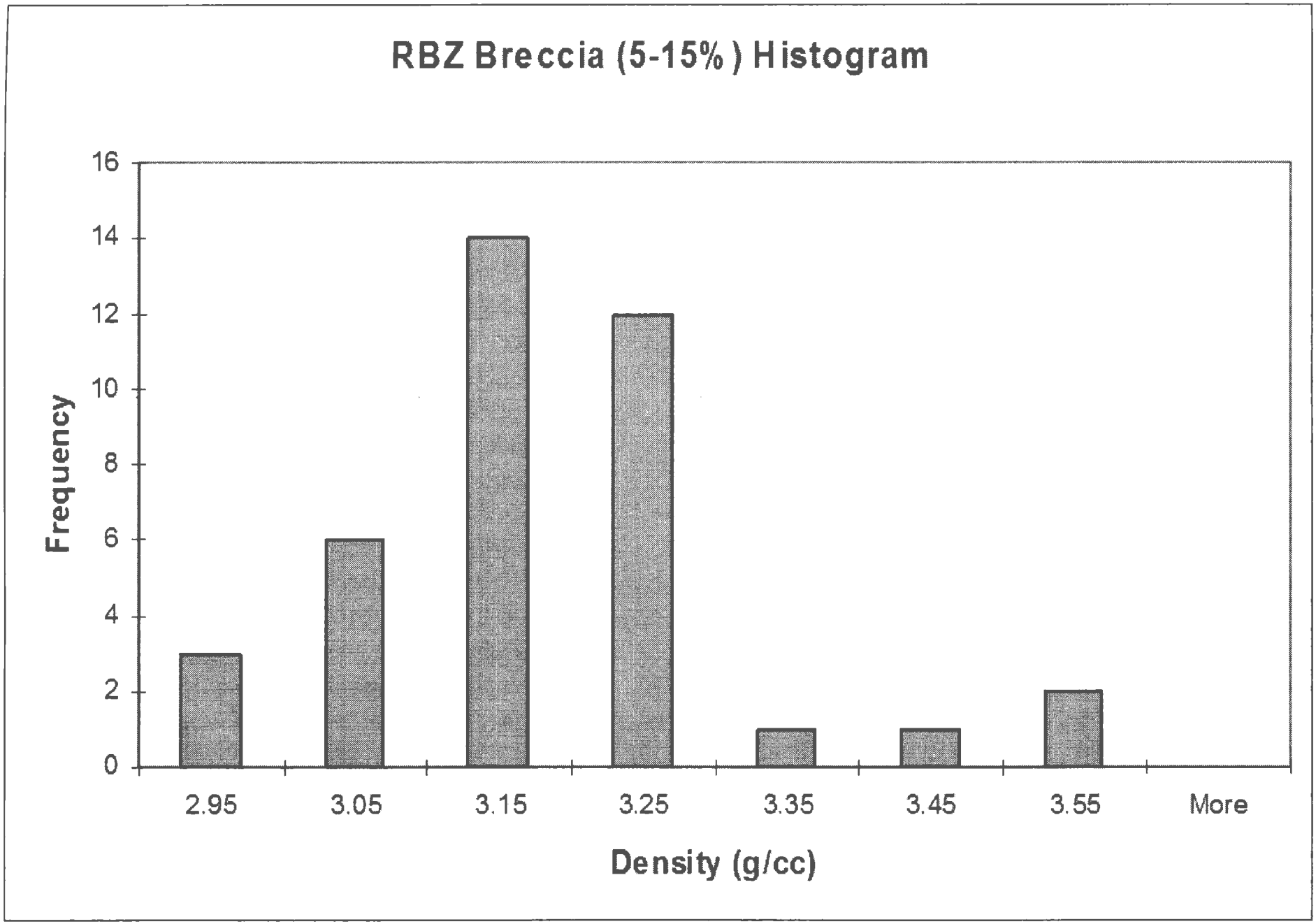


| | |
|---|---|
| Average Density | 3.13 |
| Standard Deviation | 0.136 |
| Number of Samples | 39 |

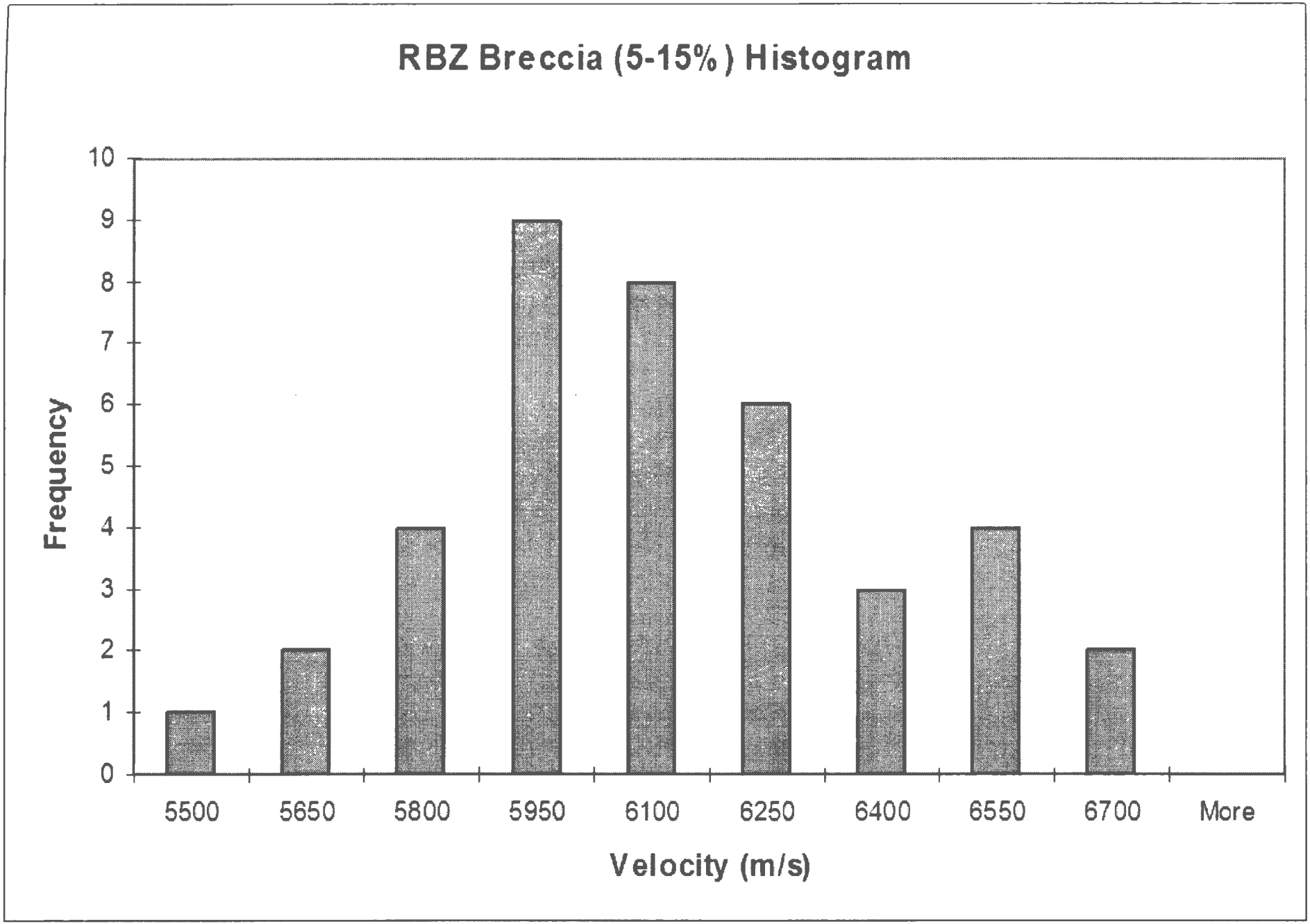


| | |
|---|---|
| Average Velocity | 6039 |
| Standard Deviation | 294 |
| Number of Samples | 39 |

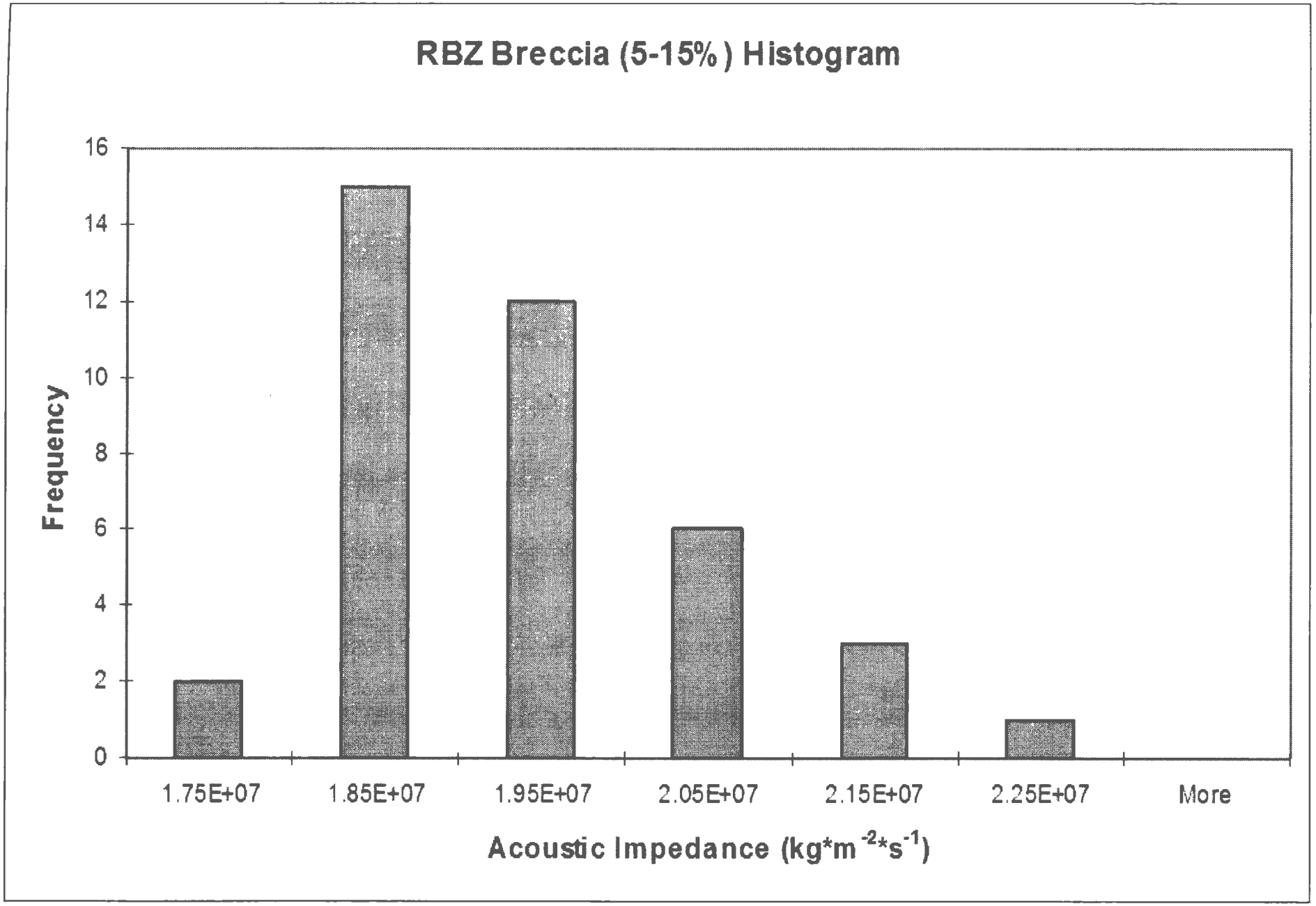


| | |
|---|---|
| Average Acoustic Impedance | 1.89 E+07 |
| Standard Deviation | 1.14 E+06 |
| Number of Samples | 39 |

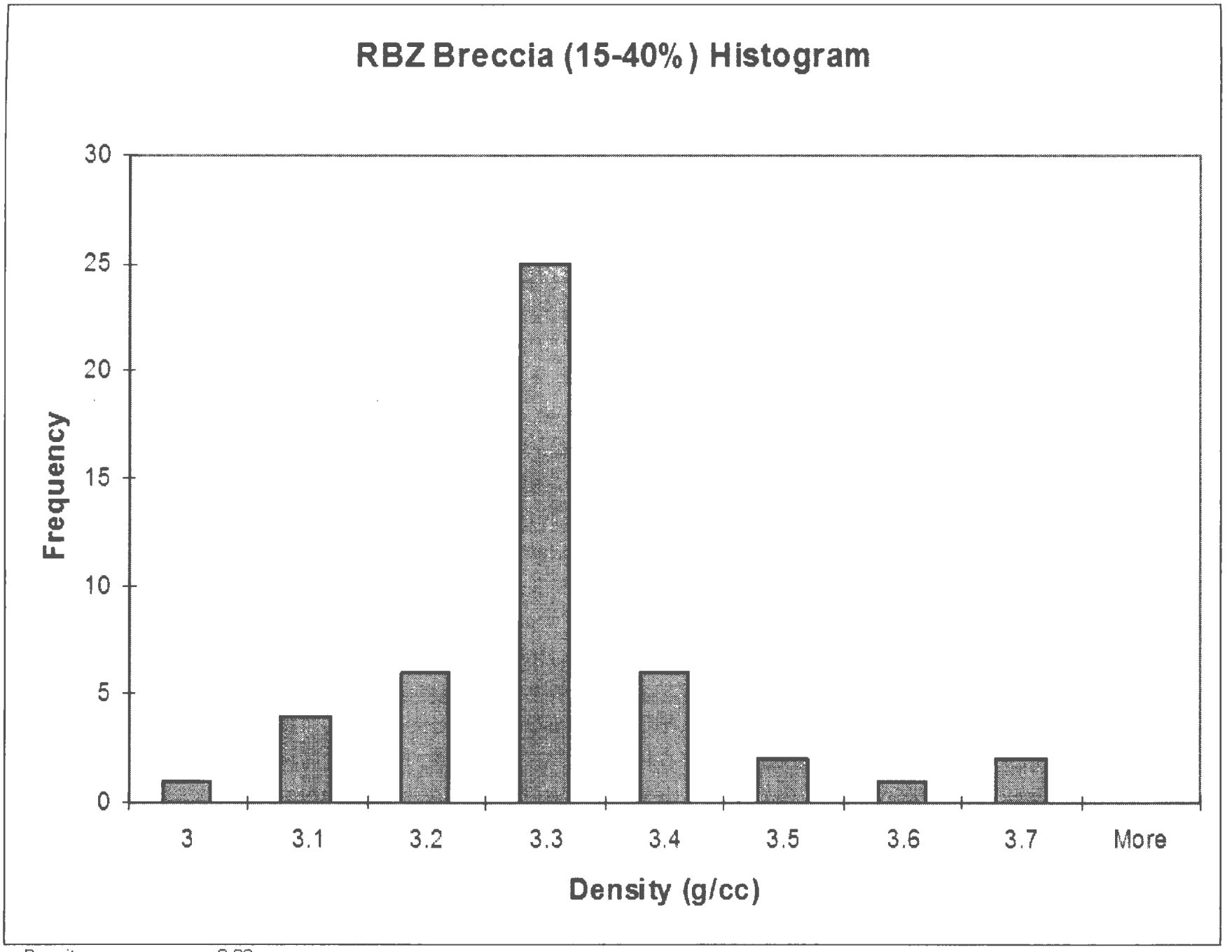


| | |
|---|---|
| Average Density | 3.26 |
| Standard Deviation | 0.131 |
| Number of Samples | 47 |

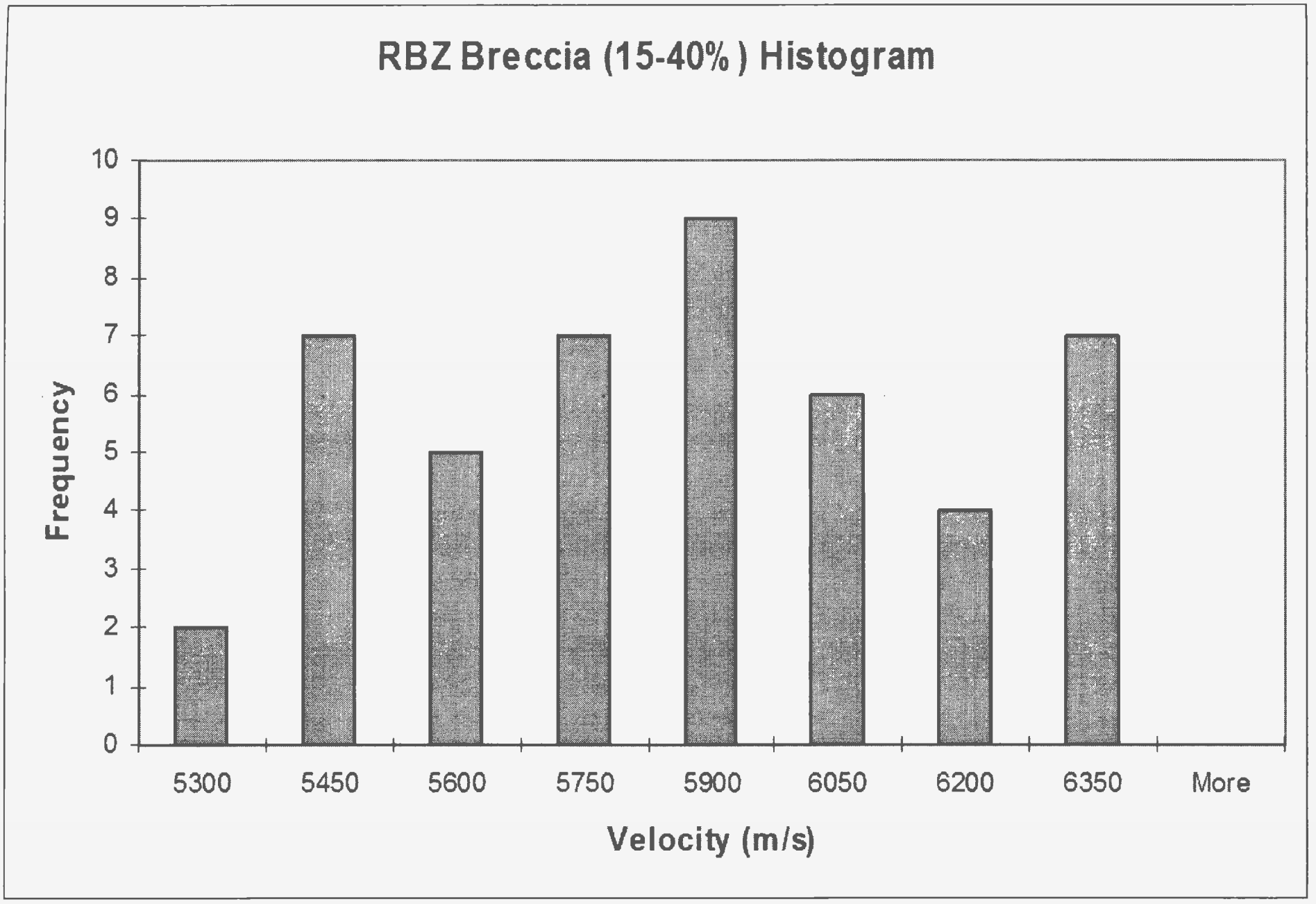


| | |
|---|---|
| Average Velocity | 5781 |
| Standard Deviation | 329 |
| Number of Samples | 47 |

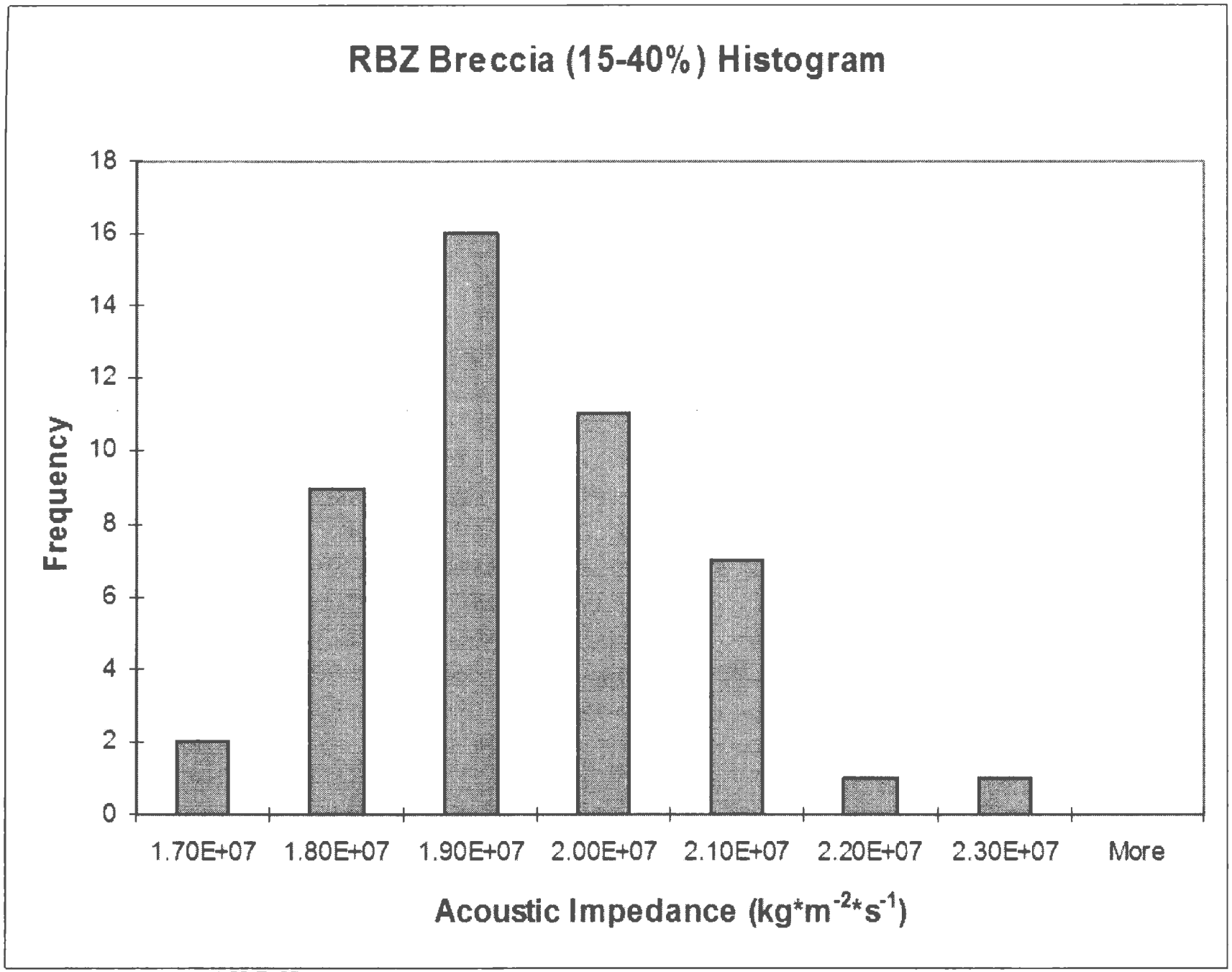


| | |
|---|---|
| Average Acoustic Impedance | 1.88 E+07 |
| Standard Deviation | 1.37 E+06 |
| Number of Samples | 47 |

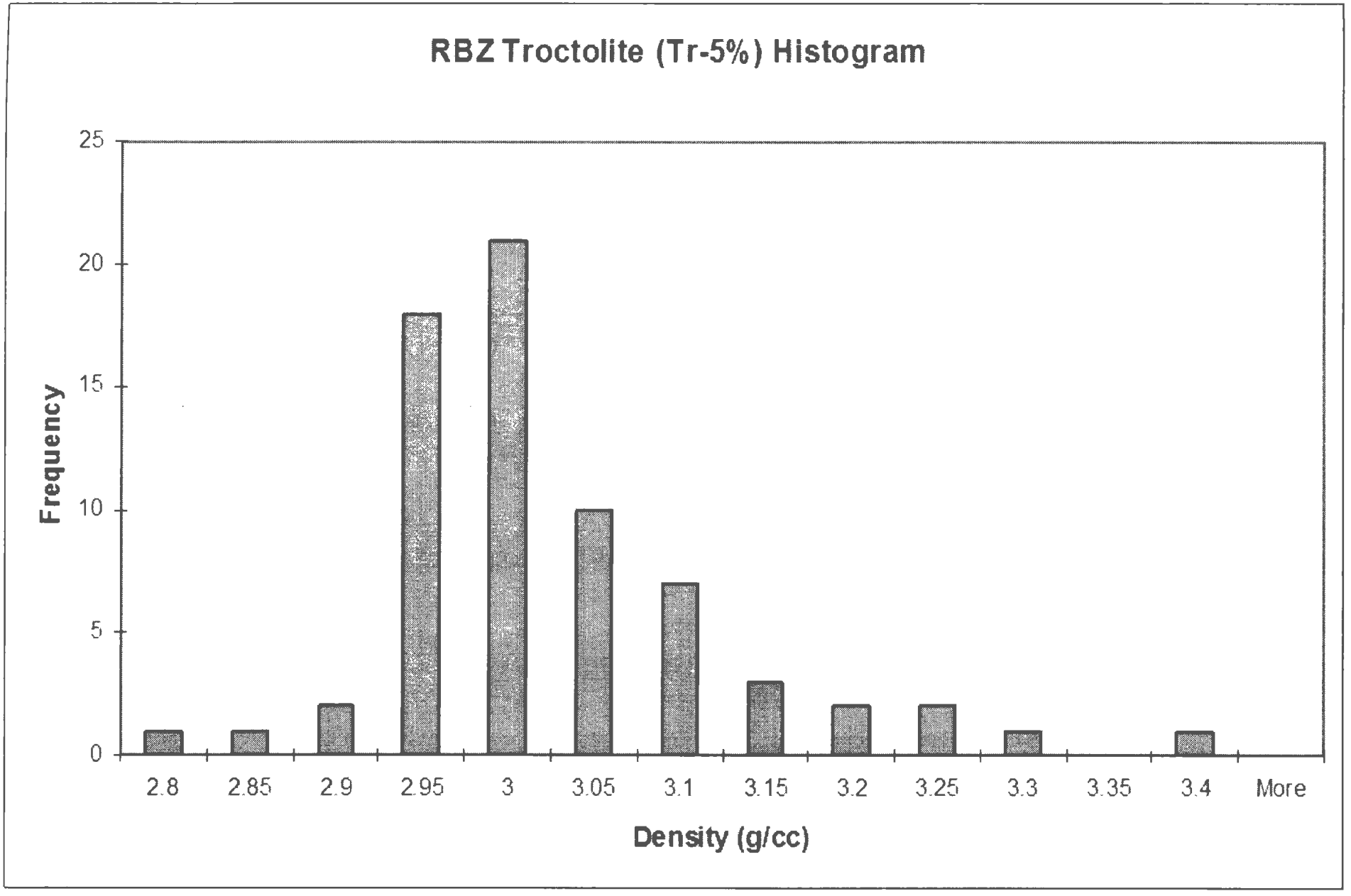


| | |
|---|---|
| Average Density | 2.99 |
| Standard Deviation | 0.0954 |
| Number of Samples | 69 |

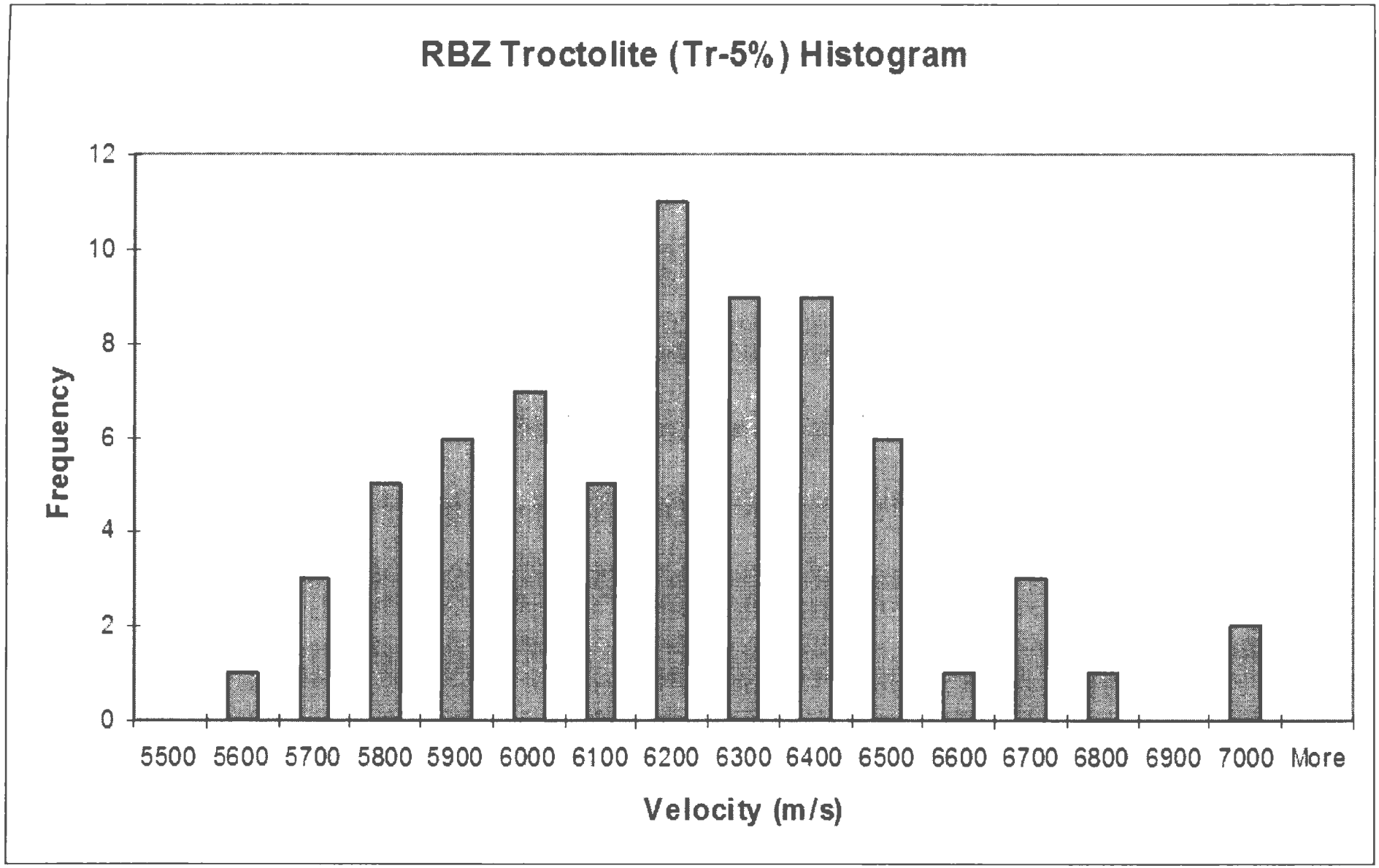


| | |
|---|---|
| Average Velocity | 6158 |
| Standard Deviation | 301 |
| Number of Samples | 69 |

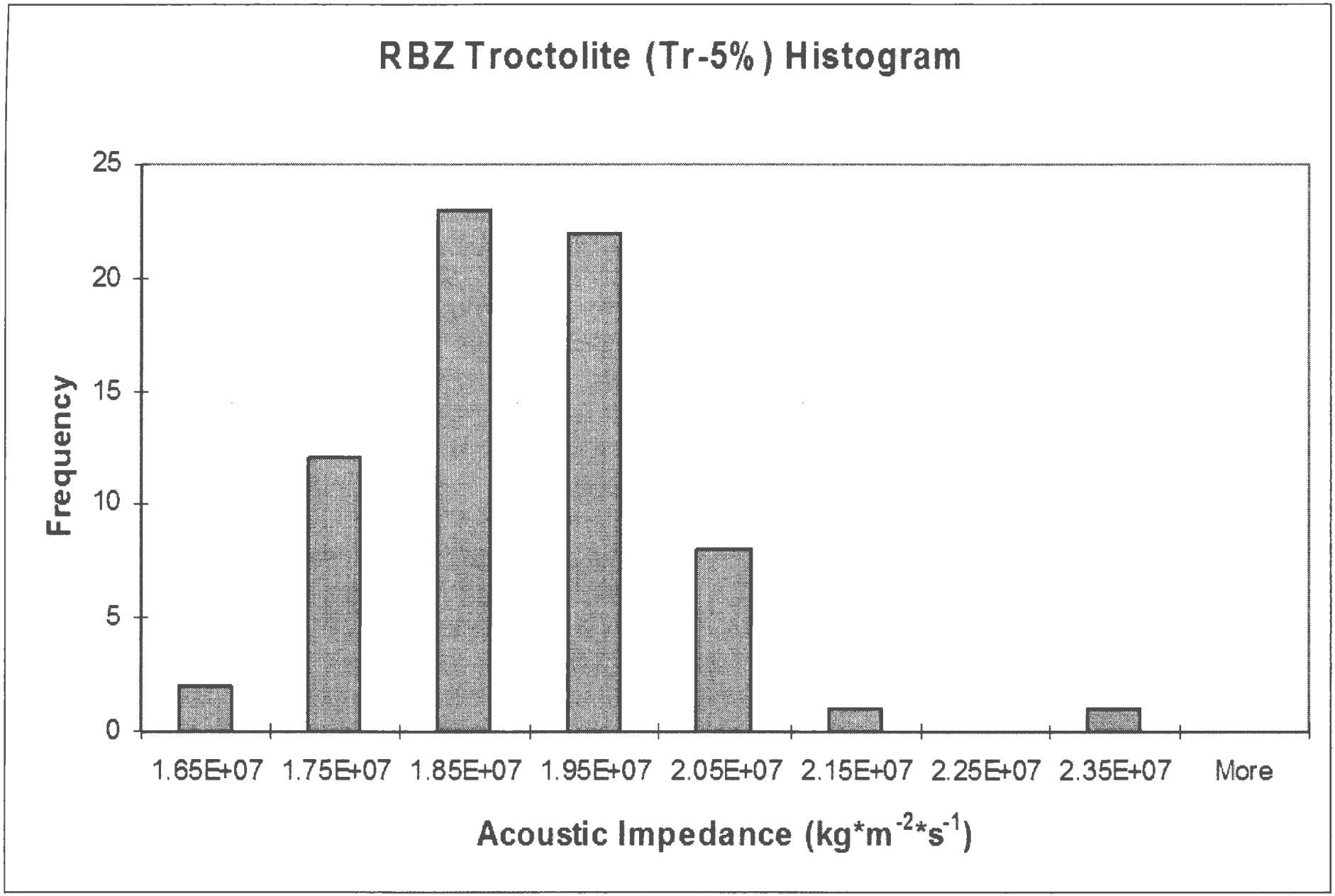


| | |
|---|---|
| Average Acoustic Impedance | 1.85 E+07 |
| Standard Deviation | 1.12 E+06 |
| Number of Samples | 69 |

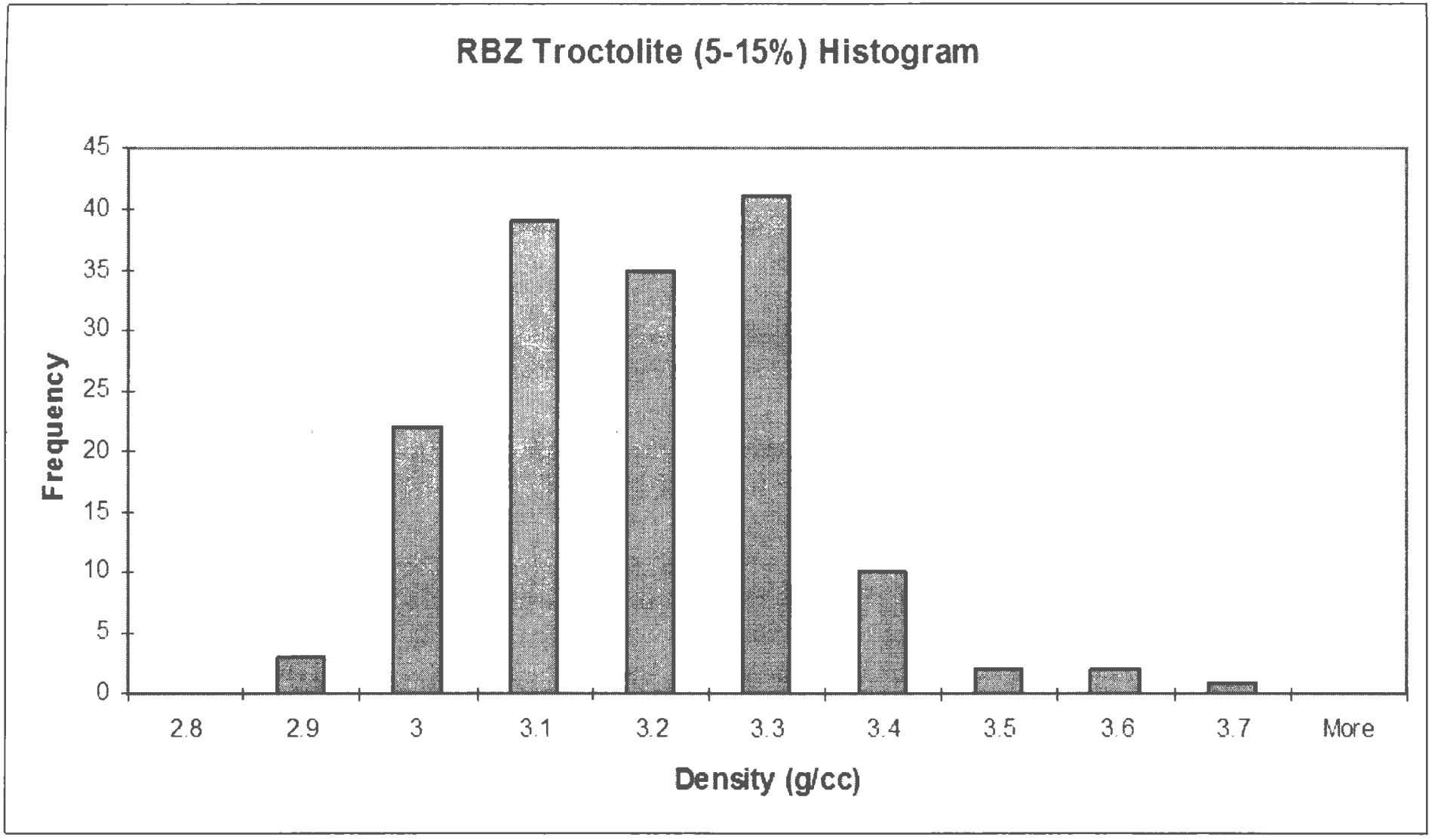


| | |
|---|---|
| Average Density | 3.14 |
| Standard Deviation | 0.138 |
| Number of Samples | 155 |

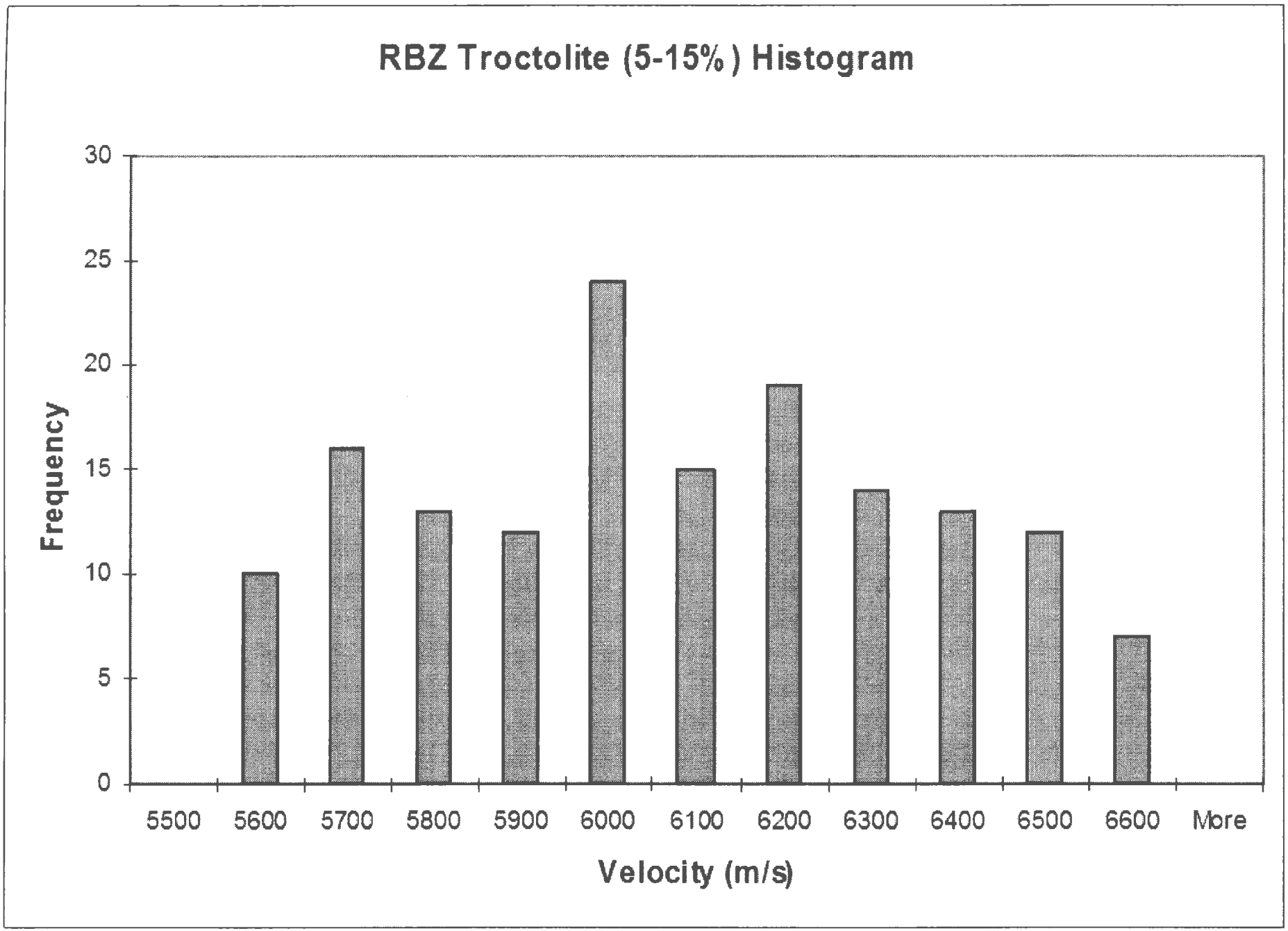


| | |
|---|---|
| Average Velocity | 6031 |
| Standard Deviation | 287 |
| Number of Samples | 155 |

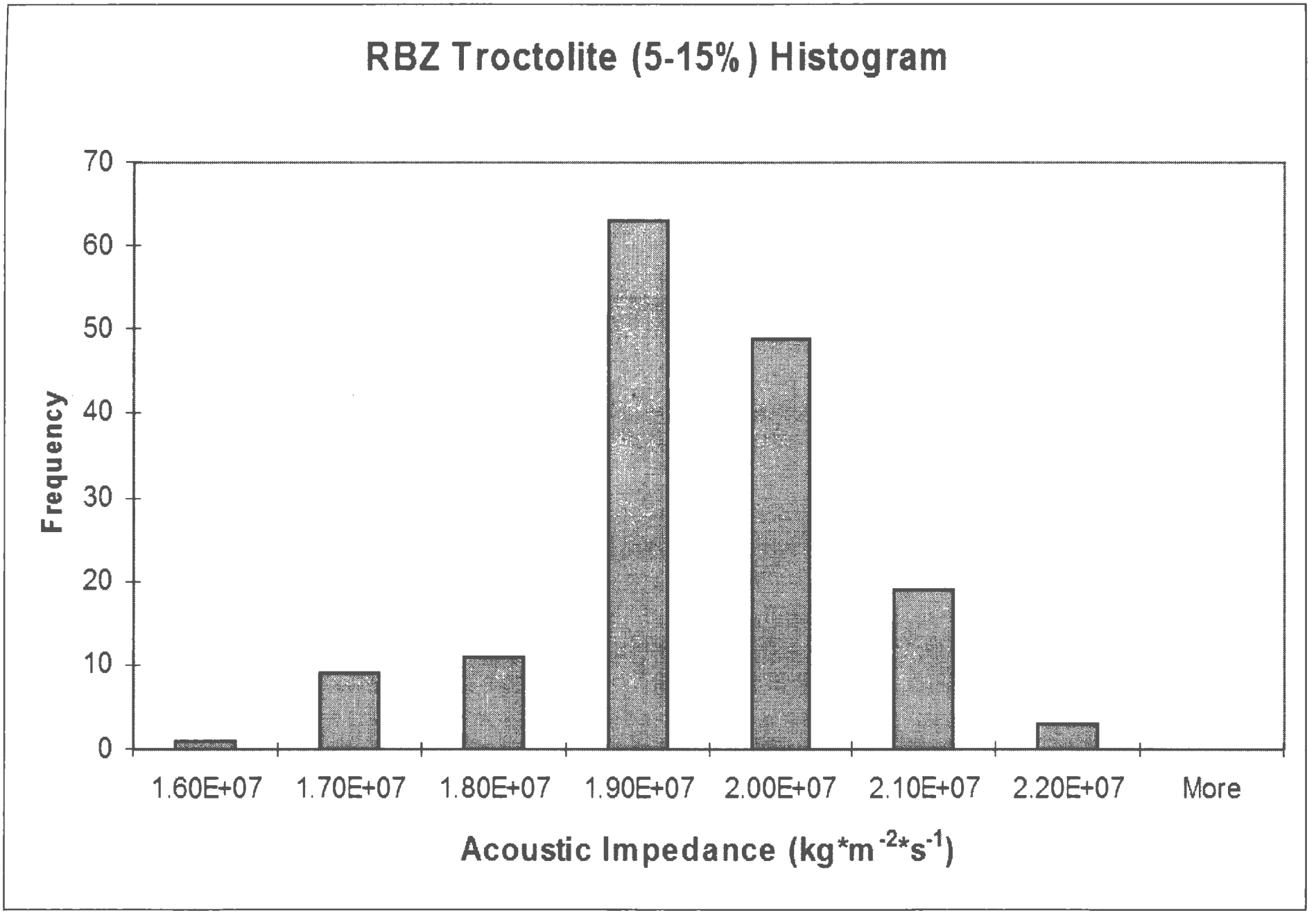


| | |
|---|---|
| Average Acoustic Impedance | 1.89 E+07 |
| Standard Deviation | 1.04 E+06 |
| Number of Samples | 155 |

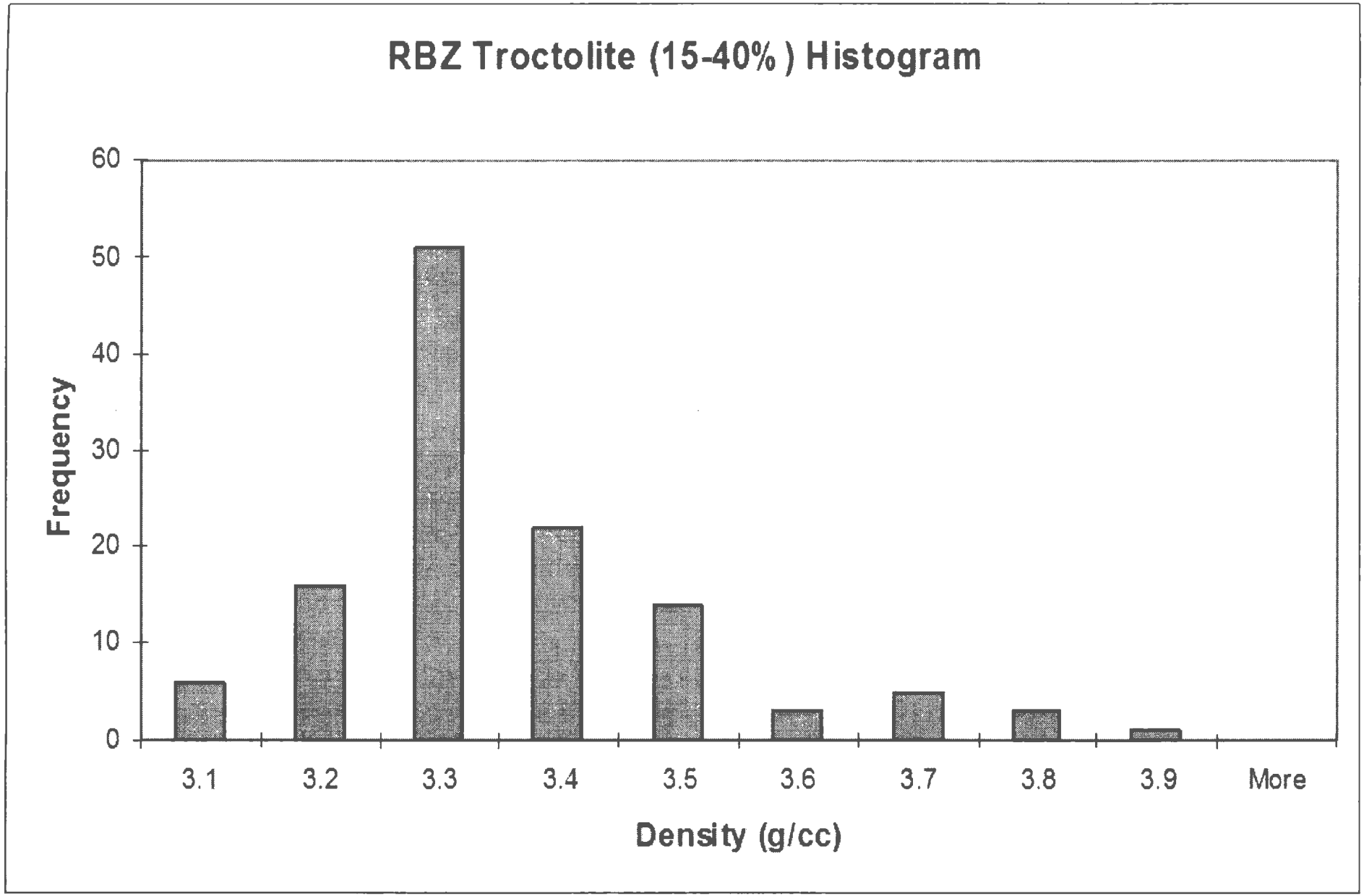




| | |
|---|---|
| Average Density | 3.31 |
| Standard Deviation | 0.153 |
| Number of Samples | 121 |

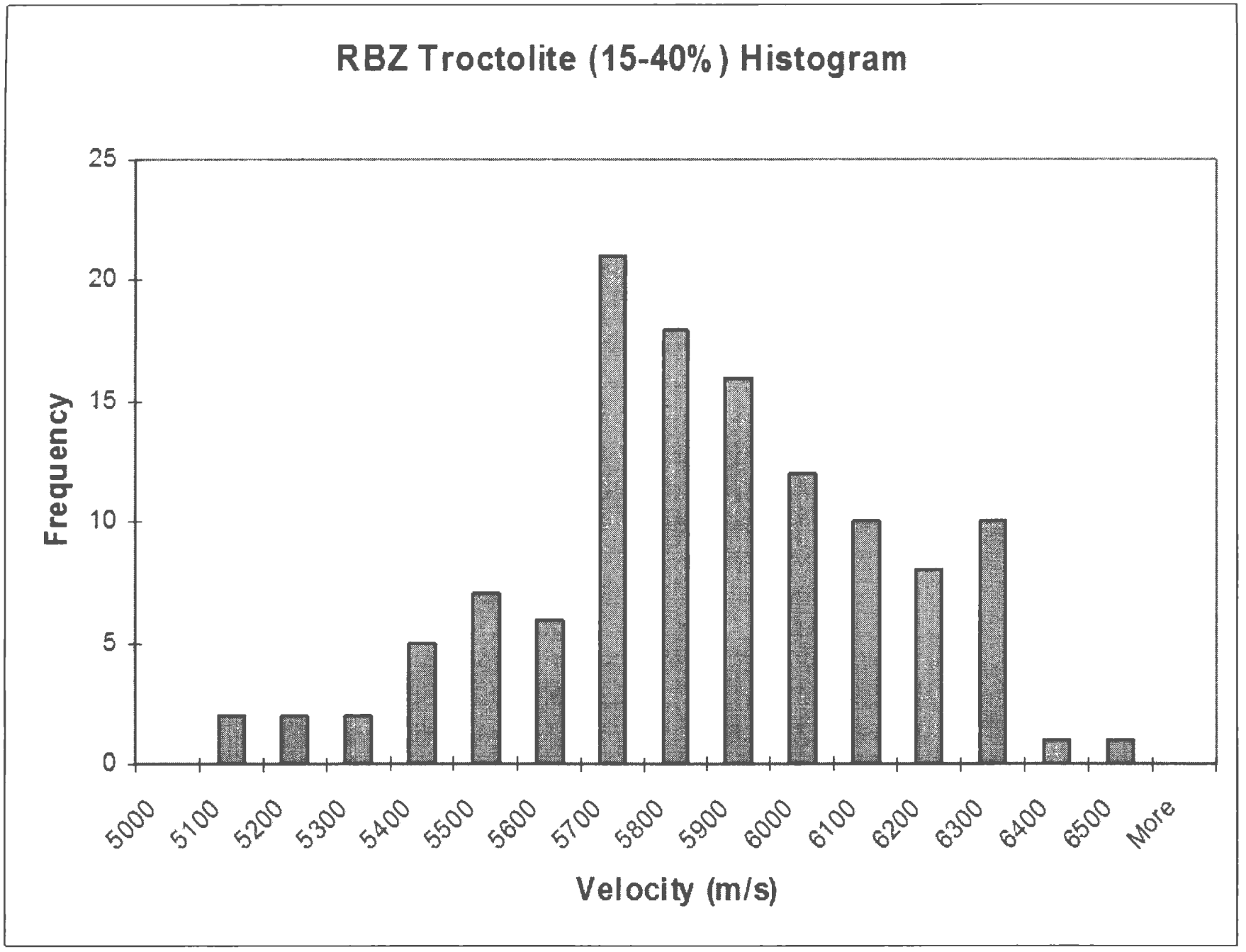


| | |
|---|---|
| Average Velocity | 5803 |
| Standard Deviation | 290 |
| Number of Samples | 121 |

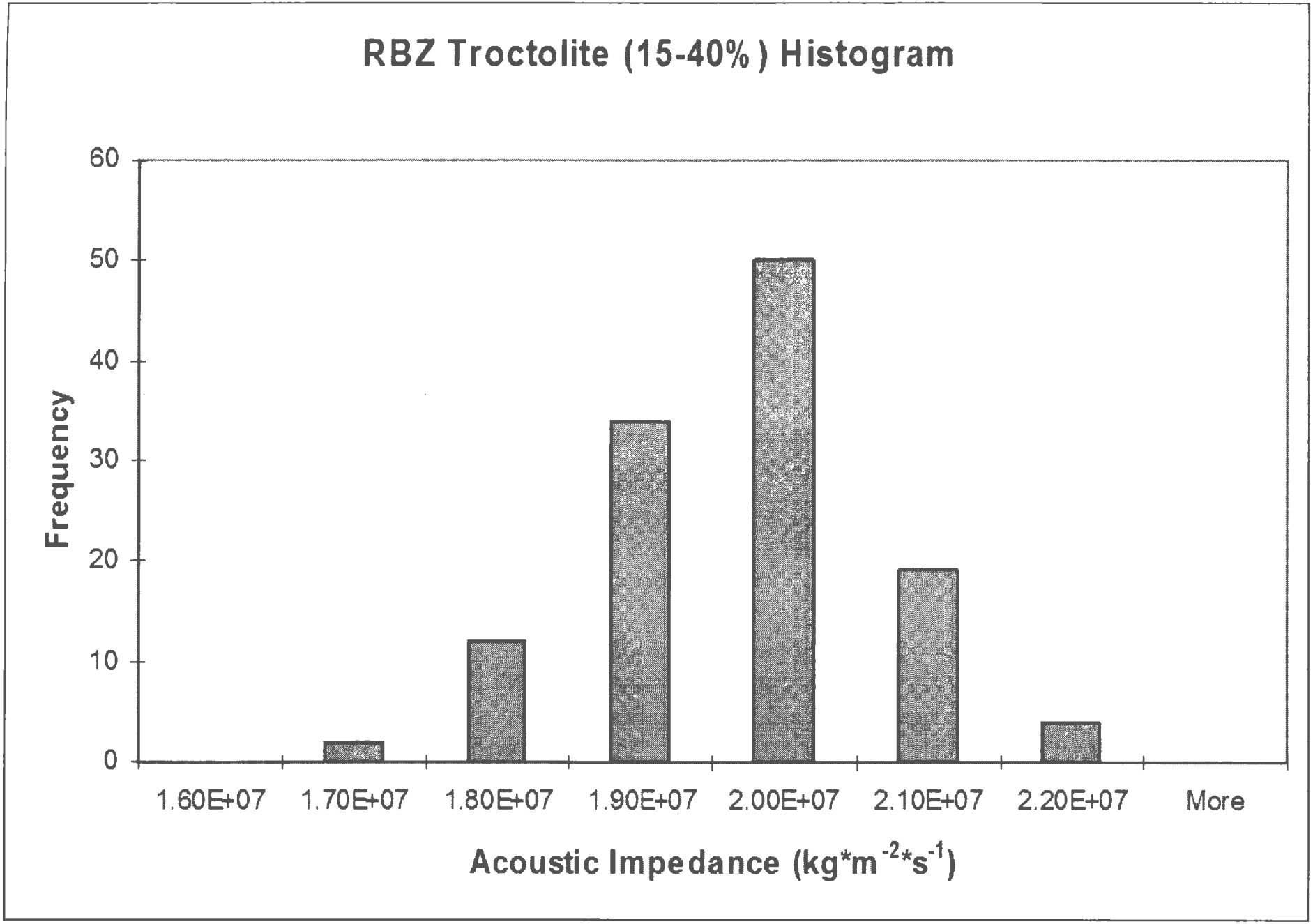


| | |
|---|---|
| Average Acoustic Impedance | 1.92 E+07 |
| Standard Deviation | 1.02 E+06 |
| Number of Samples | 121 |

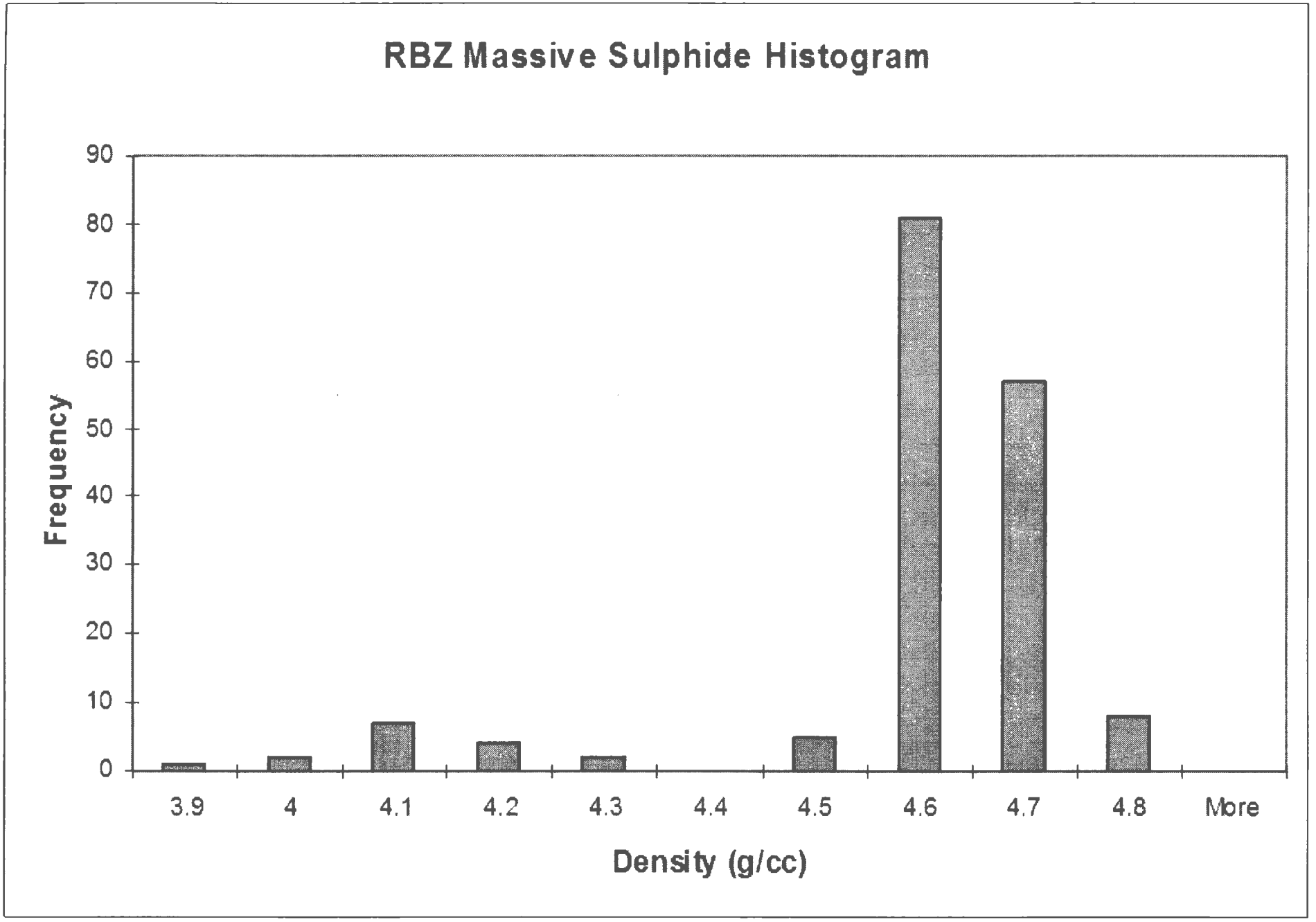


| | |
|---|---|
| Average Density | 4.55 |
| Standard Deviation | 0.167 |
| Number of Samples | 167 |

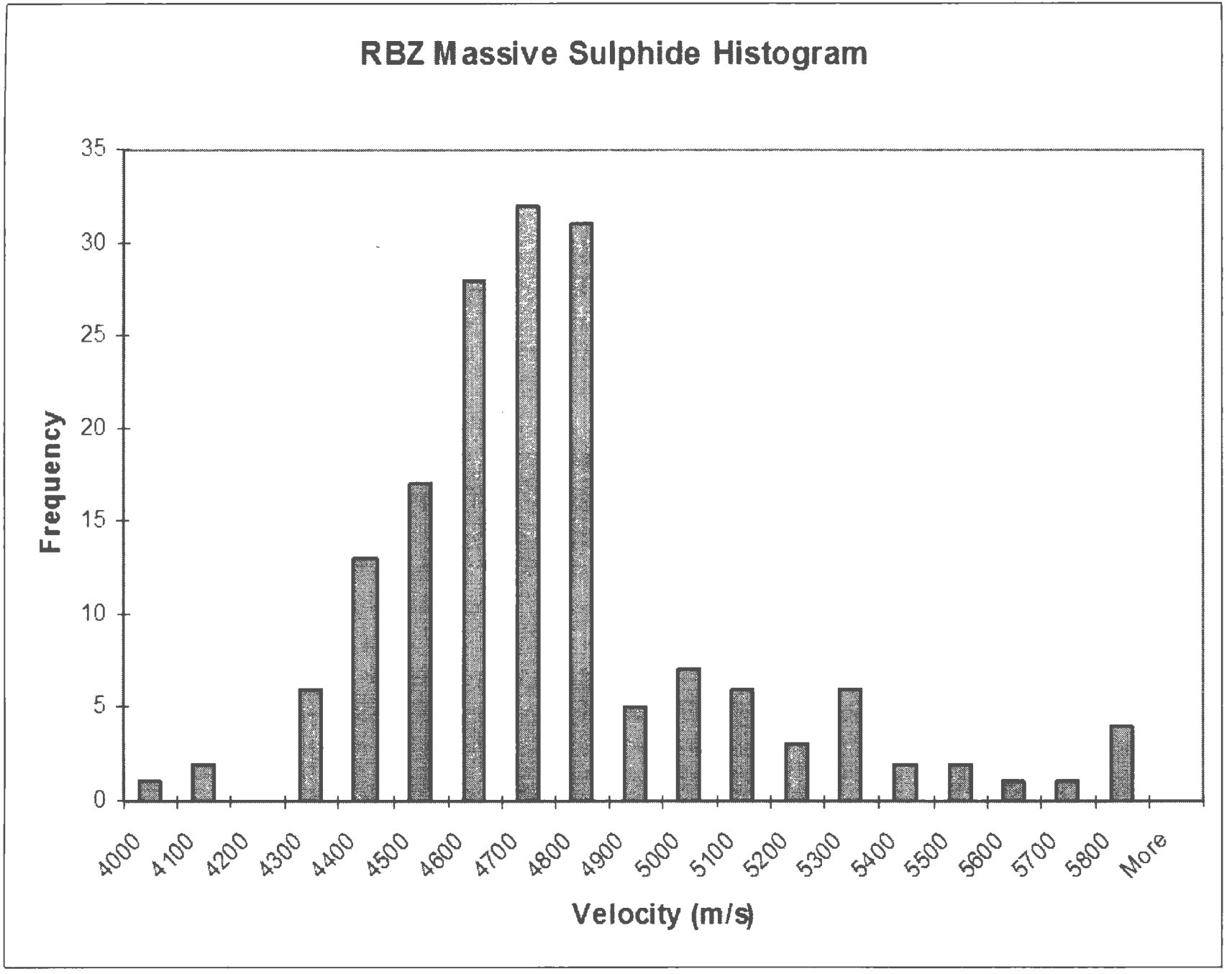


| | |
|---|---|
| Average Velocity | 4700 |
| Standard Deviation | 328 |
| Number of Samples | 167 |

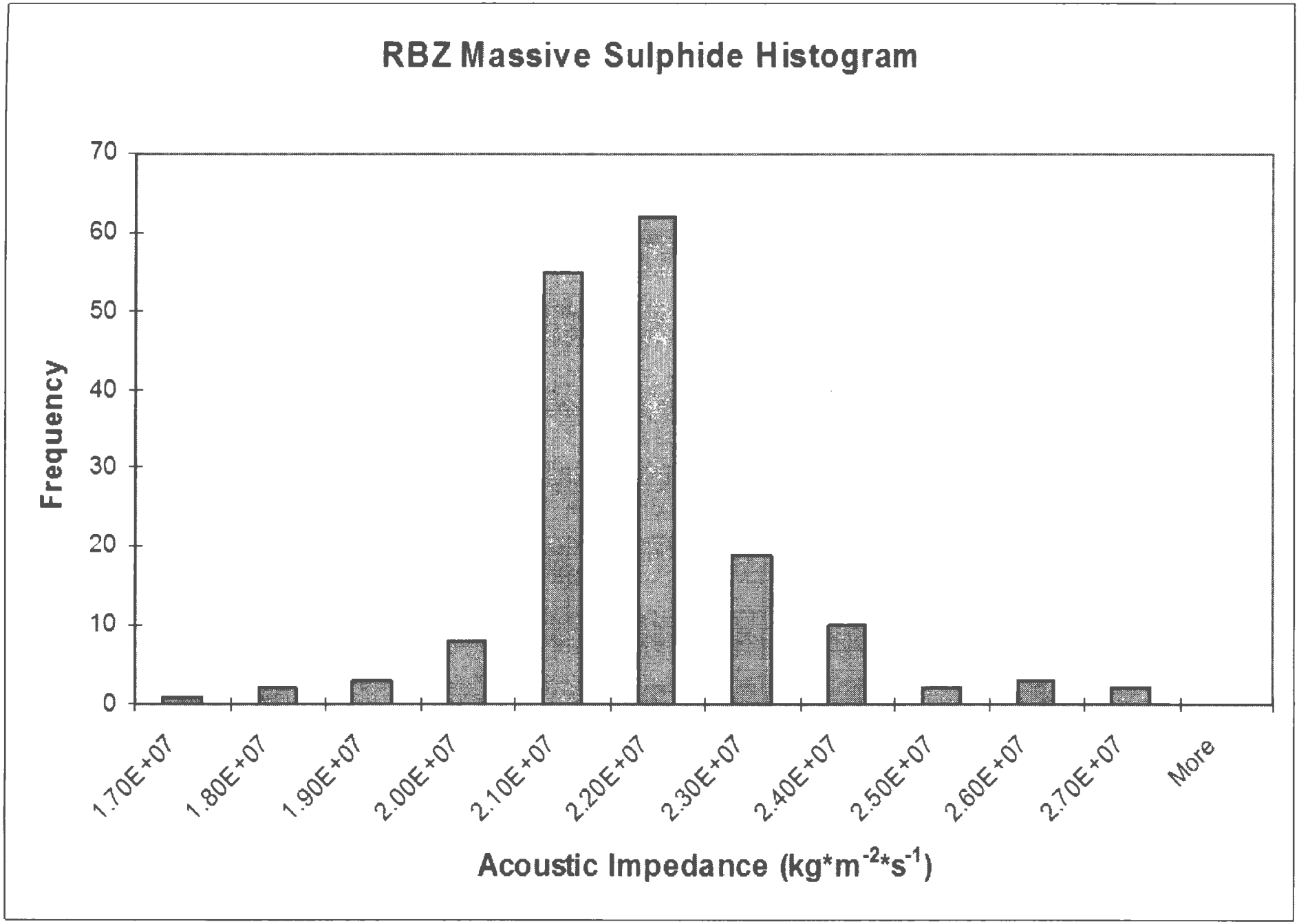


| | |
|---|---|
| Average Acoustic Impedance | 2.13 E+07 |
| Standard Deviation | 1.38 E+06 |
| Number of Samples | 167 |

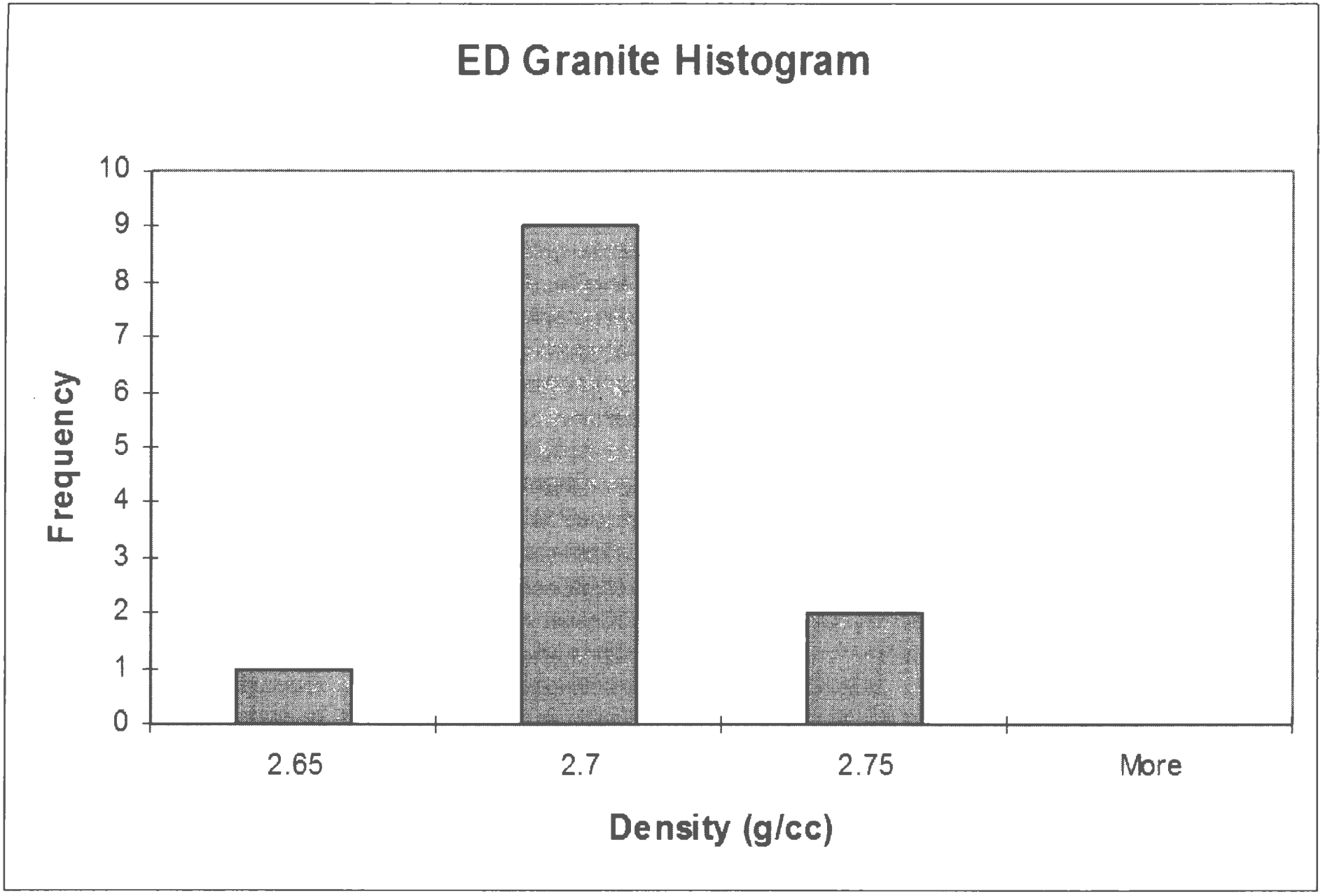


| | |
|---|---|
| Average Density | 2.69 |
| Standard Deviation | 0.0194 |
| Number of Samples | 12 |

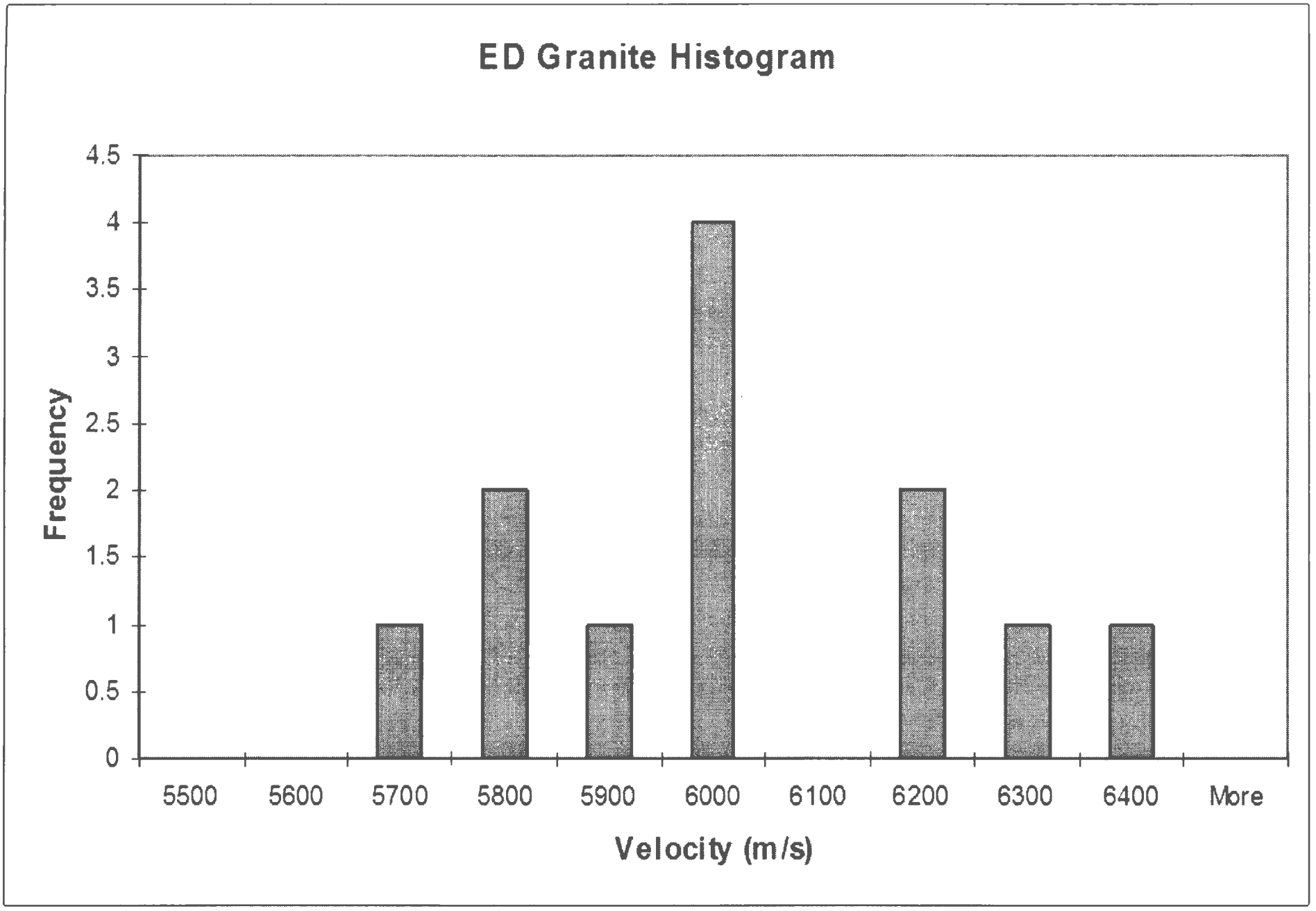


| | |
|---|---|
| Average Velocity | 5964 |
| Standard Deviation | 230 |
| Number of Samples | 12 |

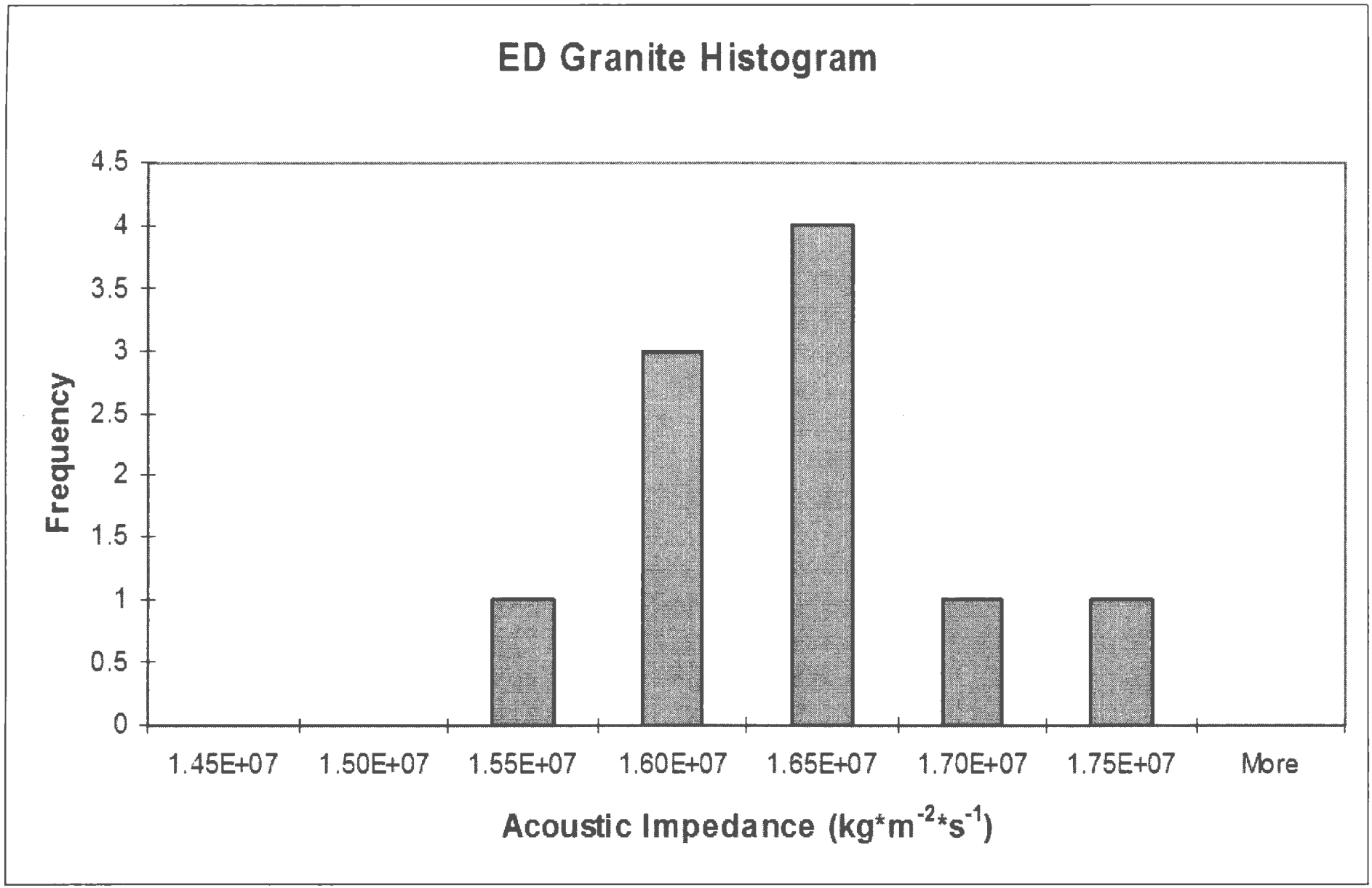


| | |
|---|---|
| Average Acoustic Impedance | 1.62 E+07 |
| Standard Deviation | 5.32 E+05 |
| Number of Samples | 12 |

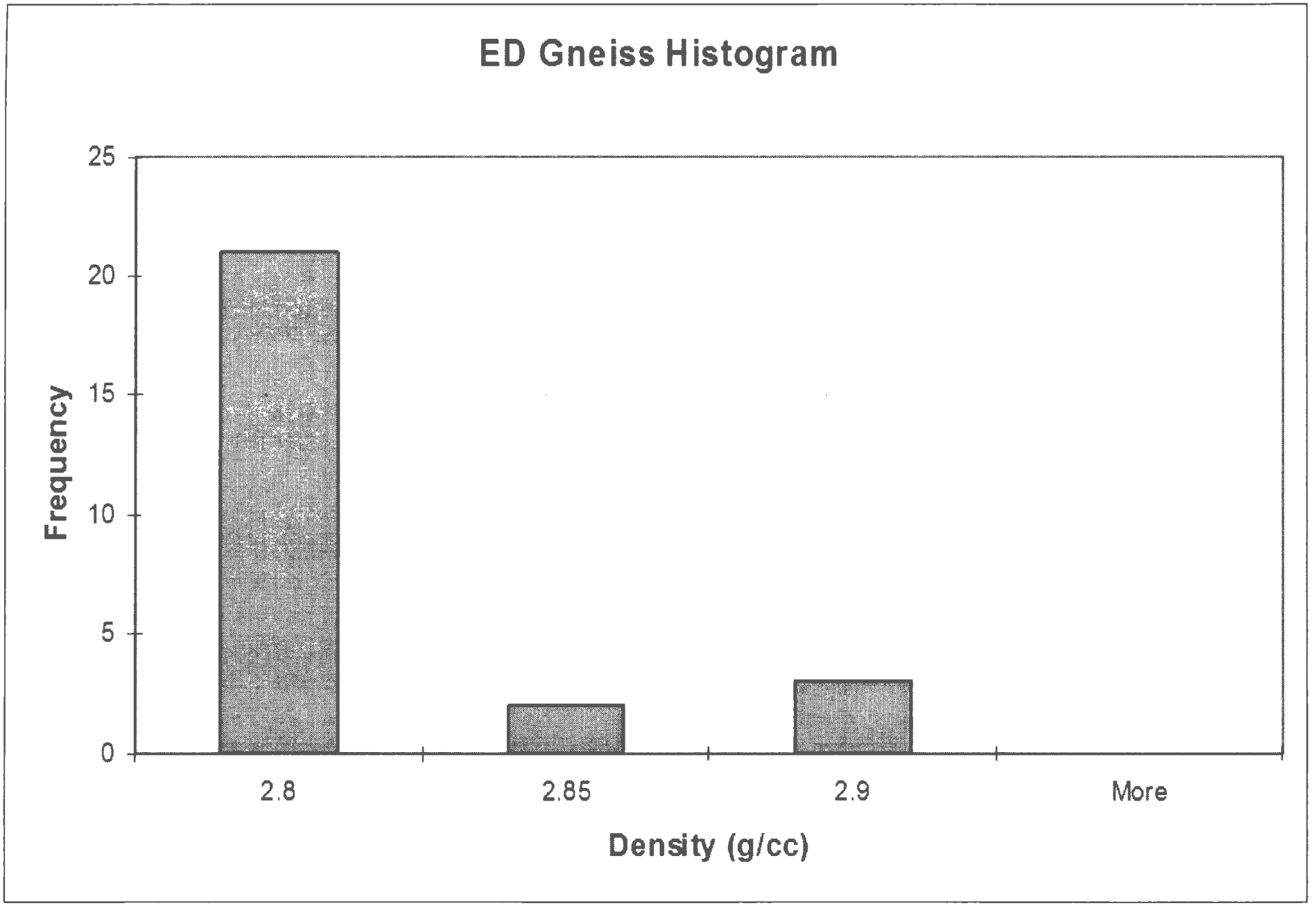


| | |
|---|---|
| Average Density | 2.79 |
| Standard Deviation | 0.0395 |
| Number of Samples | 26 |

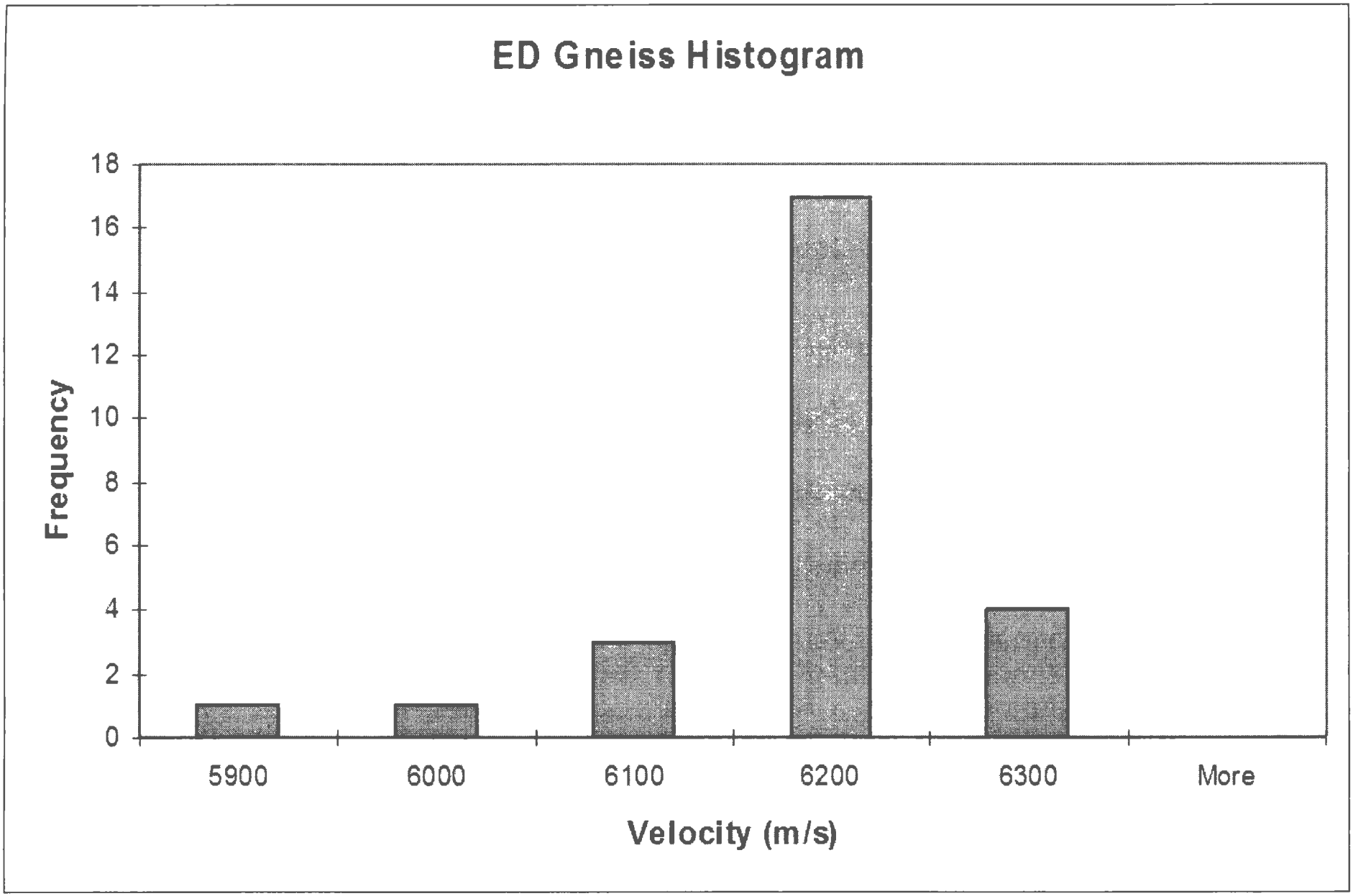


| | |
|---|---|
| Average Velocity | 6133 |
| Standard Deviation | 82 |
| Number of Samples | 26 |

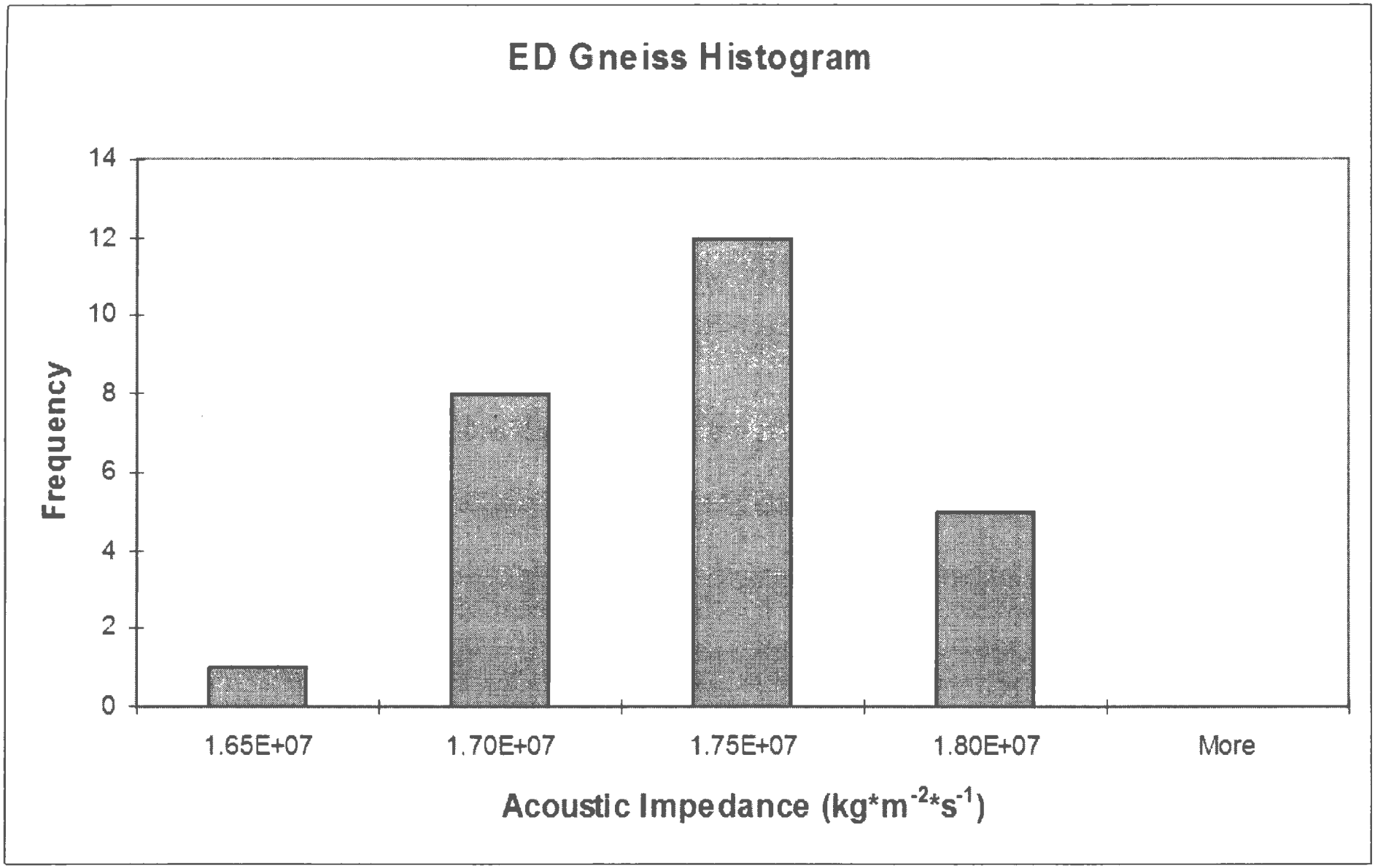


| | |
|---|---|
| Average Acoustic Impedance | 1.71 E+07 |
| Standard Deviation | 3.47 E+05 |
| Number of Samples | 26 |

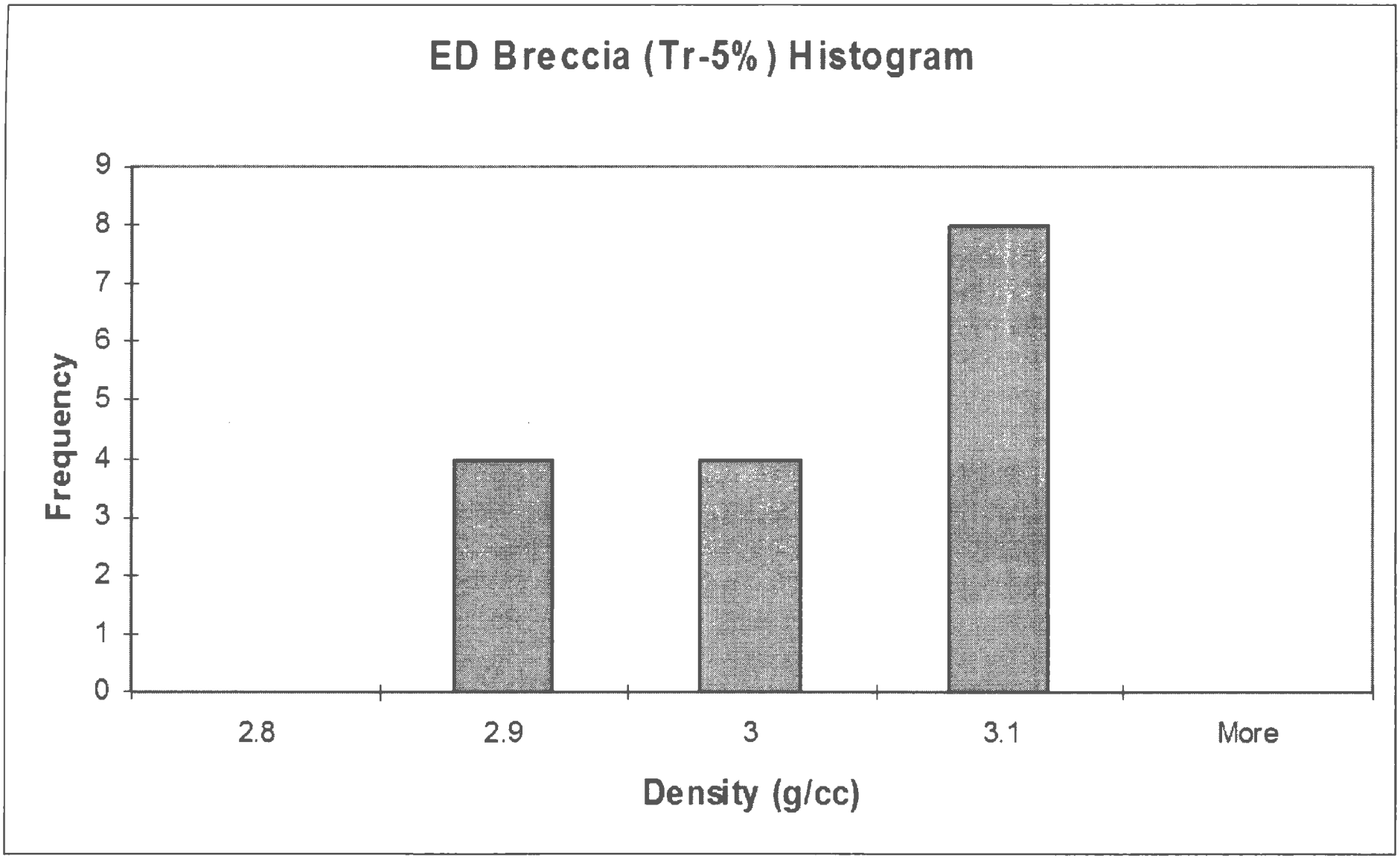


| | |
|---|---|
| Average Density | 2.98 |
| Standard Deviation | 0.0773 |
| Number of Samples | 16 |

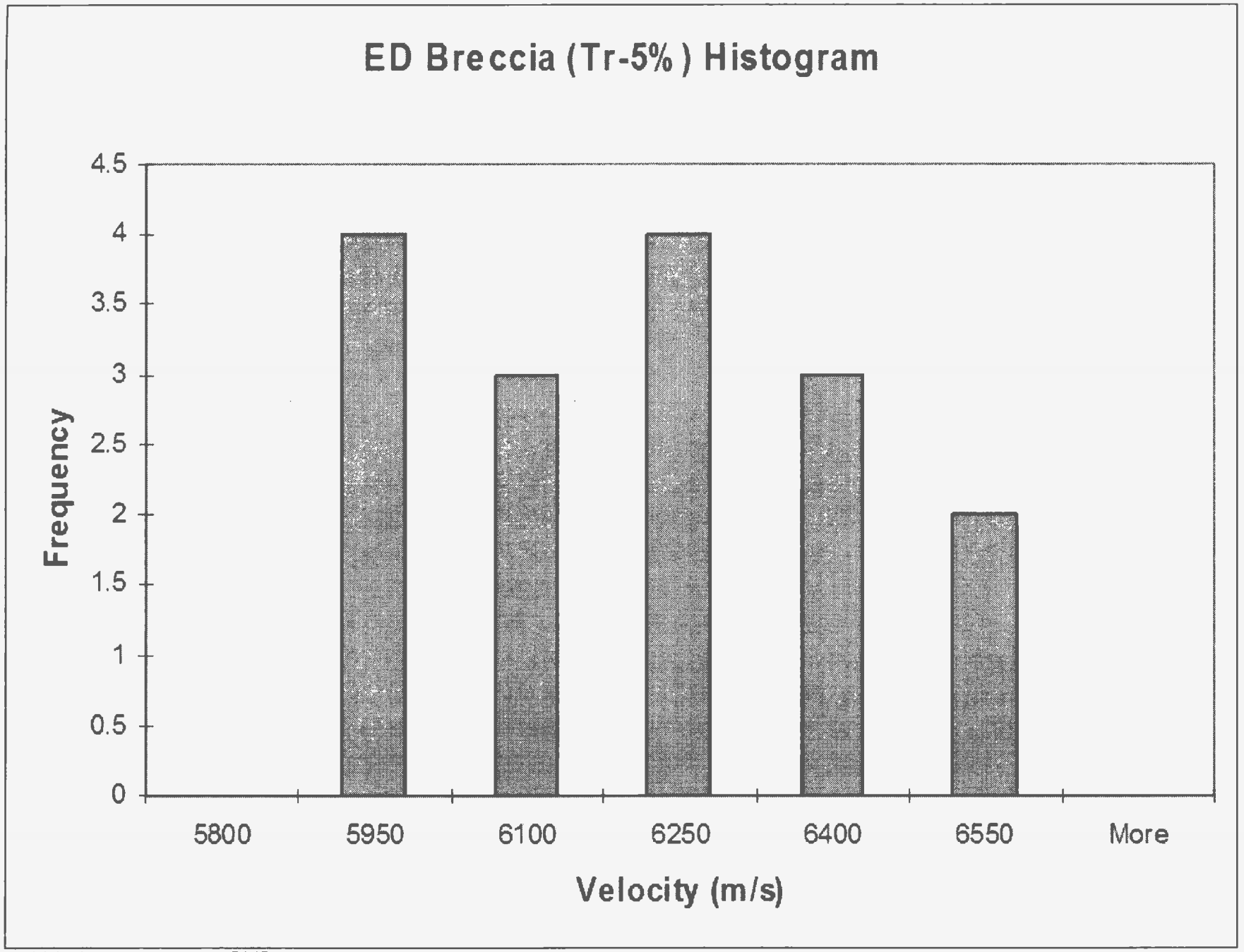


| | |
|---|---|
| Average Velocity | 6142 |
| Standard Deviation | 210 |
| Number of Samples | 16 |

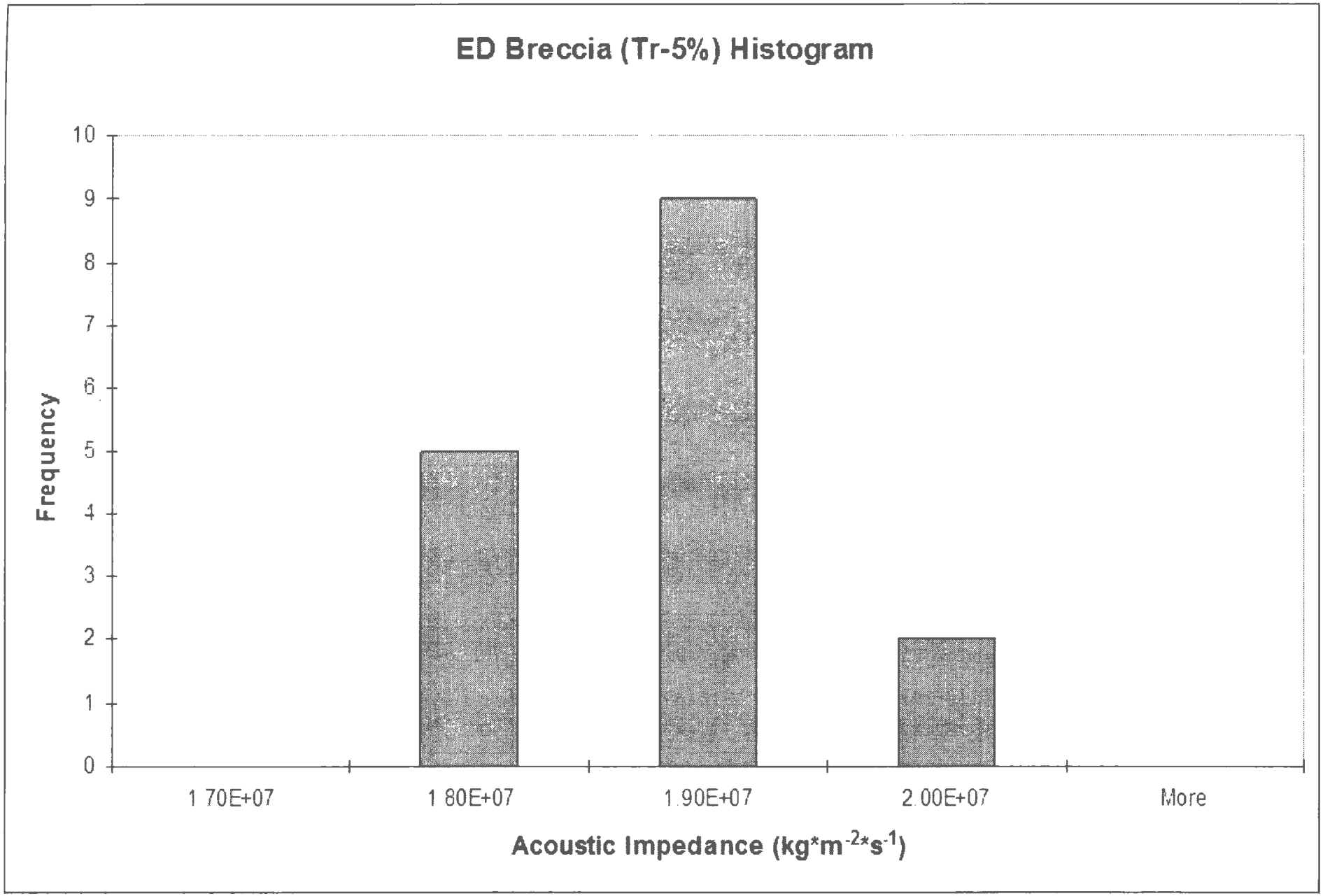


| | |
|---|---|
| Average Acoustic Impedance | 1.83 E+07 |
| Standard Deviation | 6.39 E+05 |
| Number of Samples | 16 |

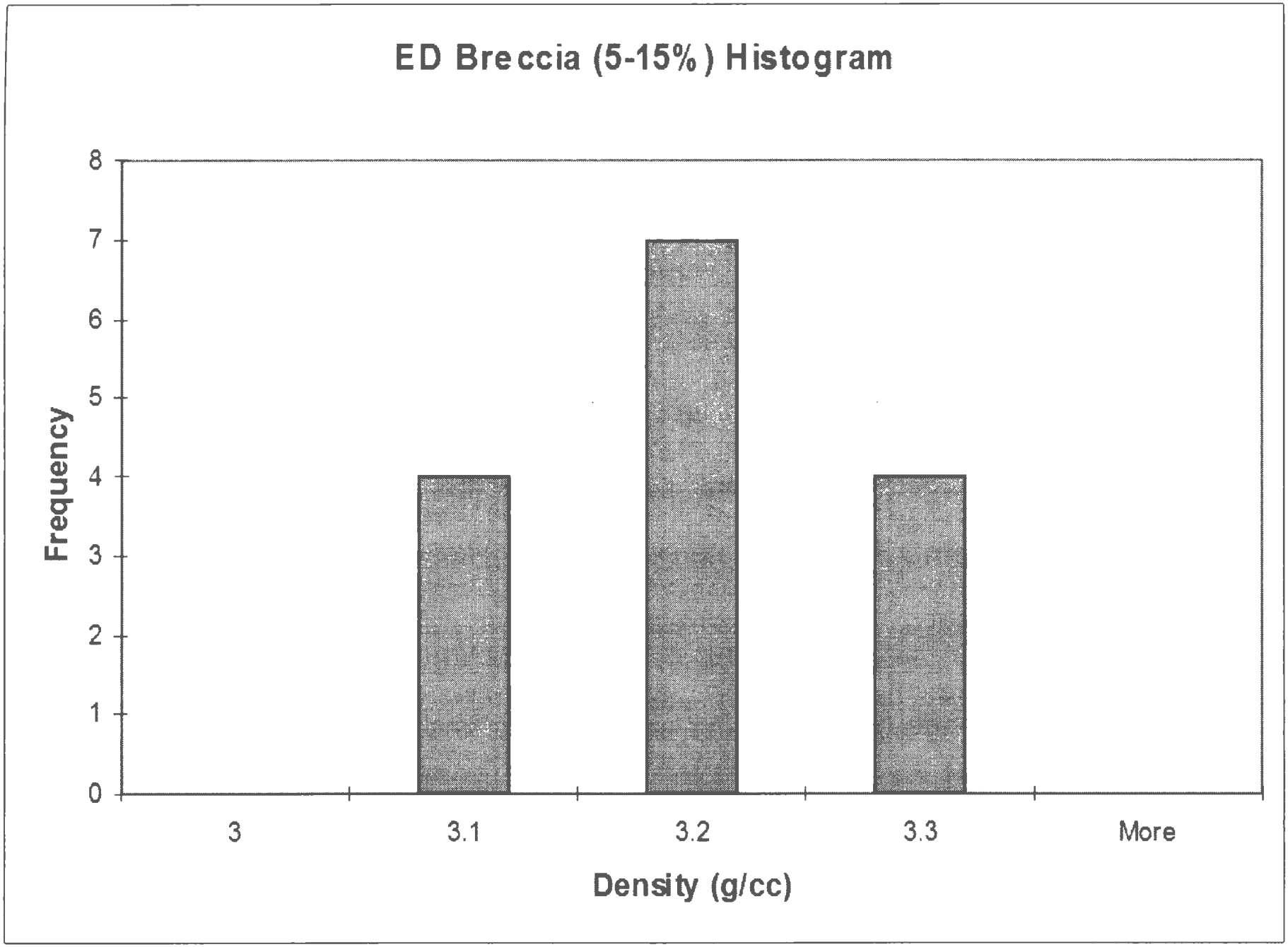


| | |
|---|---|
| Average Density | 3.14 |
| Standard Deviation | 0.0725 |
| Number of Samples | 15 |

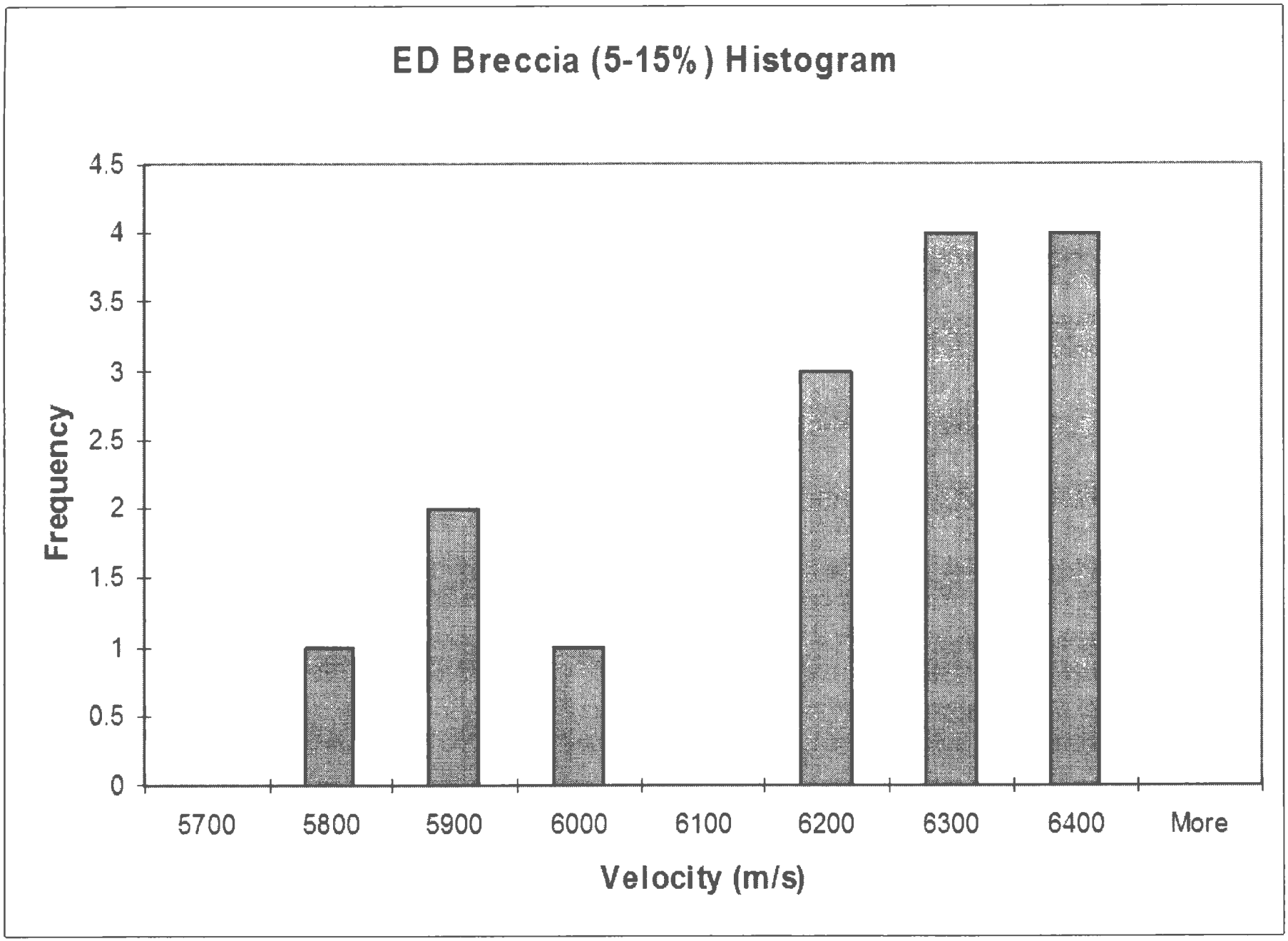


| | |
|---|---|
| Average Velocity | 6163 |
| Standard Deviation | 188 |
| Number of Samples | 15 |

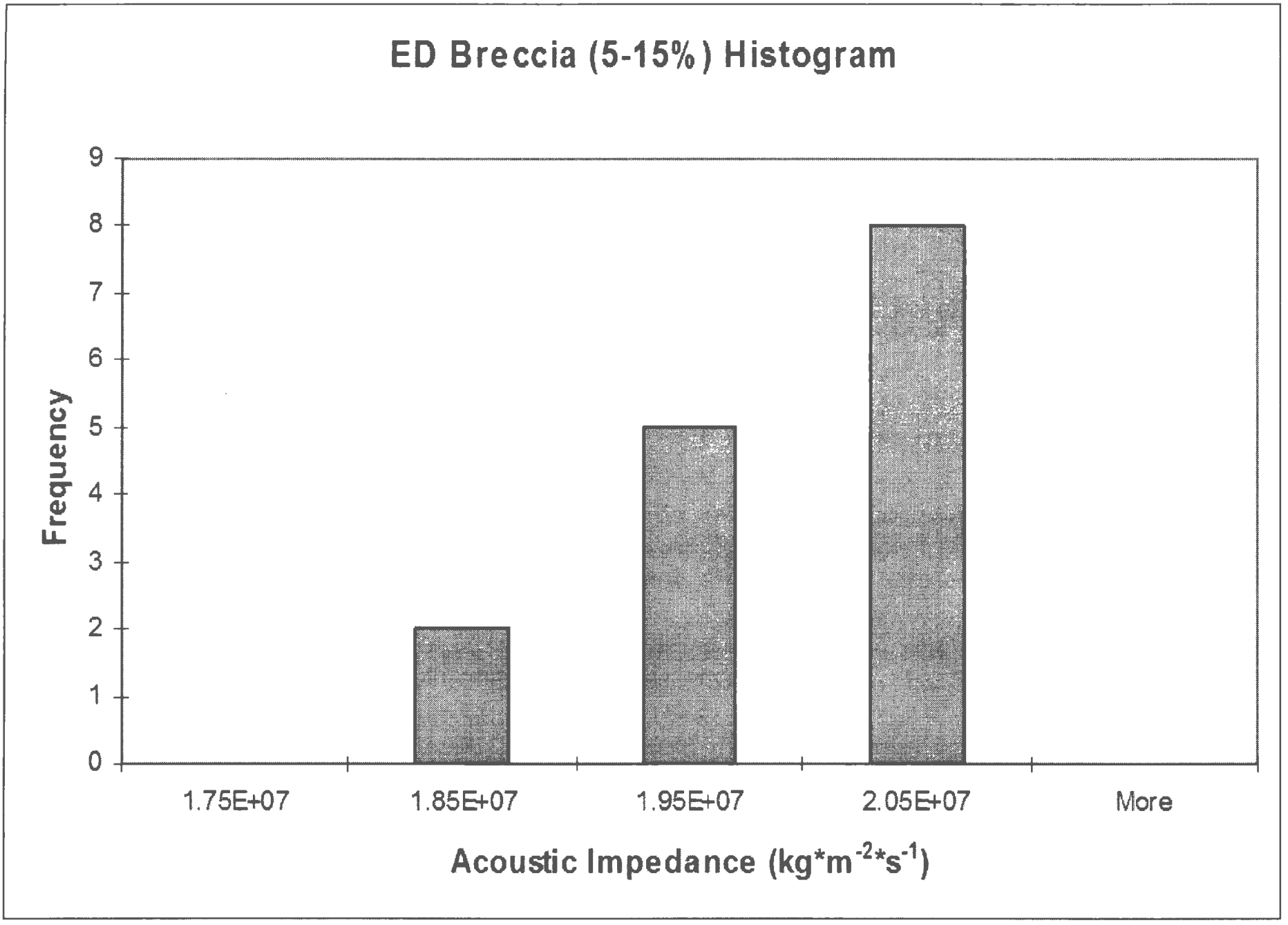


| | |
|---|---|
| Average Acoustic Impedance | 1.93 E+07 |
| Standard Deviation | 7.23 E+05 |
| Number of Samples | 15 |

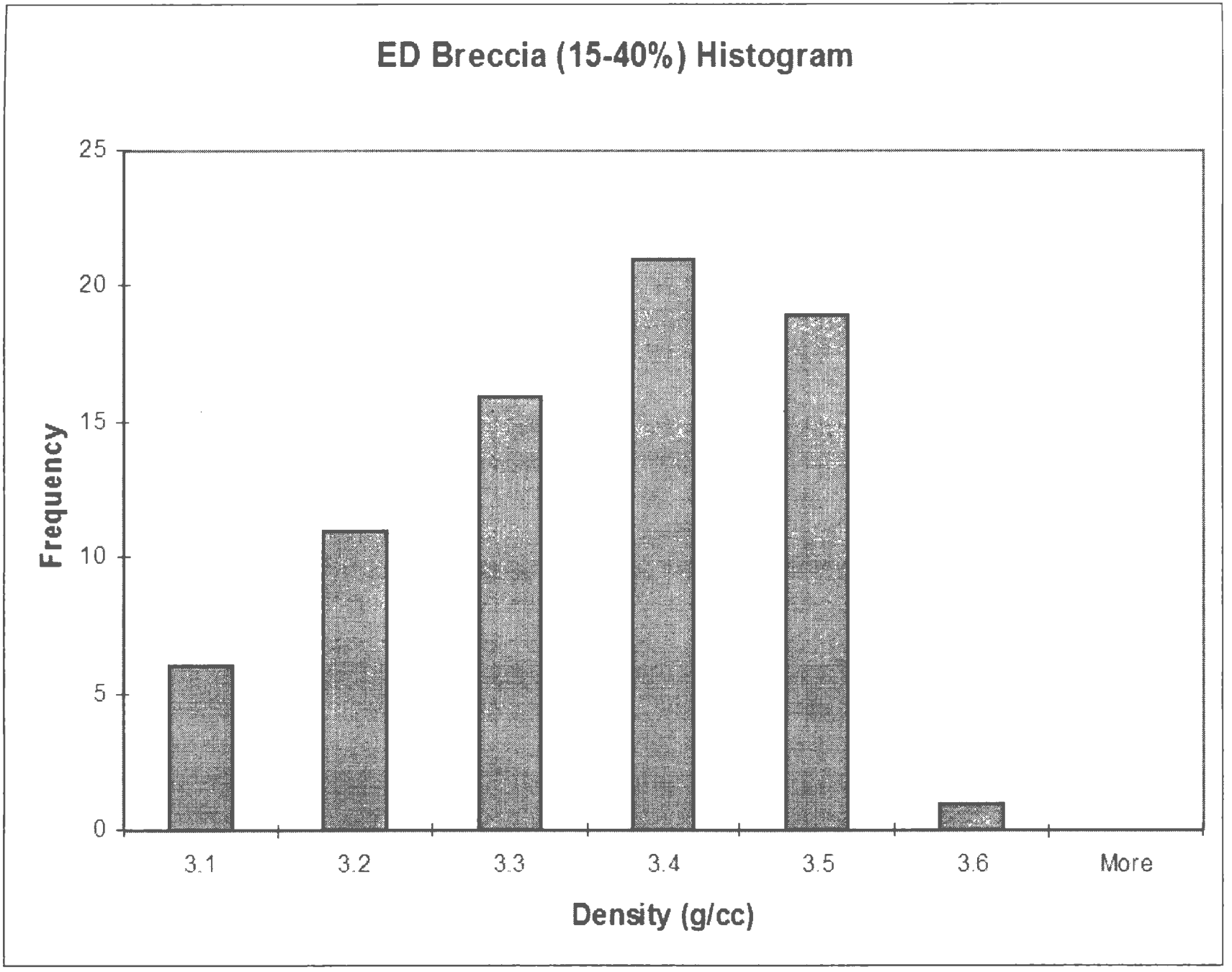


| | |
|---|---|
| Average Density | 3.30 |
| Standard Deviation | 0.122 |
| Number of Samples | 74 |

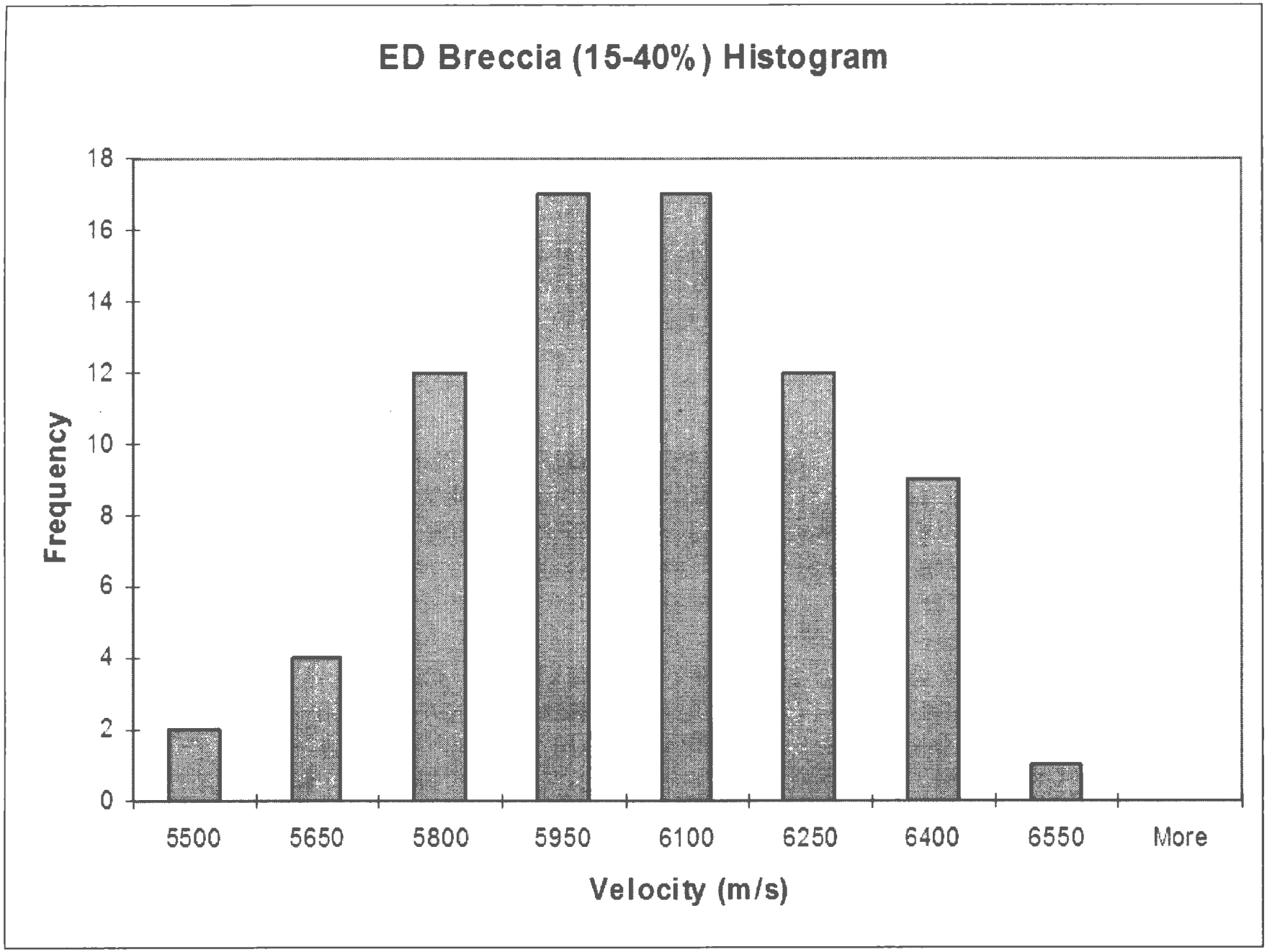


| | |
|---|---|
| Average Velocity | 5975 |
| Standard Deviation | 240 |
| Number of Samples | 74 |

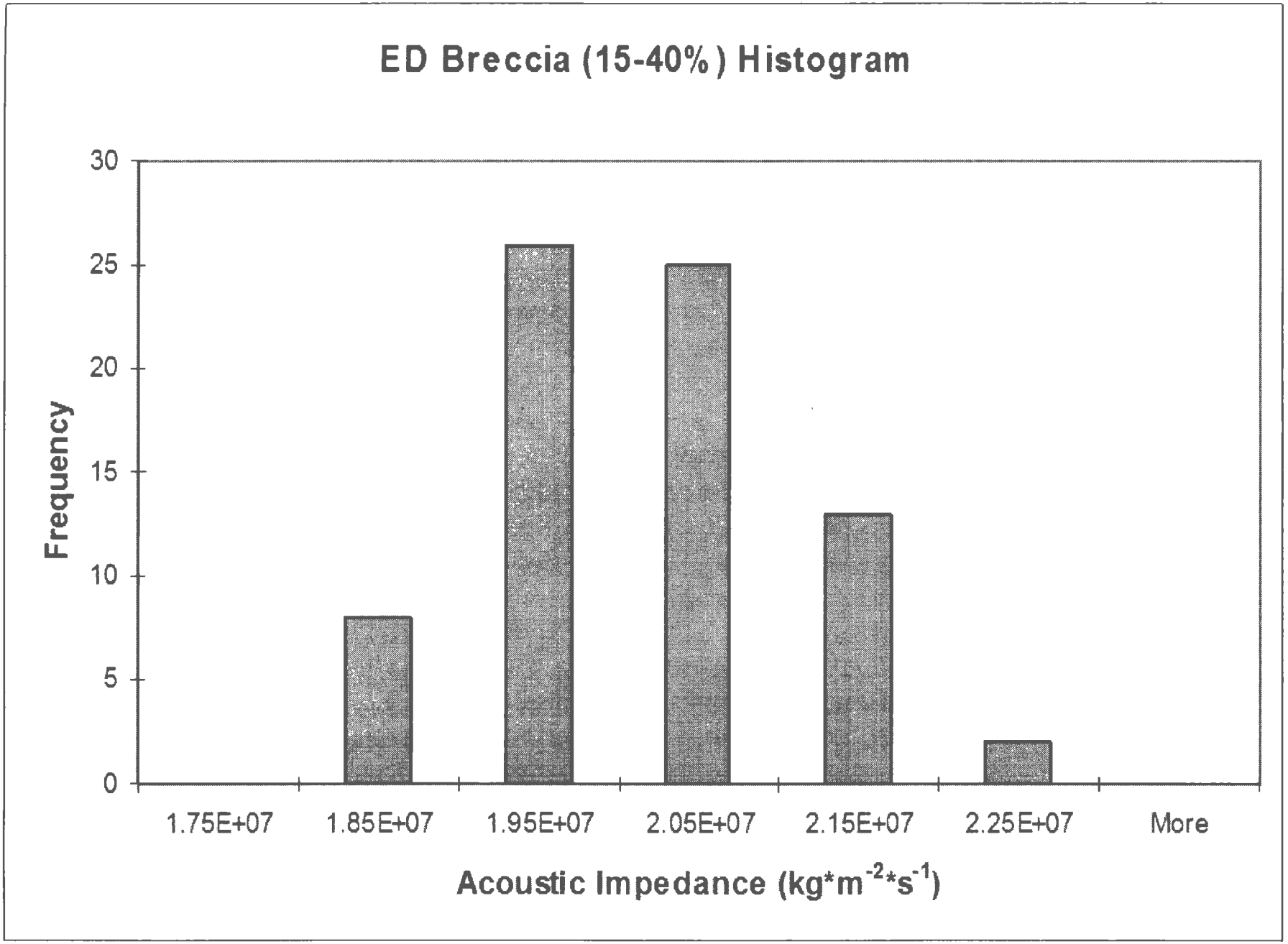


| | |
|---|---|
| Average Acoustic Impedance | 1.97 E+07 |
| Standard Deviation | 9.95 E+05 |
| Number of Samples | 74 |

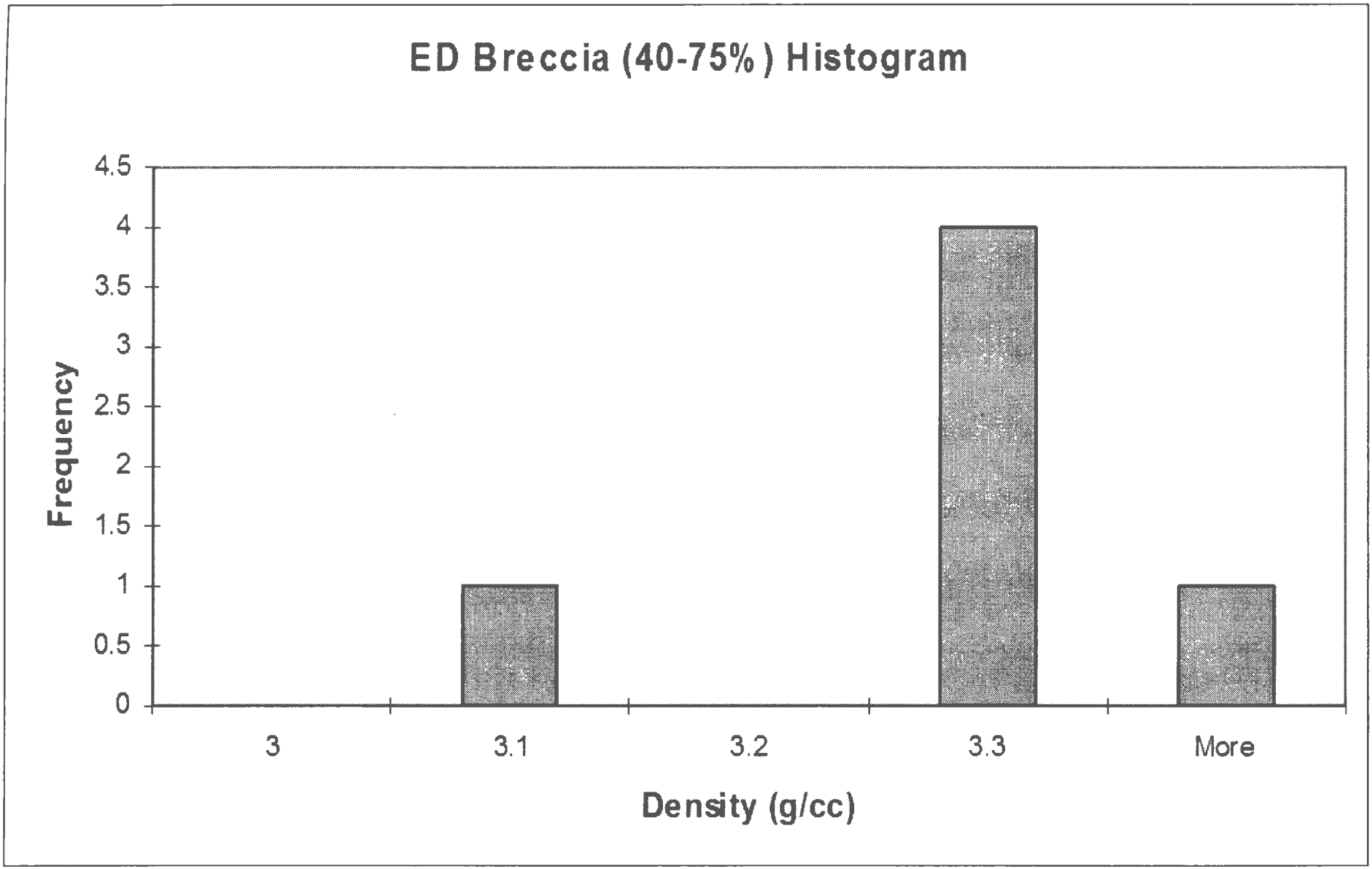




| | |
|---|---|
| Average Density | 3.25 |
| Standard Deviation | 0.112 |
| Number of Samples | 6 |

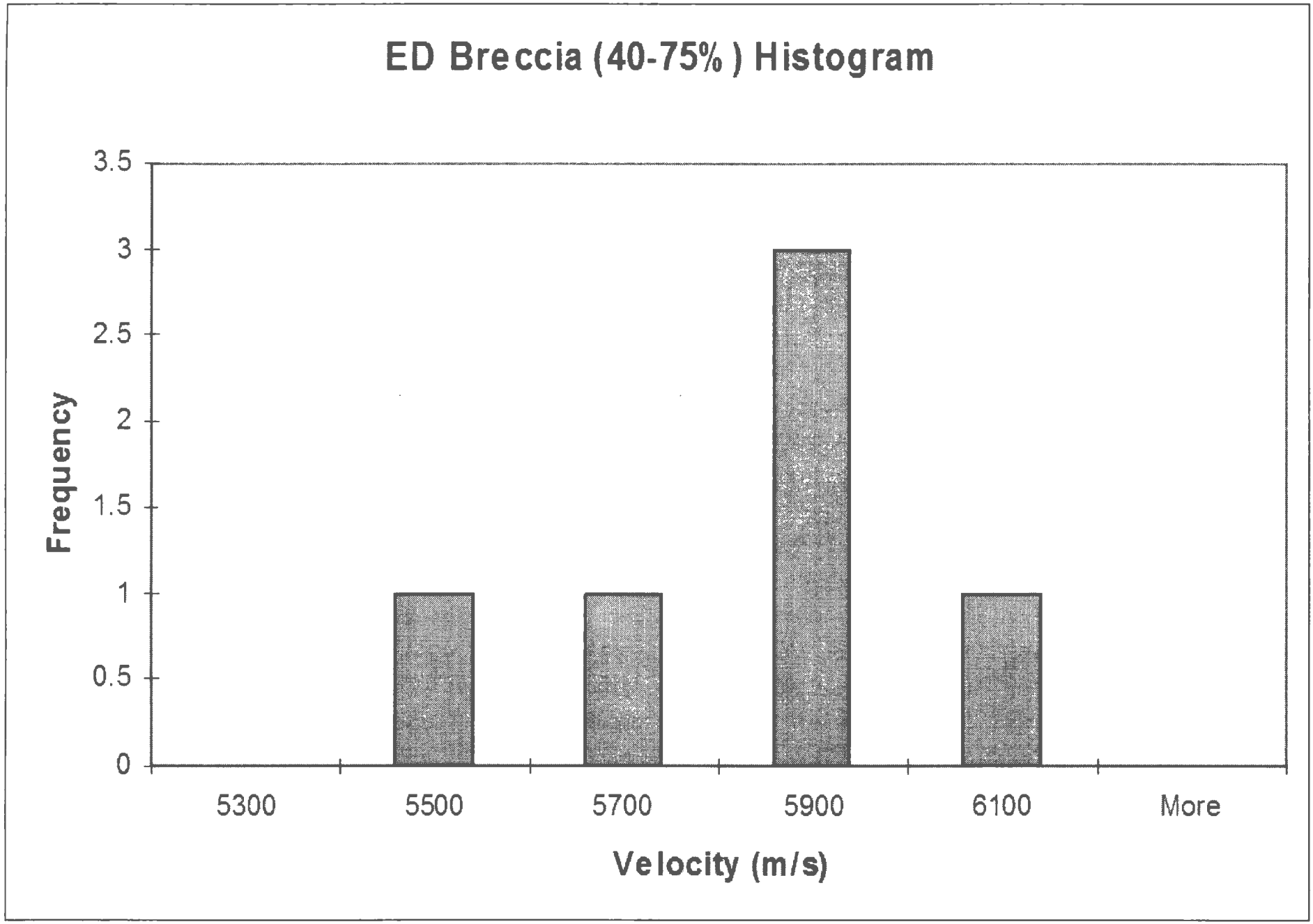


| | |
|---|---|
| Average Velocity | 5746 |
| Standard Deviation | 265 |
| Number of Samples | 6 |

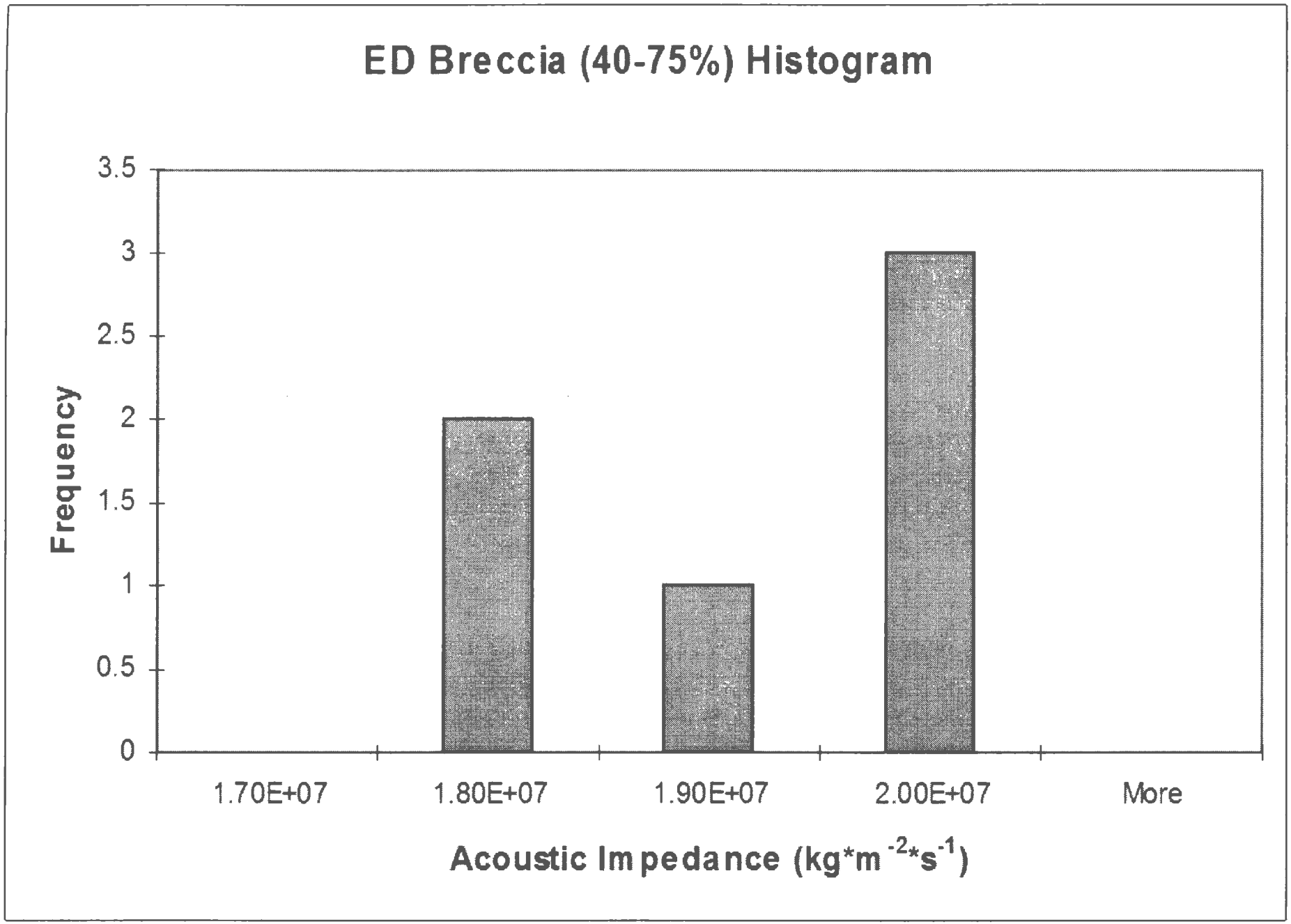


| | |
|---|---|
| Average Acoustic Impedance | 1.87 E+07 |
| Standard Deviation | 1.15 E+06 |
| Number of Samples | 6 |

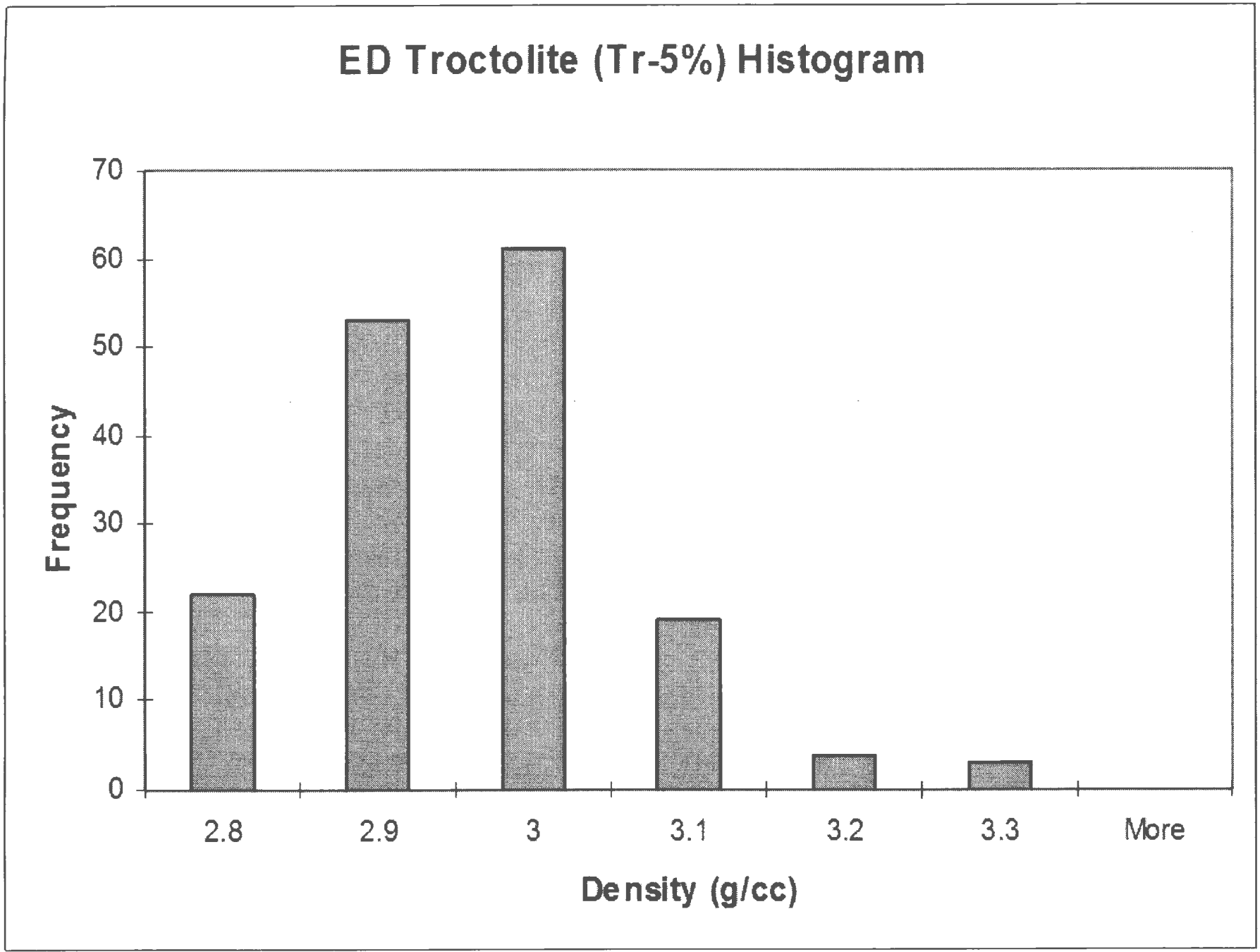


| | |
|---|---|
| Average Density | 2.91 |
| Standard Deviation | 0.0994 |
| Number of Samples | 162 |

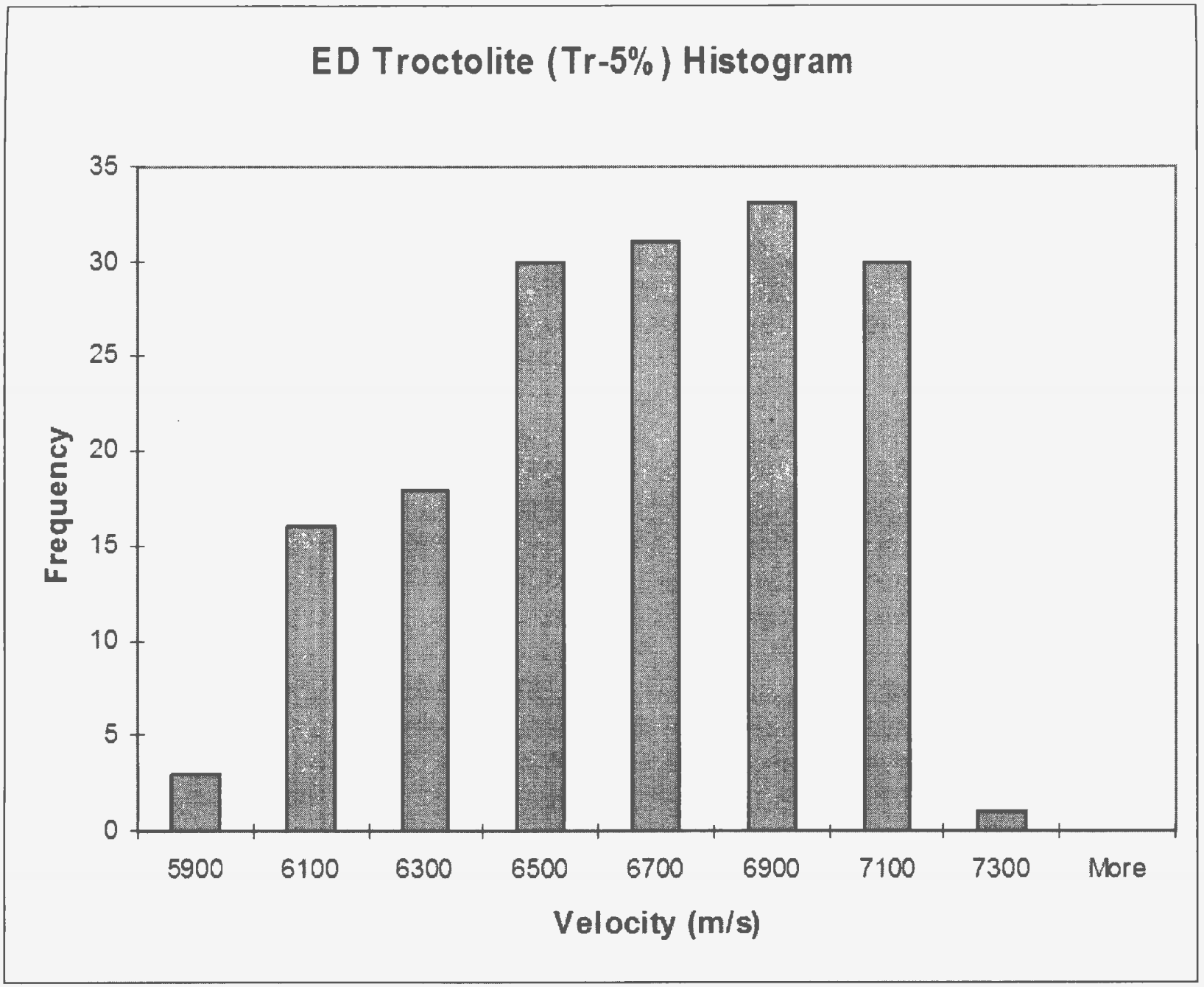


| | |
|---|---|
| Average Velocity | 6564 |
| Standard Deviation | 330 |
| Number of Samples | 162 |

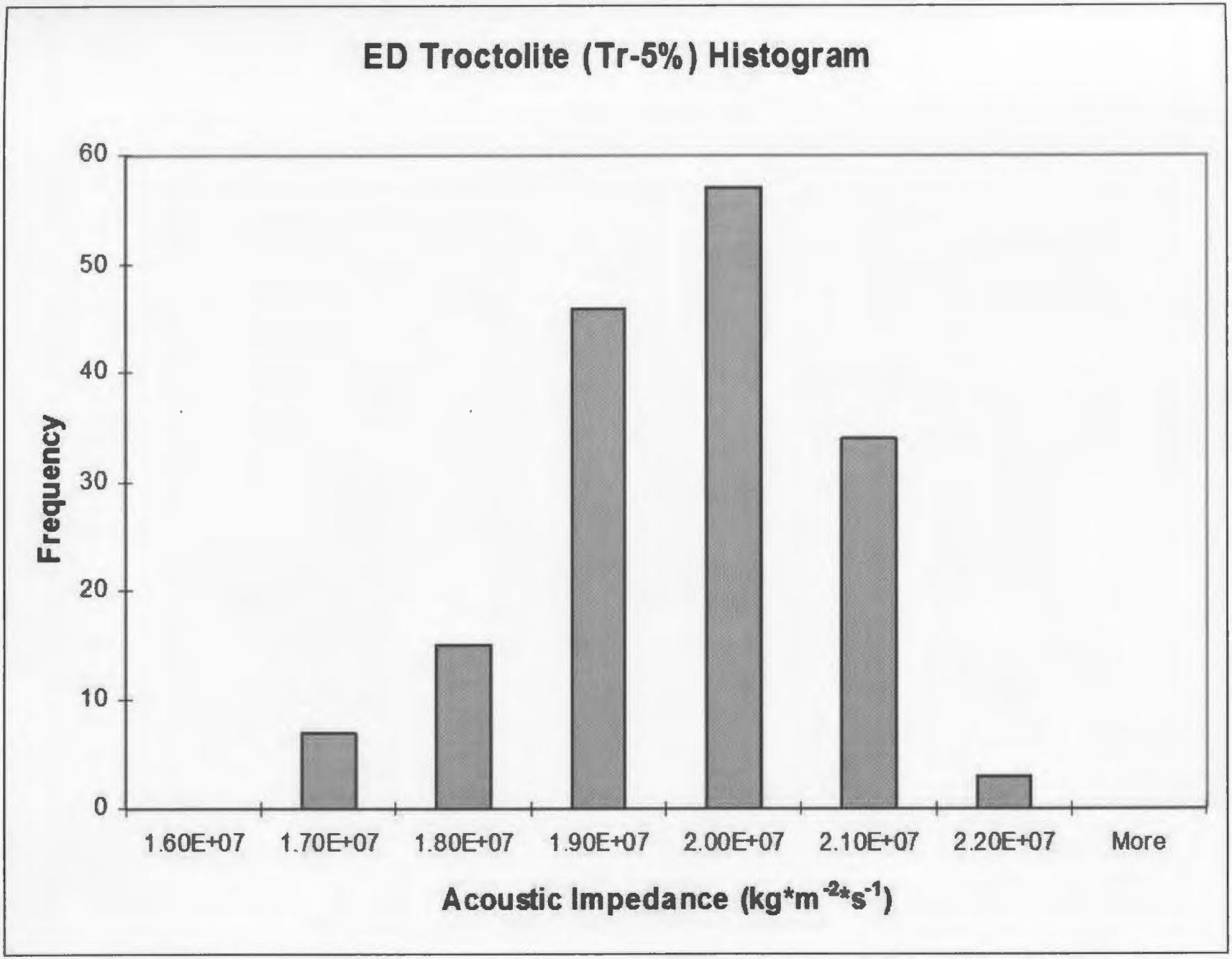


| | |
|---|---|
| Average Acoustic Impedance | 1.91 E+07 |
| Standard Deviation | 1.04 E+06 |
| Number of Samples | 162 |

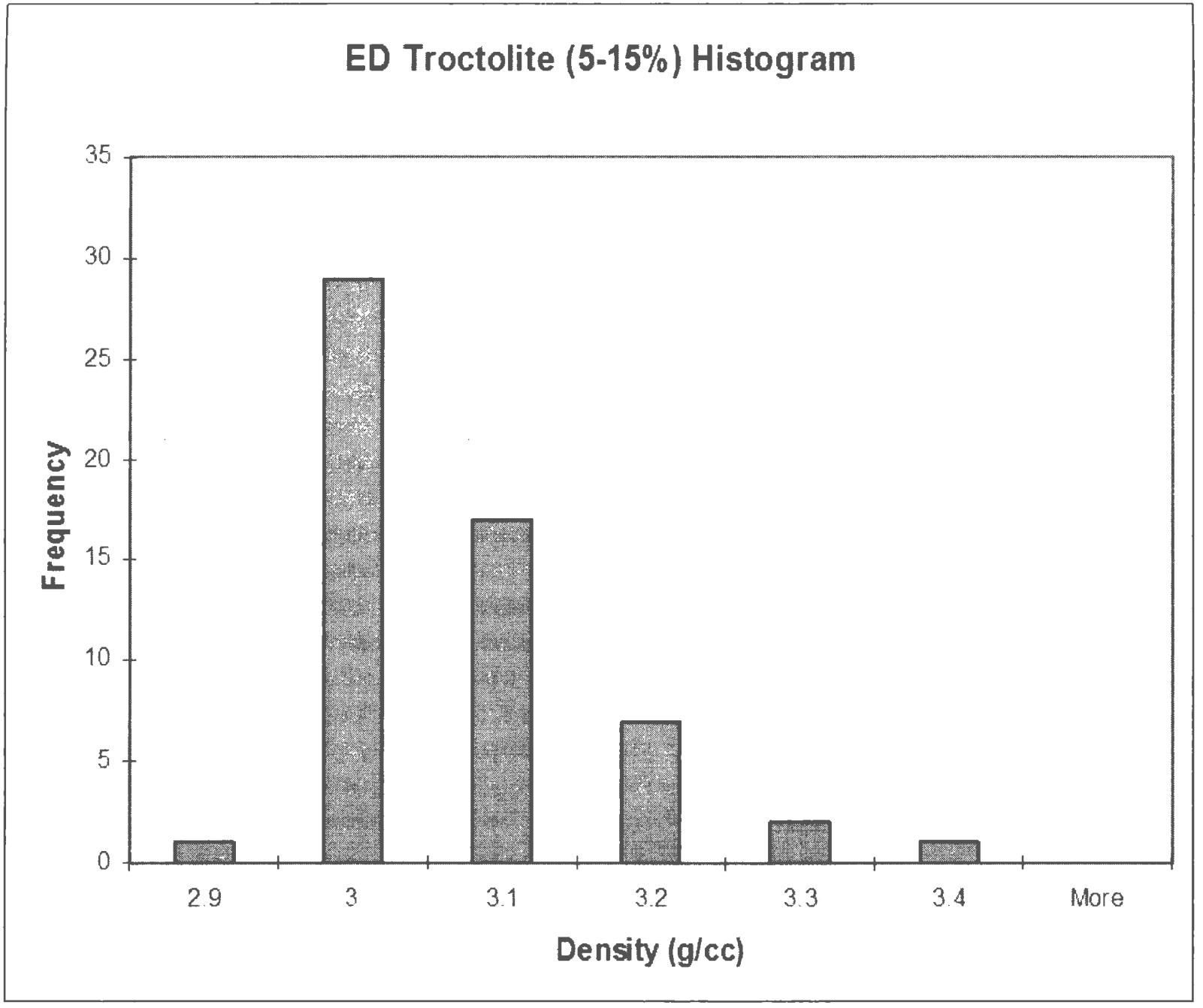


| | |
|---|---|
| Average Density | 3.02 |
| Standard Deviation | 0.103 |
| Number of Samples | 57 |

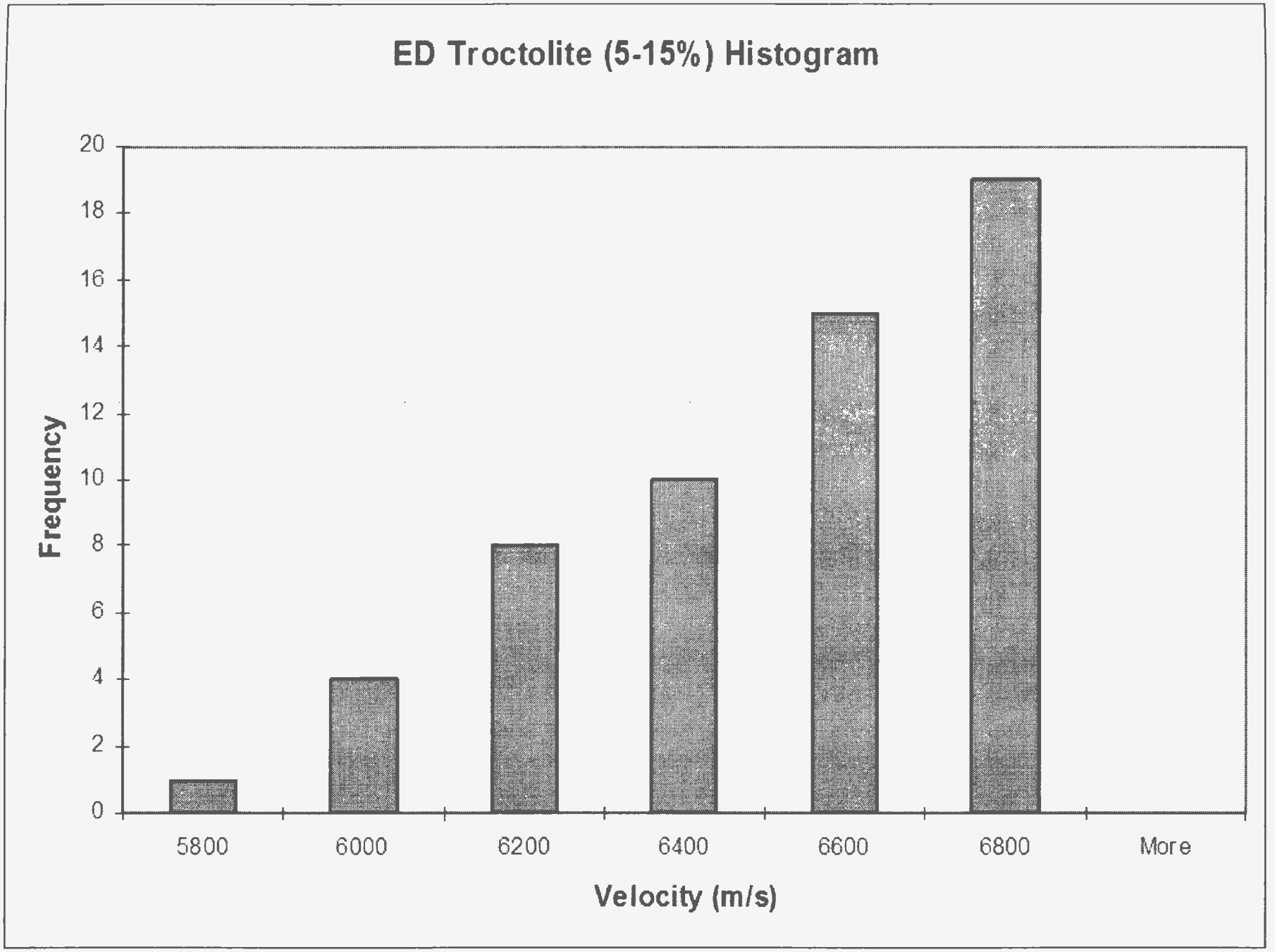


| | |
|---|---|
| Average Velocity | 6430 |
| Standard Deviation | 275 |
| Number of Samples | 57 |

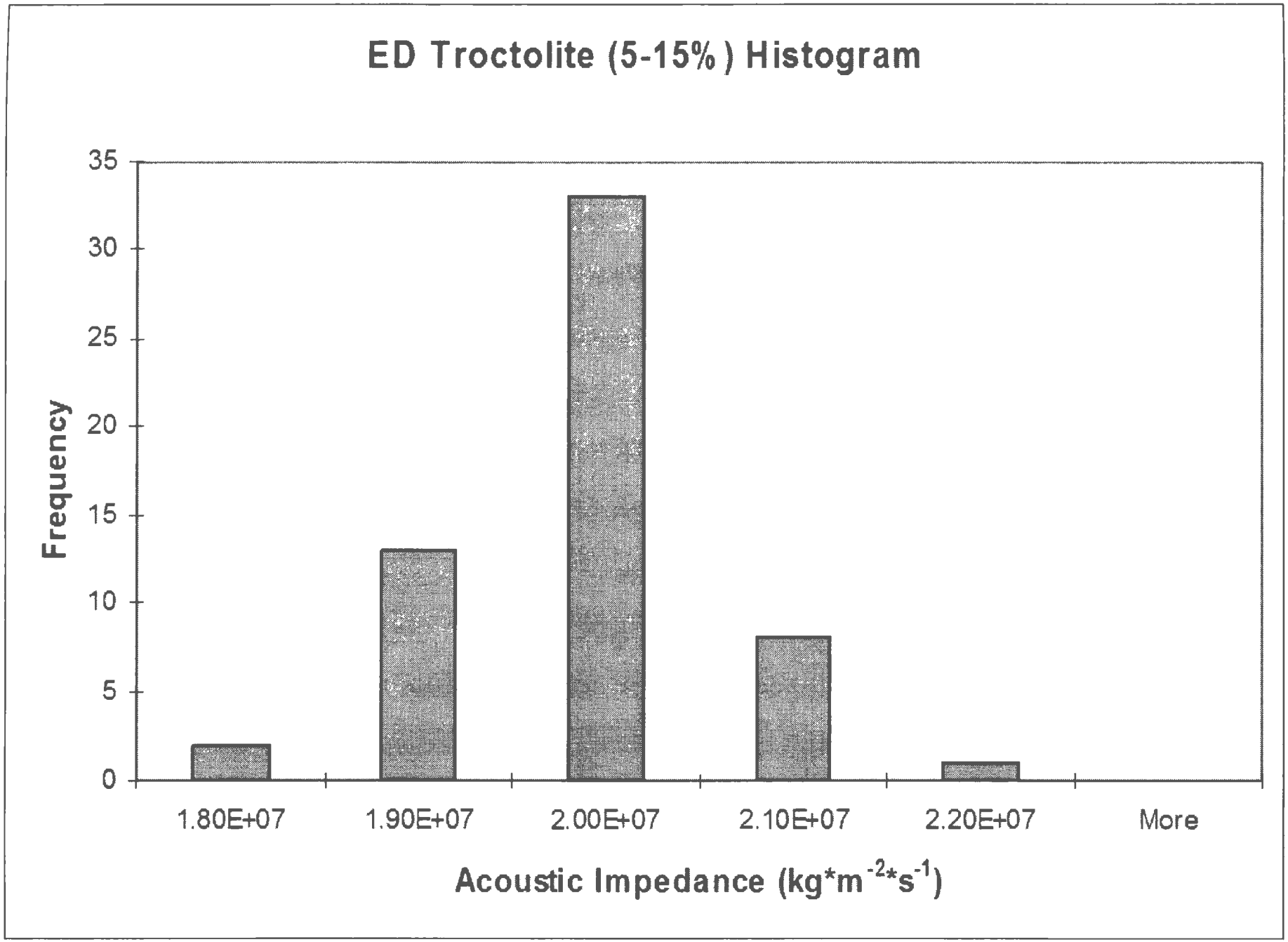


| | |
|---|---|
| Average Acoustic Impedance | 1.94 E+07 |
| Standard Deviation | 7.38 E+05 |
| Number of Samples | 57 |

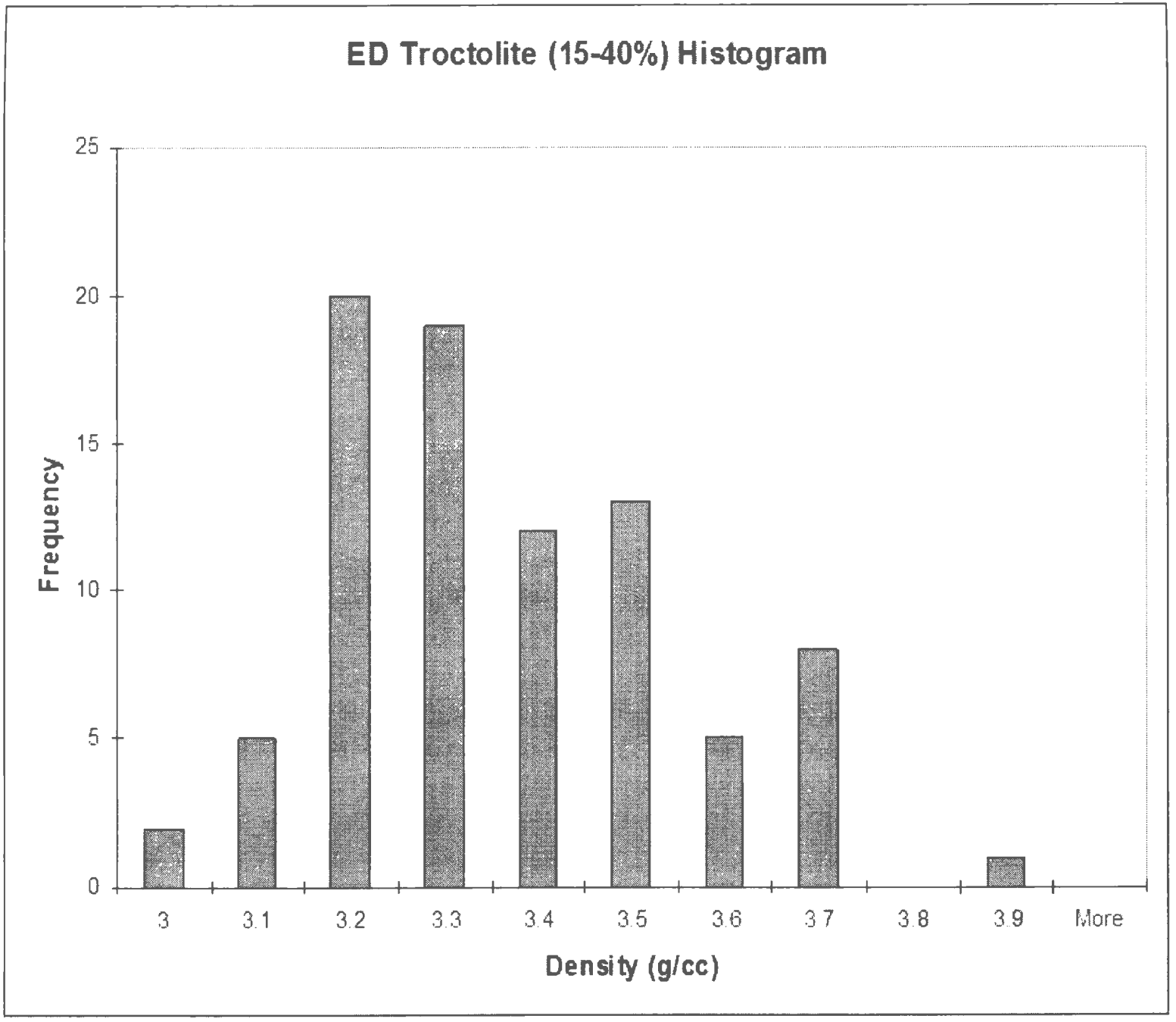


| | |
|---|---|
| Average Density | 3.31 |
| Standard Deviation | 0.196 |
| Number of Samples | 85 |

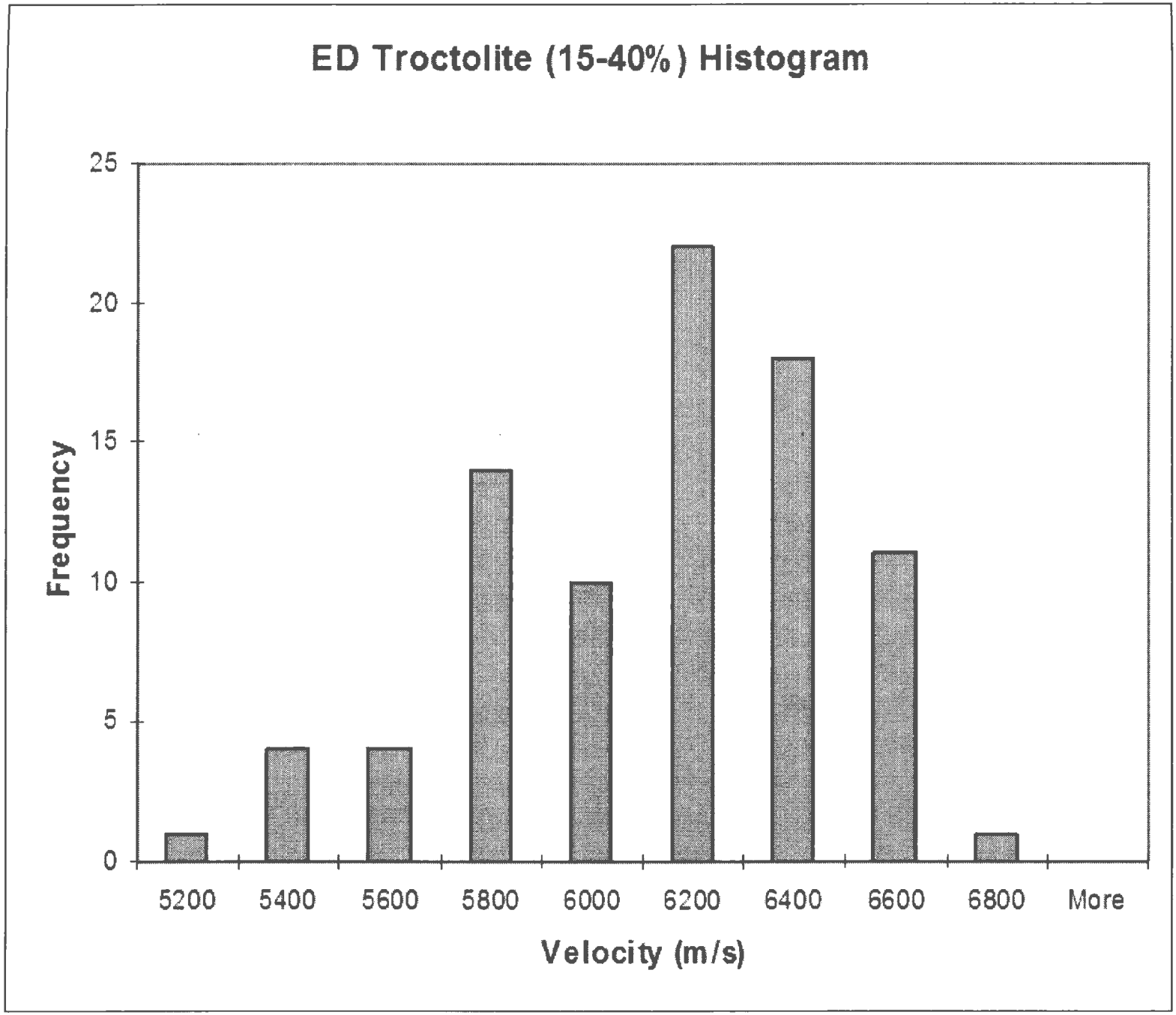


| | |
|---|---|
| Average Velocity | 6043 |
| Standard Deviation | 355 |
| Number of Samples | 85 |

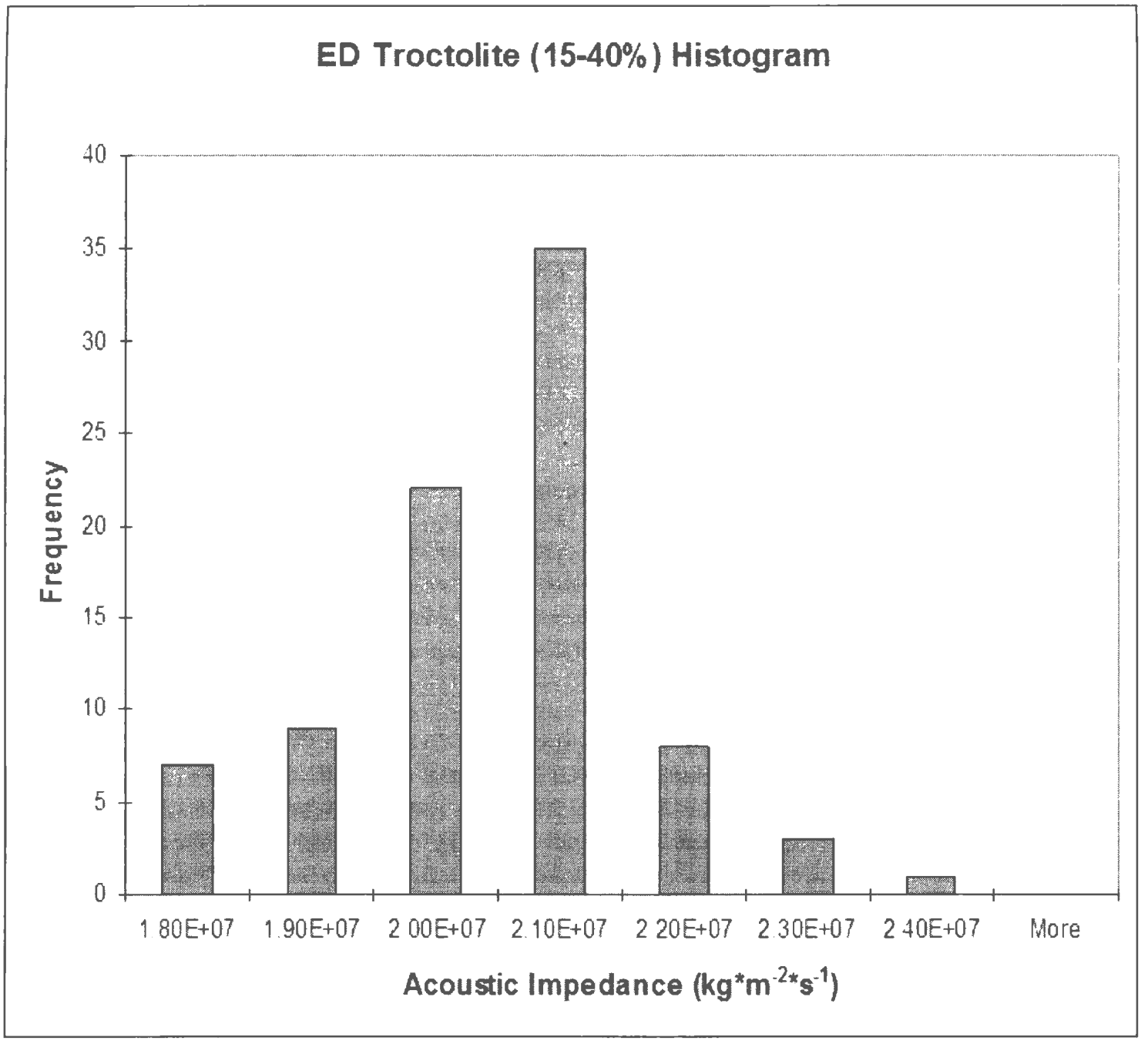


| | |
|---|---|
| Average Acoustic Impedance | 2.00 E+07 |
| Standard Deviation | 1.27 E+06 |
| Number of Samples | 85 |

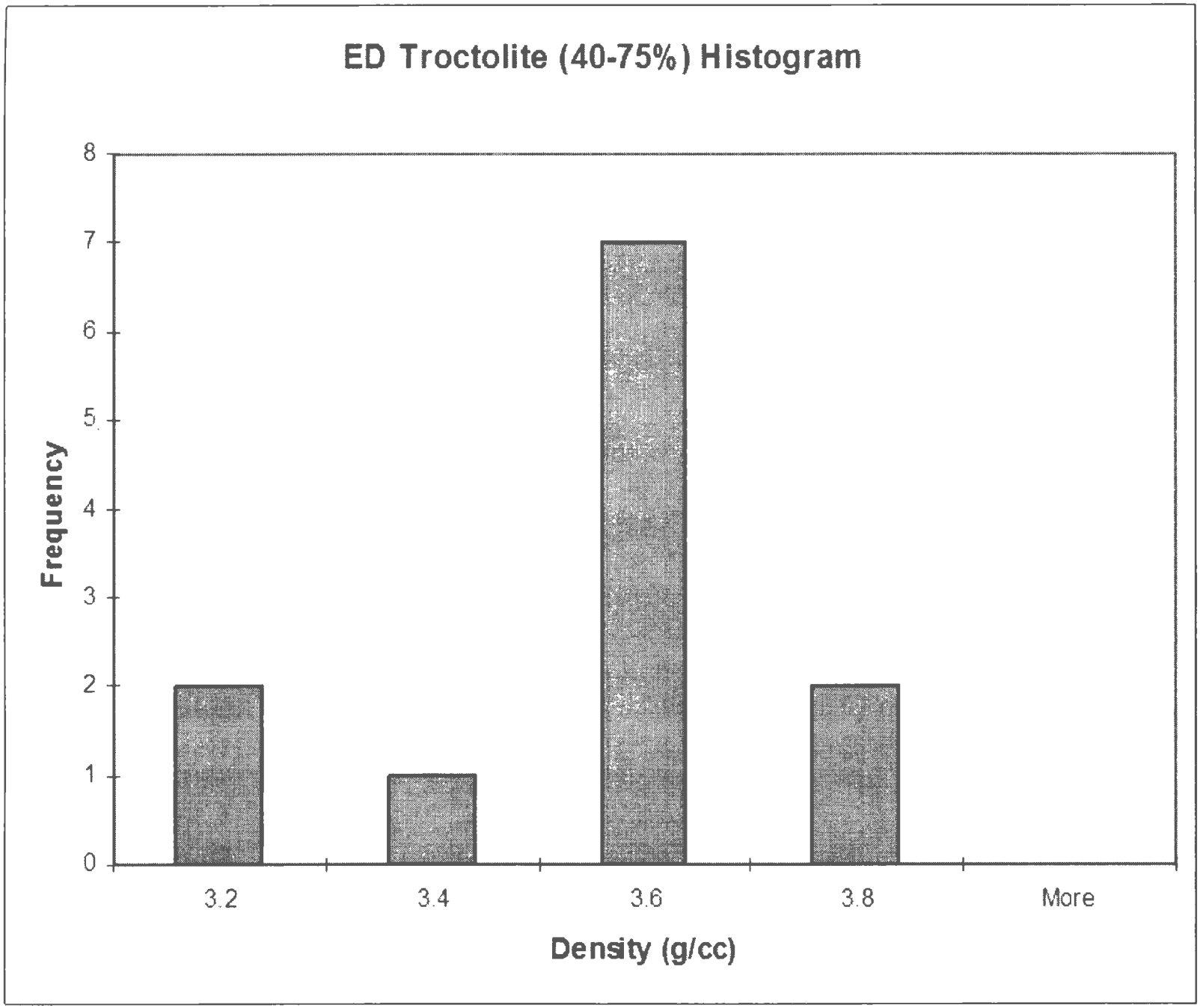


| | |
|---|---|
| Average Density | 3.44 |
| Standard Deviation | 0.198 |
| Number of Samples | 12 |

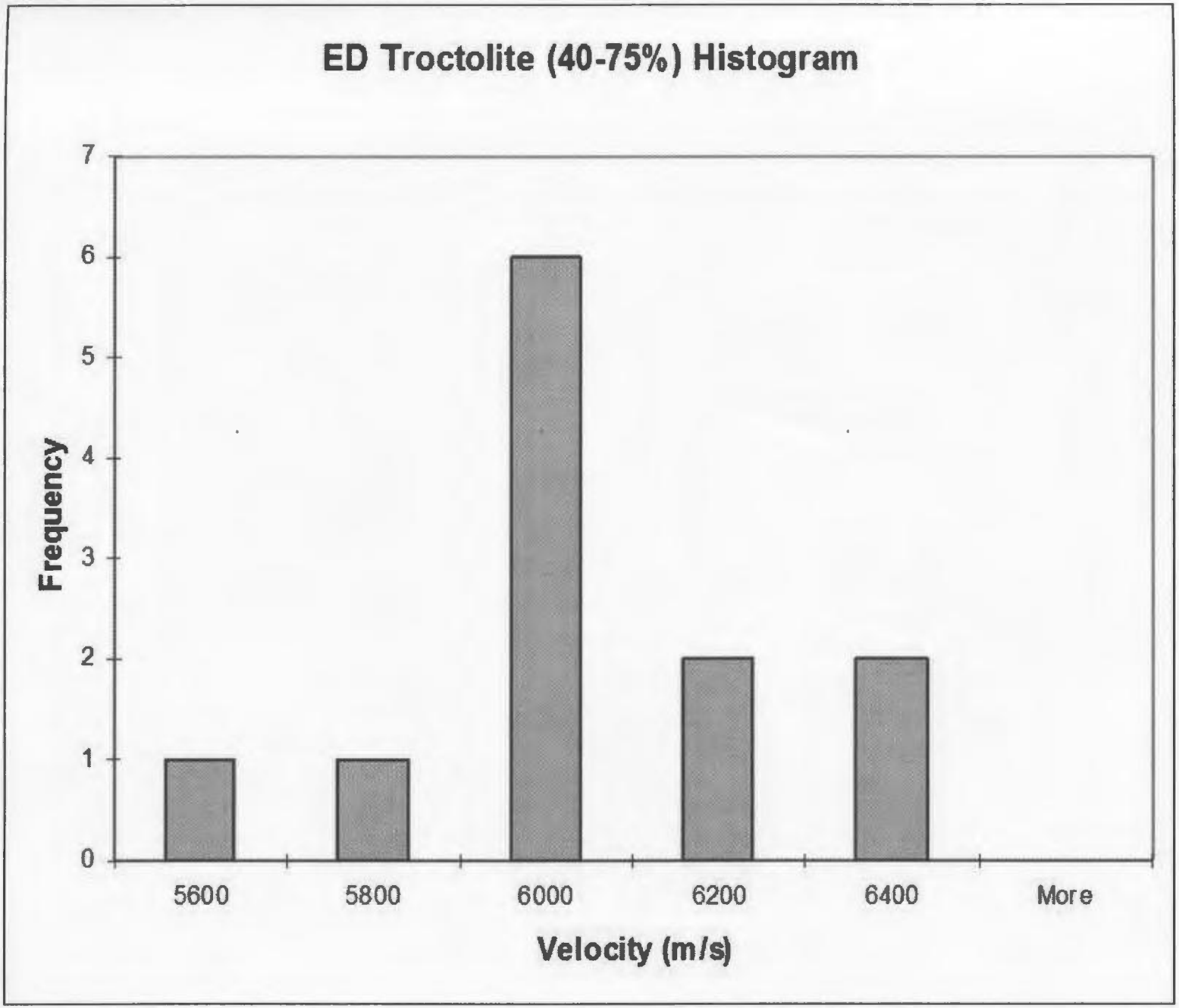


| | |
|---|---|
| Average Velocity | 5950 |
| Standard Deviation | 211 |
| Number of Samples | 12 |

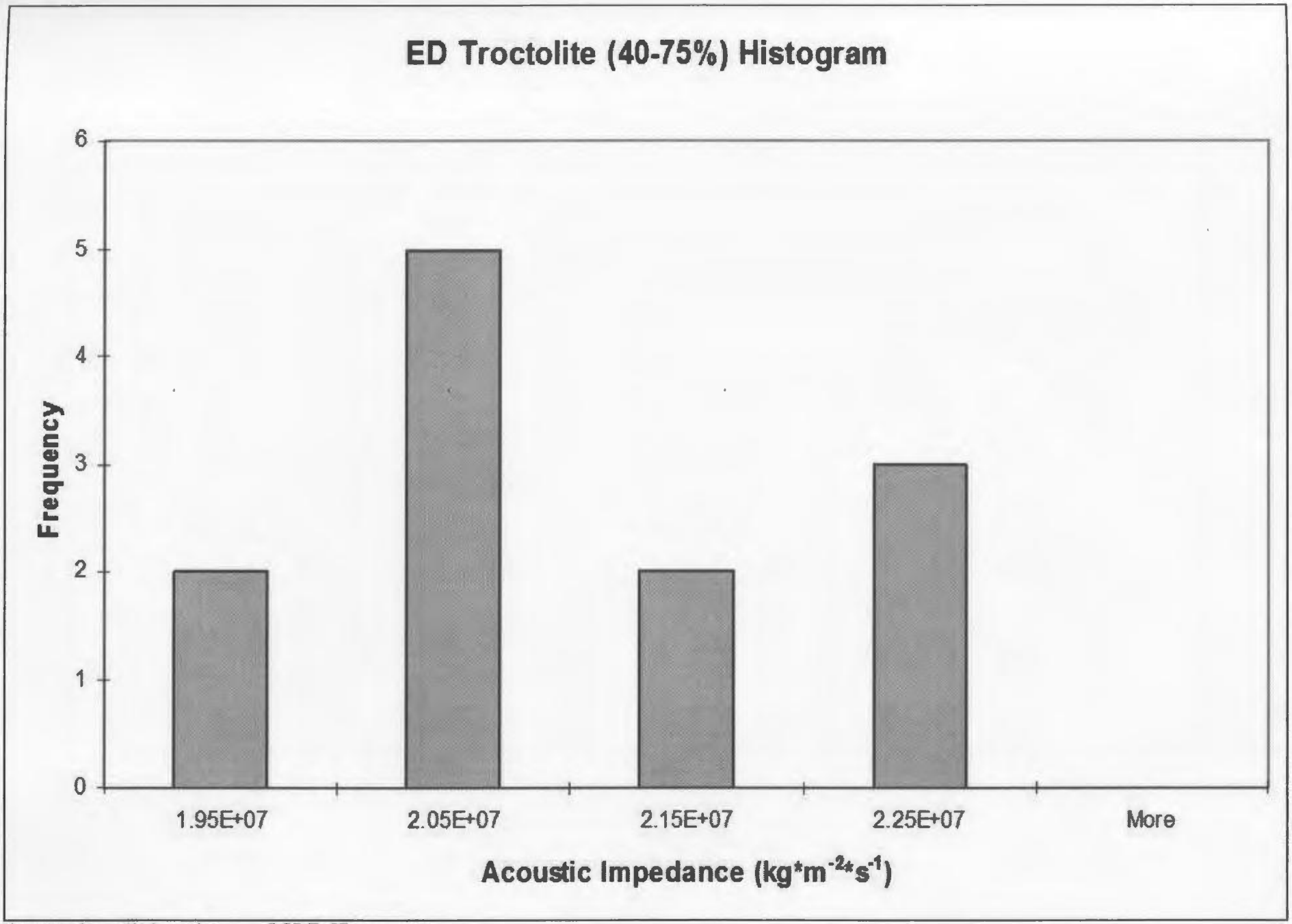


| | |
|---|---|
| Average Acoustic Impedance | 2.05 E+07 |
| Standard Deviation | 1.15 E+06 |
| Number of Samples | 12 |

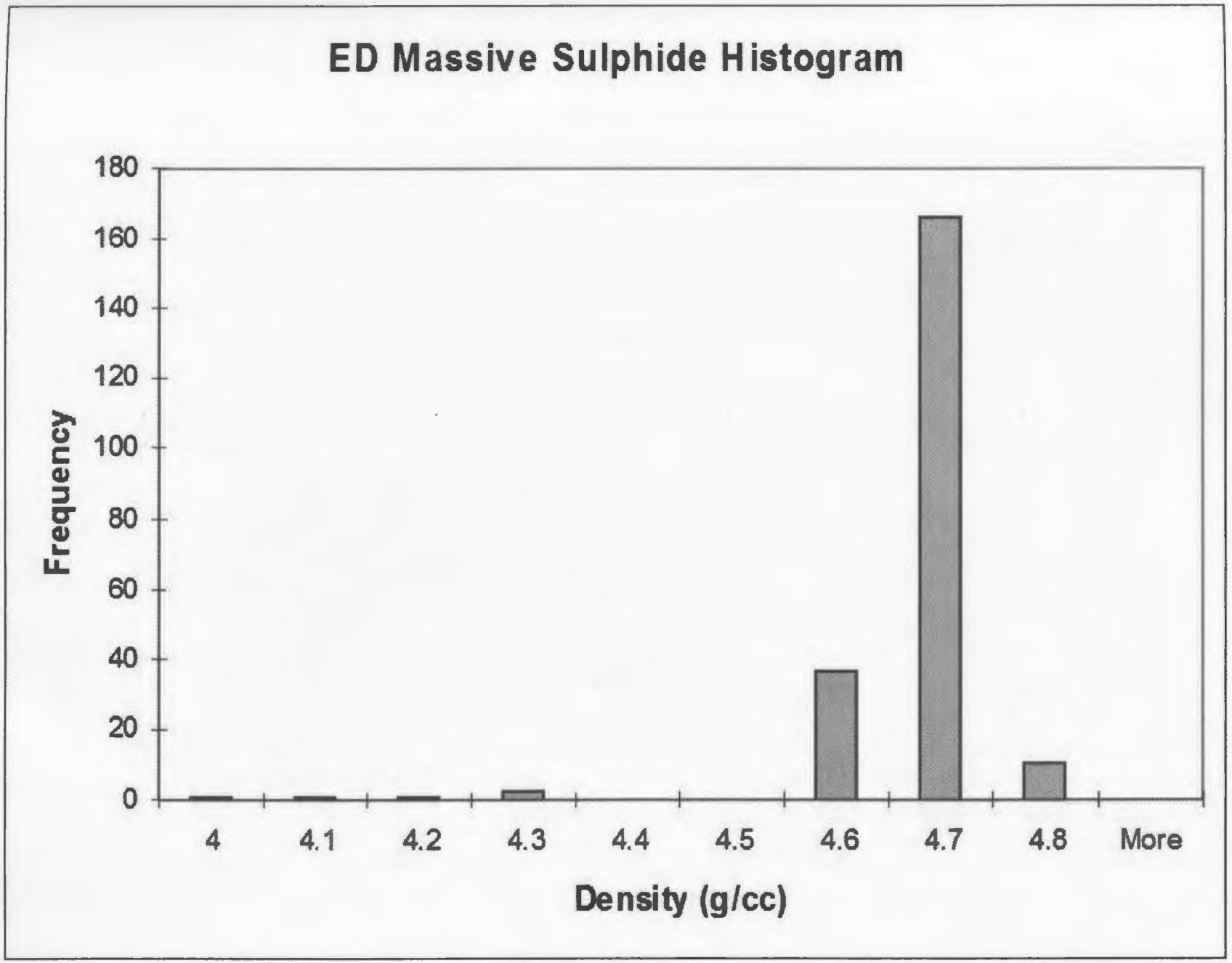


| | |
|---|---|
| Average Density | 4.62 |
| Standard Deviation | 0.122 |
| Number of Samples | 217 |

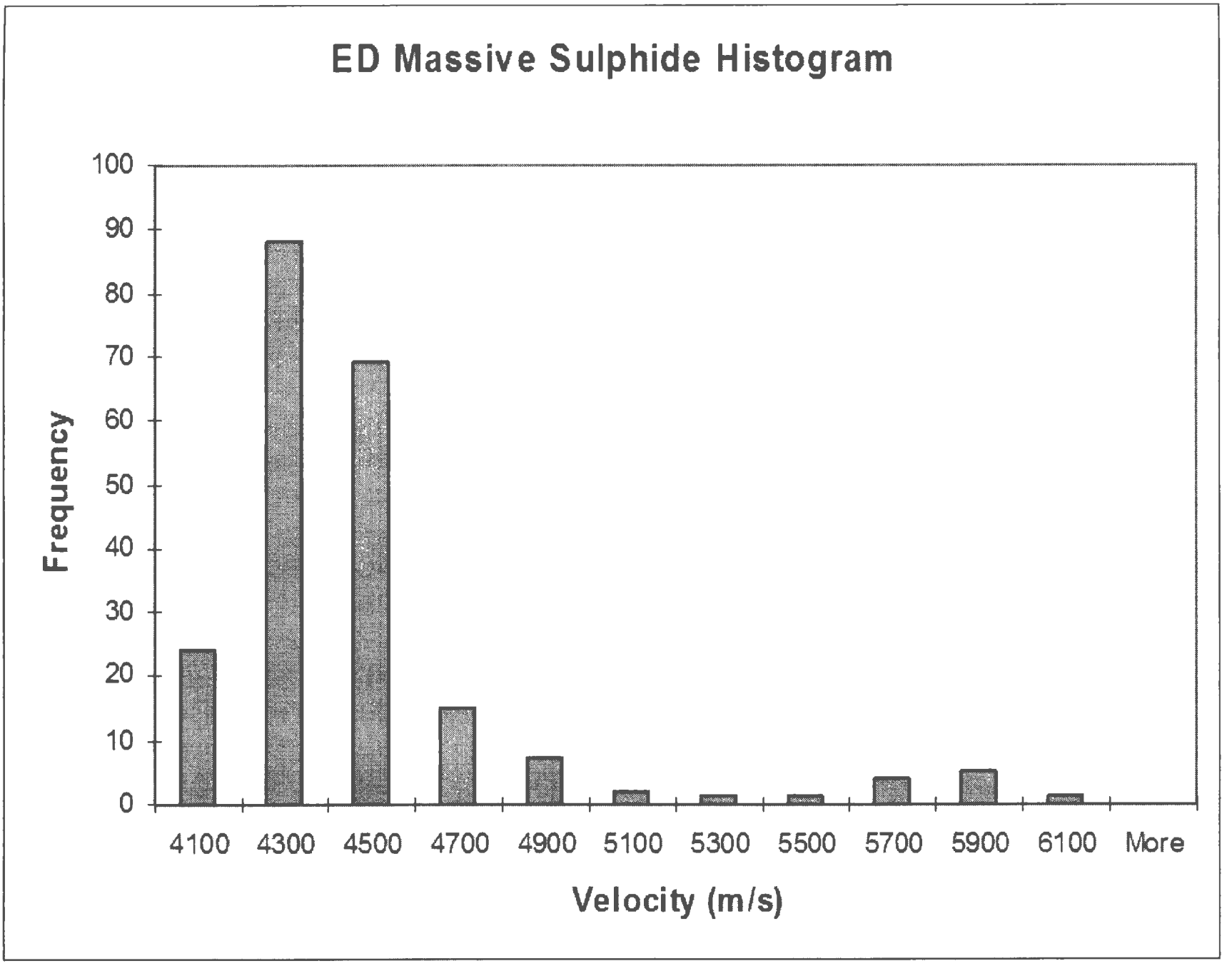


| | |
|---|---|
| Average Velocity | 4372 |
| Standard Deviation | 370 |
| Number of Samples | 217 |

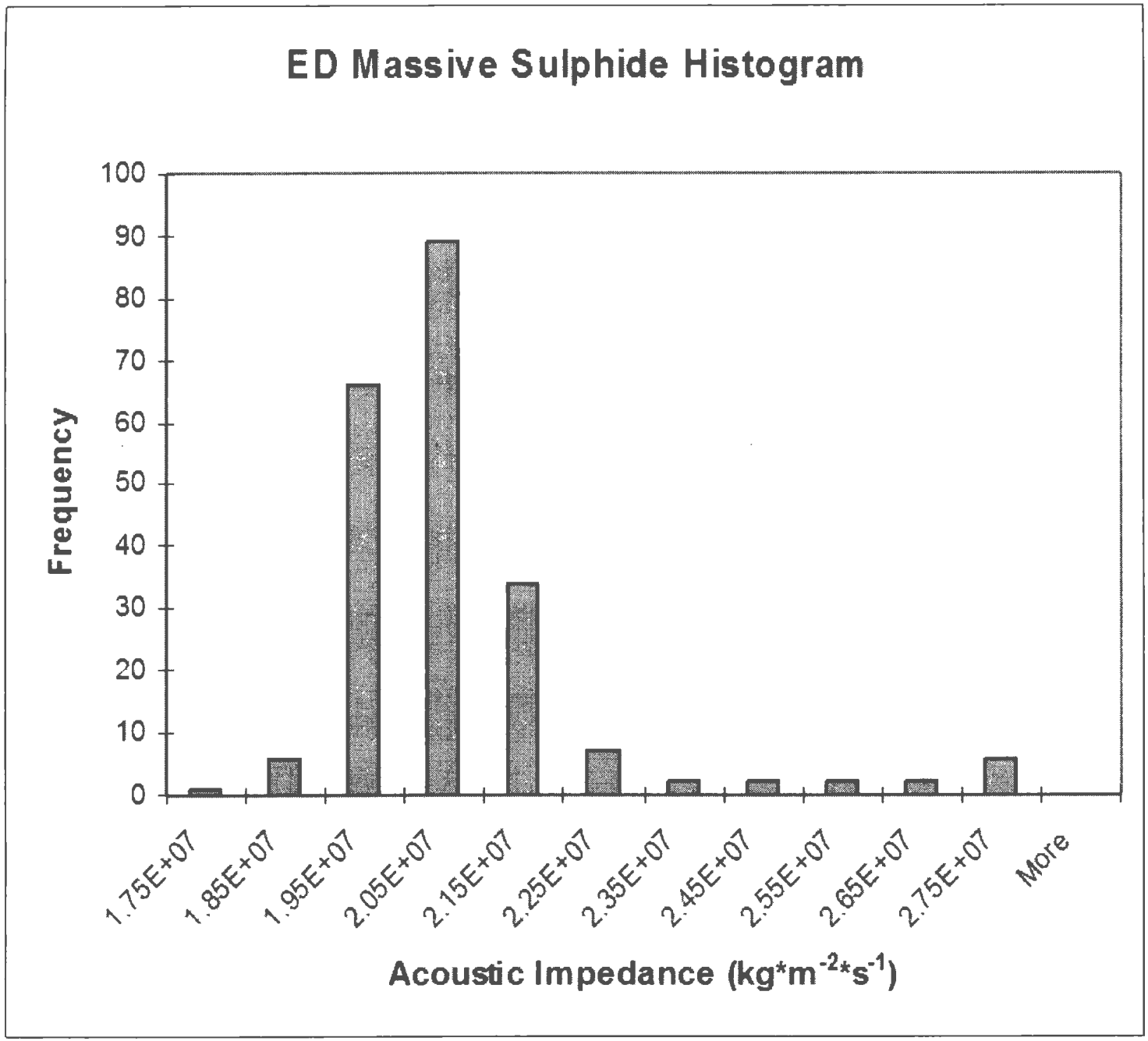


| | |
|---|---|
| Average Acoustic Impedance | 2.02 E+07 |
| Standard Deviation | 1.70 E+06 |
| Number of Samples | 217 |

# Appendix B

This appendix illustrates constant velocity stacks for velocities ranging from 4400-6600 m/s at an interval of 200 m/s for both the simple (B-1) and heterogeneity (B-2) models. The processing parameters that were applied to the data were an Ormsby bandpass filter with parameters 8-20-80-120 Hz and a top mute.

**B-1:** Constant velocity stacks for the simple model.

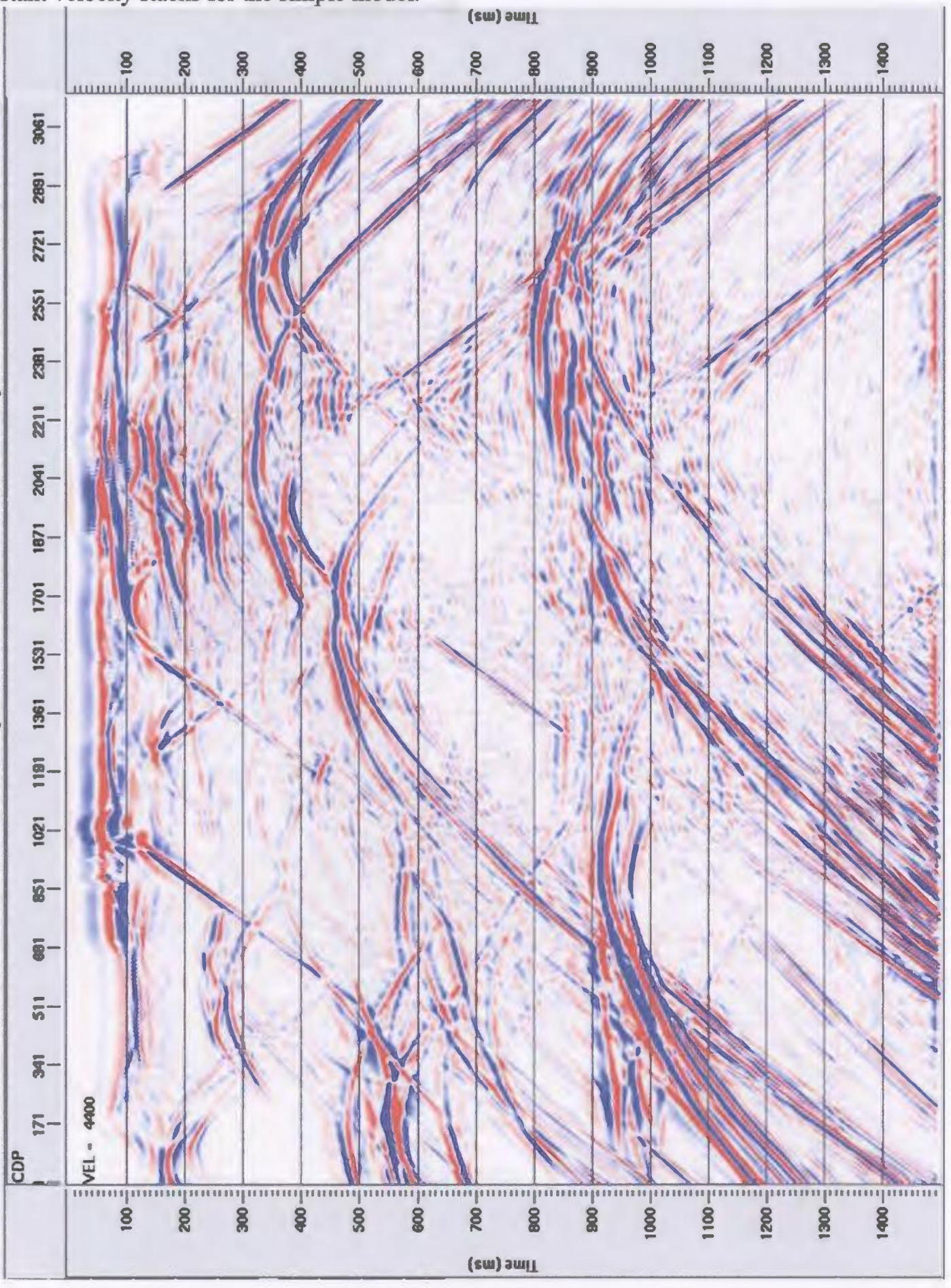

# CVS (4600 m/s)

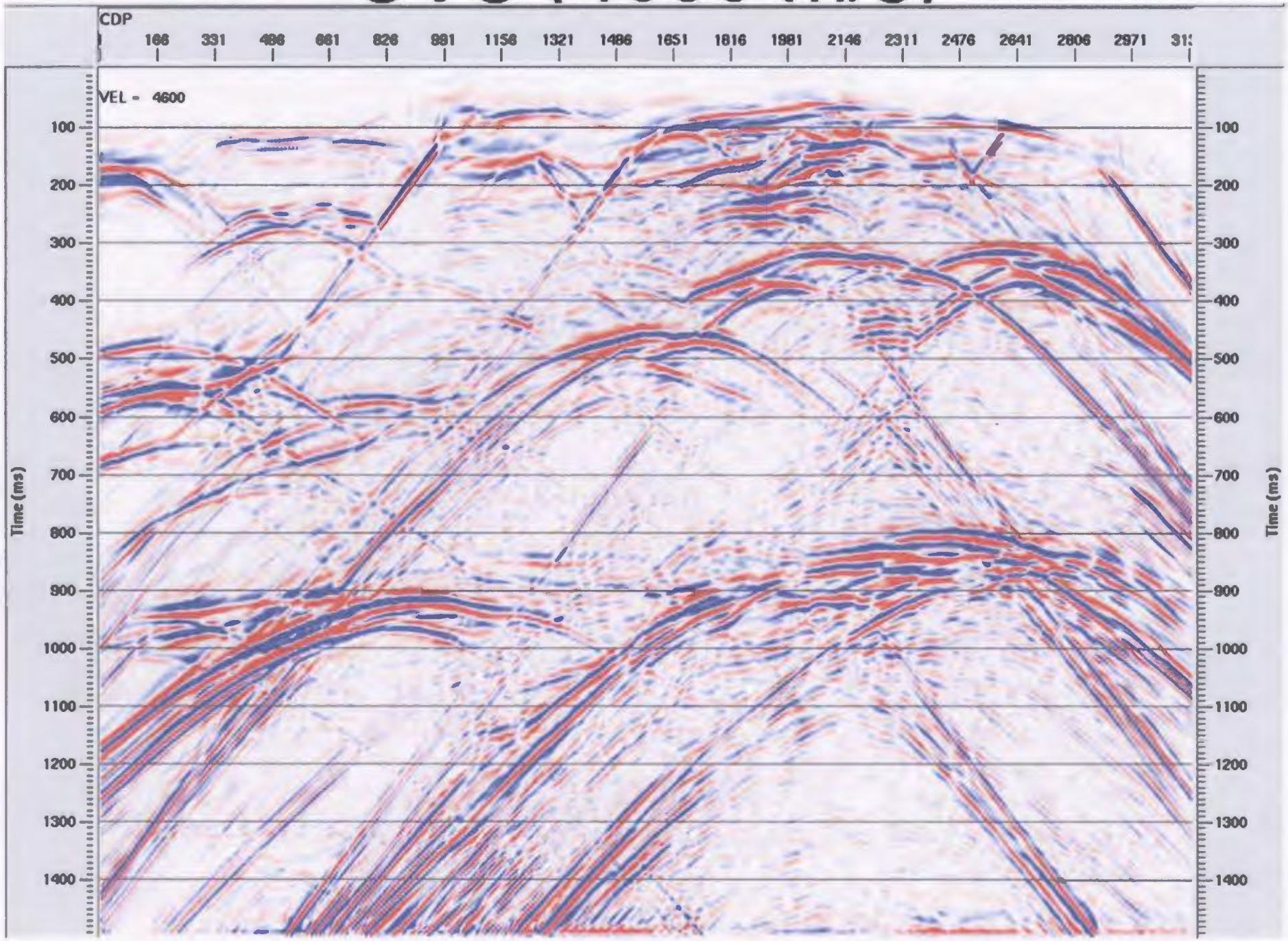
CDP
166
331
496
661
826
991
1156
1321
1486
1651
1816
1981
2146
2311
2476
2641
2806
2971
VEL = 4600
100
200
300
400
500
600
700
800
900
1000
1100
1200
1300
1400
Time (ms)

# CVS (4800 m/s)

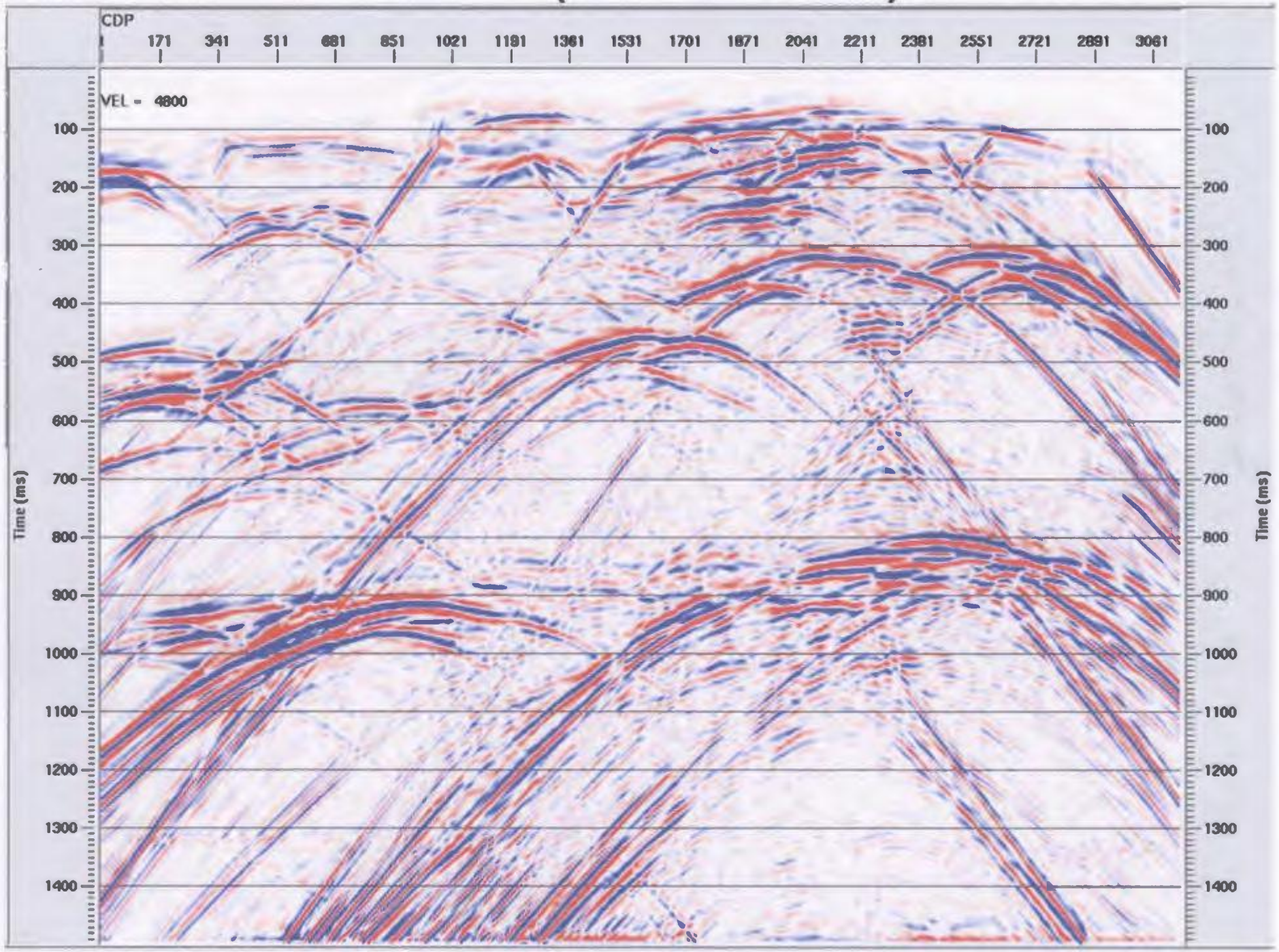
CDP
1
171
341
511
681
851
1021
1191
1361
1531
1701
1871
2041
2211
2381
2551
2721
2891
3061
VEL = 4800
100
200
300
400
500
600
700
800
900
1000
1100
1200
1300
1400
Time (ms)

# CVS (5000 m/s)

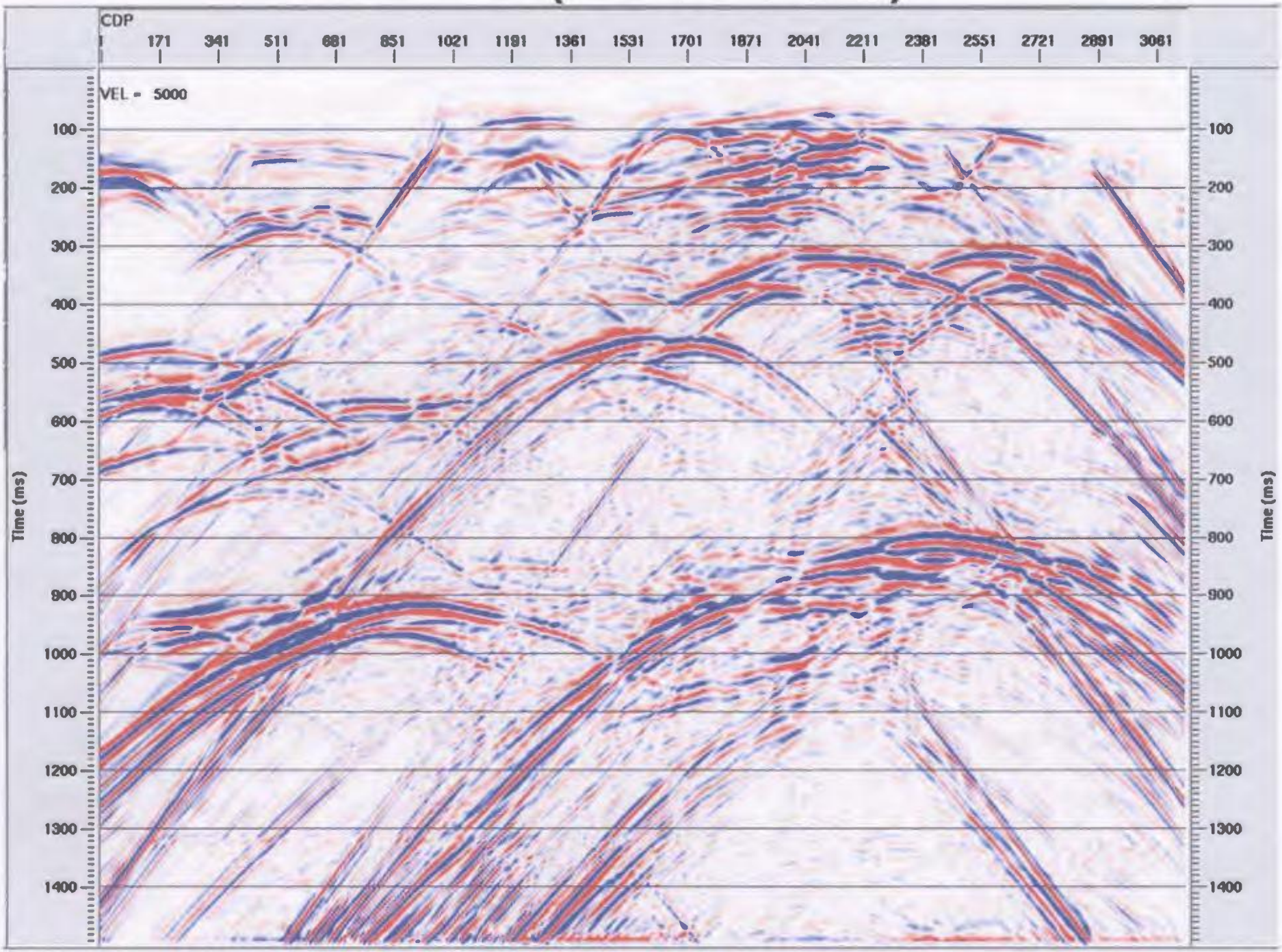
CDP
1
171
341
511
681
851
1021
1191
1361
1531
1701
1871
2041
2211
2381
2551
2721
2891
3061
VEL = 5000
100
200
300
400
500
600
700
800
900
1000
1100
1200
1300
1400
Time (ms)

# CVS (5200 m/s)

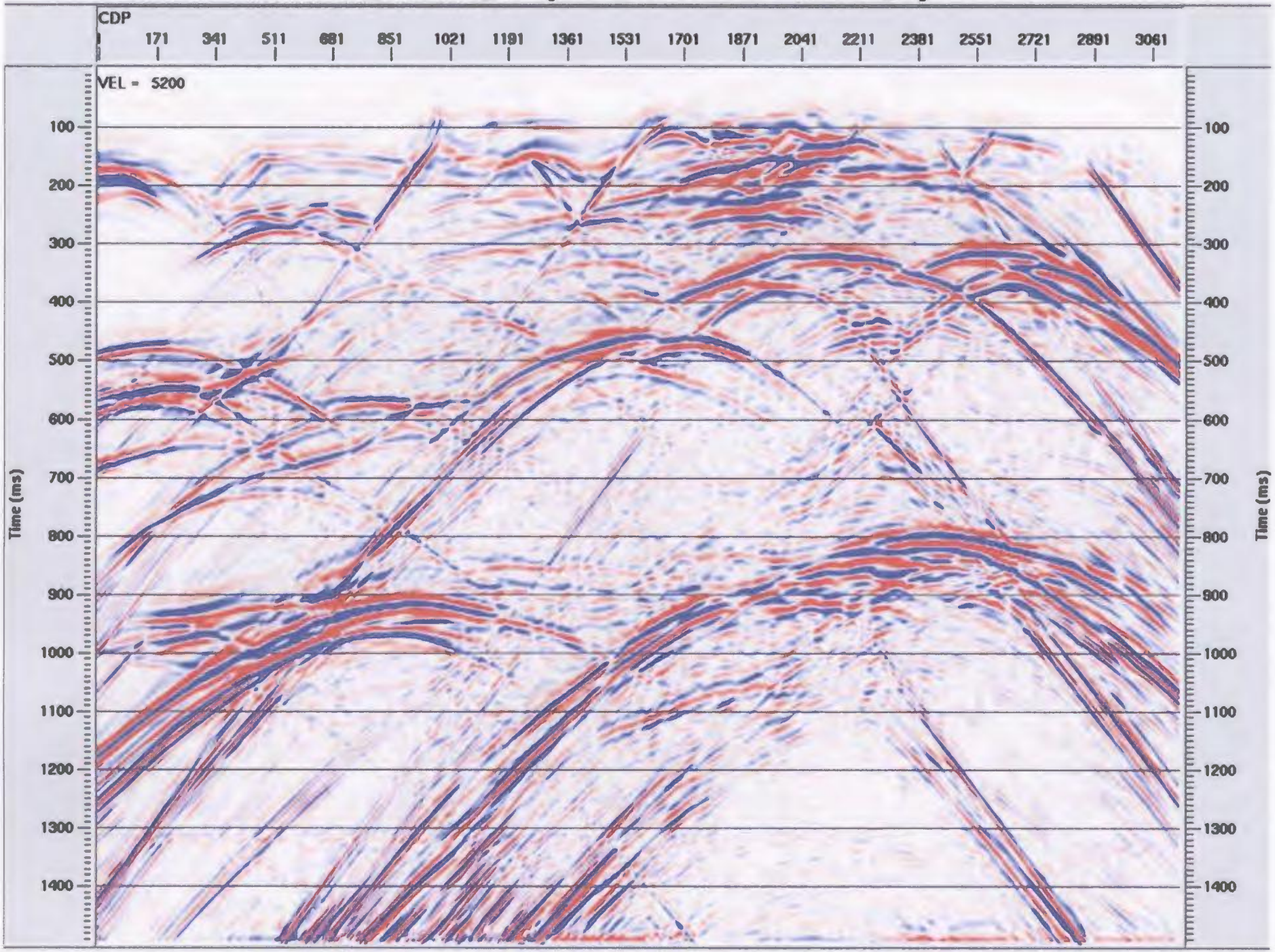
CDP
1
171
341
511
681
851
1021
1191
1361
1531
1701
1871
2041
2211
2381
2551
2721
2891
3061
VEL = 5200
Time (ms)
100
200
300
400
500
600
700
800
900
1000
1100
1200
1300
1400

# CVS (5400 m/s)

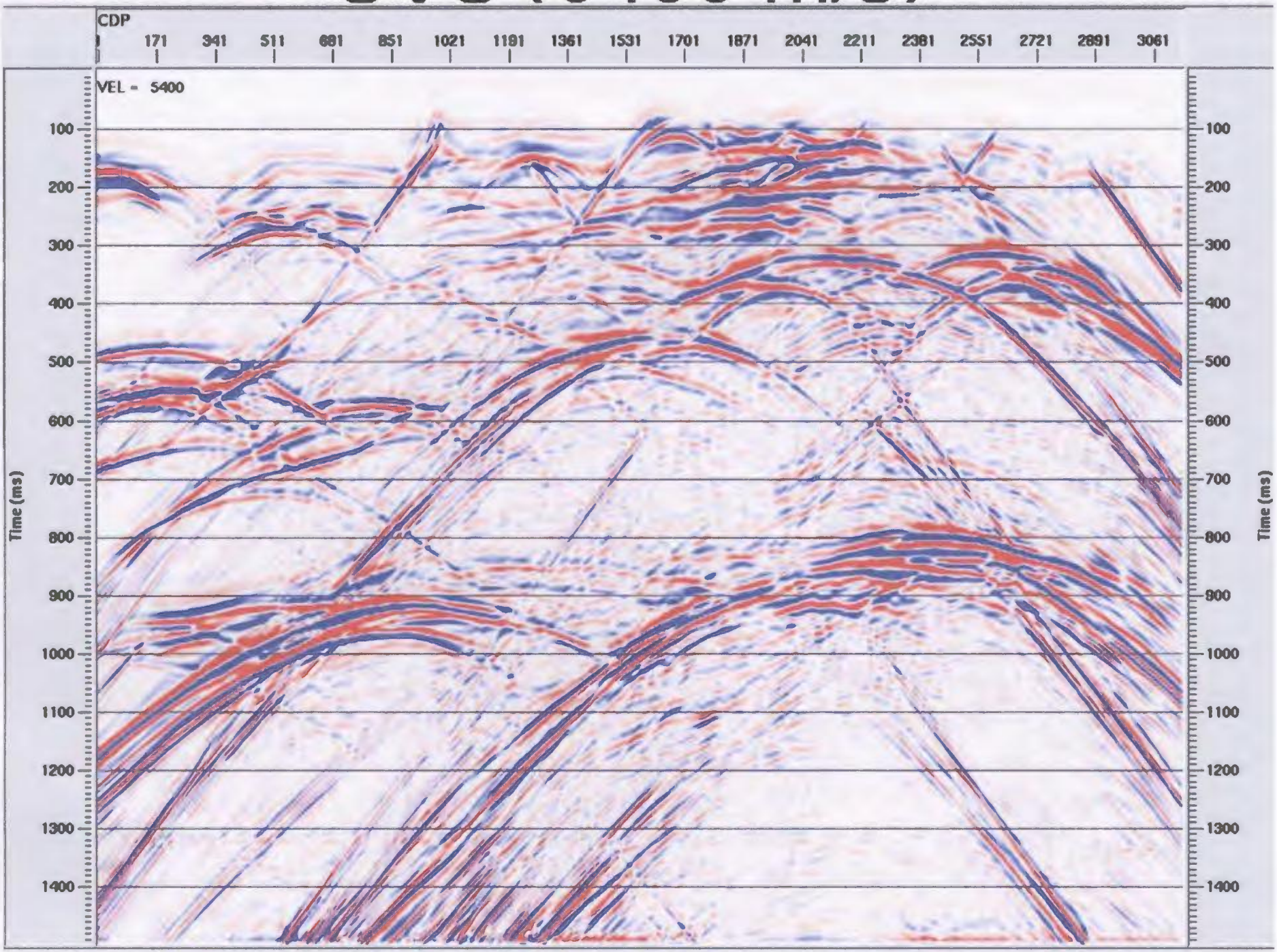
CDP
1
171
341
511
681
851
1021
1191
1361
1531
1701
1871
2041
2211
2381
2551
2721
2891
3061
VEL = 5400
100
200
300
400
500
600
700
800
900
1000
1100
1200
1300
1400
Time (ms)

# CVS (5600 m/s)

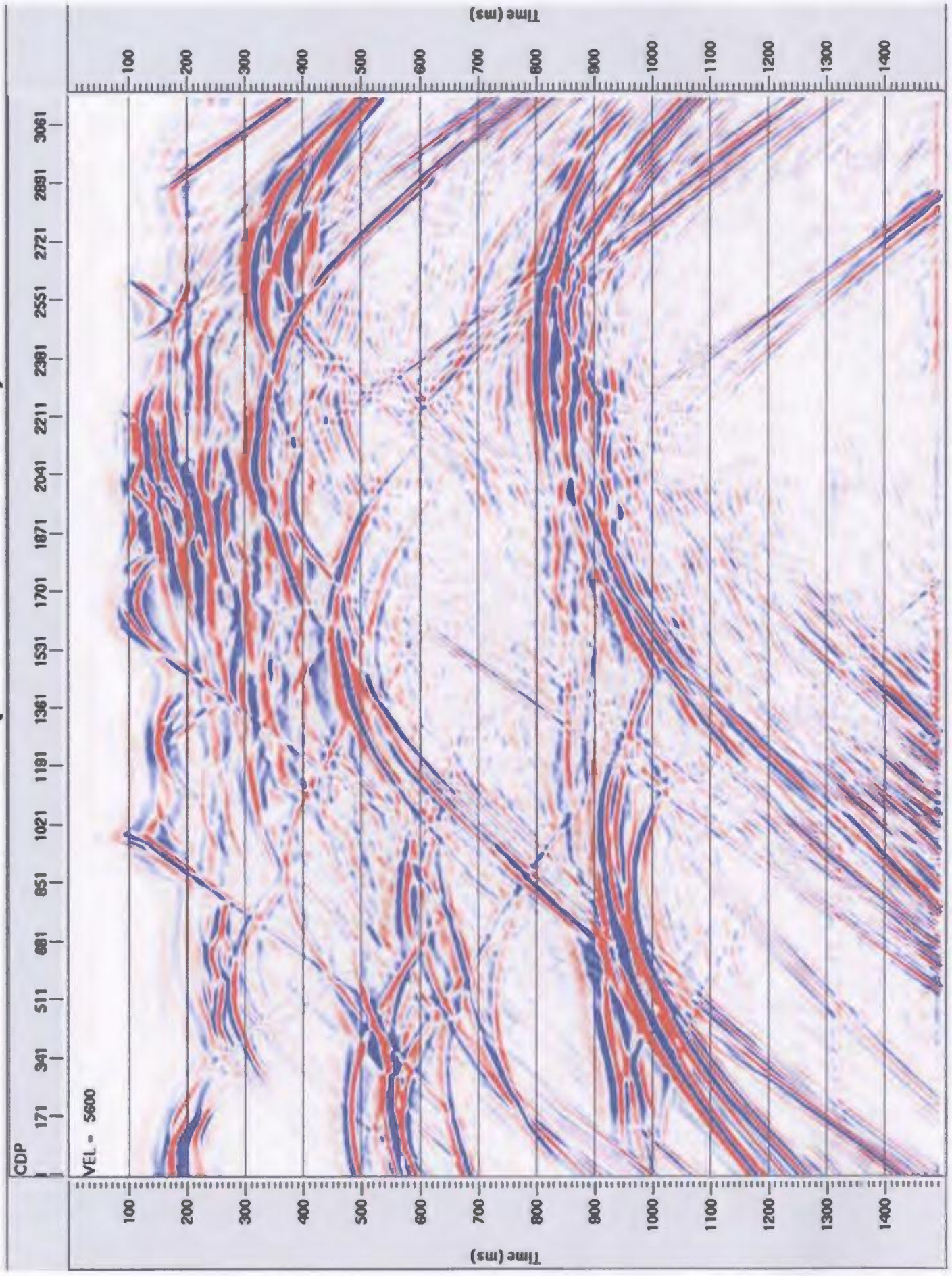
CDP
171
341
511
681
851
1021
1191
1361
1531
1701
1871
2041
2211
2381
2551
2721
2891
3061
VEL - 5600
Time (ms)
100
200
300
400
500
600
700
800
900
1000
1100
1200
1300
1400

# CVS (5800 m/s)

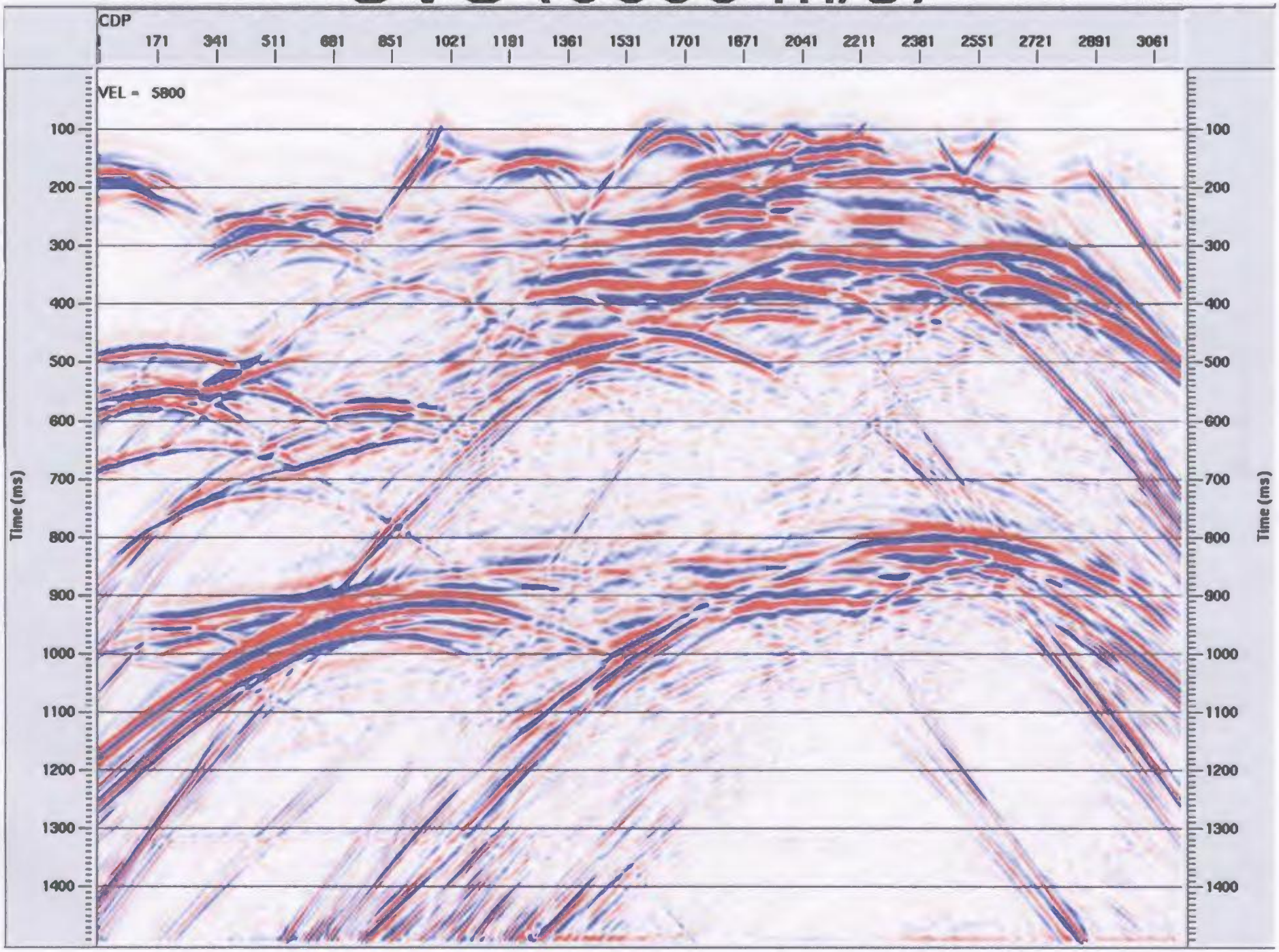
CDP
171
341
511
681
851
1021
1181
1361
1531
1701
1871
2041
2211
2381
2551
2721
2891
3061
VEL = 5800
100
200
300
400
500
600
700
800
900
1000
1100
1200
1300
1400
Time (ms)

# CVS (6000 m/s)

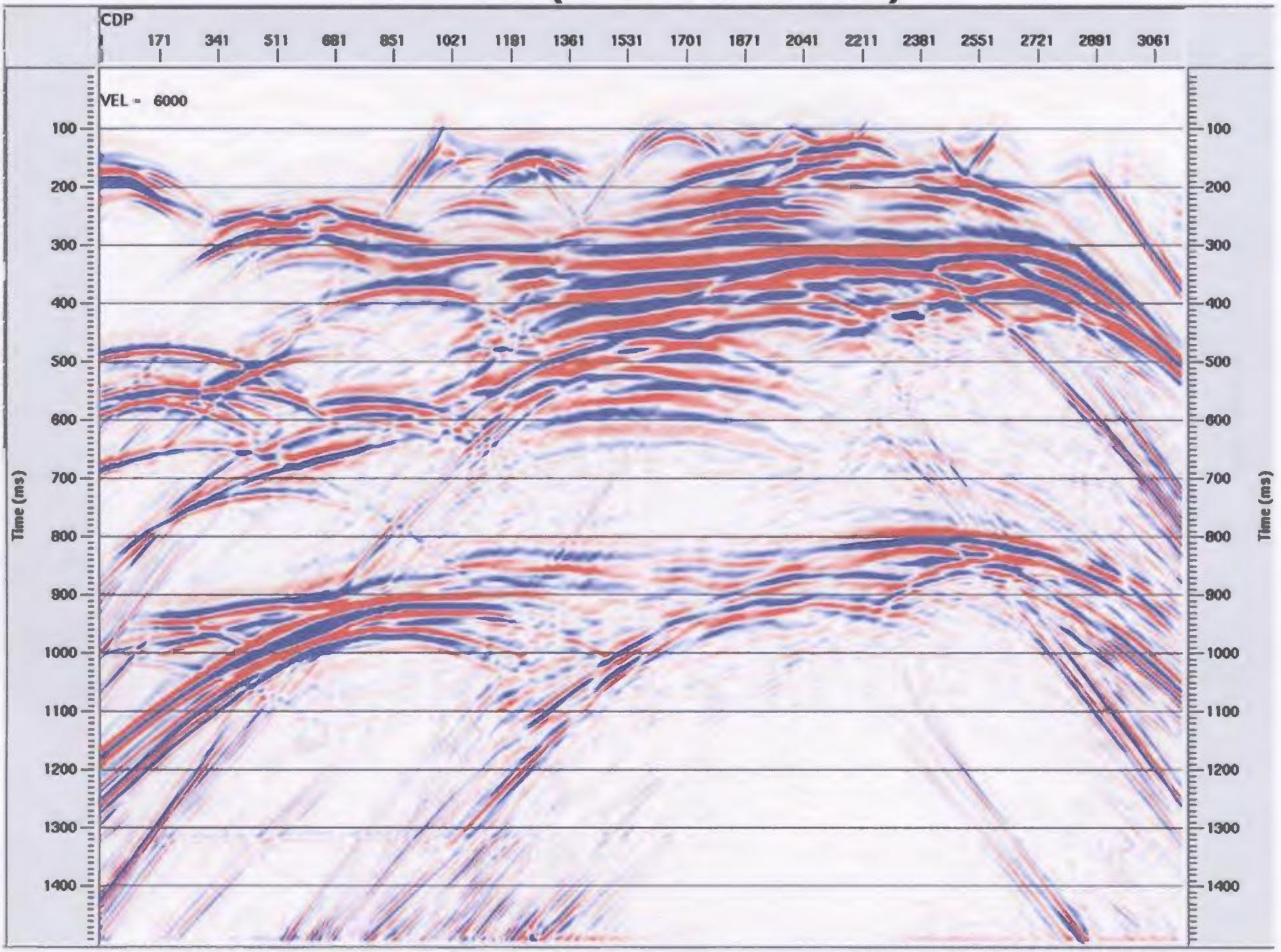
CDP
1
171
341
511
681
851
1021
1181
1361
1531
1701
1871
2041
2211
2381
2551
2721
2891
3061
VEL = 6000
Time (ms)
100
200
300
400
500
600
700
800
900
1000
1100
1200
1300
1400

# CVS (6200 m/s)

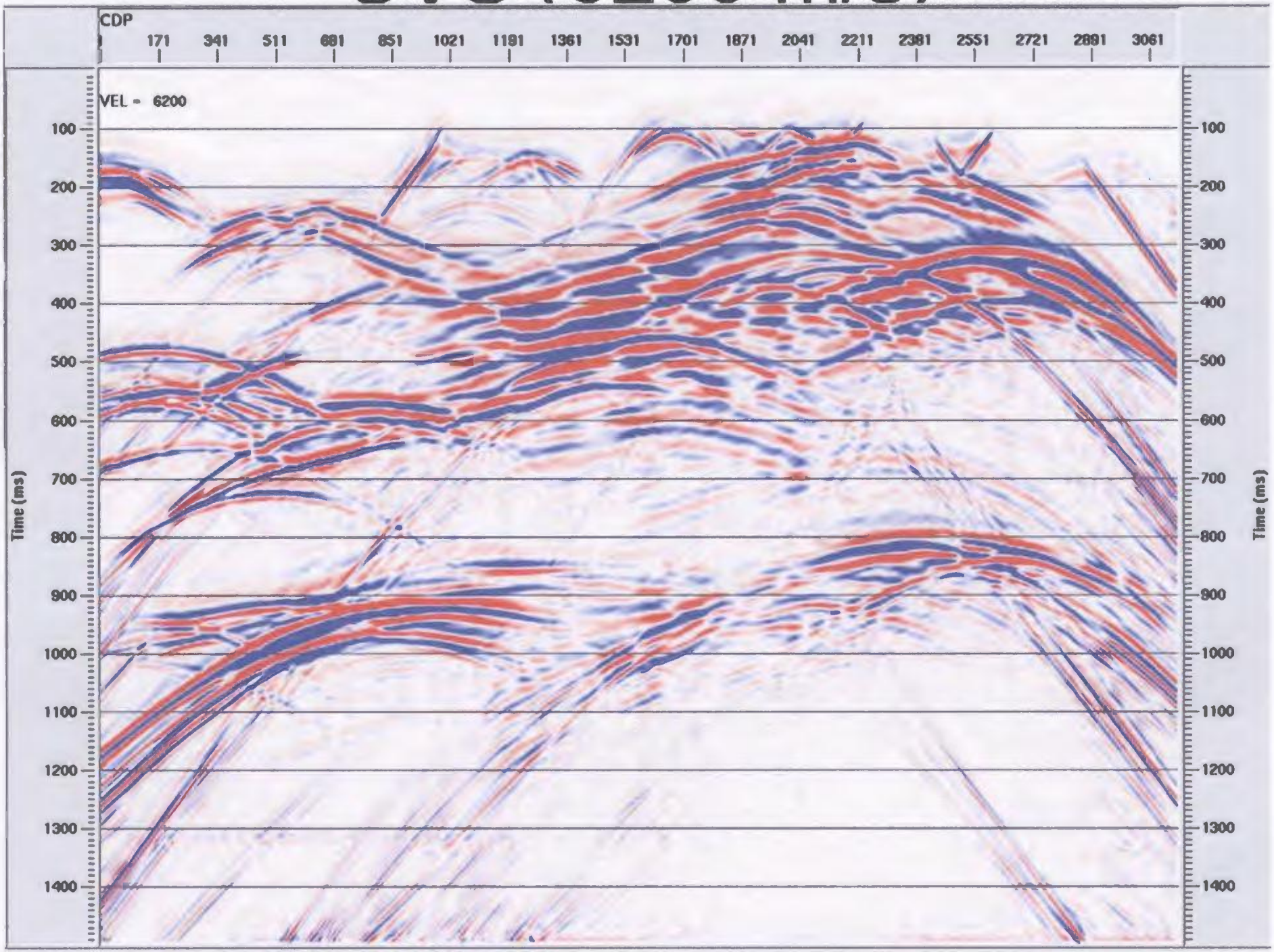
CDP
1
171
341
511
681
851
1021
1191
1361
1531
1701
1871
2041
2211
2381
2551
2721
2891
3061
VEL = 6200
100
200
300
400
500
600
700
800
900
1000
1100
1200
1300
1400
Time (ms)

# CVS (6400 m/s)

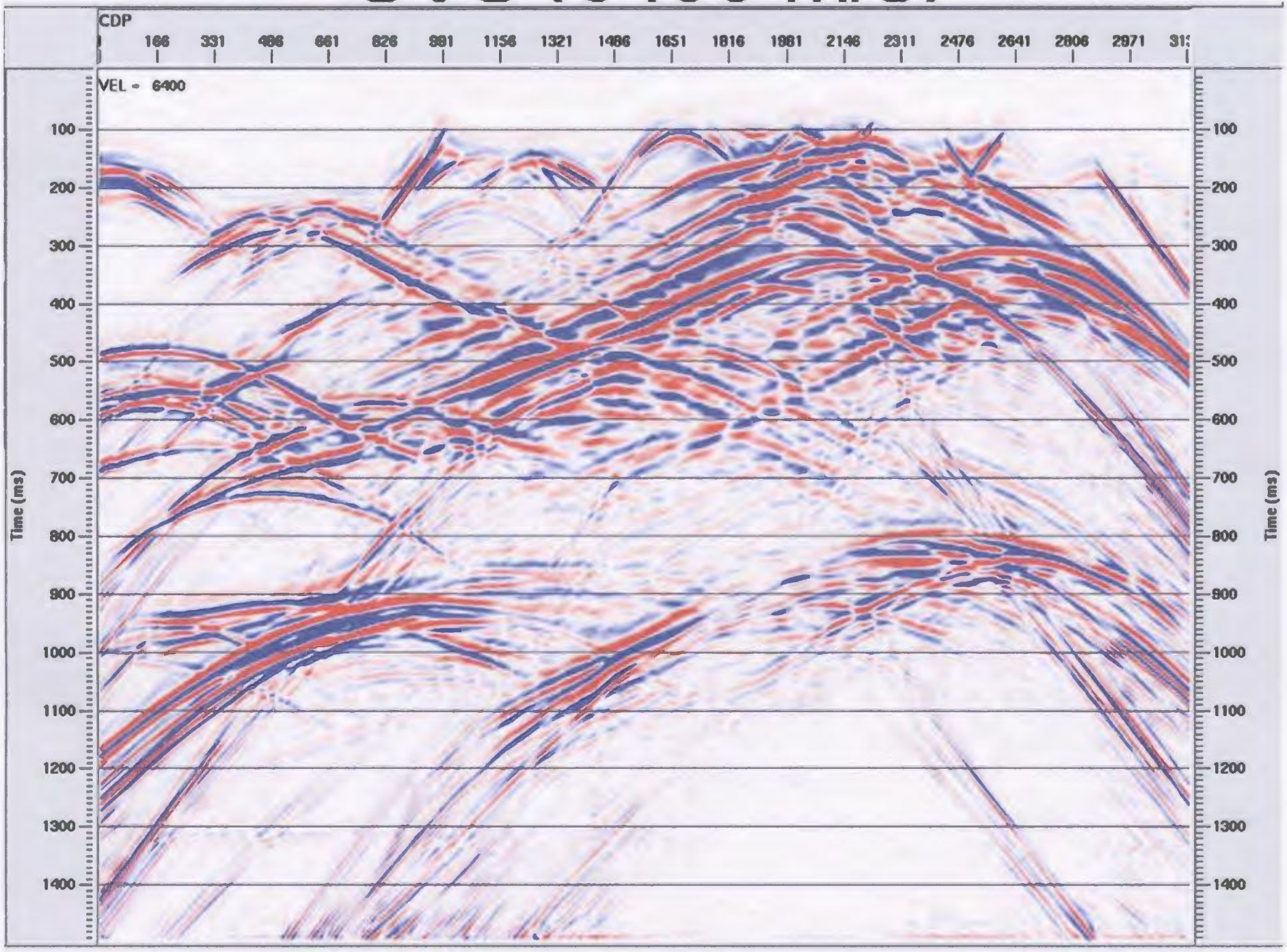
CDP
166
331
496
661
826
991
1156
1321
1486
1651
1816
1981
2146
2311
2476
2641
2806
2971
VEL = 6400
100
200
300
400
500
600
700
800
900
1000
1100
1200
1300
1400
Time (ms)

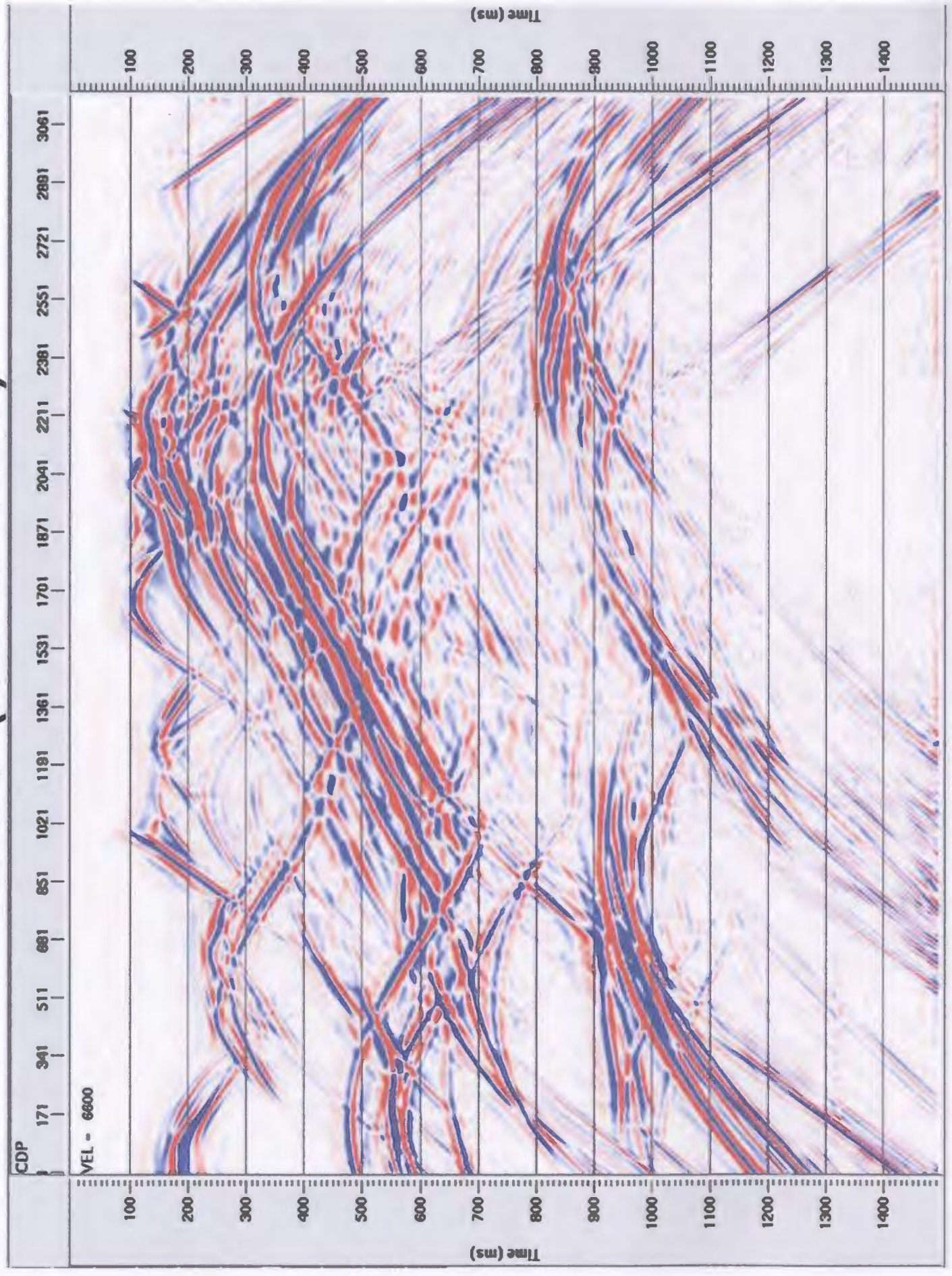
CVS (6600 m/s)
CDP
171
341
511
681
851
1021
1191
1361
1531
1701
1871
2041
2211
2381
2551
2721
2891
3061
VEL = 6600
Time (ms)
100
200
300
400
500
600
700
800
900
1000
1100
1200
1300
1400

**B-2:** Constant velocity stacks for the heterogeneity model.

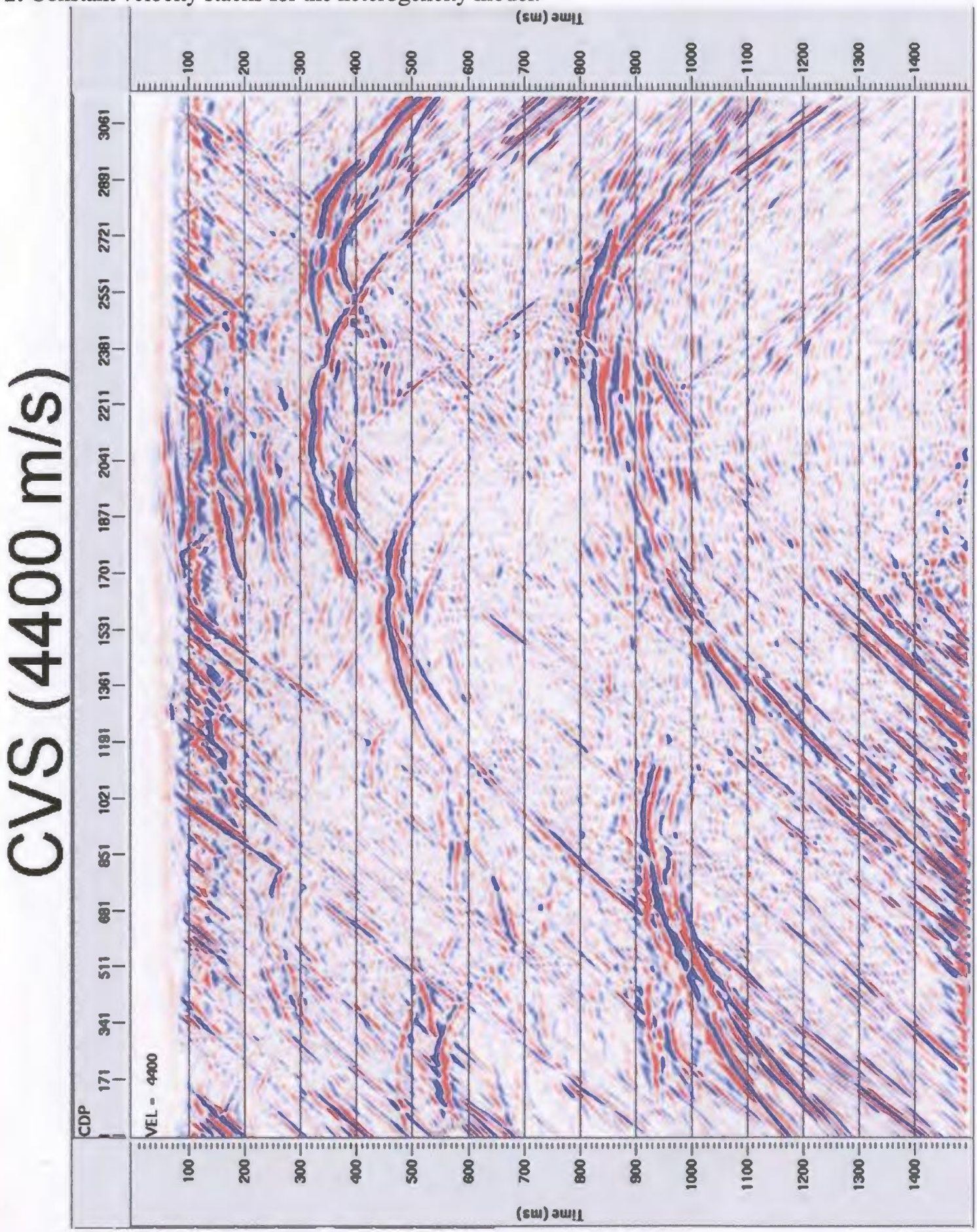

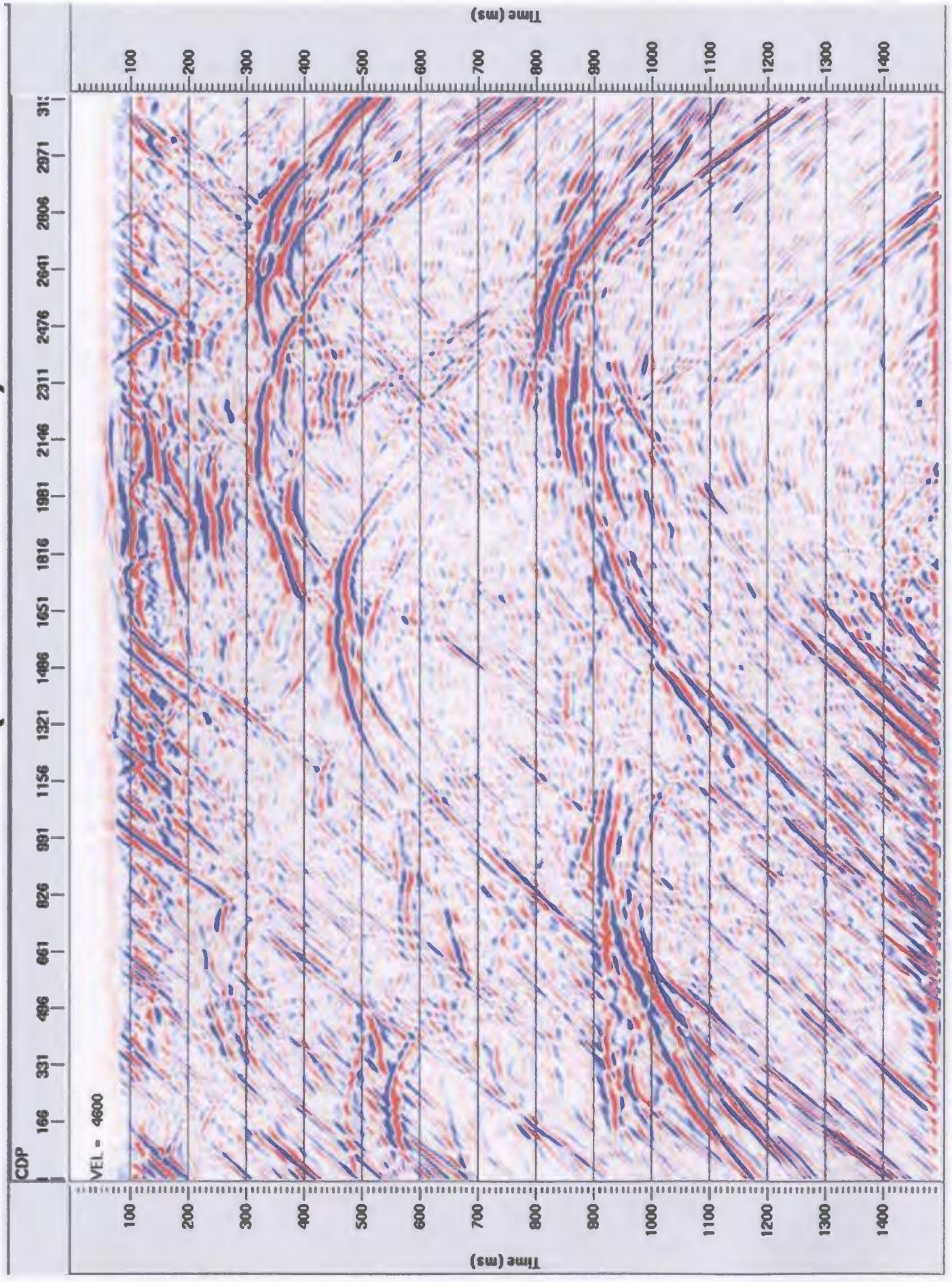
CVS (4600 m/s)
CDP
166
331
496
661
826
991
1156
1321
1486
1651
1816
1981
2146
2311
2476
2641
2806
2971
VEL = 4600
Time (ms)
100
200
300
400
500
600
700
800
900
1000
1100
1200
1300
1400

# CVS (4800 m/s)

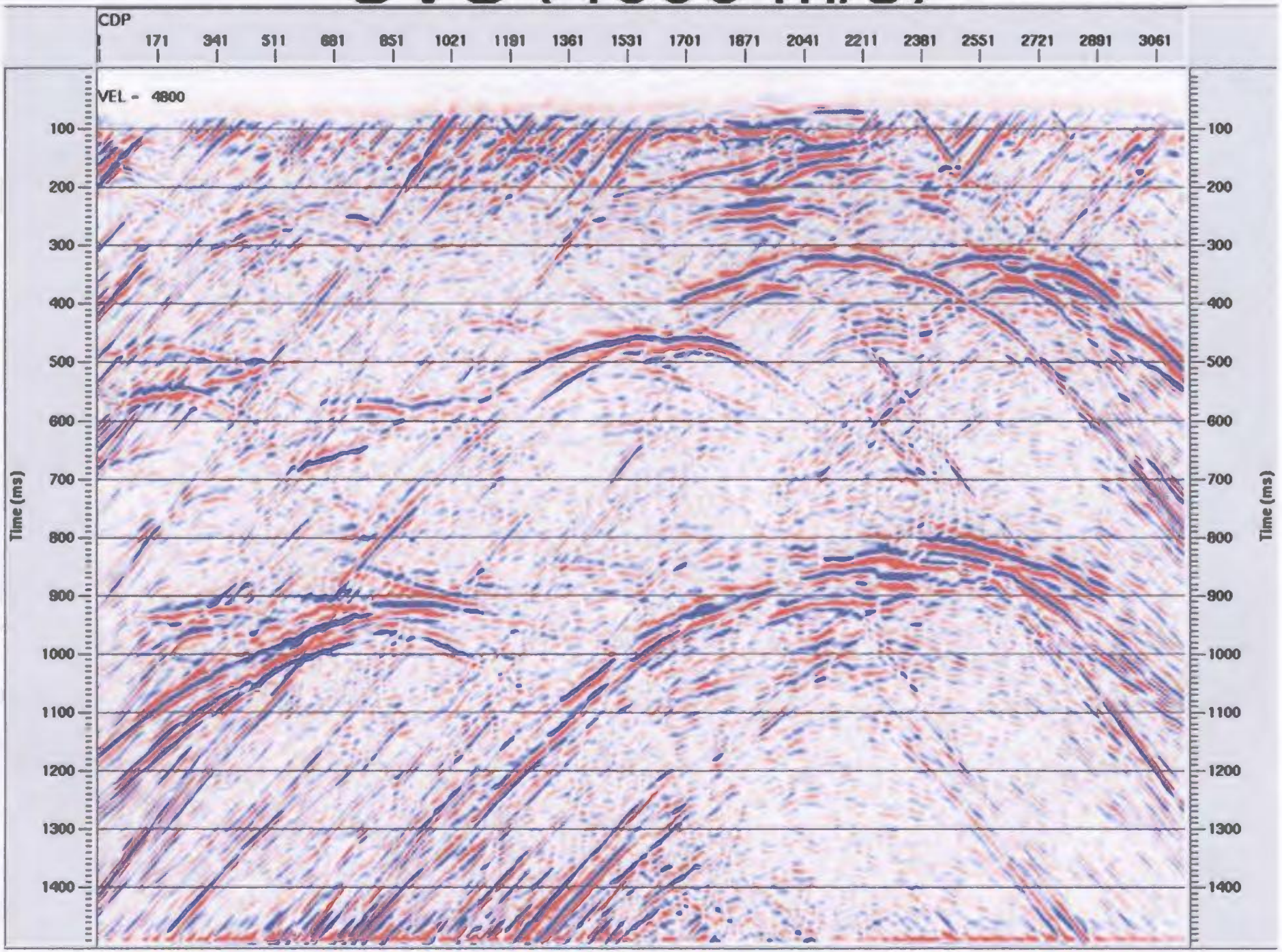
CDP
171
341
511
681
851
1021
1191
1361
1531
1701
1871
2041
2211
2381
2551
2721
2891
3061
VEL = 4800
100
200
300
400
500
600
700
800
900
1000
1100
1200
1300
1400
Time (ms)

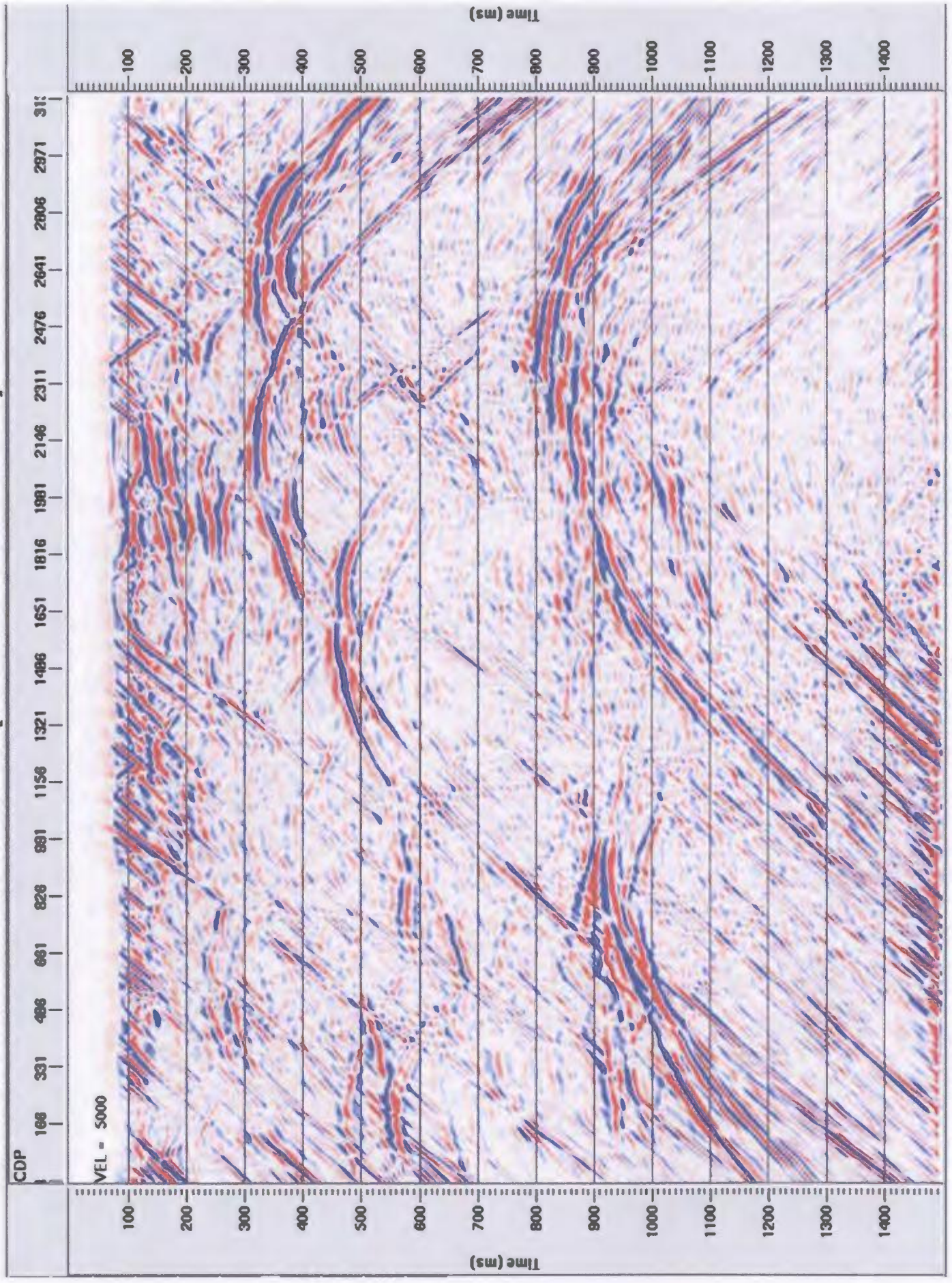
CVS (5000 m/s)
CDP
168
331
496
661
826
991
1156
1321
1486
1651
1816
1981
2146
2311
2476
2641
2806
2971
VEL = 5000
Time (ms)
100
200
300
400
500
600
700
800
900
1000
1100
1200
1300
1400

# CVS (5200 m/s)

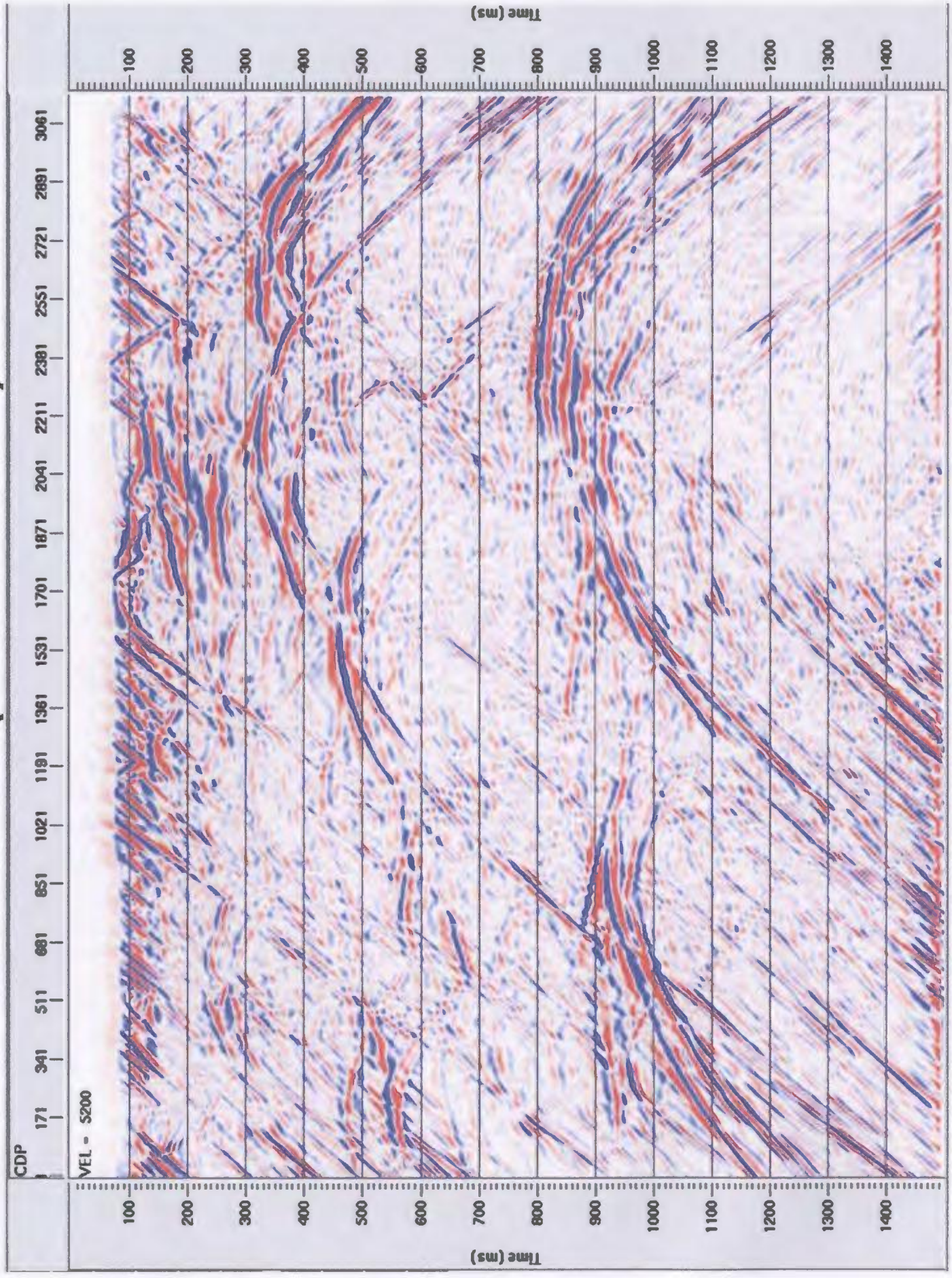
CDP
171
341
511
681
851
1021
1191
1361
1531
1701
1871
2041
2211
2381
2551
2721
2891
3061
VEL - S200
Time (ms)
100
200
300
400
500
600
700
800
900
1000
1100
1200
1300
1400

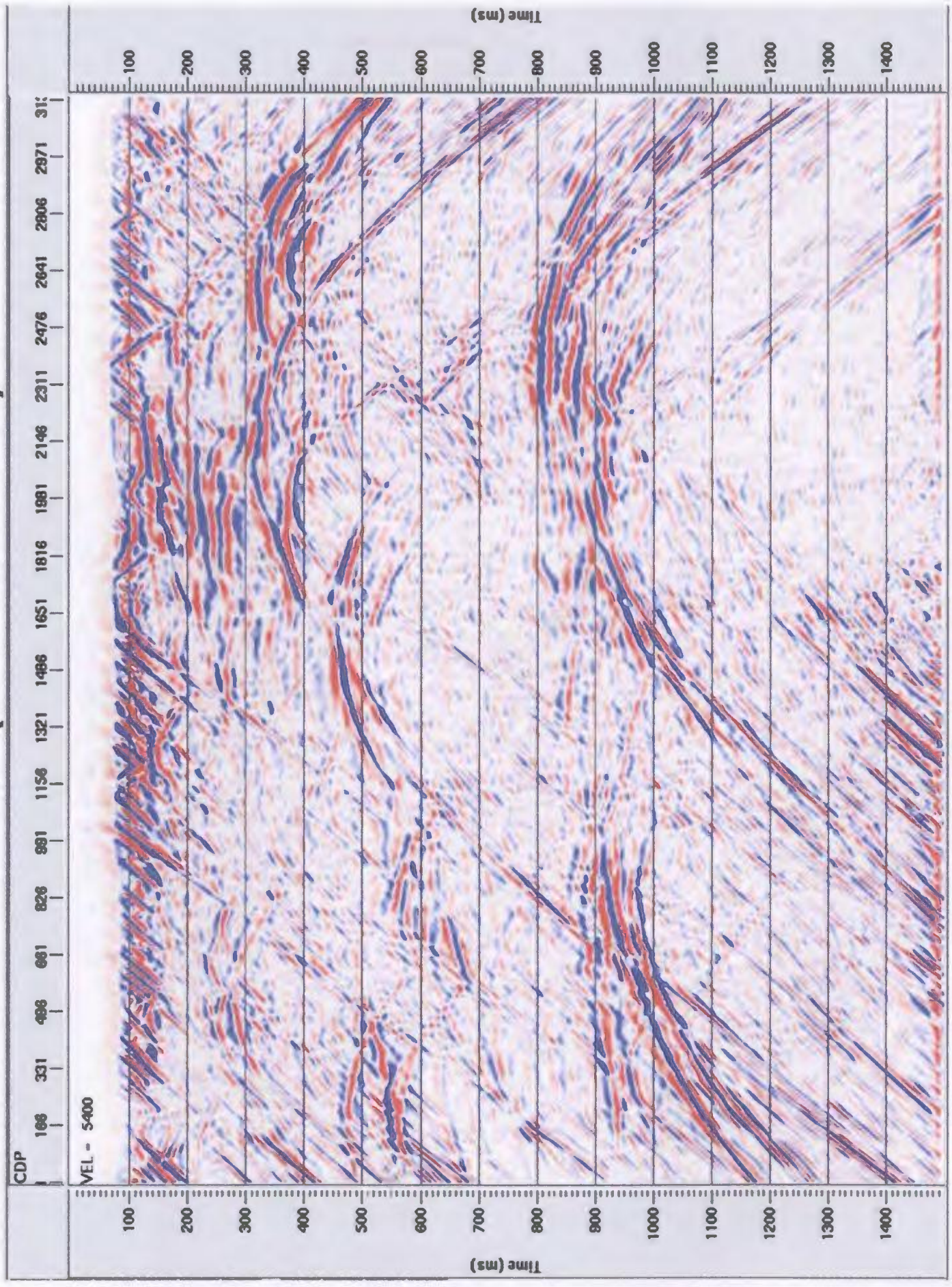
CVS (5400 m/s)
CDP
VEL = 5400
Time (ms)

# CVS (5600 m/s)

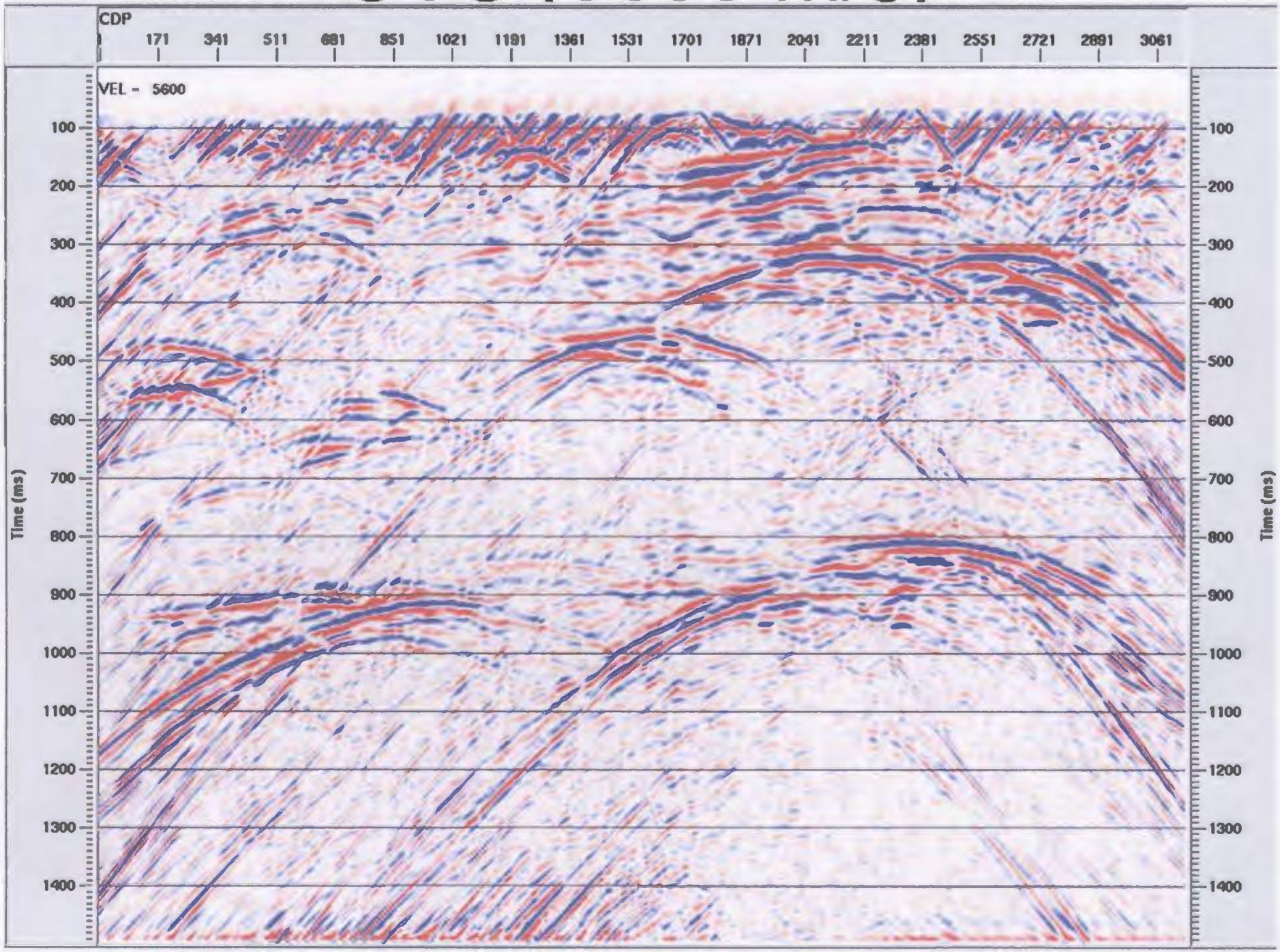
CDP
171
341
511
681
851
1021
1191
1361
1531
1701
1871
2041
2211
2381
2551
2721
2891
3061
VEL - 5600
100
200
300
400
500
600
700
800
900
1000
1100
1200
1300
1400
Time (ms)

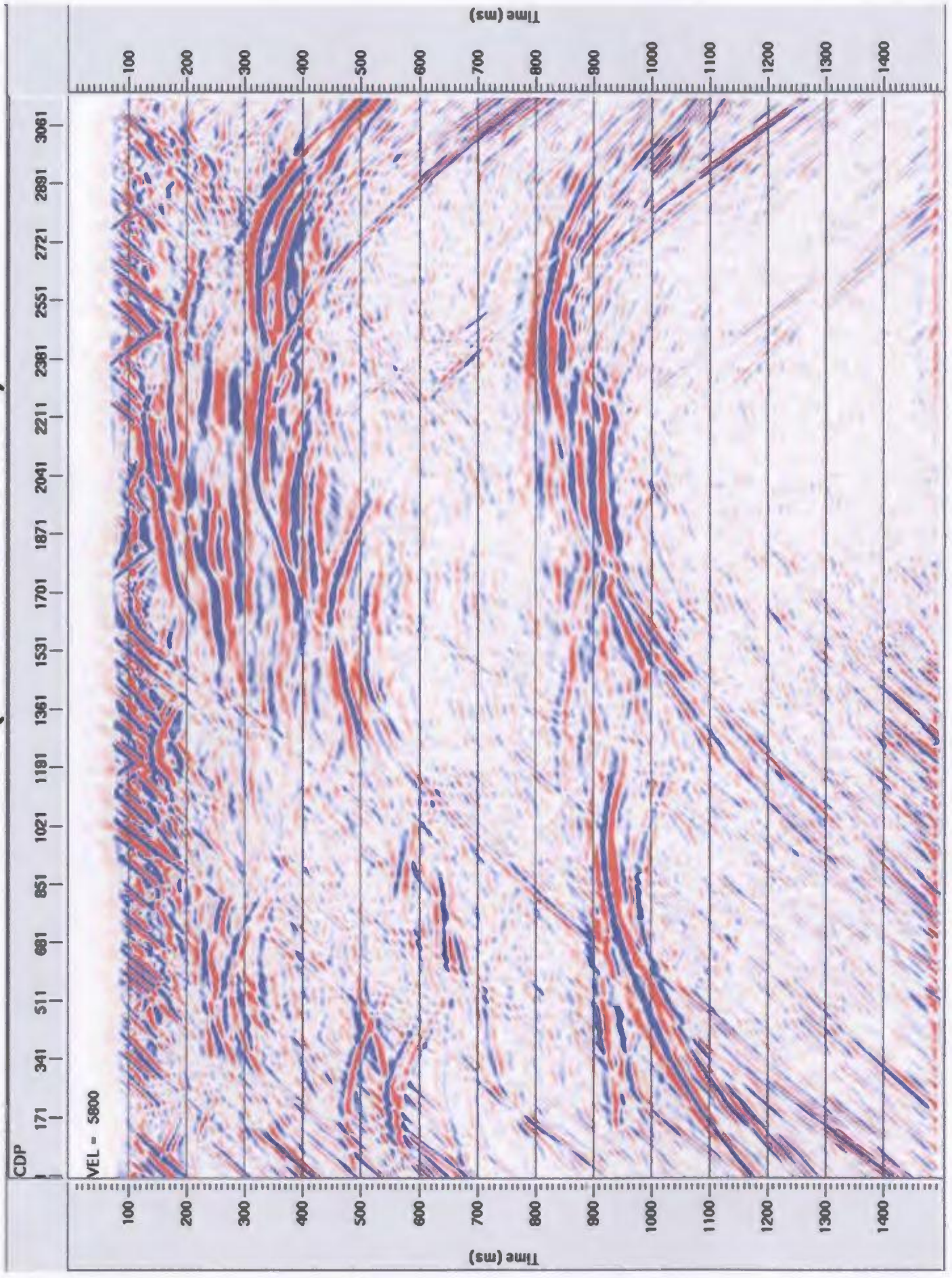
CVS (5800 m/s)
CDP
171
341
511
681
851
1021
1191
1361
1531
1701
1871
2041
2211
2381
2551
2721
2881
3061
VEL = 5800
Time (ms)
100
200
300
400
500
600
700
800
900
1000
1100
1200
1300
1400

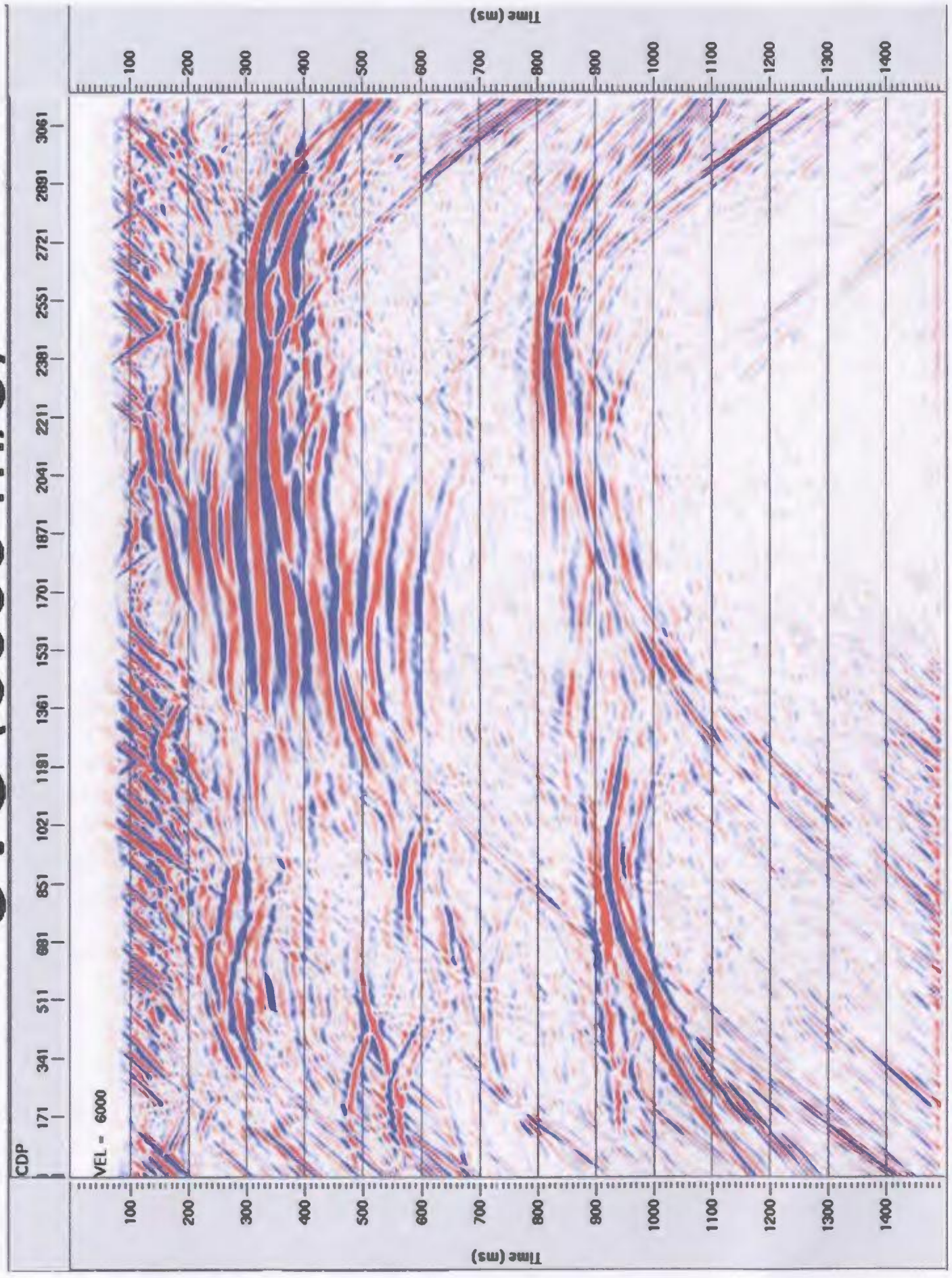
CVS (6000 m/s)
CDP
171
341
511
681
851
1021
1191
1361
1531
1701
1871
2041
2211
2381
2551
2721
2891
3061
VEL = 6000
Time (ms)
100
200
300
400
500
600
700
800
900
1000
1100
1200
1300
1400

# CVS (6200 m/s)

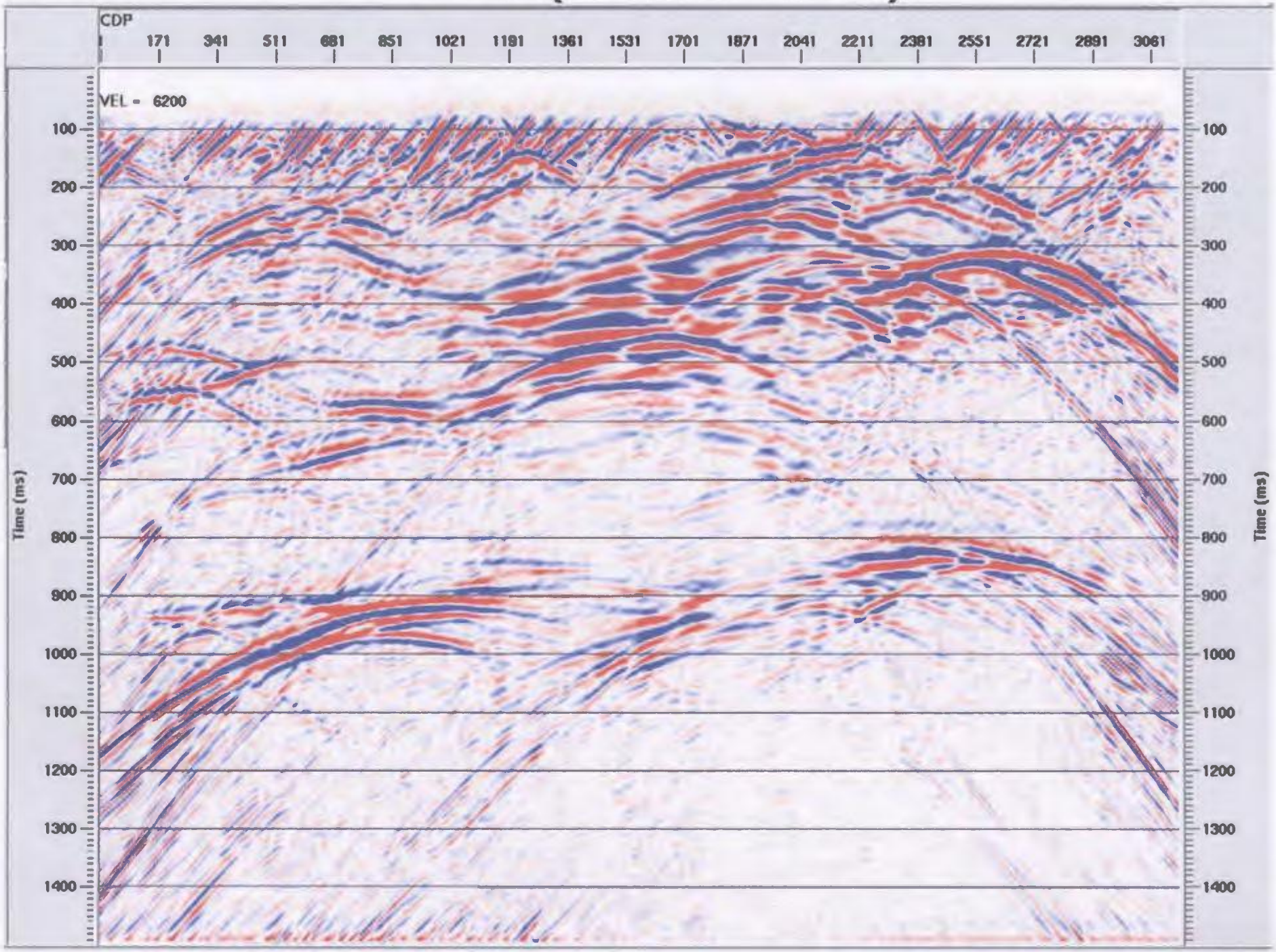
CDP
1
171
341
511
681
851
1021
1181
1361
1531
1701
1871
2041
2211
2381
2551
2721
2891
3061
VEL - 6200
Time (ms)
100
200
300
400
500
600
700
800
900
1000
1100
1200
1300
1400

# CVS (6400 m/s)

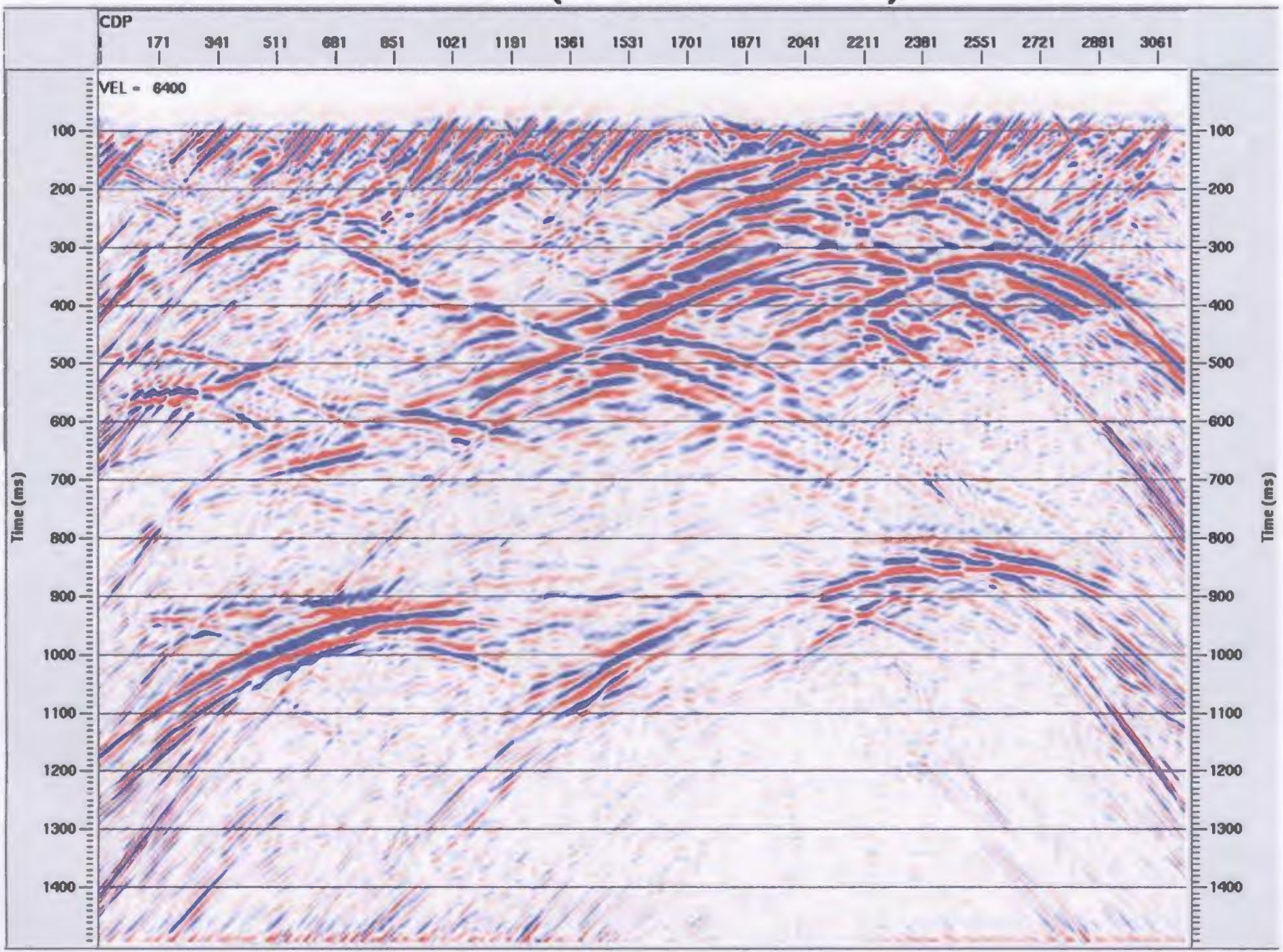
CDP
171
341
511
681
851
1021
1191
1361
1531
1701
1871
2041
2211
2381
2551
2721
2891
3061
VEL = 6400
100
200
300
400
500
600
700
800
900
1000
1100
1200
1300
1400
Time (ms)

# CVS (6600 m/s)

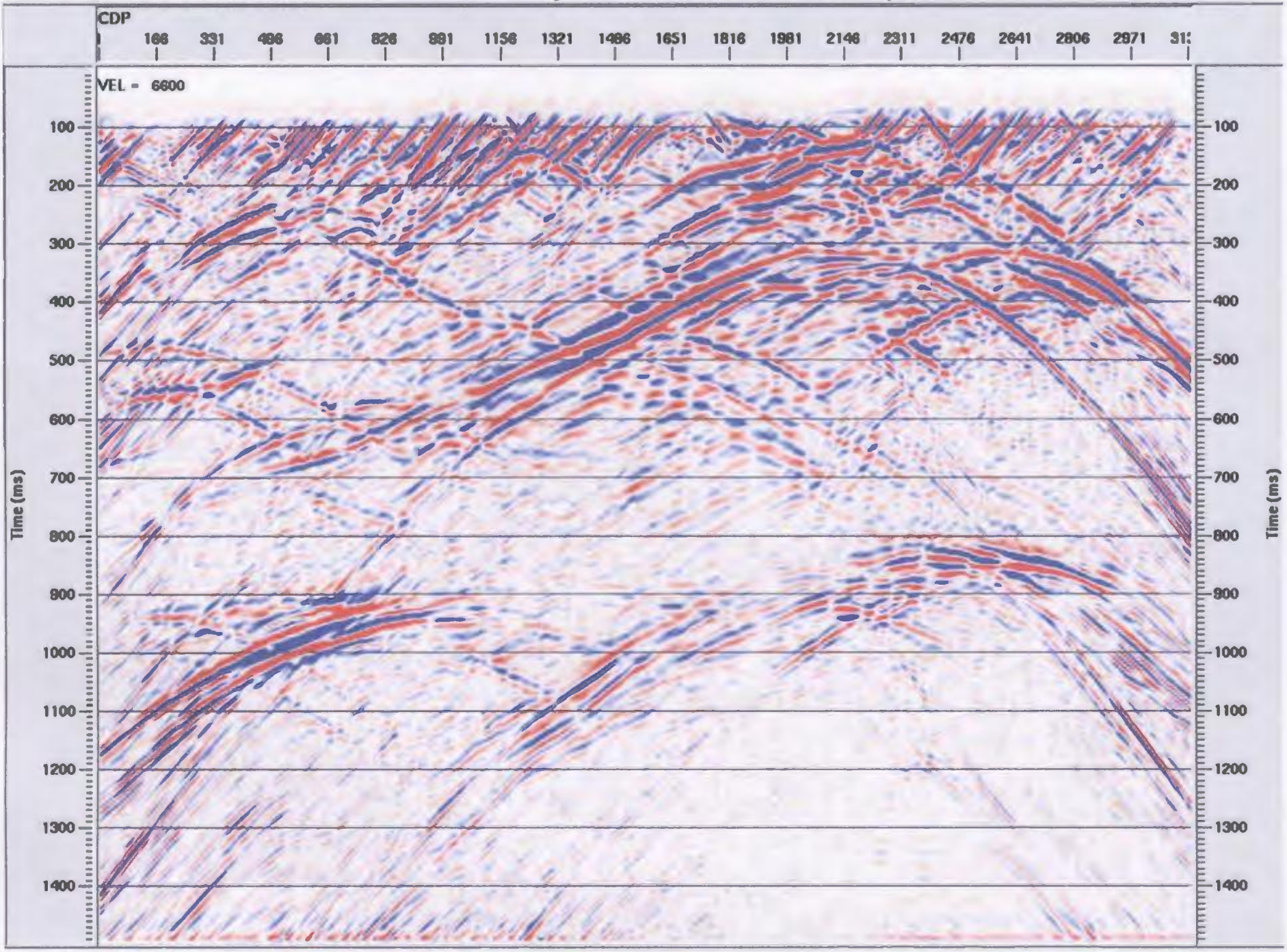
CDP
166
331
496
661
826
991
1156
1321
1486
1651
1816
1981
2146
2311
2476
2641
2806
2971
VEL = 6600
Time (ms)
100
200
300
400
500
600
700
800
900
1000
1100
1200
1300
1400

# Appendix C

## C-1: Event Alignment Statics

| Source | In-lines | | | Cross-Lines | | |
|---|---|---|---|---|---|---|
| | Max. allowable static shift | # of traces in window | Window analysis parameters | Max. allowable static shift | # of traces in window | Window analysis parameters |
| 1 | 25 ms | 60 | 2100-2180 ms | 25 ms | 60 | 2000-2260 ms |
| 2 | 20 ms | 60 | 2120-2140 ms | 20 ms | 60 | 2120-2140 ms |
| 3 | 25 ms | 60 | 2100-2200 ms | 25 ms | 60 | 2100-2200 ms |
| 4 | 20 ms | 60 | 2100-2180 ms | 20 ms | 60 | 2100-2180 ms |

## C-2: Primary Hand Statics

| Source | Datum (ms) | Peak (ms) | Shift (ms) |
|---|---|---|---|
| 1 | 1000 | 1174 | -174 |
| 2 | 1000 | 1034 | -34 |
| 3 | 1000 | 1520 | -520 |
| 4 | 1000 | 1506 | -506 |

## C-3: Re-processed Hand Statics

| End A | | | | End B | | | |
|---|---|---|---|---|---|---|---|
| Source | Datum (ms) | Peak (ms) | Shift (ms) | Source | Datum (ms) | Peak (ms) | Shift (ms) |
| 1 | 1080 | 1174 | -94 | 2 | 1000 | 1036 | -36 |
| 3 | 1080 | 1520 | -440 | 4 | 1000 | 1506 | -506 |

# Appendix D

This appendix illustrates that the complex diffracting pattern from the scatterer model in Chapter 4 is best visualized by animation of horizontal time slices. The 'bulls-eye' pattern is more evident when the time slices are assembled together and animated because the human eye tends to focus on the coherent 'bulls-eye' pattern instead of the incoherent noise.

Animations for each individual source, both stacked ends A and B, the final stack, stacks with low, moderate, and high S/N, both migrated ends A and B and the final migration are located on the CD in the back pocket.